Atomistic simulation of defects and diffusion in oxides

Samuel T. Murphy

A dissertation submitted for the degree of

Doctor of Philosophy

at Imperial College London

May 2009

Dedicated to the memory of Thomas Murphy

Cheers dad!

Abstract

Magnesium aluminate spinel, $MgAl_2O_4$, is an excellent model tertiary oxide which has been the subject to a significant number of experimental and theoretical studies since its structure was first reported by Bragg in 1915 [29]. One of the defining characteristics of this material is its ability to tolerate a significant degree of inversion between the cation sublattices: that is, magnesium ions, which Bragg allocated to the tetrahedral sublattice can become exchanged with aluminium ions that he assigned to the octahedral sublattice. This apparently simple modification has profound affects on the physical properties of this material. The presence of antisite defects can affect both the concentrations of other intrinsic point defects as well as cation migration energies. Antisite defects can also accommodate MgO or Al_2O_3 excess in nonstoichiometric spinel.

There are three principle factors that can affect transport of cation species in spinel, these are: (i) the concentration and hence availability of the mediating point defect, (ii) the activation energy for an isolated 'hop' and (iii) the diffusion prefactor, D_0. This prefactor contains information such as the number of equivalent pathways, jump distances and the attempt frequency. In this thesis atomistic simulation is used to determine the structures and relative concentrations of the isolated intrinsic point defects as well as the diffusion migration energies energies and prefactors. This allows a thorough understanding of the kinetic and thermodynamic processes occurring in a spinel (assuming defect concentrations are very low, ie. at the dilute limit). In order to extend this study to cover real materials, the accelerated dynamical technique, TAD, was applied to point defects that are clustered to oppositely charged point defects, such as those responsible for nonstoichiometry. The results demonstrate the immense complexity that can arise from the formation of defect clusters but allow some overarching conclusions to be

drawn concerning the affect of defect clustering on ion diffusion.

Atomistic simulation was also used to examine isovalent cation substitution into BO oxides. This allowed the construction of a general relationship between the difference in size of the host and substitutional cations.

Acknowledgements

I could not have completed this thesis without the invaluable contributions of many other people. First and foremost I would like to thank my supervisor Prof. Robin Grimes, not just for offering me the opportunity to work in the Atomistic Simulation Group but for his excellent supervision and guidance throughout the duration of my ordeal. This thesis really wouldn't have been possible without the other members of the ASG and so I would like the whole group, particularly those who have diligently read and corrected sections of the final document, namely; Dave Parfitt, Micheal Rushton and Alex Chroneos. The simulations presented in this thesis were dependent on the continued maintenance of our beloved cluster, tantallan, and the efforts of Donat Fatet and Antony Cleave to ensure this facility worked as it should. Jon Ball was the man from whom I took over as the ASG spinel man and I would like to thank him for his efforts in getting me started, and I would like to thank Ankoor for his floor space in Los Alamos. Lastly, from the ASG, I would like to thank Emily Michie, for introducing me to Imperial College and for moral support and beverage related team building activities throughout.

During my PhD I was fortunate enough to collaborate with people from two outstanding institutions in Los Alamos National Laboratory (LANL) and Loughborough University. From Los Alamos, I would like to recognise the efforts of Blas Uberuaga, Kurt Sickafus and Chris Stanek and from Loughborough, Roger Smith, Chris Gilbert and Pravesh Bacorisen.

I don't think it is possible for me to emphasise how grateful I am to my mum for all of her work and support through all of my 26 years, but I will try by saying a very big thank you mum! Thanks also to my brothers, Philip, Russell and William for keeping my spirits high and to Steve for keeping me in wine when I visited during my extended writing up period.

I've heard it said before that writing a PhD thesis can be a very stressful and depressing time, however, over the last two years whenever I have found the going tough there has been a beacon of light waiting for me whenever I left the office. Thank you Caroline for always being there and cheering me up when I was down and making the last two years an absolute pleasure. I can't wait to see our theses sat next to each other on our ikea bookcase! xxx

Table of Contents

List of Figures

List of Tables

1

Introduction

The evolution of materials science and the evolution of human society are inextricably linked. Such is the depth of this relationship that entire eras of human history are named after the materials that defined them (ie. the stone, bronze and iron ages). The ability to work materials to develop tools, such as spears and fish hooks, is one of the ways in which man has elevated himself to levels not witnessed elsewhere in the natural world. One of the earliest examples of what we would recognise today as materials science is the firing of clay and sand in an open fire to make pottery. The next major milestone, in both material and human evolution, was the extraction of copper and tin metals from ores and their subsequent mixing to make bronze [1]. Some of the earliest bronze artefacts can be traced back to roughly 3500 BC and this marks the beginning of the bronze age [1]. Mankind's emergence into the bronze age also signifies the dawn of the field of metallurgy. It is from metallurgy that modern materials science was born.

In a modern sense, materials science and engineering is a multidisciplinary field with the joint goals of understanding material properties and the development of new materials capable of greater performance. A developed understanding of the underlying principles responsible for a material's properties will aid in the development of new materials. Willard Gibbs [2], in the late 19th century, observed a link between the thermodynamic properties relating to atomic structure and the macroscopically observable properties of a material. The atomic structure of a material depends on factors such as; the constituent atoms or ions, how the material was processed, the material's history and external conditions, such as irradiation. Consequently it is essential to understand how these factors can affect the atomic structure and therefore a material's properties. Recent developments in experiential techniques and in particular the rapid

expansion of computational modeling have enabled more in-depth investigations into material's behaviour and have opened up new fields within materials science, such as nanotechnology and biomaterials.

Since the industrial revolution began in Great Britain, in the late 18th century, there has been a dramatic increase in the burning of fossil fuels for energy. The rapid industrialisation of developing countries (such as China, India and Brazil) coupled to an ever increasing global population suggests that demand for energy will continue to increase at an alarming rate. Unfortunately, as fossil fuel use has been stepped up over the last three centuries, the level of carbon dioxide in the atmosphere has increased accordingly. Carbon dioxide, along with numerous other gasses (eg. methane, CH_4), in the atmosphere absorb energy from the sun which has been reflected off the earth's surface. As the concentration of these 'greenhouses gasses' in the atmosphere increases the amount of this energy that is trapped will increase and a concomitant rise in global temperature can be expected. This phenomenon was first explained by Joseph Fourier in 1824 [3]. The impact of even a small increase in global temperature could be catastrophic, particularly for people living in low lying regions of the world, which would be flooded by rising sea levels.

Crafting a solution to the climate change problem, whilst continuing to meet the demand for energy, is one of the great challenges of the 21st century. Any attempt to reduce the impact of man made climate change will need to be multifaceted and consist of new methods of generating energy but also increasing efficiency and ultimately taming demand. There are many technologies, currently under development that have the possibility to generate the energy required, with significantly reduced carbon emissions. These include nuclear fission and fusion, fuel cells, wind, solar, tidal, geothermal and biofuels. The successful implementation of many of these technologies is and will continue to be dependent on materials from which they are constructed. Materials science is also essential in increasing efficiency, that is, constructing buildings out of more thermally insulating materials that can reduce energy waste.

Over the course of the last 50 years, nuclear power stations throughout the world have been generating electricity without the enormously large carbon emissions associated with fossil fuel based methods of electricity generation. However, following the accident at Chernobyl in 1986 public opinion turned strongly against nuclear power. Consequently there have been very few new reactors opened since. More recently, owing to the threat posed by man made

climate change, nuclear power appears to be undergoing a renaissance as governments look to meet their emissions targets, as laid out in the Kyoto Protocol [4]. New fission reactors, termed Generation IV, are currently being designed to take into account recent advances in both materials science and engineering physics.

Generation IV reactors are the state of the art in terms of energy generation from nuclear fission, however, looking to the longer term there is the possibility of producing electricity from nuclear fusion. Nuclear fusion involves the fusing together of two light atoms to form a heavier one, as shown in equation 1.1, releasing a large amount of energy in the process. It is this process that occurs at the very centre of stars.

$$ {}^{3}_{1}\mathrm{T} + {}^{2}_{1}\mathrm{D} \quad {}^{4}_{2}\mathrm{He} + {}^{1}_{0}\mathrm{n} + \mathit{Energy} \tag{1.1} $$

In order to overcome the nuclear repulsion between the two ions, very high temperatures are required. A fusion plasma is, therefore, very hot and must be suspended within a magnetic field, for example, in a toroid shaped reactor, commonly referred to as a tokamak. Despite the magnetic confinement, the materials from which these reactors are constructed will be required to operate at high temperatures and under high flux, fast neutron bombardment over large timescales.

Previous fission reactor designs incorporated the extensive use of traditional building materials, however, there is now an impetus to move away from materials such as steel and make greater use of ceramic materials. Ceramic materials are currently employed in the nuclear industry as a fuel matrix (ie. UO_2 [5]) and are being seriously considered as a host matrix for the immobilisation of actinide waste that is to be stored in a geological repository [6]. There are numerous design proposals for a commercial nuclear fusion power station and many of these incorporate a significant use of ceramic materials. The region immediately behind the 'first' wall (the first wall directly faces the plasma) of a fusion reactor could be made up of a lithiated ceramic material (eg. Li_4SiO_4 [7] or Li_2TiO_3 [7]) which will be used to generate the tritium ($^{3}_{1}\mathrm{T}$) fuel essential to maintain the fusion plasma as well as protecting the external structure from high energy neutrons.

Owing to its excellent neutron irradiation tolerance, magnesium aluminate spinel, $MgAl_2O_4$, has been selected as a candidate material for use in fusion reactors. More specifically it has

been suggested for use as dielectric windows in the radio frequency heating systems or as an insulating material for the magnetic coils [8]. This thesis aims to investigate, using atomistic simulation techniques, the defect structure, stability and transport process in an equilibrated spinel as well as considering how these processes are likely to be influenced by factors such as nonstoichiometry and irradiation. It is also hoped that the defect and transport properties of this relatively simple system can be confirmed experimentally and the fundamental understanding obtained may prove applicable to other similar systems (ie. more than one cation sublattice).

2

Literature review

2.1 Disorder in crystalline materials

2.1.1 Crystal structures

Early in the history of modern science it was suggested that the regular external form of crystals implied an internal regularity of their constituents. In 1784 Haüy [9] created the *law of rational intercepts* which states that the form of crystals could be uniquely described by reference to crystal axes, their relative lengths and angle of inclination. Once defined these axes marked out a unit cell that is the smallest unit to possess the symmetry of the crystal as a whole. This led to the recognition that there are seven systems of crystal symmetry; cubic, hexagonal, tetragonal, orthorhombic, rhombohedral, monoclinic and triclinic. These seven systems of crystal symmetry represent the simplest seven shapes that can be infinitely tessellated in three dimensional (3D) space without leaving any empty space. Bravais established in 1848 that there are 14 distinct ways of arranging networks of points within these seven crystal systems [10]. Centered on each lattice point is a motif (or basis) consisting of one or more atoms, which is replicated throughout the crystal.

The space group of a crystal structure is a mathematical description of the symmetry inherent in the structure. In three dimensions the space groups are made up from the 32 crystallographic point groups and the 14 Bravais lattices. This results in a space group being a combination of the translation symmetry of a unit cell, the point group symmetry operators of reflection, rotation and improper rotation as well as screw axis and glide plane symmetry operations.

Screw axis and glide planes are compound symmetry operations as they are combinations of rotation or reflection with a translation equal to less than the unit cell size. These generate 230 unique space groups, which describe all possible crystal systems [11–13].

The description of a crystal, given above, describes a 'perfect' unit cell, however, a 'real' material will have imperfections in its crystal lattice. For simplicity it is customary to discuss these imperfections as either point defects or extended defects. Point defects are imperfections that are localised over a few atomic sites whilst extended defects are those that influence larger volumes of a material. Defects formed within a material that do not include the presence of any foreign atoms are known as intrinsic defects. Conversely a defect that incorporates a foreign atom is referred to as an extrinsic defect. A brief overview of the intrinsic point defect processes is given in section 2.1.2 whilst extended defects also include grain boundaries and surfaces. The inclusion of defects into a crystal can have a profound affect on the macroscopic properties of a material, and in many cases a material's desirable properties arise as a consequence of intrinsic or extrinsic defects. An understanding of defect properties may facilitate the development of many useful materials and devices which could not be obtained if constrained to be designed and developed from 'perfect' systems [14].

2.1.2 Intrinsic point defects

During crystal growth, as a result of irradiation damage or simply as a result of a thermally activated process, atoms become displaced from their lattice site thus generating unoccupied or vacant lattice sites. These vacancies are generally stable at room temperature (ie. remain unoccupied on timescales much greater than atomic vibrations) and may be mobile at higher temperatures (that is the unoccupied site receives an atom or ion from an adjacent site, which itself becomes the vacant site). The removal of an atom from a lattice site disrupts the local bonding causing a distortion in the local crystal structure, this lattice distortion in the region surrounding the vacancy is known as the defect's strain field. If the vacancy is produced by displacing a lattice atom, then either (i) the released atom may be trapped within the lattice as an interstitial ion or (ii) move out to the surface to form new layers. These two distinct disorder processes are termed Frenkel and Schottky disorder and are illustrated in figures 2.1 and 2.2.

If we consider a binary metal oxide, MO, the defect reactions associated with the cation and

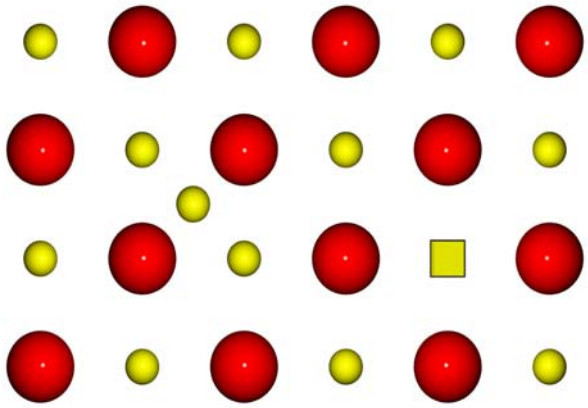

Figure 2.1: An MO crystal lattice containing cation Frenkel disorder. The yellow spheres represent, M^{2+}, cations and the red spheres represent O^{2-}. The transparent box represents a vacant lattice site.

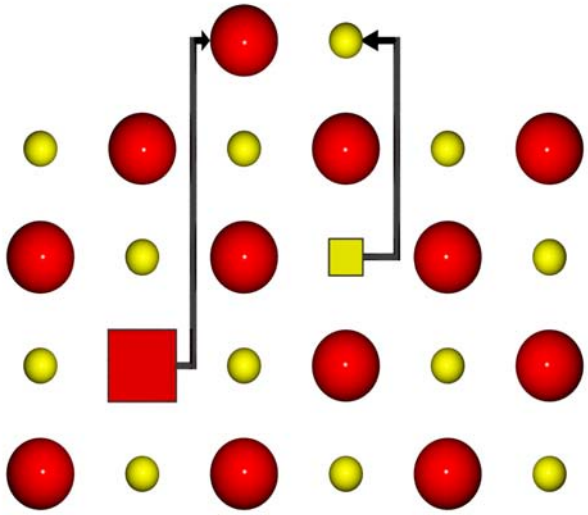

Figure 2.2: An MO crystal containing Schottky disorder. M^{2+} and O^{2-} ions have been transported form their lattice sites (represented by transparent boxes) to form new bulk material.

anion Frenkel processes are reported in equations 2.1 and 2.2 (these equations use Kröger-Vink notation [15], which is explained in Appendix A.

$$M_M \quad V_M + M_i^{\bullet\bullet} \tag{2.1}$$

$$O_O \quad V_O^{\bullet\bullet} + O_i \tag{2.2}$$

The reaction for Schottky disorder is reported in equation 2.3.

$$M_M + O_O \quad V_M + V_O^{\bullet\bullet} + MO \tag{2.3}$$

The Frenkel and Schottky reactions are referred to as intrinsic defect process because they are thermally activated process, requiring the addition of no external impurities. The other form of intrinsic disorder process that can make a significant impact on a crystal's properties is antisite disorder, where two ions swap lattice sites. In the simple binary oxide MO, this is a high energy process as it involves placing a positively charged cation on a site previously occupied by a negatively charged anion and vice-versa. This antisite reaction is reported in reaction 2.4 and figure 2.3.

$$M_M + O_O \quad M_O^{\bullet\bullet\bullet\bullet} + O_M \tag{2.4}$$

In crystals containing more than one cation (or anion) species it is possible for either the like charged cations or anions to exchange, as described in equation 2.5 for ABO_2, where A and B are divalent cations (in this example the resultant antisite defects are not charged).

$$A_A + B_B \quad B_A + A_B \tag{2.5}$$

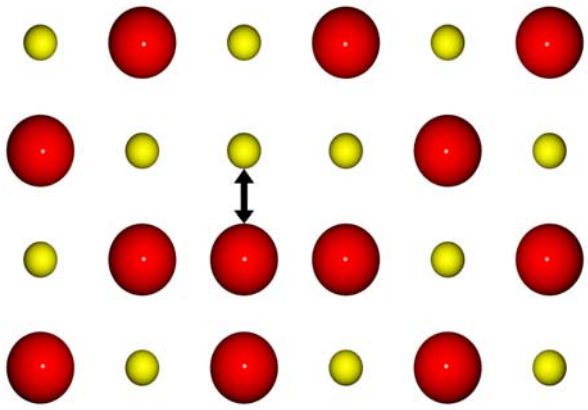

Figure 2.3: An MO crystal lattice containing antisite disorder. Here, a M^{2+} cation has been exchanged with an O^{2-} ion. In this example the defects are located on adjacent lattice sites and are therefore clustered, however, it is also possible for the defects to be located at a large enough separation that they are effectively 'infinitely' separated (ie. in the dilute limit).

2.1.3 Intrinsic defect concentrations

Isolated defects

As temperature is increased, the number of lattice ions that acquire sufficient energy to move away from their lattice site increases, thus leading to an increased concentration of intrinsic defects and a concomitant increase in the internal energy of the system. As the number of defects increases, so does the number defect configurations (arrangements) within the crystal (ie. the configurational entropy) which leads to a decrease in the overall energy of the system. It is convenient to consider the system at constant pressure and temperature, in which case, the change in Gibb's free energy (ΔG) is given by equation 2.6,

$$\Delta G = \Delta U - T\Delta S \tag{2.6}$$

where, ΔU is the change in internal energy of the crystal and ΔS is the change in entropy. Consider the solid, MO, containing n_s Schottky defects, there will be n_s cation vacancy and n_s anion vacancies. If the energy to form one Schottky pair is E_f^s then the change in internal energy is the product of the number of the these defect pairs and the energy to form one pair (equation 2.7) [10].

$$\Delta U = n_s E_f^s \tag{2.7}$$

The simultaneous increase in entropy can be obtained from the Boltzmann relation [16],

$$\Delta S = k_B \ln w \tag{2.8}$$

where, k_B is the Boltzmann constant and w is the number of ways of arranging n Schottky pairs in the crystal. The number of ways of arranging n_s cation vacancies on N cation sites can be found using equation 2.9.

$$w_{cation} = \frac{N!}{n_s!(N-n_s)!} \tag{2.9}$$

An equivalent expression can be found for determining the number of ways of arranging n_s anion vacancies on N anion sites and therefore the configurational entropy can be given by,

$$\Delta S = k_B \ln(w_{cation} w_{anion}) \tag{2.10}$$

$$\Delta S = k_B \ln\left(\frac{N!}{n_s!(N-n_s)!} \cdot \frac{N!}{n_s!(N-n_s)!}\right) \tag{2.11}$$

$$\Delta S = 2k_B\{\ln(N!) - \ln(N-n_s)! - ln(n_s!)\}. \tag{2.12}$$

If n_s is sufficiently large then Stirling's approximation [17] ($\ln n_s! \quad n_s \ln n_s$) can be applied to equation 2.12 to give,

$$\Delta S = 2k_B[N\ln N - (N-n_s)\ln(N-n_s) - n_s \ln n_s] \tag{2.13}$$

which can be combined with equations 2.6 and 2.7 to leave,

$$\Delta G = n_s E_f^s - 2k_B T[N\ln N - (N-n_s)\ln(N-n_s) - n_s \ln n_s] \tag{2.14}$$

At thermodynamic equilibrium the free energy is at a minimum, therefore the first derivative of 2.14 with respect to n_s is equal to zero.

$$\frac{\partial G}{\partial n_s} = E_f^s - 2k_B T \ln\left(\frac{N-n_s}{n_s}\right) = 0 \tag{2.15}$$

Assuming that the number of defects is small compared to the number of lattice sites (ie. $n_s \quad N$) then equation 2.15 can be rearranged to give,

$$\frac{n_s}{N} = \exp\left(\frac{-E_f^s}{2k_B T}\right) \tag{2.16}$$

where the quantity n_s/N represents a concentration of Schottky pairs (a shorthand notation for defect concentration is given by $[n]$). It is possible to conduct an analogous derivation for each type of intrinsic disorder discussed section 2.1.2.

Defect clusters

In the derivation above it is assumed that the concentration of defects is sufficiently low that their mutual interactions can be neglected. In reality, for higher concentrations, the electrical and elastic interactions between defects are relevant and may give rise to changes in the spatial distribution of defects. Again considering the crystal, MO, defect association can be written as shown in equation 2.17.

$$\mathrm{V_M} + \mathrm{V_O^{\bullet\bullet}} \qquad \{\mathrm{V_M} : \mathrm{V_O^{\bullet\bullet}}\} \tag{2.17}$$

The binding energy, BE, is defined as the difference between the defect energies of the clustered defects, $E_f^{cluster}$ and the energies of the isolated defects, $E_f^{isolated}$, as shown in equation 2.18.

$$BE = E_f^{cluster} - \sum_i E_f^{isolated} \tag{2.18}$$

A negative binding energy implies that it is energetically favourable for the defects to exist in a 'bound' cluster rather than in isolation.

2.2 Solid state diffusion

2.2.1 Introduction

Diffusion can be considered as the net number of atoms to pass through a plane of unit area per unit time. This process is driven by a non-uniform gradient, generally referred to as a driving force. One of the most common driving forces is the presence of a concentration or chemical gradient, whereby atoms move from a region of high concentration to a region of low

concentration. The formal mathematical description of diffusion was derived by Fick [18] and is given in equation 2.19 for a single spatial dimension,

$$J = -D\frac{\partial C}{\partial x} \tag{2.19}$$

where, J is the flux of atoms, D is the diffusion coefficient and $\frac{\partial C}{\partial x}$ represents a concentration gradient.

From a microscopic point of view, diffusion occurs by Brownian motion [19] of atoms or molecules. By studying the motions of granules from pollen in water the Scottish botanist Robert Brown [19] observed a chaotic motion of the particles. Albert Einstein [20] argued that the motion of mesoscopic particles is due to presence of molecules in the liquid. Furthermore, that these molecules, owing to the Boltzmann distribution of their energies, are subject to thermal movements of a statistical nature. These statistical fluctuations are the source of stochastic motions occurring in matter all the way down to the atomic scale [21]. Einstein related the mean square displacement (MSD) of particles to the diffusion coefficient, which will be discussed later.

In gases, diffusion occurs by the free flights of atoms (or molecules) between collisions; the individual path lengths are distributed around some well defined mean free path. Atomic motion in liquids is more subtle and can be though of as a ‘shuffling‘ process where each motion is less than the average spacing of atoms in a liquid. Diffusion in the solid state is the result of random atomic ‘hops’ in a lattice. The diffusivity of each ‘hop’ can be expressed by considering a number of physical quantities that describe the elementary jump processes. These factors include: the jump rates, jump distances, geometric and correlation factors [21].

The intrinsic point defects, mentioned previously, are often the vehicles that allow atoms to perform the tiny jumps, which constitute diffusion. For each defect type there is a specific migration mechanism and in many cases, combinations of these point defects lead to more complex diffusion mechanisms. What follows is a brief description of the most simple mechanisms by which atoms can be transported through a crystal lattice.

Vacancy mechanism

The vacancy mechanism is facilitated by the presence of vacancy point defects. In the process an atom on a lattice site hops into a neighbouring vacant lattice site as illustrated in figure 2.4.

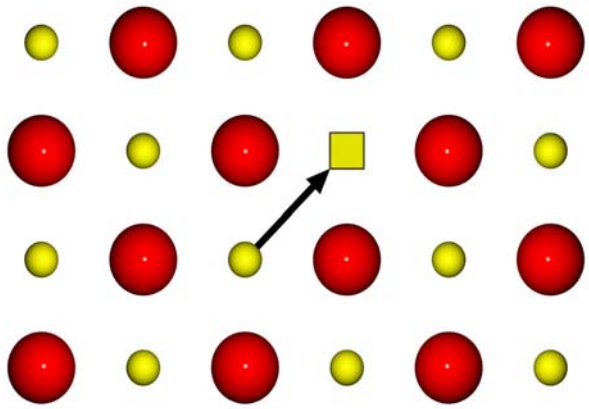

Figure 2.4: A M^{2+} cation migrating via a vacancy mechanism.

Figure 2.4 shows a cation migrating via a vacancy mechanism on the cation sublattice but vacancy migration can occur on either sublattice, or in some cases between sublattices.

Interstitial mechanism

An interstitial migration process occurs when an ion moves from one interstitial site to a neighbouring interstitial site. This process is illustrated in figure 2.5.

Interstitialcy mechanism

If the migration energy is too great to facilitate migration via a direct interstitial mechanism, there is another mechanism by which an interstitial ion can be transported. In this process an

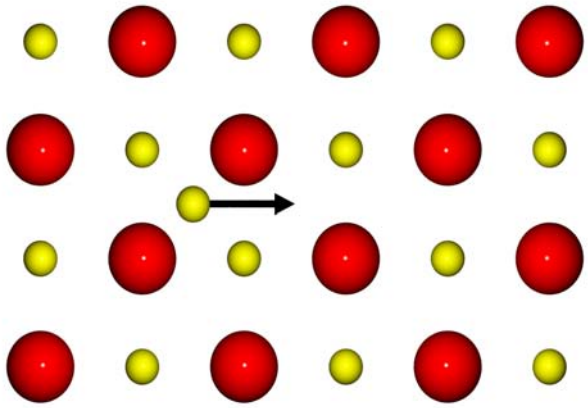

Figure 2.5: A M^{2+} cation migrating via a interstitial mechanism.

interstitial ion moves onto an occupied lattice site. The atom formally occupying the lattice site is forced to form a new interstitial, which can then continue the process (figure 2.6).

2.2.2 Transition state theory (TST)

Having examined the processes by which point defects can facilitate diffusion it is essential to examine the rate at which these processes can occur. The formalism that underpins our understanding of these random walk diffusion processes is transition state theory. Consider the vacancy mediated diffusion mechanism shown in figure 2.4; clearly the migrating cation has to squeeze between the two adjacent oxygen anions, a process that requires energy (ie. the atom enters an activated state often referred to as a transition state). This energy is usually greater than the thermal energy, $k_B T$, consequently these activated events are infrequent. At a finite temperature all atoms in a lattice will oscillate about their equilibrium positions because they do not posses enough energy to access the activated state and hence complete the jump so they simply continue to oscillate within the initial state. However, should, as a result of thermal activation, an atom have enough energy to reach the activated state along a given trajectory then a jump will occur.

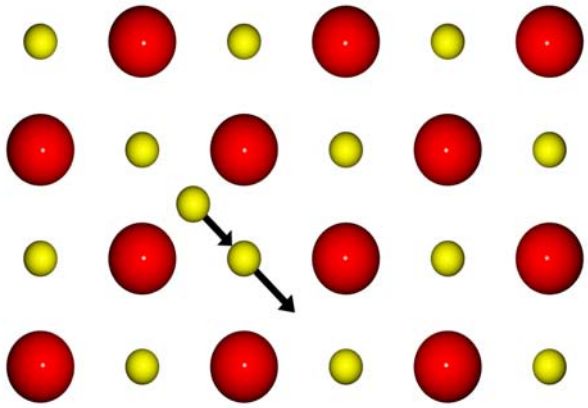

Figure 2.6: Pictorial representation of a M^{2+} cation migrating via a interstitialcy mechanism. An interstitial ion moves onto a lattice site thereby displacing a lattice atom onto a neighbouring interstitial site.

In the TST approximation, the classical rate constant for escape from a state A to an adjacent state B is taken to be the equilibrium flux through the dividing surface between A and B. Assuming that there are no correlated events (correlation and its possible affects will be discussed later) then this is, in fact, the exact rate constant. Figure 2.7 shows an example of a potential energy surface for a simple system with two possible equilibrium states A and B separated by an activated transition state. Our starting point finds an atom oscillating about state A until such a time as it oscillates along the trajectory leading to state B with sufficient energy to enter the transition state and cross over into state B.

It is possible to determine the time spent in each of the two states A and B as well as determining the number of times the dividing surface is crossed during the simulation. The rate of migration from state A is then half the number of crossings divided by the fraction of time spent in state A.

Another useful approximation to TST can be applied once a saddle point on the potential energy surface has been located and identified. Harmonic Transition State Theory (HTST) assumes that it is possible to consider the potential energy surface near a basin (at least the region

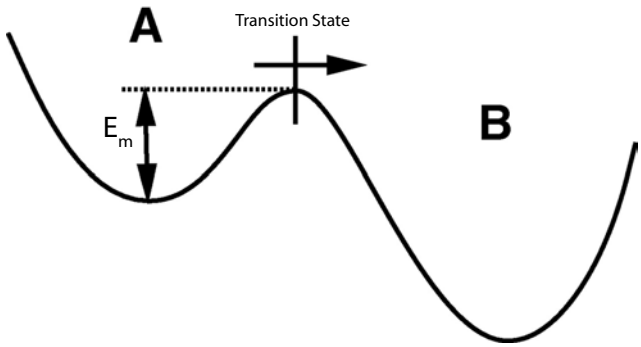

Figure 2.7: A two-state system that illustrates the definition of transition state theory as the flux through the transition state bounding A [22].

sampled thermally), as well as that near a saddle point using a second order expansion, ie. the vibrational modes are harmonic. The TST rate then becomes a simple Arrhenius term, as shown in equation 2.20,

$$k^{HTST} = v_0 \exp\left(\frac{-G_m}{k_B T}\right) \tag{2.20}$$

where,

$$G_m = E_m - TS_m \tag{2.21}$$

and

$$v_0 = v_0 \exp\left(\frac{S_m}{k_B}\right) = \frac{\prod_i^{3N} v_i^{min}}{\prod_i^{3N-1} v_i^{sad}}. \tag{2.22}$$

giving

$$k^{HTST} = v_0 \exp\left(\frac{-E_m}{k_B T}\right). \tag{2.23}$$

In the equations above, G_m is the Gibbs free energy for the process, E_m is the migration enthalpy (the enthalpy difference between the initial state and the saddle point), S_m is the entropy associated with this process, v_o is the Vineyard term [23] (which is simply the product of the exponent of the migrational entropy and the attempt frequency), v_i^{min} and v_i^{sad} are the nonimaginary normal mode frequencies at the minimum and the saddle respectively.

2.2.3 The diffusion coefficient

The diffusion coefficient is the mathematical function that relates the gradient in the concentration of a given species with the flux at a given temperature. As there are several different mechanisms (eg. vacancy and interstitial mechanisms) by which matter can be transported through the lattice, the overall diffusion coefficient can be given as the sum of these contributions, shown in equation 2.24.

$$D_{\text{Total}} = D_{\text{Vacancy}} + D_{\text{Interstitial}} \tag{2.24}$$

Here D_{Total} is the total diffusion of a species and D_{Vacancy} and $D_{\text{Interstitial}}$ (this includes both methods of interstitial diffusion) represent the contributions of the individual diffusion processes. There are numerous factors that combine to determine which of the diffusion processes is responsible for the majority of atomic transport. The two predominant factors are the concentration of the transport mediating point defects and the ease with which that mechanism can provide transport, often referred to as the diffusivity, d_x. Equation 2.25 shows how these factors combine to give the overall diffusion coefficient for a given species,

$$D_{\text{Total}} = \frac{n_{\text{Vacancy}}}{N} d_{\text{Vacancy}} + \frac{n_{\text{Interstitial}}}{N} d_{\text{Interstitial}} \tag{2.25}$$

where, n_{Vacancy} and $n_{\text{Interstitial}}$ are the number of vacancies and interstitials respectively and d_{Vacancy} and $d_{\text{Interstitial}}$ are the diffusivities of the vacancy and interstitials. The determination of the defect fraction has been covered previously (section 2.1.3), however, the diffusivity will be addressed here. Assuming harmonic transition state theory is valid, then the relationship between the diffusivity and the rate constant, is given by equation 2.26,

$$d_x = \frac{1}{6} f z a^2 k^{HTST} \tag{2.26}$$

where, f is the correlation factor which relates diffusion of actual atoms to the diffusion of the defect and will be examined more closely in the next section, z is the number of equivalent pathways the diffusing mechanism can follow and a is the jump distance. In order to simplify the expression shown in equation 2.26, the temperature independent terms are collected together in the constant D_0^x for a given process, shown in equation 2.27.

$$d_x = D_0^x \exp\left(\frac{-E_m}{k_B T}\right) \tag{2.27}$$

Including the defect concentration then gives,

$$D = D_0^x \exp\left(\frac{-E_m}{k_B T}\right) \exp\left(\frac{E_f}{k_B T}\right) = D_0^x \exp\left(\frac{-(E_m + E_f)}{k_B T}\right) = D_0^x \exp\left(\frac{-E_a}{k_B T}\right) \tag{2.28}$$

where E_a is the overall activation energy for the process. In the majority of experimental investigations of diffusion in the solid state, a plot of 1000 T^{-1} against $\log D$ is a straight line and values for E_a and D_0 are obtained from this Arrhenius plot [24].

2.2.4 Correlation factor

Up to this point it has been assumed that each random activated event has been independent of those that have gone before (ie. the correlation factor is unity), often however, subsequent vacancy jumps are correlated. Consider a radioactive tracer ion migrating via a vacancy mechanism. When the vacancy and the tracer atom jumps onto the vacant site, they move in opposite directions. Immediately after this exchange the vacancy resides adjacent to the tracer, therefore, there is finite probability of the tracer making a reverse jump. Consequently the tracer atom does not diffuse as far as expected for a completely random walk process, (ie. $f < 1$). The extreme example of this tracer diffusion via a vacancy mechanism in one dimension, as shown in figure 2.8.

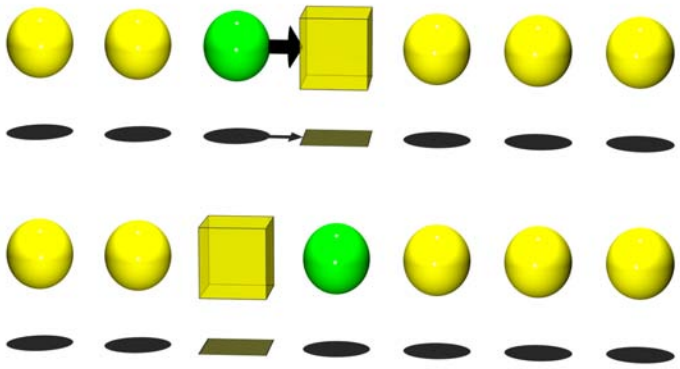

Figure 2.8: Diagram representing impurity diffusion via a vacancy mechanism in one dimension. The yellow spheres represent lattice atoms, the green sphere is the impurity atom and the transparent cube represents a vacancy.

In the example given in figure 2.8 the correlation factor is zero as once the vacancy and the tracer ion have exchanged the only possible migration the tracer ion could possibly make is to jump back onto the site it had just vacated. For self-diffusion the correlation factor is entirely dependent on the structure of the lattice and is independent of the atoms involved. A table of many of the most common correlation factors can be found on page 116 of Mehrer [21], however, these generally fall in the region 0.4-1.0. Unfortunately, the correlation factor can be significantly more complex when considering substitutional solutes, where the correlation factor is now dependent on the jump specific attempt frequency, migration energy and temperature.

2.3 Magnesium aluminate spinel

2.3.1 Introduction

Magnesium aluminate spinel ($MgAl_2O_4$) is an abundant naturally occurring mineral, found in the Earth's crust. The MgO-Al_2O_3 system is particularly important for the understanding of metallurgical slags, refractories, ceramic materials and the formation of microstructures in geological systems [25]. Magnesium aluminate is the intermediate phase in what appears, at first glance, to be a relatively simple system, ie. there is only one intermediary phase, spinel (figure 2.9).

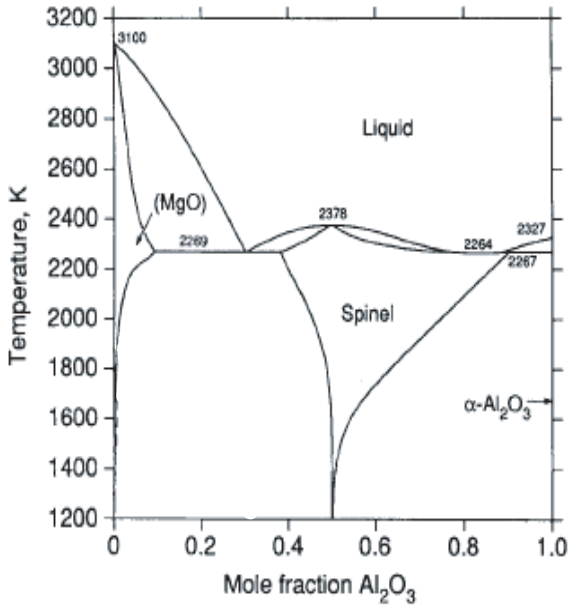

Figure 2.9: Phase diagram for the MgO-$MgAl_2O_4$ system from Hallstedt *et al.* [25].

2.3.2 Crystallography

Magnesium aluminate is the parent compound of the spinel group that has the general formula AB_2X_4 where A and B are cations and X is an anion. Some examples of other spinel materials which have been investigated previously are; Si_3N_4 and Ge_3N_4 [26], Ga_3O_3N [27] and γ-Fe_2O_4 [28]. The structure of $MgAl_2O_4$ as first reported by Bragg [29] and Nishikawa [30], assigned all Mg^{2+} cations to sites of tetrahedral symmetry and all Al^{3+} ions to octahedral sites within an Face Centred Cubic (FCC) Bravais lattice. What neither Bragg nor Nishikawa were aware of was that a number of the Mg^{2+} and Al^{3+} cations are exchanged. This phenomenon was first observed in spinel by Barth and Posjnak [31] and, in fact, such cation antisite defects occur in most spinels [32].

Nevertheless, from a formal crystallographic point of view spinel exhibits the $F\bar{4}3m$ space group [33], however, the simpler $Fd3m$ is usually adopted [34]. A magnesium aluminate spinel unit cell consists of eight formula units making a total of 56 atoms; 32 anions and 24 cations, consequently the spinel lattice parameters are large, ie. $a = 8.09$ Å [35]. The structure can be considered as a pseudo FCC arrangement of O^{2-} ions. Of the 64 tetrahedral

interstices eight are occupied by Mg^{2+} cations and of the 32 octahedral sites half are occupied by Al^{3+} cations. More formally, within the $Fd3m$ space group, the Mg^{2+} cations occupy $8a$ and Al^{3+} cations occupy the $16d$ Wyckoff positions. The O^{2-} anions occupy $48f$ Wyckoff positions, which are displaced approximately 0.1 Å in a $\langle 111 \rangle$ direction from the ideal FCC positions. This displacement from the ideal lattice sites, defined by the Wykoff site, is defined using the u parameter, which is simply a measure of this displacement. Figure 2.10 shows the structure of spinel, highlighting a number of tetrahedrally co-ordinated Mg^{2+} and octahedrally co-ordinated Al^{3+} cations.

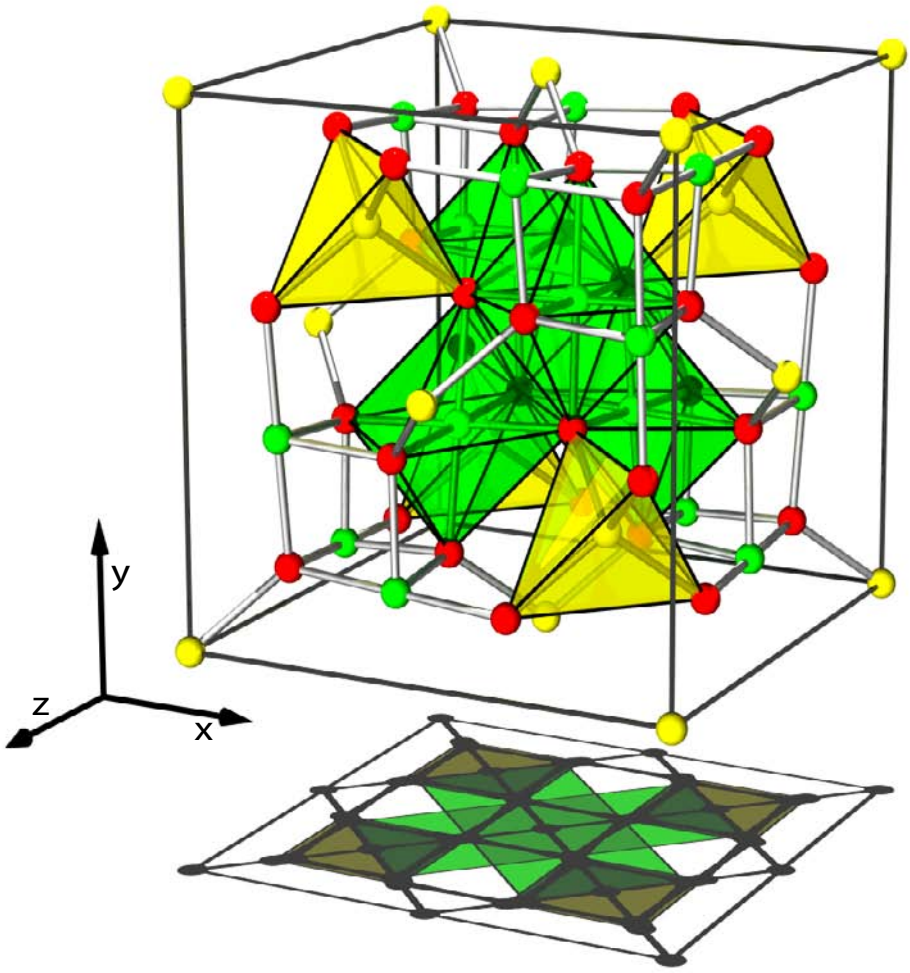

Figure 2.10: A perfect spinel unit cell. The red spheres represent oxygen anions while the green and yellow spheres represent the aluminium and magnesium cations respectively.

2.3.3 Cation antisite disorder in $MgAl_2O_4$

The crystallographic arrangement described above is referred to as normal spinel. However, as mentioned previously, it is usual for a number of octahedral Al^{3+} ions (Al_{Al}) to become exchanged for tetrahedral Mg^{2+} ions (Mg_{Mg}) via reaction 2.29,

$$Mg_{Mg} + Al_{Al} \rightleftharpoons Al'_{Mg} + Mg_{Al} \tag{2.29}$$

where, Mg_{Al} is a Mg^{2+} ion on a lattice site usually occupied by an Al^{3+} cation and the dash indicates that the Mg^{2+} cation has one less positive charge than the Al^{3+} it has replaced. Equation 2.29 is the cation antisite reaction and results in a degree of cation sublattice inversion. The level of inversion present in $MgAl_2O_4$ can be quantified using the inversion parameter, i, defined as $(Mg_{1-i}Al_i)[Mg_iAl_{2-i}]O_4$ where parentheses refer to the tetrahedral sites and square brackets to the octahedral sites. The level of inversion found in natural spinel, which has been allowed to equilibrate over geological timescales, can be relatively small ($0.05 < i < 0.12$) [36–38]. Conversely, cation disorder in synthetic magnesium aluminate spinel is generally more significant, with values as high as $i = 0.33$ [39]. There are, however, a number of other spinel materials which can exhibit far higher degrees of inversion. For example, $MgIn_2O_4$ where i 1 is considered to be fully inverse (ie. all the tetrahedral sites are occupied by In^{3+} cations and the remaining cations are randomly arranged on the octahedral sites). $MgGa_2O_4$ exhibits an inversion i 0.66; effectively a random arrangement of cations over both the tetrahedral and octahedral sites.

In geologic environments, the chemical and structural variations in spinels are dependent on both paragenesis and pressure-temperature ($P-T$) history; because of this, they are used as a petrogenetic indicator [40, 41]. There have been numerous experimental studies into the relationship between temperature and the degree of inversion, these include electron spin resonance (ESR) of impurity Cr ions (in $MgAl_2O_4$) [37], X-ray diffraction [42, 43], nuclear magnetic resonance (NMR) [44, 45], neutron diffraction [46, 47] and *in-situ* Raman spectroscopy [48]. At higher temperatures the number of atoms that have sufficient energy to vacate their lattice site is increased, consequently there are more interstitial and vacancy defects that can annihilate. There is a finite probability that a $Mg_i^{\bullet\bullet}$ (interstitial) defect will annihilate with a V_{Al} defect (or an $Al_i^{\bullet\bullet\bullet}$ defect will annihilate with a V_{Mg}defect) thus creating an antisite defect. Therefore as

the number of these defects is increased, annihilation will be increased leading to an increase in the overall level of inversion. Within the literature there is conflict concerning the maximum temperature at which an increase in inversion is observed, ie. Schmocker and Waldner [38] suggest that above 1220 K there is no further increase in cation inversion, however, other studies by Yamanaka and Takéuchi [42], Maekawa *et al.* [45], Redfern *et al.* [47], Seko *et al.* [49] and Andreozzi *et al.* [43] suggest that increases in cation disorder are evident up to temperatures approaching 1600 K. The ^{27}Al NMR spectroscopy experiments on quenched samples by Wood *et al.* [44] also suggest that there is no increase in inversion above 1170 K, however, they attribute this to higher temperature samples reordering to the 1170 K distribution during cooling. Andreozzi *et al.* [43] used quenched single crystals and detected a linear increase in cation disorder up to a temperature of 1370 K. As the temperature of the disordering run was increased, Andreozzi *et al.* [43] also observed a linear decrease in the lattice parameter, consequently they predicted a linear decrease in the lattice parameter as a function of cation inversion.

Ball *et al.* [50] used a combined energy minimization-Monte Carlo (CEMMC) atomistic simulation technique to reproduce the relationship between the degree of inversion and the lattice parameter. Whilst the magnitude of the decrease in lattice parameter as a function of inversion observed from this model is very similar to that obtained from experiment, the atomistic simulations suggested that the relationship was non-linear.

In order to avoid any possible loss of the high temperature equilibrium disorder, Redfern *et al.* [47] investigated high temperature cation disorder *in situ* using neutron diffraction. Their data suggests an inversion parameter in the region of 0.2 until a temperature of 800 K is obtained, at which point a linear increase in i with temperature up to about 1900 K is observed. They also note that the cell parameters appear to be insensitive to the degree of order, however, Andreozzi *et al.* [43] argues that this is due to the vibrational expansion due to the high temperature dominating the slight lattice parameter decrease resulting from inversion. One physical property that both sets of results seem to suggest is the variation in the oxygen positional parameter, u, as a function of inversion. From Redfern *et al.* [47] the relationship is $u = 0.26344 - 0.01021i$ versus $u = 0.2651 - 0.0123i$ obtained form Andreozzi *et al.* [43]. As the degree of inversion is increased it is expected that the local bonding around the cations sites will be disturbed. Redfern *et al.* [47] and Andreozzi *et al.* [43] both observe an increase in the average metal-oxygen bond distance around the octahedral site and a decrease in the average

metal-oxygen bond distance around the tetrahedral site, which is consistent with a decrease in the *u* parameter.

In recent years there has been considerable interest in developing modeling techniques capable of predicting cation ordering in spinels. In particular, it has been demonstrated that the thermodynamic model of O'Neill and Navrotsky [51] is very effective at describing ordering in end-member spinels. The O'Neill and Navrotsky [51] model states that the enthalpy of disorder can be represented as a quadratic function of the inversion parameter, as shown in equation 2.30,

$$H_D = \alpha i + \beta i^2 \tag{2.30}$$

where, α and β are coefficients that can be determined for a particular spinel from experimental data concerning the cation distribution as a function of temperature [52]. Initially it was suggested the vast majority of spinels could be described by assuming that β was negative with magnitude -20 kJ mol^{-1} [53]. Many of the experimental studies mentioned obtained values for the α and β coefficients of equation 2.30 by fitting to the experimental data; examples are shown in table 2.1.

Table 2.1: α and β parameters derived for the O'Neill and Navrotsky [51] model that relates the enthalpy for disorder and the degree of inversion (equation 2.30).

Author	$\alpha/kJmol^{-1}$	$\beta/kJmol^{-1}$	Reference
Redfern *et al.*	32.8	4.7	[47]
Andreozzi *et al.*	23(2)	13(4)	[43]
Millard *et al.*	25(5)	5.8(9.5)	[54]
Peterson *et al.*	31(1)	-10(3)	[46]
Wood *et al.*	36(1)	-23(2)	[44]

Clearly, there is still quite significant disagreement in the experimental literature concerning the values of the α and β coefficients, and indeed even the sign of β. This is almost certainly a result of the immense difficulty in creating perfectly stoichiometric samples, compounded by the challenging task of determining the degree to which a sample has been disordered, added to the inate problems associated with quenching or making experimental observations *in situ*.

Atomistic simulation is a useful technique when attempting to understand disorder in materials, as it becomes possible to investigate the atomistic forces that are responsible for the macroscopic observations made in the experiments mentioned above. Monte Carlo techniques, based on making random swaps within a system have been shown to be particularly effective in modeling cation disorder in spinels [50, 52, 55, 56]. The work of Palin *et al.* [52] attempted to address the variation in β values obtained experimentally by isolating the contributions of the chemical potential, η, tetrahedral-tetrahedral (T-T), octahedral-octahedral (O-O) and the T-O interactions. They demonstrated that the value of β depends on the relative enthalpy contributions of (T-T + O-O) vs. T-O interactions. Furthermore, they determined that there is little short range order found in normal spinels, although this is reversed when considering inverse spinels. Lavrentiev *et al.* [55] used an atomistic Monte Carlo technique to investigate the implications of cation inversion on the bulk modulus and the thermal expansion coefficient. Their results appear to agree with the conclusions proposed by Redfern *et al.* [47], in that, as the temperature is increased there is a concomitant increase in the lattice parameter, however, again this is likely to be due to thermal expansion rather than a disordering affect. Furthermore, they observed that pressure has no significant impact on the degree of inversion, an observation confirmed by the compressibility and structural behaviour study conducted recently by Nestola *et al.* [57].

2.3.4 Radiation damage in $MgAl_2O_4$

Up until the early 1980s there was comparatively little literature detailing how ceramic materials, as opposed to metals, respond to irradiation. In 1982 Clinard *et al.* [58] subjected MgO, Al_2O_3 and $MgAl_2O_4$ to fast-neutron (>0.1 MeV) irradiation over a range of temperatures. In contrast to MgO and Al_2O_3 there was negligible swelling observed in $MgAl_2O_4$ single crystals which led to spinel being proposed for use near the first wall of a fusion reactor [59]. Sickafus *et al.* [60] explained the three probable reasons for this: (i) Complex chemistry causes the critical size of a dislocation loop nucleus to become unusually large [61], which necessarily suppresses loop nucleation; (ii) Complex structure generates constraints that prohibit dislocation loops from easily unfaulting; (iii) Spinel can readily accommodate significant degrees of disorder on its cation sublattices. When spinel was exposed to high neutron fluences ($> 5 \quad 10^{26}$ n m^{-2}) Sickafus *et al.* [62] found, using neutron diffraction, that roughly 35% of the cations have experienced ion exchange. These results indicate that interstitial-vacancy recombination is a highly efficient point defect annihilation mechanism, even when as, a result, there are increased

levels of disorder on the cation sublattices. This last point is important as one consequence of neutron irradiation in spinel is an increased level of disorder on the cation sublattices [62]. As discussed in the previous section any increase in the degree of disorder on the cation sublattice involves only a relatively small change in the lattice parameter [43, 50]. Whilst many of the crystal properties of spinel, including the elastic modulus remain unaffected by neutron irradiation [63], others such as the hardness are slightly increased [64]. Taken together this indicates that spinel is a highly neutron irradiation tolerant material and consequently may find many possible applications in the nuclear industry, such as an inert matrix for actinide transmutation [65].

The depth dependent microstructural evolution of ion-irradiated spinel is dependent on the mass and energy of the bombarding ion, as opposed to other simple radiation parameters such as damage energy density, average primary knock-on atom recoil energy, displacement damage rate or ionizing dose rate [66]. Irradiation with light ions leads to increased levels of observable diffusion which, it is postulated, promotes defect recombination. This suggests that light ion and electron irradiation do not produce microstructures representative of those that would form in the material during fission or fusion neutron irradiation [67]. Conversely, after irradiation with Zr^{+} ions at 920 K a moderate number of dislocation loops, of interstitial character, (average diameter 15 nm) were observed [66]. Shimada *et al.* [68] irradiated spinel with Xe^{14+} ions at ambient temperatures and detected heavily disordered columns along the tracks with a high density of electronic excitation. Additionally, they observed Al^{3+} disorder occurring over a larger area than the Mg^{2+} ions are disordered over. By conducting their ion irradiations at cryogenic temperatures, effectively suppressing the point defect recombination, Yu *et al.* [69] observed a crystalline-to-amorphous phase transformation, via a 'metastable' crystalline phase. Devanthan *et al.* [70] examined the physical properties of this amorphous material and found that the Young's modulus and the hardness had decreased by 30% and 60% respectively. The structure of this 'metastable' crystalline phase was established by Ishimaru *et al.* [71] by bombarding spinel with Ne^{+} ions at 120 K and examining the samples, using transmission electron microscope (TEM) and selected area electron diffraction (SAED). Their SAED patterns correspond to the rock salt structure, where the lattice parameter is reduced to roughly 4 Å and the cations are distributed randomly on the octahedral interstices within a 'pseudo' cubic close packed oxygen sublattice. Molecular dynamics simulations of defect accumulation in spinel [72], modeled by regularly introducing randomly placed Frenkel pairs into

the simulation supercell, showed the spinel-rocksalt transformation, providing further support for the work of Ishimaru *et al.* [71].

Molecular dynamical simulations have also been used to simulate ballistic process in spinel [73]. These simulations show that during the initial phase of the cascade there are a large number of defects formed, however, after just 10 ps nearly all of these defects have annihilated leaving a small number of antisite defects and other small defect clusters. The increase in the concentration of antisite defects is consistent with the experimental observations of irradiated spinel [62]. Similar cascade simulations were conducted by Bacorisen *et al.* [74] on $MgAl_2O_4$, $MgGa_2O_4$ and $MgIn_2O_4$: they noted that materials with higher levels of inversion retained increased levels of point defects after the same recombination period. The work of Smith *et al.* [73] was also the first occasion that complex, split interstitial defects were predicted in spinel type materials. Rather than a simple interstitial ion occupying a previously unoccupied octahedral interstice, two cation interstitial ions occupy two octahedral interstices surrounding a vacant tetrahedral lattice site as shown in figure 2.11. Lattice static calculations by Ball *et al.* [75] found split interstitial structures to be lower in energy than isolated simple interstitials for all interstitial species in spinel.

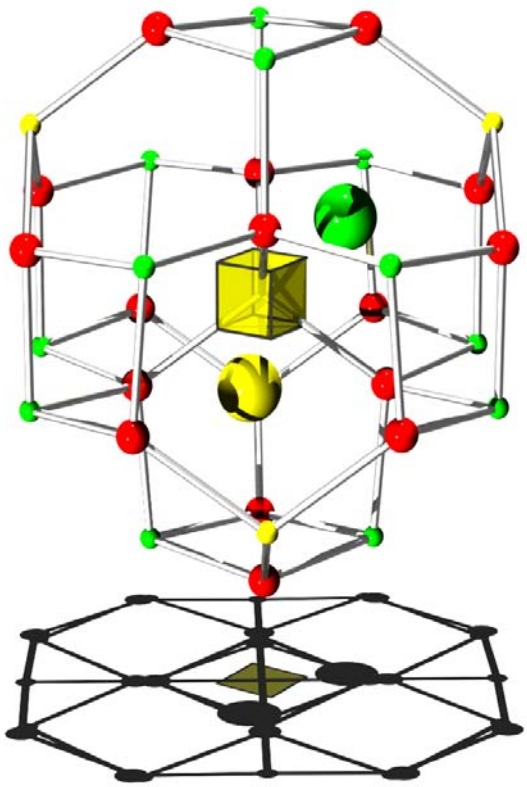

Figure 2.11: A split $Al_i^{\bullet\bullet\bullet} - V_{Mg} - Mg_i^{\bullet\bullet}$ interstitial. Both cation species in spinel form split interstitials by forcing a lattice atom from its site and then residing in two of the four octahedral interstices surrounding the vacancy site. In this image the large spheres represent the interstitial ions split across a vacant tetrahedral magnesium site represented by a transparent yellow box. In this figure the cation and anions are shown in their relaxed positions (ie. their minimum energy positions), in other figures in this thesis ions are shown in the ideal unrelaxed positions for greater clarity.

3

Methodology

This chapter will provide a brief overview of the atomistic simulation techniques employed in this thesis. Each of the subsequent chapters will go into the specific details of how each technique was applied and all of the appropriate potentials and parameters used in the specific calculations will be presented.

3.1 Atomistic simulation

Over the course of the last few decades there has been a significant increase in the use of computational simulation within the scientific community. Through a combination of the dramatic increase in computational processing power (a phenomenon described by Moore's Law [76]) and continuing algorithm development, atomistic scale modeling has become a valuable asset, providing a useful insight into the behaviour of atoms on a scale often inaccessible to traditional experimental investigation.

Broadly speaking atomistic simulations can be broken down into two categories, quantum mechanical calculations and classical calculations based on empirically derived parameters. Quantum mechanical simulations (often referred to as *ab initio*) attempt to solve the many-body Schrödinger equation. Solving the Schrödinger equation [77] gives a large quantity of information concerning the electronic structure of the system. For the most simple cases quantum mechanical calculations are considered to be formally exact, however, as larger systems are studied various approximations have to be adopted to make the calculations tractable. Despite

the introduction of these approximations to improve their applicability, quantum mechanical methods place significant demands on computational resources. Early quantum mechanical simulations were limited to all but simplest of systems (ie. H_2^+), however, the advent of Density Functional Theory (DFT) has expanded the scope of *ab initio* type simulations to include condensed matter.

The second category of atomistic simulations are those which use empirically derived potential parameters to describe the interactions between ions. As they do not solve the Schrödinger equation they do not yield information about the electronic structure. Despite this apparent limitation, classical pair potential simulations can be extremely useful for predicting trends in atomic structure and defect processes as well as predicting macroscopic properties, such as the bulk modulus. Compared to quantum mechanical simulations, pair potential techniques require significantly less computing power which means they can be applied to much larger systems, in some cases millions of atoms. The successful implementation of these classical techniques is dependant on the development and application of appropriate potential parameters. A description of how appropriate potential parameters can be derived will be discussed later.

3.2 Empirical pair potentials

3.2.1 Introduction

The empirical simulations conducted in this thesis assume that it is possible to treat an ionic lattice using a classical Born like model [78, 79], whereby the constituent ions are represented by a periodic array of point charges. To calculate the total energy, $\Phi(r_1 \ldots r_n)$, of the system requires the summation of the interactions experienced by each atom as a result of the other atoms in the system. This can be expressed formally using equation 3.1.

$$\Phi(r_1 \ldots r_n) = \sum_{i,j=1}^{n} \Phi_2(r_{ij}) + \sum_{i,j,k=1}^{n} \Phi_3(r_{ijk}) + \sum_{i,j,k,l=1}^{n} \Phi_4(r_{ijkl}) + \ldots \tag{3.1}$$

In equation 3.1, the $\sum_{i,j=1}^{n} \Phi_2(r_{ij})$ term refers to the interactions between pair of ions i and j at

a given separation r_{ij}. The $\sum_{i,j,k=1}^{n} \Phi_3(r_{ijk})$ and $\sum_{i,j,k,l=1}^{n} \Phi_4(r_{ijkl})$ terms describe the interactions of ion triplets and quartets respectively: these terms as well as interactions between higher numbers of ions are generally truncated owing to the dominance of the pairwise interaction. Equation 3.1 then becomes equation 3.2,

$$\Phi_a(r_1 \ldots r_n) = \sum_{i,j=1}^{n} \Phi_2(r_{ij}). \tag{3.2}$$

From this point onwards, $\Phi_2(r_{ij})$ will be written as $E_{ij}(r_{ij})$. The form this pair potential function takes is a important factor in determining the success of the model.

3.2.2 Coulombic potential

It is a fundamental concept in science that the potential energy of a charged body will be affected by the presence of another charged body (or more accurately, by its electric field). If two ions i and j, with charges q_i and q_j respectively are separated by a distance, r_{ij}, then their potential energy can be expressed using the Coulomb potential:

$$E_{ij}^{Coulomb} = \frac{q_i q_j}{4\pi\varepsilon_0 r_{ij}}. \tag{3.3}$$

$E_{ij}^{Coulomb}$ represents the potential energy resulting from the interaction of charges on ions i and j and ε_0 is the permittivity of free space. As the magnitude of the Coulombic potential energy decreases as a function of $1/r_{ij}$, it converges slowly, ie. the Couloumbic interaction is long range. Whilst this term may seem very simple to calculate, the slow rate of convergence means it is necessary to considering the influence of a great number of ions for each ion in the system, thus placing large demands on computational resources. A method of achieving quick convergence was devised by Ewald (a good explanation is given by Kittel [80]), which involves partitioning the calculation into a short range real space component and a long range reciprocal space component. The long range reciprocal component is used to mask the charges at longer ranges thus simplifying the calculation.

The form of equation 3.3 ensures that the interaction between two like charged atoms will

be repulsive whilst the interaction between atoms with opposite charges will be attractive. In fact, considering the Coulombic potential alone, for two oppositely charged ions, as $r \quad 0$ Å, $E_{ij}(r_{ij}) \quad -\infty\ eV$. This implies that the lowest energy configuration for this system would be for the ions to be sitting atop one another, which is clearly unphysical. Therefore, there must be some other force coming into play, at shorter separations, to ensure that the ions do not collapse onto each other.

3.2.3 Short range potential

At small separations (ie. less than 10 Å) the charge distributions of two adjacent ions will begin to overlap, resulting in a repulsive force. As the separation, r_{ij}, decreases, the extent of this overlap is increased further, to a point at which it becomes the dominant force, thus preventing the ions moving to occupy the same space. This repulsive force arises as a result of the Coulombic interactions between the nuclei as well as, indirectly, from the Pauli exclusion principle. The Pauli exclusion principle states that no two fermions may occupy the same quantum state [81]. When electron clouds overlap the Pauli exclusion principle dictates that the ground state charge distribution will be of a higher energy, thus increasing the electronic energy. The earliest attempt at modeling this short range interaction was by Born and Landé [82] and takes the form described by equation 3.4,

$$E_{ij}^{sr} = \frac{b}{r_{ij}^{n}} \tag{3.4}$$

where, E_{ij}^{sr} is the potential energy resulting from the short range interactions discussed above and b and n are variables chosen to reproduce the equilibrium interionic separation; this early work took $n = 9$. This model was later expanded in the light of quantum mechanical calculations, which suggested that, while it was a useful approximation, it was not universally applicable. With this in mind, Born and Mayer [78] developed the short range potential described by equation 3.5:

$$E_{ij}^{sr} = A_{ij} \exp\left(-\frac{r_{ij}}{\rho_{ij}}\right) \tag{3.5}$$

where A_{ij} and ρ_{ij} are variable parameters.

At intermediate/small separations (ie. between approximately 10+ 20 Å), although larger than those considered above, there is an attractive force which arises from the fluctuations of the instantaneous positions of the electrons. Consider, two ions separated again by r_{ij}; should the electrons in i arrange such that there is an instantaneous dipole on i, then the resultant electric field will induce an instantaneous dipole on j. The two dipoles then attract each other and the potential energy of the pair is lowered. Although i will change the size and direction of its instantaneous dipole the electron distribution on j will follow it accordingly. Because of this correlation the overall attraction between i and j is not zero. This induced-dipole induced-dipole interaction is called either the dispersion or London interaction [16]. The strength of this dispersion interaction depends on polarisability of i as the instantaneous dipole moment is dependant on the polarisability of i and j as this determines how easily a dipole can be induced upon it. London derived a general expression for the potential energy of ions i and j by describing dipole formation as a correlated motion of the electrons in both. The result is the London formula, shown in equation 3.6, where C_{ij} is again a variable parameter.

$$E_{ij}^{London} = -\frac{C_{ij}}{r_{ij}^{6}} \tag{3.6}$$

By incorporating the London interactions with the models proposed by Born and Lange and Born and Mayer we arrive at the two most commonly adopted short range potential forms. These are the Lennard-Jones (12,6) potential [83] and the Buckingham potential [84], as shown in equations 3.7 and 3.8 respectively.

$$E_{ij}^{sr} = \frac{A_{ij}}{r_{ij}^{12}} - \frac{C_{ij}}{r_{ij}^{6}} \tag{3.7}$$

$$E_{ij}^{sr} = A_{ij}\exp\left(-\frac{r_{ij}}{\rho_{ij}}\right) - \frac{C_{ij}}{r_{ij}^{6}} \tag{3.8}$$

The simulations conducted in this thesis use the Buckingham potential to model the short range interactions and the pair potential parameters used are reported in later chapters. For most cation species the orbitals are considered to be sufficiently compact that they are therefore unlikely to undergo much polarization so the C parameter is zero, effectively reducing the Buckingham potential to a Born - Mayer potential. A certain degree of care has to be taken

when using the Buckingham potential because at very small separations the energy tends to negative infinity. This is not generally a problem for simple static lattice calculations but can be extremely significant in Molecular Dynamics (MD) simulations, which will be discussed later.

3.2.4 The pair-potential model

The total potential energy between the ion pair ij is the sum of the Coulombic potential energy and the short range potential energy:

$$E_{ij}^{Total} = E_{ij}^{Coulomb} + E_{ij}^{sr} \tag{3.9}$$

Figure 3.1 gives an example of how the interactions discussed previously vary as a function of r_{ij} for a Mg^{2+}- O^{2-} ion pair. As shown in figure 3.1 at large values of r_{ij} the total potential energy is dominated by the Coulombic term, $E_{ij}^{Coulomb}$, and then at smaller separations the short range potential, E_{ij}^{sr}, prevents the ions from collapsing in on each other.

In order to determine the overall energy for the system it is necessary to sum the interactions between all ion pairs in the system, which is described by equation 3.10.

$$E_{System} = \sum_{i}^{n} \sum_{j>i}^{n} E_{ij}^{Total} \tag{3.10}$$

3.2.5 Derivation of short range potential parameters

The success of any simulation based on empirically derived pair-potentials will depend on the successful determination of the potential parameters A_{ij}, ρ_{ij} and C_{ij}. There are two methods used to derive these potential parameters: empirical and non-empirical. Empirical potential derivation involves adjusting the parameters to reproduce known experimental properties, such as the lattice parameter, ionic positions and in some cases the dielectric elastic constant matrix. Conversely, non-empirical potentials are developed by fitting to a potential energy surface

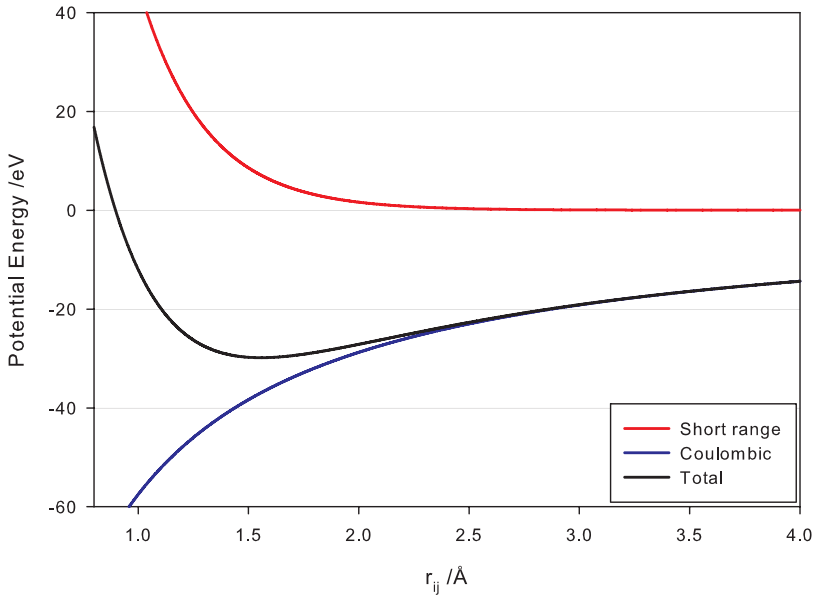

Figure 3.1: Plot showing the variation in the Coulombic, short range and total potential energies as a function of r_{ij} for an Mg^{2+}- O^{2-} ion pair. The Born - Mayer potential is used here to model the short range interactions.

derived using a quantum mechanical technique. Non-empirical potential derivation is particularly useful when there is a paucity of experiential data. In general, pair potential parameters are derived for a specific system, which means that the potential is only tested at a single configuration of ions. Whilst this approach is valid for examining the perfect lattice, once defects are introduced the potential may not be able to reliably reproduce the lattices response, that is, where ions shift away from their equilibrium positions. This problem can be remedied by generating generalised potentials that are fitted to numerous systems thereby improving their applicability to non-equilibrium structures.

3.2.6 Modeling polarisability

The effects of ionic polarisation are included in the calculations by employing the shell model of Dick and Overhauser [85]. In this model an ion is represented by a positively charged core (with charge $X|e|$) coupled to a massless, negatively charged shell (with charge $Y|e|$) via a harmonic force of spring constant, k. The overall charge of the ion is then the sum of the charge on the core and the shell (X+Y$|e|$). This allows the core and shell to move independently thus simulating dielectric polarisability. An isolated atom has a polarisability, α_e given by ,

$$\alpha_e = \frac{1}{4\pi\varepsilon_0}\frac{Y^2}{k}. \tag{3.11}$$

The parameters (X, Y and k) are fitted empirically to the dielectric and to a lesser extent the elastic properties of the crystal. In the absence of an external electric field then the core and the shell will be centred on the same point in space, however, when placed in a non-symmetrical electric field the core and shell will move with respect to this external field. By allowing the core and shell to move independently creates extra degrees of freedom thereby allowing the lattice to relax into a more energetically stable state. As the core and shell are no longer centred on the same point in space, a slight energy penalty is incurred as they move apart, this is described by,

$$E_i^{shell} = \frac{1}{2}k.\delta r_i \tag{3.12}$$

where, δr_i represents the separation (vector length) between the core and the shell. Figure 3.2

provides a pictorial representation of the core and the shell.

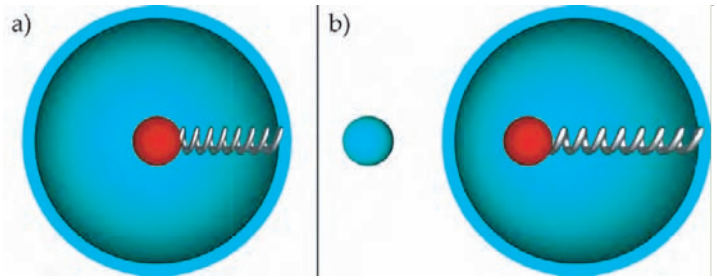

Figure 3.2: Representation of the shell model of Dick and Overhauser [85] used to model polarisation. (a) shows an unpolarised ion where both the core and shell are centred on the same point and in space; (b) shows the effect of an asymmetrical field on an ion, the core and shell are now centred on two different points in space [86].

3.3 Energy minimisation

As mentioned previously the potential parameters used in the empirical simulations are obtained by fitting to either experimental or quantum mechanical data. It is, however, extremely unlikely that the potential parameters will be capable of exactly reproducing either the experimental crystal structure or the structure predicted by quantum mechanics. This means that before energies can be calculated the crystal must be allowed to relax to the lowest energy configuration dictated by the potentials used. The reason this must be carried out prior to calculating the energy of the lattice, or any defects, is that there will be an energy change associated with this process that is not related to the energy desired. Whilst it is expected that the lowest energy configuration determined using empirical potentials and the experimentally observed structure will not be identical it is important to ensure that any discrepancy is minimised by choosing suitable potential parameters.

During an energy minimisation all the ionic interactions are calculated and each ion subsequently moves a distance proportional to the force acting on the particle in the direction of the net field. Energy minimisation calculations can be conducted in one of two ways. The first is to maintain a constant volume, whereby the minimum energy is determined by ionic co-ordinates whilst only considering the strains on the individual ions. The other is minimisation at a constant pressure which involves determining the minimum energy by adjusting both

ionic co-ordinates and the unit cell parameters. An energy minimisation carried out at a constant pressure is significantly more computationally demanding, however, it has become the standard and is used in this thesis unless otherwise mentioned.

The minimisation technique employed in the simulations presented in this thesis are based on the Newton-Raphson method. Considering a simplistic case with a 2D potential energy surface, which can be assumed to be quadratic, the second order expansion for the energy can be described by,

$$E(x+\delta x) = E + \delta E = E(x) + \frac{dE(x)}{dx}\delta x + \frac{1}{2}\delta x \frac{d^2E(x)}{dx^2}\delta x \tag{3.13}$$

At a minimum the change after a step should be zero, ie.

$$\delta E = \frac{dE(x)}{dx}\delta x + \frac{1}{2}\delta x \frac{d^2E(x)}{dx^2}\delta x = 0 \tag{3.14}$$

giving

$$\delta x = -2\frac{\left(\frac{dE(x)}{dx}\right)}{\left(\frac{d^2E(x)}{dx^2}\right)}. \tag{3.15}$$

This means that the search direction on the surface depends on both the first and second derivatives of the potential energy surface. In higher dimensions the second derivatives gives rise to the Hessian matrix, H. Equation 3.15 then becomes,

$$\delta x = -2H^{-1}g \tag{3.16}$$

where g is the gradient vector. The equation above shows that matrix inversion is involved in this method, which can make it computationally demanding. However, near a minimum, real potential energy surfaces can be described as roughly quadratic meaning that the Newton-Raphson technique can achieve quick convergence. For large systems the calculation and inversion of the Hessian may be impractical so intermediate techniques such as Broyden, Fletcher, Goldfard and Shanno (BFGS) [87] method that updates H^{-1} directly are used.

3.4 Defect calculations

Once the lattice has been relaxed into a state of mechanical equilibrium it is possible to investigate the effects of introducing defects on the local environment, as it is, ultimately, the behaviour of these defects that influence a materials performance. The defect energy can be defined as the energy difference between the lattice containing the defect and the perfect lattice plus the defect at an infinite separation. Some of the earliest defect calculations, looking at how to introduce charged defects [88], concluded that it was essential to calculate the polarisation response of the lattice to the defects presence. This idea was taken forward by Mott and Littleton [89], who proposed a two region approach to calculating defect energies. Firstly, an inner region containing the defect itself, which is treated atomistically using energy minimisation and an outer region where a continuum approximation is sufficient. The explicit atomistic technique used in the inner region is essential because of the strong forces that the defect will impart on the atoms nearest to it.

In contrast, for the more distant weak field regions, the defect forces are relatively weak and lattice relaxation may be treated using a more approximate method. The Mott and Littleton approach, appropriate to ionic materials, calculates the polarization, **P**, per unit cell using the continuum approximation:

$$\mathbf{P} = \frac{Vq\mathbf{r}}{r^3}(1-\varepsilon^{-1}) \tag{3.17}$$

where, V is the unit cell volume and ε is the static dielectric constant. Equation 3.17 is strictly only valid for dielectrically isotropic systems, however, this approach can be extended to anisotropic systems [90]. Formally, the calculated polarization can then be broken up into atomistic components and the defect energy can be obtained using,

$$E(\mathbf{x},\mathbf{y}) = E_I(\mathbf{x}) + E_{I-II}(\mathbf{x},\mathbf{y}) + E_{II}(\mathbf{y}) \tag{3.18}$$

In equation 3.18, **x** and **y** are the co-ordinates of the ions in region I and the displacements of the ions in region II respectively, the terms E_I and E_{II} are the energies arising from the interactions within each region and E_{I-II} is the interaction energy between the two regions. If the size of

the innermost region is large enough, then we can assume that the outermost region consists of perfect crystal with harmonic displacements so that,

$$E_{II}(\mathbf{y}) = \frac{1}{2}\mathbf{y}\mathbf{A}\mathbf{y} \tag{3.19}$$

where, $\mathbf{A}$ is the force constant matrix. Applying the equilibrium condition to region II gives,

$$\left(\frac{\delta E_{I-II}(\mathbf{x},\mathbf{y})}{\delta \mathbf{y}}\right)_x = -\mathbf{A}\mathbf{y} \tag{3.20}$$

which can then substituted into 3.19 and 3.18 to yield,

$$E(\mathbf{x},\mathbf{y}) = E_I(\mathbf{x}) + E_{I-II}(\mathbf{x},\mathbf{y}) + -\frac{1}{2}\left(\frac{\delta E_{I-II}(\mathbf{x},\mathbf{y})}{\delta \mathbf{y}}\right)_x \cdot \mathbf{y}. \tag{3.21}$$

As can be seen from equation 3.21, the energy of the defect is no longer explicitly dependent on E_{II}, which is computationally convenient.

The procedure for calculating a defect energy is then to relax region I using energy minimisation, followed by calculation of the displacements in region II by the Mott-Littleton methodology and then the resulting values of E_I and E_{I-II} and the derivative of the later [91]. Figure 3.3 gives a pictorial representation of the Mott-Littleton [89] methodology.

There have been numerous attempts at determining the reliability of the Mott-Littleton approach by comparing with data obtained using quantum mechanical simulations, an excellent comparison is given in [93].

3.5 Defect volume calculations

When a defect is introduced into a crystal there will be a characteristic change in the overall volume as the lattice relaxes to accommodate it. Catlow *et al.* [94] developed a method of calculating the change in volume within the Mott-Littleton methodology. The defect relaxation volume, v, is given by,

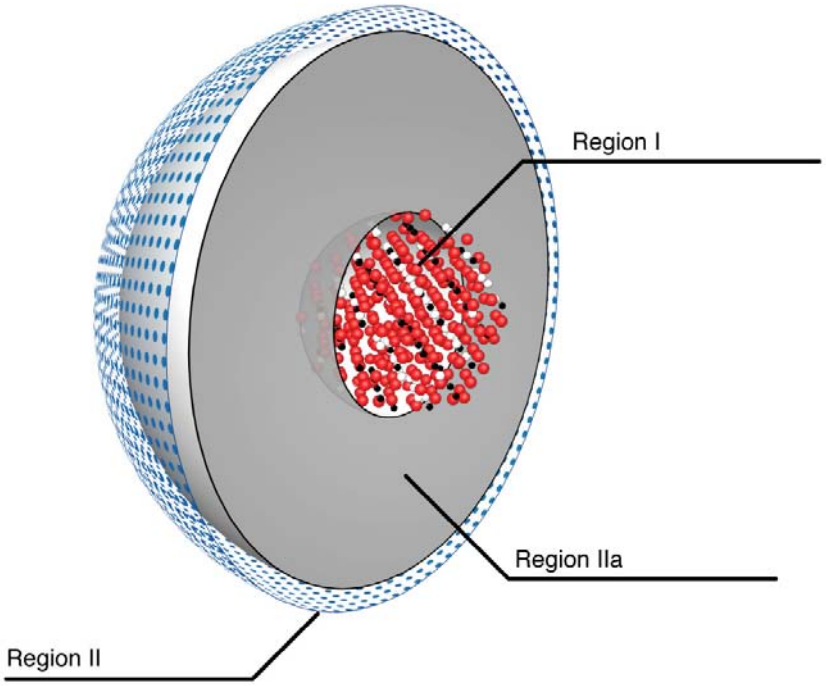

Figure 3.3: Pictorial representation of the Mott-Littleton regions [92].

$$v = -K_T V_C \left(\frac{\delta f_v}{\delta V_C} \right)_T \tag{3.22}$$

where, K_T (Å^3 eV^{-1}) is the isothermal compressibility, V_C is the unit cell volume of the perfect lattice and f_v is the defect formation energy determined using the Mott-Littleton approach. Therefore, $\left(\frac{\delta f_v}{\delta V_C} \right)_T$ is the change, for a given temperature, in the Helmholtz defect formation energy as a function of change in the unit cell volume.

For a cubic crystal, the isothermal compressibility can be obtained from the elastic constants, using,

$$K_T = \left[\frac{1}{3}(c_{11} + 2c_{12}) \right]^{-1} \tag{3.23}$$

where, c_{11} and c_{12} are components of the elastic constant matrix. $\left(\frac{\delta f_v}{\delta V_C} \right)_T$ can be obtained by plotting the defect energy as a function of the lattice parameter, a, under constant volume conditions (ie. only the lattice positions can relax, the cell dimensions remain constant), then

solving equation 3.24,

$$\left(\frac{\delta(f)_v}{\delta V_C}\right)_T = \frac{1}{3a^2}\left(\frac{\delta f_v}{\delta a}\right)_T \tag{3.24}$$

since,

$$\left(\frac{\delta(f)_v}{\delta V_C}\right)_T = \left(\frac{\delta f_v}{\delta a}\right)_T \left(\frac{\delta a}{\delta V_C}\right) = \left(\frac{\delta f_v}{\delta a}\right)_T \left(\frac{\delta V_C}{\delta a}\right)^{-1} = \left(\frac{\delta f_v}{\delta a}\right)_T \left(\frac{\delta a^3}{\delta a}\right)^{-1} \tag{3.25}$$

A negative defect volume implies that the crystal has shrunk upon introduction of the defect, however, a positive defect volume means the lattice expands in order to accommodate the defect.

3.6 Molecular dynamics

The Molecular Dynamics (MD) simulations described in this section do not form a prominent part of this thesis, however, it is necessary to have a basic grasp of the fundamental ideas and concepts as they underpin the long scale dynamical method, Temperature Accelerated Dynamics (TAD), which is used later.

Molecular dynamics proceeds by solving Newton's equations of motion to predict the behaviour of atoms within a given supercell. The crystal lattice is represented using a supercell (formed from a number of unit cells) which is iterated through space. In addition to being assigned a position, each ion is also assigned an initial velocity with a random direction and a magnitude that is (on average) representative of the temperature of interest. An ion in the system at, x_0, with an initial velocity, u, will feel a force, F, as a result of interactions with surrounding ions. According to Newton's second law the force acting on the ion will cause it to accelerate in the direction of the overall force with a magnitude which can be determined using:

$$a = \frac{F}{m}. \tag{3.26}$$

The magnitude and direction of this force can be determined using either a pair potential approach or quantum mechanically, and the mass, m, of the ion. If x then moves under the influence of force, F, for a period of time, τ, then its new velocity, v, is given by,

$$v = u + \int_0^\tau \frac{F}{m} dt = u + \frac{F}{m}\tau. \tag{3.27}$$

However, the velocity itself is the rate of change of atom position, x. Equation 3.28 shows this relationship between velocity and position.

$$v = \frac{dx}{dt} \tag{3.28}$$

The final location of an ion can be found by integration as shown by,

$$x = x_0 + \int_0^\tau \frac{dx}{dt} dt = x_0 + \int_0^\tau \left(u + \frac{F}{m}\tau \right) = x_0 + u\tau + \frac{1}{2}\frac{F}{m}\tau^2. \tag{3.29}$$

With these simple relationships it is possible to follow the evolution of a lattice as a function of time elapsed. At a given value for τ the positions of the ions can be used to determine the force acting on each of the ions in the system. From this force it is possible to calculate an acceleration, which can in turn be used to determine each ion's velocity and then finally their new positions. By following this procedure it is possible to 'watch' the ions move.

There is obviously a very significant assumption being made, that is, the force experienced by each ion does not change during each timestep. By making each timestep as small as possible this error can be reduced, as, ensuring that the ion movement is small, the change in the force on an ion will not be significantly altered from its original state. The solution to this problem is to use timesteps that are as small as is computationally tractable (typically 10^{-15} seconds) as well as ensuring that the simulation can also produce data on a relevant timescale. Another method of reducing the error at larger timesteps is to examine higher order expansions of the position, ie.

$$x = x_0 + u\tau + \frac{1}{2}\frac{F}{m}\tau^2 + \frac{\dddot{x}}{m}\tau^3 \ldots \tag{3.30}$$

where, $\dddot{x}$ is the third derivative of the position. Whilst considering the higher order terms may yield greater accuracy, it leads to an increase in the computational demand. It is also possible to use information from previous timesteps to determine future positions. The position of any atom at a time $t+\tau$ can be obtained using,

$$x(t+\tau) = x(t) + u(t)\tau + \frac{1}{2}\frac{F(t)}{m}\tau^2 + \frac{\dddot{x}(t)}{m}\tau^3 \ldots. \tag{3.31}$$

It is equally valid to back track in time by taking a negative timestep with the result being,

$$x(t-\tau) = x(t) - u(t)\tau + \frac{1}{2}\frac{F(t)}{m}\tau^2 - \frac{\dddot{x}(t)}{m}\tau^3 \ldots. \tag{3.32}$$

By adding these two terms together and rearranging it is possible to eliminate the velocity term, thus negating the need to calculate this quantity when determining how ion positions will evolve. This is shown in equation 3.33, which is known as the Verlet algorithm [95].

$$x(t+\tau) = 2x(t) - x(t-\tau) + \frac{F(t)}{m}\tau^2 \tag{3.33}$$

The trajectory described by the Verlet algorithm will more accurately represent the 'real' trajectory than the simple expressions for x because the third order terms have been included but merely cancel each other out. It should also be noted that as the Verlet algorithm effectively measures the change in position over two timesteps, the timesteps should be made smaller.

There are a number of ensembles in which MD simulations can be conducted. Conceptually the simplest ensemble in statistical mechanics is the microcanonical ensemble which represents a thermodynamically isolated system (ie. the number of particles, N, volume, V, and the overall energy of the system are all kept constant). If the system is connected to a heat bath, ensuring a constant, T, then the microcanonical (N, V, E) ensemble is replaced with a (N, V, T) canonical ensemble. Connection to a pressure reservoir via a piston gives the constant enthalpy ensemble (N, P, H), whilst connection to a diathermic piston with constant T and P gives the (N, P, T) ensemble. All of these ensembles can be examined using MD but the microcanonical ensemble is by far the most common [96].

3.7 Temperature accelerated dynamics

Owing to the requirement for MD simulations to have timesteps on the order of femto seconds it is extremely difficult, even for today's fastest processors, to reach timescales greater than a tenth of a microsecond. There are numerous methods, derived from transition state theory, for accelerating molecular dynamics simulations of infrequent event systems. These methods, hyperdynamics [97], parallel replica dynamics [98], temperature accelerated dynamics [99] and kinetic Monte Carlo [100], are capable of reaching simulation times many orders of magnitude greater than traditional MD whilst still retaining full atomistic detail.

The starting point for temperature accelerated dynamics is to define our system as an infrequent event system. An infrequent event system is one in which the dynamical evolution can be described as vibrational excursions within a single minima on the potential energy surface punctuated by occasional transitions, across a dividing surface, to another minima on the surface. These transitions are referred to as infrequent as the time between events is many vibrational periods (in some cases many orders of magnitude longer). Figure 3.4 gives a simplified example of an infrequent event system.

Whilst there may be a large number of different crossings of the dividing surface between two states, the trajectory only 'sees' the particular crossing it is making. Nevertheless, the trajectory chooses an escape direction with the correct probability (relative to other possible escape directions), despite having no prior information about the other possible crossings. It is assumed here that these crossings are infrequent, however, it is possible for two such events to occur within a few vibrational periods. These successive events are called correlated dynamical events [21]. Here we presume that these correlated dynamical events do not occur (this is a fundamental assumption in transition state theory), which is a very good approximation for solid state diffusion processes [101]. This also means that when the trajectory leaves a state it will have no 'memory' of how it entered that state.

The rates for transitions between states depend sensitively on the temperature; when the temperature is raised all processes occur more quickly. Therefore, by conducting an MD simulation at a higher temperature the dynamical evolution of the lattice will occur more quickly. The time at which an event occurs could then be determined at the higher temperature and then scaled back to yield a representation of the waiting time at the lower temperature. Unfortunately, not

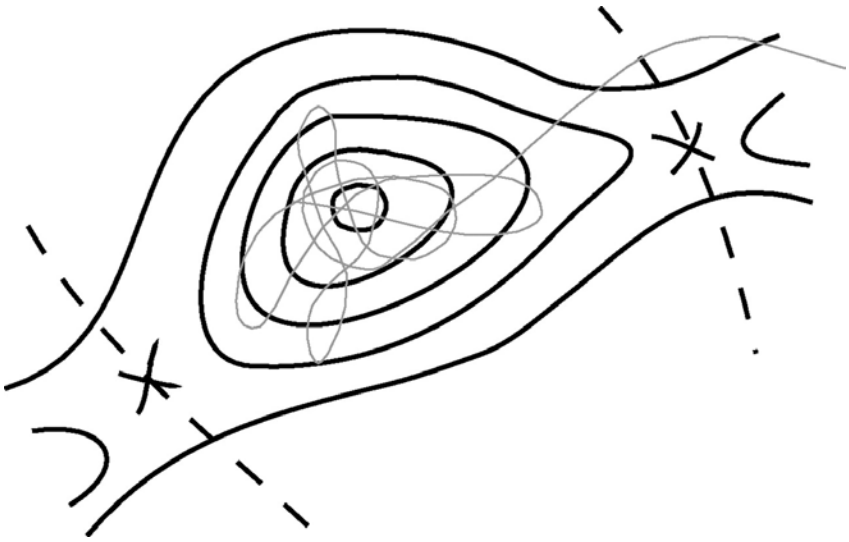

Figure 3.4: Illustration of an infrequent event system (reproduced from [22]). The trajectory explores the well on the potential energy surface for a time scale of many vibrational periods. At some point in time, when enough energy has been localised in one reactive mode, the trajectory crosses the dividing surface and enters a new state. During the brief period of excitation, during which this process occurs, it is possible for the trajectory to re-cross the dividing surface, otherwise it will settle into the new state.

only do the rate constants change as a function of temperature but the ratio of a high-barrier rate to a low-barrier rate constant also increases. It is, however, possible to correct for this temperature induced bias. Therefore the essence of a TAD simulation is to conduct an MD simulation at high temperature and determine the waiting time for an event at this higher temperature, then filter out some of the transitions and only allow those that should occur at the original temperature.

To conduct a TAD calculation a special kind of MD simulation, called *basin-constrained* MD, is used. In a *basin-constrained* MD simulation the trajectory is constrained to a particular potential energy basin. When the system tries to make the transition from one state to the next the trajectory is reflected back into the original state. It is not necessary to know the location of the dividing surface before this can be achieved, it is merely necessary to be able to detect that a transition has taken place. Detecting whether a transition has occurred or not is achieved by stopping the high temperature MD simulation at regular intervals and then relaxing the system using energy minimization. If the system relaxes back to the initial state then no transition has taken place and the simulation is allowed to continue. Should a transition have occurred (ie. the

relaxed structure is not the same as the initial state), then the Nudged Elastic Band (NEB) [102] technique is used to determine the activation energy for the process, and the waiting time for the transition at high temperature is recorded. The trajectory then continues from a point just before the dividing surface but with all the atom's velocities reversed, as shown in figure 3.5.

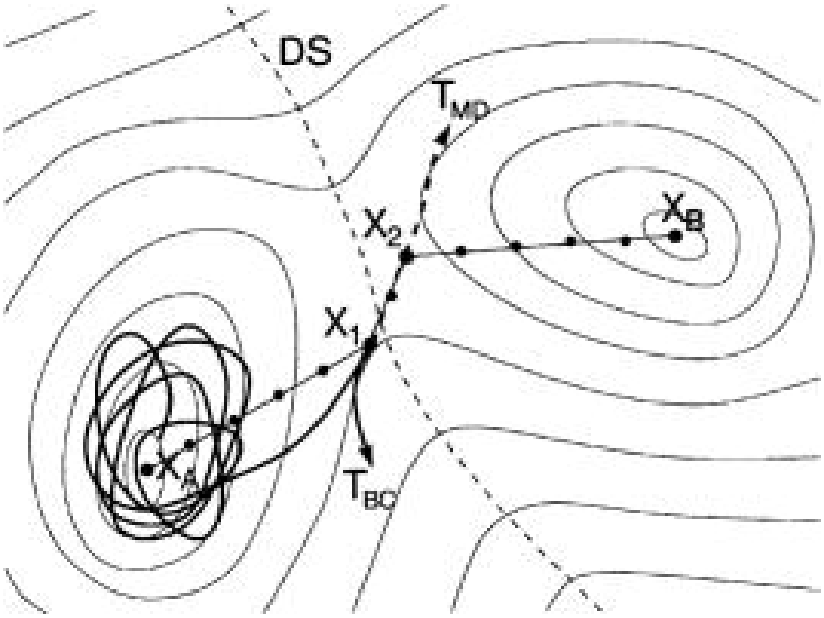

Figure 3.5: Illustration of the TAD procedure (reproduced from [99]). A two dimensional potential energy surface is indicated using the thin contour lines. The dashed line, DS, then marks the dividing surface between two states, A and B. The thick black line represent the high temperature MD trajectory. Between the points X_1 and X_2 the trajectory crosses the dividing surface. An energy minimisation, starting from X_1 will relax back to the initial state with a minimum at X_A, however, an energy minimisation from X_2 will relax to the minima X_B. The saddle is found by defining a discretised path connecting the points X_A, X_1, X_2 and X_B which is then optimized using the NEB technique. The original high temperature trajectory, T_{MD}, is then reflected from X_1 by reversing all the velocities to give T_{BC}. Finally, a Langevin thermostat injects noise into the trajectory to ensure that it does not retrace its previous path.

As first order kinetics are expected for our infrequent event system, the waiting time, t, for a particular transition is exponentially distributed with a probability distribution,

$$f_i(t)dt = k_i \exp^{-k_i t} dt \tag{3.34}$$

where k_i is the rate constant. The rate constant can be assumed to display Arrhenius like

behaviour as shown in equation 3.35.

$$k_i = v_i \exp^{-\beta E_{a,i}} \tag{3.35}$$

In equation 3.35, v_i is the temperature independent pre-exponential factor (the components of this pre-exponential factor are discussed in section 2.2.3), $E_{a,i}$ is the activation energy for process, i, and β is equal to $1/(k_B T)$.

Consider a process, i, at two different temperatures, T_{high} and T_{low} (where T_{low} T_{high}) with corresponding rate constants $k_{i,high}$ and $k_{i,low}$. Since, as mentioned previously, the waiting times, $t_{i,low}$ and $t_{i,high}$ are exponentially distributed, it follows that the products $k_{i,low}t_{i,low}$ and $k_{i,high}t_{i,high}$ have identical distributions, ie.

$$k_{i,high}t_{i,high} = k_{i,low}t_{i,low} \tag{3.36}$$

which, combined with equation 3.35 and rearranging yields an expression that allows the observed high temperature waiting time to be extrapolated to give the low temperature waiting time.

$$t_{i,low} = t_{i,high} \exp^{E_{a,i}(\beta_{low} - \beta_{high})} \tag{3.37}$$

Once the transition has been detected, the activation energy for the process found, and the low temperature waiting time determined, the trajectory is left to follow the reflected path away from X_1 until it finds another transition at which point the process begins again. This process is repeated until at some time $t_{i,high}$ the high temperature MD simulation is stopped (a criterion for ceasing the high temperature MD will be discussed below). At this point the transition with the shortest waiting time at the lower temperature is accepted and the system moves to this new state, at which point the whole simulation starts again. This process is illustrated in figure 3.6.

When conducting a TAD simulation it is essential that the high temperature MD simulation is run for a long enough time to determine the transition with the shortest waiting time at the low temperature. To achieve this it is assumed there is a lower bound, v_{min}, on the prefactor for

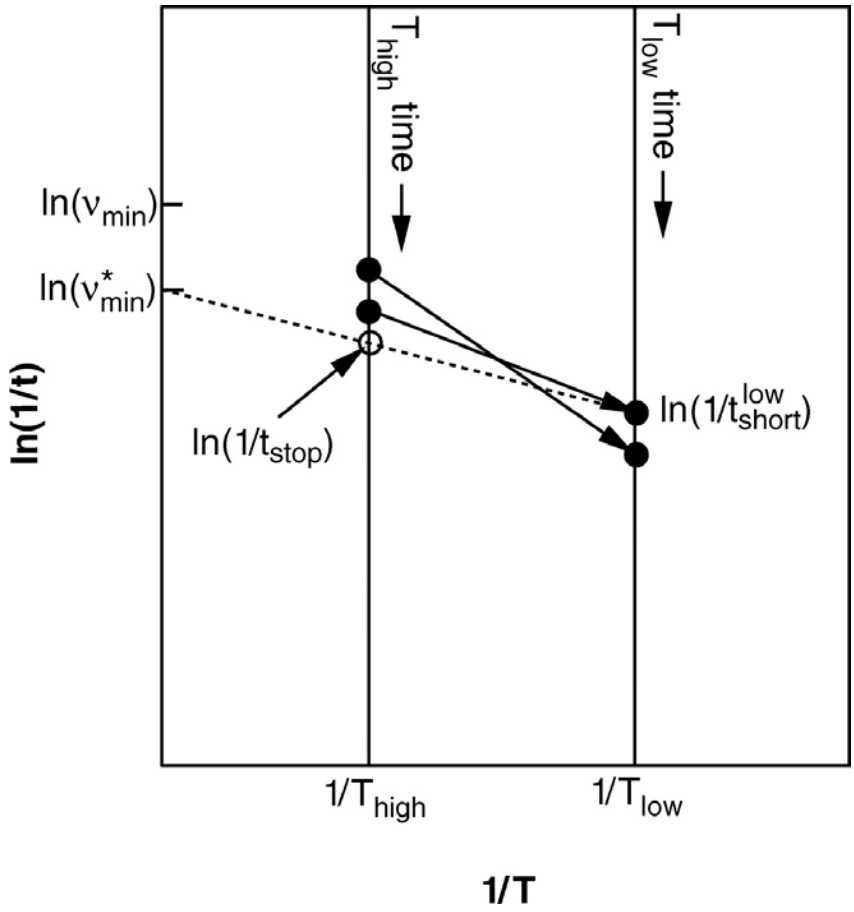

Figure 3.6: Schematic illustration of the TAD method (reproduced from [22]). The progress of the high temperature MD simulation is followed by tracing down the line marked T_{high} time and a detected transition is marked with a solid circle. When a transition occurs during the high temperature *basin-constrained* MD simulation the waiting time is transformed (arrow) into a low temperature waiting time. Plotted in this Arrhenius-like form, the transformation is a simple extrapolation along a line whose slope is the negative of $E_{a,i}$ for that event. The dashed termination line connects the shortest-time transition recorded so far on the low temperature time line with the confidence modified minimum pre-exponential ($v_{min} = v_{min}/\ln(1/\delta)$ on the y axis). Where this line intersects T_{high} time gives $t_{high,stop}$.

the system. Based on this assumption it is possible to quantify a MD simulation time, $t_{high,stop}$, such that there is only a small probability of a new transition occurring with an extrapolated escape time shorter than $t_{low,short}$. It follows from examining figure 3.6 that if a transition that occurs later than $t_{high,stop}$ is to have an extrapolated waiting time shorter than $t_{low,short}$ then the barrier for this transition must be lower than $E_x = \ln(t_{low,short}/t_{high,stop})/(\beta_{low} - \beta_{high})$. Should the energy barrier be greater than E_x then the waiting time will extrapolate to greater than $t_{low,short}$ and so is not a concern. Using this information and introducing a probability term, δ, allows the required high temperature MD simulation time to be found using,

$$t_{high,stop} = \frac{\ln(1/\delta)}{\nu_{min}} \left(\frac{\nu_{min} t_{low,short}}{\ln(1/\delta)} \right)^{\beta_{high}/\beta_{low}} . \tag{3.38}$$

For example, if δ=0.0001 indicates a simulation time required to be 99.9% confident that no new transition exists with a waiting time shorter than $t_{low,short}$. As equation 3.38, shows it is possible to combine ν_{min} and δ into a single term, however, it is more transparent to keep them separate. The effect of stopping the high temperature MD simulation at a relatively short time is that high barrier transitions tend to be accepted too frequently over low-barrier transitions. By choosing ν_{min} and δ carefully it is possible to ensure that an incorrect transition is only accepted rarely.

3.8 Quantum mechanics

3.8.1 The Schrödinger equation and the Hamiltonian

An exact theory for a system of ions and interacting electrons is inherently quantum mechanical and is based on solving the many-body Schrödinger equation of the form,

$$H\Psi([\mathbf{R}_I; r_i]) = E\Psi([\mathbf{R}_I; r_i]) \tag{3.39}$$

where, H is the Hamiltonian operator [16], $\Psi([\mathbf{R}_I; r_i])$ is the many-body wavefunction of the system and E is the energy of the system. The Hamiltonian operator contains all of the kinetic

and potential energy operators arising as a result of the the ion-ion, electron-electron and ion-electron interactions. Equation 3.40 describes how the total kinetic energy of the system is the sum of the kinetic energies of each particle (ion or electron) in the many-body system.

$$KE = -\sum_{I} \frac{\hbar^2}{2M_I} \nabla^2_{\mathbf{R}_I} - \sum_{i} \frac{\hbar^2}{2m_e} \nabla^2_{r_i} \tag{3.40}$$

Here, $\hbar$ is Planck's constant, h, divided by 2π, M_I is the mass of the ion, I, m_e is the mass of the electron and $\{R_I\}$ and $\{r_i\}$ are the positions of the ion and the electrons. Arising as a result of the interactions of the charges in a system the potential energy can be described by,

$$PE = -\sum_{iI} \frac{Z_I e^2}{\mid \mathbf{R}_I - r_i \mid} + \frac{1}{2} \sum_{ij(j=i)} \frac{e^2}{\mid r_i - r_j \mid} + \frac{1}{2} \sum_{IJ(J=I)} \frac{Z_I Z_J e^2}{\mid \mathbf{R}_I - \mathbf{R}_J \mid}. \tag{3.41}$$

The $-\sum_{iI} \frac{Z_I e^2}{\mid \mathbf{R}_I - r_i \mid}$ term in equation 3.41 is an attractive term, which accounts for the attraction between the electrons in the system with its constituent ions, whilst the $\frac{1}{2} \sum_{ij(j=i)} \frac{e^2}{\mid r_i - \mathbf{R}_j \mid}$ and $\frac{1}{2} \sum_{IJ(J=I)} \frac{Z_I Z_J e^2}{\mid \mathbf{R}_I - \mathbf{R}_J \mid}$ terms represent the repulsive electron-electron and ion-ion interactions. Based on the huge disparity in the mass between ions and electrons it is intuitive to consider the ions as moving very slowly and the electrons 'instantaneously' responding to any ionic motion. By separating the ionic and electron motions it is possible to construct ψ, such that it has an explicit dependence on the electron positions alone; this is known as the Born-Oppenheimer approximation [103]. Consequently, it is possible to ignore the kinetic energies of the nuclei and also to discount the ion-ion interactions as this will be constant for any given electron. Taking these approximations into account the Hamiltonian can be described by equation 3.42, shown below,

$$H = -\sum_{i} \frac{\hbar^2}{2m_e} \nabla^2_{r_i} + \sum_{i} V_{ion}(r_i) + \frac{e^2}{2} \sum_{ij(j=i)} \frac{1}{\mid r_i - r_j \mid} \tag{3.42}$$

where, $V_{ion} r_i$ is the ionic potential felt by every electron, i.

3.8.2 The Hartree and Hartree-Fock approximations

Owing to the introduction of the Born-Oppenheimer approximation it is only necessary to construct ψ based on the electron positions. The simplest way to achieve this, is to treat the electrons as a series of non-interacting particles, as shown in equation 3.43,

$$\psi^H(\{r_i\}) = \phi_1(r_1)\phi_2(r_2)\cdots\phi_N(r_N) \tag{3.43}$$

where, $\phi_i(r_i)$ represent the normalised wavefunctions of the individual electrons. This simple model is called the Hartree approximation and the energy of a system can be expanded to give,

$$E^H = \psi^H \mid H \mid \psi^H \tag{3.44}$$

$$= \sum_i \phi_i \mid \frac{-\hbar^2\nabla_r^2}{2m_e} + V_{ion}(r_i) \mid \phi_i \; + \frac{e^2}{2} \sum_{ij(j=i)} \phi_i\phi_j \mid \frac{1}{\mid r-r \mid} \mid \phi_i\phi_i \tag{3.45}$$

where, $\psi^H \mid H \mid \psi^H$, in Dirac bracket notation [104], is a short hand way to represent the integral, $\int \psi^H H \psi^H d\tau$ which represents the expectation value for the Hamiltonian energy of a system described by ψ^H [105].

Using a variational argument the single-particle Hartree equations can be given as,

$$\left[\frac{-\hbar^2\nabla_r^2}{2m_e} + V_{ion}(r_i) + e^2 \sum_{j=i} \phi_j \mid \frac{1}{\mid r-r \mid} \mid \phi_j \right] \phi_i(r) = \varepsilon_i\phi_i(r) \tag{3.46}$$

where the constants ε_i are Lagrange multipliers introduced to take the normalisation of the single-particle wavefunctions into account. Each orbital, $\phi_i(r_i)$, can then be determined by solving the Schrödinger equation, assuming all $\phi_j(r_j)$ are known. As this is not the case, a set of ϕ_i's is assumed and the problem is resolved iteratively until the input and output orbitals are self consistent, for an example of this process refer to page 45 of [106].

There are, however, two rather severe approximations included in this simple approach. Firstly it ignores the fact that electrons are fermions. The Pauli exclusion principle, with a single-valued many-particle wavefunction, is equivalent to the assumption that the wavefunction is an-

tisymmetric. Combining the Hartree-type wavefunctions to form a properly anti-symmerterised wavefunction for the system gives the Slater determinant [107], shown in equation 3.47:

$$\psi^{HF}(\{r_i\}) = \frac{1}{\sqrt{N!}} \begin{vmatrix} \phi_1(r_1) & \phi_1(r_2) & \cdots & \phi_1(r_N) \\ \phi_2(r_1) & \phi_2(r_2) & \cdots & \phi_2(r_N) \\ \vdots & \vdots & & \vdots \\ \phi_N(r_1) & \phi_N(r_2) & \cdots & \phi_N(r_N) \end{vmatrix} \tag{3.47}$$

This approach, called the Hartree-Fock approximation has the desired effect, as when two electrons 'exchange' positions then the determinant changes sign. Following a similar methodology to that employed in the Hartree approximation, the single-particle Hartree-Fock equations are,

$$\left[\frac{-\hbar^2\nabla_r^2}{2m_e} + V_{ion}(r_i) + e^2 + V_i^H(r)\right]\phi_i(r) - e^2\sum_{j=i}\phi_j \mid \frac{1}{\mid r-r \mid} \mid \phi_i \ \phi_j(r) = \varepsilon_i\phi_i(r) \tag{3.48}$$

This equation has one extra term compared to the equivalent Hartree single particle equation, the last of which is known as the 'exchange' term.

Despite this added level of sophistication there is still one significant approximation contained within the Hartree and Hartree-Fock approaches. In both instances each electron is said to move in the mean field of the other electrons. This is clearly a simplification, as the electron interactions will depend explicitly on the positions of other electrons in the system. This approximation is referred to as neglect of 'correlation' [108]. Including the effects of correlation into first principles simulations, while ensuring that the method is computationally tractable, has led to the development of an entirely different approach to building the wavefunction.

3.8.3 Density functional theory

The density functional

Density functional theory (DFT) was developed in a series of seminal papers by Hohenburg, Kohn and Sham [109, 110]. The underlying concept is to reformulate the problem in terms of

the total density, $n(r)$, of the electrons rather than by dealing with the many-body wavefunction, $\psi(\{r_i\})$. $n(r)$ is defined in equation 3.49 [106]. Unlike, the Hartree and Hartree-Fock approaches, DFT avoids introducing the approximations associated with the many-body wavefunctions, the single-particle equations can be developed in an exact manner.

$$n(r) = N \int \Psi\ (r, \ldots, r_N)\Psi(r, \ldots, r_N) dr_2 \ldots dr_N \tag{3.49}$$

The key concept in DFT is that the density, $n(r)$, is a unique function of the external potential, $V(r)$, which in turn is identified by the ionic potential (this will be examined later). As the external potential determines the wavefunction, the wavefunction must also be a function of the density. The other terms, which form part of the Hamiltonian, other than $V(r)$, are the kinetic energy, T, and the electron-electron interaction, W. As the kinetic energy and electron-electron interactions are common to all solids, they can be described as by a universal function with explicit dependence on the electron density, that is,

$$F[n(r)] = \ \Psi|(T+W)|\Psi\ . \tag{3.50}$$

The total energy of a system can then be described by equation 3.51, and it can be shown, using variational theory, that this functional attains a minimum for the correct density $n(r)$ for an external potential $V(r)$.

$$E[n(r)] = \ \Psi|H|\Psi\ = F[n(r)] + \int V(r)n(r)dr \tag{3.51}$$

Using the one-particle and two-particle density matrices, denoted by, $\gamma(r, r\ )$ and $\Gamma(r, r\ |r, r\ )$ respectively, (the physical significance of these terms is explored on pages 536-537 of [106]) an explicit expression for $E(n)$ can be obtained,

$$\begin{aligned} E[n(r)] = \ \Psi|H|\Psi\ &= -\frac{\hbar^2}{2m_e} \int \nabla_r^2 \gamma(r, r\ )|_{r=r} dr \\ + \int \int \frac{e^2}{|r - r\ |} \Gamma(r, r\ |r, r\ ) dr dr\ &+ \int V(r)\gamma(r, r\ )dr). \end{aligned} \tag{3.52}$$

Again this expression can be reduced to a set of single-particle equations, however, this time the single particle states do not correspond directly to the electrons, as in the Hartree and Hartree-Fock approaches. Rather, they represent fictitious fermion particles with a density identical to that of the electrons. Equation 3.53 describes the single-particle equations,

$$\left[-\frac{\hbar^2}{2m_e}\nabla_r^2 + V^{eff}(r,n(r))\right]\phi_i(r) = \varepsilon_i\phi_i(r) \tag{3.53}$$

where,

$$V^{eff}(r,n(r)) = V(r) + e^2\int\frac{n(r\,)}{|r-r\,|}dr\; + \frac{\delta E^{XC}[n(r)]}{\delta n(r)} \tag{3.54}$$

and $E^{XC}[n(r)]$ describes the exchange-correlation interactions contribution to the effective potential. Unfortunately, an exact form, derived from first-principles, for $E^{XC}[n(r)]$ has not been developed, however, some simplified approximate functions have been developed and applied with considerable success.

Exchange-correlation functionals

The simplest approximation to $E^{XC}[n(r)]$ is known as the Local Density Approximation (LDA) [110], which states that, for each infinitesimal element of density, $n(r)dr$, the exchange correlation energy is that of a uniform electron gas. Clearly, this is an approximation, as the charge density surrounding an atom is highly non-uniform. An attempt to improve upon the LDA, by accounting for spatial variations in the density, is provided by the Generalised Gradient Approximation (GGA) [111]. In the GGA approach, the exchange correlation energy is modified to include a dependence on the gradient of the density.

The ionic potential

In order to solve the single-particle equations, however, they may have been generated, it is necessary to specify the ionic potential. When modeling properties of solids it is intuitive to consider only the valence electrons, therefore it is possible to separate the electron density into

core and valence parts. The electron density in the core is largely unaffected by the valance states, however, beyond the core region the electron density is dominated by the valence states. Based on this observation it is possible to take the core electrons out of the picture and develop a smoother (ie. simpler) potential for the valance electrons. This approach is known as the 'pseudopotential method' [112], and its application is a corner stone in achieving computationally tractable DFT simulations for large numbers of atoms [113]. Figure 3.7, shows a schematic representation of the pseudo-wavefunction and pseudopotential.

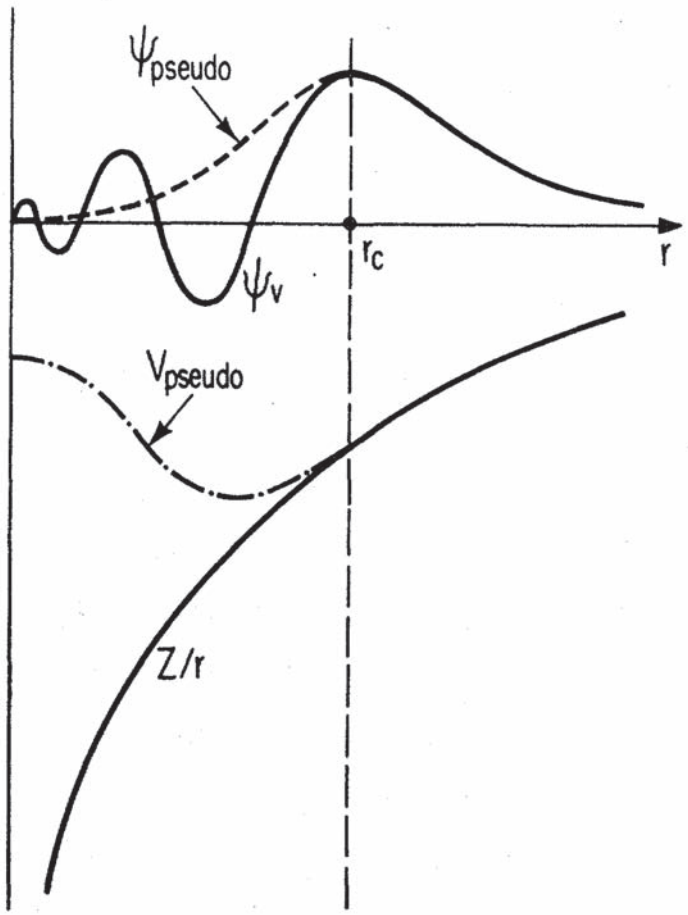

Figure 3.7: Schematic illustration of all electron (solid lines) and pseudoelectron (dashed lines) and their corresponding wave functions. r_c is the cutoff radius beyond which the wavefunction and the potential are not affected (reproduced from Payne *et al.* [114]).

4

Defects and defect clusters in spinel

Aspects of this work have previously been published in Solid State Sciences [75].

4.1 Introduction

An ideal crystal displays an exact stoichiometric ratio between its constituents, where each ion is situated on the appropriate lattice site and each lattice site is occupied by the appropriate ion. Such a crystal can only be in 'true equilibrium' at 0 K, as at any temperature greater than this, there is a finite probability of a lattice ion having enough energy to leave its lattice site, generating vacancy, interstitial and/or antisite defects. It is for this reason that ideal or perfect crystals are never observed, ie. all ionic crystals (and in fact all solids) will contain some level of intrinsic point defects. Many of the important properties of ionic crystals are influenced and often determined by the defect structure and particularly by the properties of the point defects [115]. It is not merely the concentration and structure of the isolated point defects themselves that can determine a material's properties but also the interactions between them. Voids are examples of large formations of point defects, clustering together and becoming visible on a microscopic level and creating the possibility of a serious mechanical failure.

The way in which a material is processed has a significant impact on the concentration and distribution of point defects within a solid, however, there is a thermodynamic driving force to achieve a state of equilibrium at a given temperature. Thermodynamics is not the only factor controlling the concentration of point defects, kinetics can also play a significant role. An-

nealing processes, such as interstitial-vacancy recombination, require that either the vacancy or interstitial defects are mobile enough to move through the lattice and annihilate. Migration through the lattice can be considered to involve millions of tiny 'hops' each of which has an associated migration energy, E_m. If the migration energy for any of the necessary 'hops' is particularly high then point defect recombination will be retarded; this is known as kinetic hinderance. Defects can also be introduced into an ionic lattice by bombardment with high energy particles, such as neutrons, protons or heavy ions. Elastic collisions between the bombarding particle and a lattice ion may transfer energy to displace the lattice ion. For example, MD simulations by Smith *et al.* [73] show how the transfer of energy from the bombarding particle to a lattice atom can lead to the formation of a large disordered region.

In this chapter, atomistic simulation techniques have been employed to investigate the thermodynamics of intrinsic point defects in spinel (kinetics will be considered in later chapters). Initially the point defects are treated in isolation, ie. a perfect crystal containing one defect (this is known as the dilute limit). The relative concentrations of the intrinsic point defects, in a fully equilibrated spinel, can then be predicted by comparing the reaction energies for the disorder processes. This approach is then extended to examine how antisite defects cluster together and finally to investigate the stability of some of the more exotic small defect clusters observed in the MD cascade simulations of Smith *et al.* [73].

4.2 Methodology

The simulations presented in this chapter are a mixture of classical pair potential simulations and, where applicable, DFT calculations. For the classical pair potential simulations a full charge model was adopted (ie. Mg^{2+}, Al^{3+} and O^{2-}) and short range interactions were described using the Buckingham potential form (equation 3.8). The A_{ij}, ρ_{ij} and C_{ij} parameters for these are reported in table 4.1. Previously, in addition to the cascade simulations of Smith *et al.* [73] this set of potentials have been used successfully to model the decrease in lattice parameter as a function of inversion [50] as well as defect evolution [116].

In addition to these potential parameters the shell model of Dick and Overhauser [85] was adopted to simulate polarisation of the O^{2-} anions. Here, a core with a positive charge of 0.8 $|e|$ is 'attached' via a harmonic force constant, k = 54.8 eV.Å^{-2}, to a shell of charge -2.8 $|e|$.

Table 4.1: Short range Buckingham potential parameters used to model spinel [73].

Species	A_{ij} /eV	ρ_{ij} /eV	C_{ij} /eV.Å^{-6}
$O^{2-}-O^{2-}$	9547.96	0.21916	32.00
$Mg^{2+}-O^{2-}$	1279.69	0.29969	0.00
$Al^{3+}-O^{2-}$	1361.29	0.30130	0.00

This shell model has been used in all calculations presented in this thesis, unless otherwise stated.

As detailed in chapter 3, there has been a significant increase in the use of computational modeling to investigate the processes that occur on the atomic scale in solids. The usefulness of computer simulation should not be underestimated, but nevertheless it is essential that, where possible, comparisons are made with available experimental data to ensure the accuracy of the model. In order that the simulations presented here are realistic every effort has been made to find parallel data in the literature, both computational and experimental, with which to compare.

4.3 Results and discussion

4.3.1 Perfect lattice

In order to further justify the model employed here, the perfect unit cell was relaxed to zero strain using energy minimization at constant pressure. Once the lattice had equilibrated into a state of mechanical equilibrium, a number of physical properties were determined based on the resulting structure and the results compared with similar experimental and theoretical data found in the literature (see table 4.2).

An examination of the data given in table 4.2 shows that the lattice parameter, a, predicted by the pair potential technique is closer to the experimentally observed value, given by Yoneda [118], than that predicted using the quantum mechanical techniques. Unfortunately the level of inversion present in the single crystal sample used by Yoneda *et al.* [118] is not reported, however, as shown in section 2.3.3 the affect on the volume is likely to be extremely small assuming that the level of inversion, i, is not significant. The volume predicted by the pair

Table 4.2: Comparison of physical properties of a perfect spinel unit cell determined using the potential model of Smith *et al.* [73] both with and without the shell model, DFT calculations of Yao *et al.* [117] and the single crystal experimental data of Yoneda [118].

Property	This Study (Shells)	This Study (No Shells)	LDA/GGA [117]	Experimental [118]
a /Å	8.09	8.11	8.02/8.16	8.086
V_0 /Å^3	529.48	533.41	515.82/543.82	528.69
c_{11} /GPa	367.75	405.27	273.6/256.5	282.9
c_{12} /GPa	234.47	212.09	149.6/133.2	155.4
c_{44} /GPa	178.82	186.31	150.7/142.4	154.8
Bulk Modulus /GPa	278.97	276.48	190.93/174.3	197.9

potential method is also found to be very good at reproducing the unit cell volume obtained by experiment, with a difference of only 0.19%. There is a relatively large discrepancy between the elastic constants obtained from the pair potential simulations and experimental techniques; consequently, there is also a discrepancy in the bulk modulus. One explanation for this is the use of a full charge model (ie. the ions are assigned their fully ionized charges) increasing the energy penalty for any deviation from the equilibrium structure, as the interactions between the charge defect and the charged ions in the surrounding lattice will be modified. Conversely, the LDA simulations, in particular, reproduce the elastic constants closely.

Overall, as the model is intended for the calculation of lattice and defect energies, as well as migration energies and not the calculation of parameters dependent on phonon interactions the model is considered to be a satisfactory description of the spinel system.

4.3.2 Intrinsic defect processes

There are eight unique intrinsic defect species found in magnesium aluminate spinel, these are the: V_{Mg}, V_{Al}, $V_O^{\bullet\bullet}$, $Mg_i^{\bullet\bullet}$, $Al_i^{\bullet\bullet\bullet}$, O_i , Mg_{Al} and $Al_{Mg}^{\bullet}$, all of which can be formed by one of the Schottky, Frenkel or antisite disorder processes. The intrinsic disorder process specific to spinel are the antisite process, shown in equation 4.1 (repeated here for convenience), the magnesium, aluminium and oxygen Frenkel processes (equations 4.2-4.4) and the Schottky process (equation 4.5).

$$Mg_{Mg} + Al_{Al} \rightleftharpoons Al^{\bullet}_{Mg} + Mg_{Al} \tag{4.1}$$

$$Mg_{Mg} \rightleftharpoons V_{Mg} + Mg^{\bullet\bullet}_{i} \tag{4.2}$$

$$Al_{Al} \rightleftharpoons V_{Al} + Al^{\bullet\bullet\bullet}_{i} \tag{4.3}$$

$$O_{O} \rightleftharpoons V^{\bullet\bullet}_{O} + O_{i} \tag{4.4}$$

$$Mg_{Mg} + 2Al_{Al} + 4O_{O} \rightleftharpoons V_{Mg} + 2V_{Al} + 4V^{\bullet\bullet}_{O} + MgAl_2O_4 \tag{4.5}$$

A list of the defect energies obtained using the Mott-Littleton [89] methodology, implemented in the CASCADE simulation package [119], is given in table 4.3.

Table 4.3: Dilute limit defect energies in $MgAl_2O_4$ calculated via the Mott-Littleton method, both with and without shells.

Defect	Defect Energy (Shells) /eV	Defect Energy (no Shells) /eV
V_{Mg}	26.70	28.09
V_{Al}	56.48	57.00
$V^{\bullet\bullet}_{O}$	25.00	25.48
$Mg^{\bullet\bullet}_{i}$	-15.30	-15.23
$Mg^{\bullet\bullet}_{i}$-V_{Mg}-$Mg^{\bullet\bullet}_{i}$	-15.87	-15.71
$Al^{\bullet\bullet\bullet}_{i}$	-41.86	-40.97
$Al^{\bullet\bullet\bullet}_{i}$-$V_{Mg}$-$Mg^{\bullet\bullet}_{i}$	-42.78	-41.91
O_i	-13.04	-10.08
O_i -$V^{\bullet\bullet}_{0}$-O_i	-14.01	-13.00
Mg_{Al}	29.98	29.94
$Al^{\bullet}_{Mg}$	-28.53	28.40

The defect energies shown in table 4.3 agree very well with some similar calculations conducted by De Souza and Blak [120] who found V_{Mg}=25.99 eV, V_{Al}=55.60 eV and $V_O^{\bullet\bullet}$=25.44 eV. Additionally, table 4.3 gives a comparison between the isolated interstitial species, whereby an ion is merely accommodated on an unoccupied 8*b* Wyckoff position, and the equivalent split interstitial structures. In the case of magnesium and aluminium, the split interstitial structure can be thought of as either two Mg^{2+} cations (for a magnesium interstitial) or one Mg^{2+} and one Al^{3+} cations (for an aluminium split interstitial) on two of the four unoccupied 8*b* Wyckoff sites surrounding a vacant tetrahedral 8*a* site. An idealised version of the tetrahedral site as well as idealised split cation interstitials can be found in figure 4.1. For both cation species in spinel the defect energy, both with and without shells, of the split interstitial species was lower than the simple octahedral interstitial. Comparable simulations conducted by Gilbert *et al.* [121], using the DFT code PLATO [122] were exchange correlation is modelled using the LDA, also found that the formation energy for split cation interstitial defects was lower than for isolated interstitial defects (the formation energy for $Mg_i^{\bullet\bullet}$ was 7.58 eV whilst for $Mg_i^{\bullet\bullet}$-V_{Mg}-$Mg_i^{\bullet\bullet}$ a value of 6.68 eV was found).

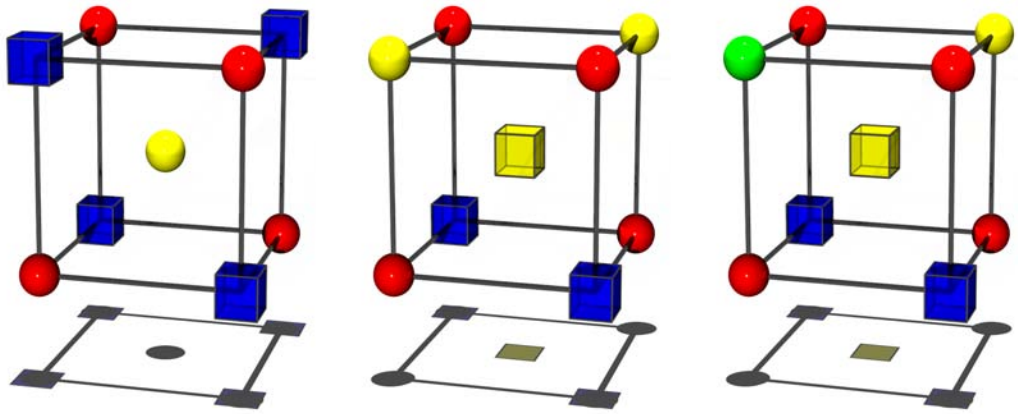

(a) (b) (c)

Figure 4.1: Split cation interstitial species in spinel. Figure (a) shows an idealised (idealised indicates that the oxygen anions are shown on perfect lattice positions dictated by the $Fd3m$ space group) tetrahedral, 8*a*, site and the four transparent blue cubes represent the surrounding unoccupied 8*b* sites. Figures (b) and (c) represent the split magnesium and aluminium interstitial structures respectively. In these structures the magnesium lattice atom has become displaced and there are now two of the 8*b* sites surrounding the vacancy occupied with cations.

The defect energy for the oxygen split interstitial is also lower then that obtained for the equivalent octahedral interstitial defect. A pictorial representation of the oxygen split interstitial

defect is given in figure 4.2. Gilbert *et al.* [121] also predict that oxygen also forms split interstitials.

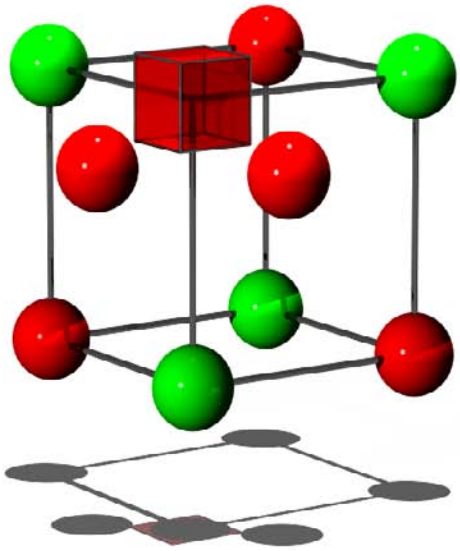

Figure 4.2: Idealised oxygen split interstitial defect, aligned along the 110 direction.

When a defect is introduced into a lattice there can be an associated change in the volume of the crystal. The defect volumes for each of the intrinsic point defects in spinel is reported in table 4.4.

The data shown in table 4.4 predicts, that when an ion is removed the lattice will expand. That is, instead of the surrounding ions relaxing to fill the void left by the removal of an ion, they actually relax away from the vacant site. This is because, by removing an ion, the attractive electrostatic interaction drawing in the, oppositely charged, neighbouring ions is removed. An increase in the volume of a crystal is also observed when extra ions are placed into a crystal. Placing an Al^{3+} cation onto a tetrahedral site causes the crystal to contract owing to the increased electrostatic attraction between the tetrahedrally co-ordinated cation and the surrounding O^{2-} ions. The opposite effect is observed when a Mg^{2+} cation is substituted onto an aluminium site.

Using the defect energies given in table 4.1 it is possible to determine the reaction energies for the intrinsic disorder equilibria discussed above. These are shown in table 4.5. For the Frenkel processes the split interstitial defect is used to determine the reaction energy as opposed to the

Table 4.4: Defect volumes for the intrinsic point defects calculated both with and without as shell model.

Defect	Defect Volume (Shells) /Å^3	Defect Volume (no Shells) /Å^3
V_{Mg}	4.44	8.42
V_{Al}	9.11	9.41
$V_O^{\bullet\bullet}$	4.00	4.45
$Mg_i^{\bullet\bullet}$-V_{Mg}-$Mg_i^{\bullet\bullet}$	7.90	7.90
$Al_i^{\bullet\bullet\bullet}$-$V_{Mg}$-$Mg_i^{\bullet\bullet}$	9.43	9.67
O_i -$V_0^{\bullet\bullet}$-O_i	12.23	13.60
Mg_{Al}	4.70	4.54
$Al_{Mg}^{\bullet}$	-4.12	-4.49

simple octahedral interstitial as they are predicted to be lower in energy.

Table 4.5: Normalised reaction energies for the intrinsic defect reactions in spinel, both with and without shells and again compared with DFT results of Gilbert [121].

Reaction	Reaction Energy (Shells) /eV	Reaction Energy (no Shells) /eV	Reaction Energy (DFT) /eV
Schottky	5.32	5.99	3.53
Mg Frenkel	5.41	6.19	5.46
Al Frenkel	6.86	6.44	4.99
O Frenkel	5.49	6.24	4.43
Antisite	0.73	0.77	0.64

The pair potential and quantum mechanical simulations agree that the reaction energies for the antisite process are nearly an order of magnitude lower than their corresponding Schottky and Frenkel processes. As a consequence of this, the concentration of antisite defects will be several orders of magnitude greater than for other point defects. The values in table 4.5 are in a similar range to that suggested by Chiang *et al.* [123], who predict values in the region 4.5-7.0 eV. There is considerable disagreement between the empirical and DFT calculations. Both empirical models (ie. with and without accounting for the affects of polarisation) suggest that the Schottky, oxygen Frenkel and magnesium Frenkel are all very similar in energy, how-

ever,the aluminium Frenkel is clearly higher, thus suggesting that whilst the concentration of Mg^{2+} and O^{2-} defects will be roughly equal, they will both be greater than the concentration of Al^{3+} defects. Conversely, the DFT simulations of Gilbert *et al.* [121] predict that the Schottky process is noticeably lower than the aluminium and oxygen Frenkel processes whilst it is the magnesium Frenkel process which is lowest in energy.

There are many factors which could be responsible for this discrepancy. The empirircal simulations, employed to calculate the reaction energies use a full charge model, therefore when defects are introduced into the lattice the defect is assigned a full charge which will then overestimate the attraction to oppositely charged neighbours. In the LDA, DFT simulations of Gilbert *et al.* [121], a Bader charge analysis gives charges of 1.78, 2.56 and -1.73 $|e|$ for magnesium, aluminium and oxygen respectively, which suggests the use of a partial charge model may be appropriate. Additionally, the DFT simulations may be able to detect more complex charge distributions than is possible using the empirical simulations. Although it is important to note that DFT simulations are incapable of including Van der Waals forces. This means that when modelling the attraction between defects in clusters the defects in the DFT simulations are likely to experience less attracted to each other due to the reduction in the Coulombic interaction the complete lack of Van der Waals attraction.

Conversely, owing to the computationally demanding nature of the DFT simulations a supercell method was used therefore it is possible that the defects in neighbouring cells (periodic boundary conditions were employed) [121] may interact, which may also affect the defect energies. Furthermore, it is possible that implementation of GGA for modelling the exchange-correlation energy may improve the defect, and therefore process energies, however, this has not been done when considering defects in spinel. Where a direct comparison of the GGA and LDA has been applied on spinel is in the prediction of the elastic constant matrix [117]. In this study Yoneda *et al.* found that implementing the GGA did not lead to an improvement in the predicted elastic constant matrix or lattice parameter compared with experimental values.

4.3.3 Intrinsic defect clustering

Overall a crystal must remain charge neutral. This means that if there is a positively charged defect in the crystal, there must be other oppositely charged point defects elsewhere in the

lattice to compensate. In a similar way to the attractive electrostatic force felt by oppositely charged ions, oppositely charged defects will be attracted to each other. Consequently, it is possible that many of the defects found in a solid will be in clusters. In the previous section it was shown that the antisite process had a reaction energy nearly an order of magnitude lower than the other processes. Therefore, there will be a large number of antisite defects present in the lattice, which could form partially or fully charge compensated, clusters with each other or with vacancy and interstitial defects.

Perhaps the easiest defect cluster to examine first is the fully charge compensated antisite pair $\{Al^{\bullet}_{Mg}{:}Mg_{Al}\}$ cluster. Figure 4.3 shows that as the separation between the defects is increased then the electrostatic attraction between them is lessened and so the defect energy is increased. The solid lines represent the energy of the defects when infinitely separated, and as such the difference between the point and the solid lines is the binding energy between the two defects. Clearly the empirical simulations predict that as the separation is increased the defect energy tends towards the solid line. Gilbert *et al.*'s [121] DFT simulations predicted that at separations greater than 5.5 Å the defects are no longer bound and that it is more thermodynamically favourable for them to occur at infinite separation. Clearly, owing to the form of the Coulombic interaction (equation 3.3) between charged defects, the interaction energy will decrease as the separation increases. Therefore it is surprising that the defect energy for infinitely separated charged defects is predicted by the DFT simulations to be lower than at a separation of 5.5 Å. Gilbert *et al.* [121] argue that their simulations may be detecting a complex local strain effect that can overcome the attraction of the opposite charges. The DFT simulations here employ a supercell method for determining the binding energies between the antisite defects, therefore, the pair empirical simulations should be repeated using a similar technique to determine whether the predictions made from the DFT data arises from an image effect. In the nearest neighbour configuration, in which both empirical and DFT techniques predicted a bound cluster, the observed binding energy (ie. the difference between the points and the solids line) is greater in the empirical case than predicted by the DFT. Again this is due to the use of a full charge model in the empirical simulations, overestimating the electrostatic attraction between the defects.

Interestingly, the empirical data suggests that there are two symmetrically distinct configurations of the $\{Al^{\bullet}_{Mg}{:}Mg_{Al}\}$ cluster where the separation between the antisite defects is 5.3 Å. As the separations are practically identical then the electrostatic contribution to the defect en-

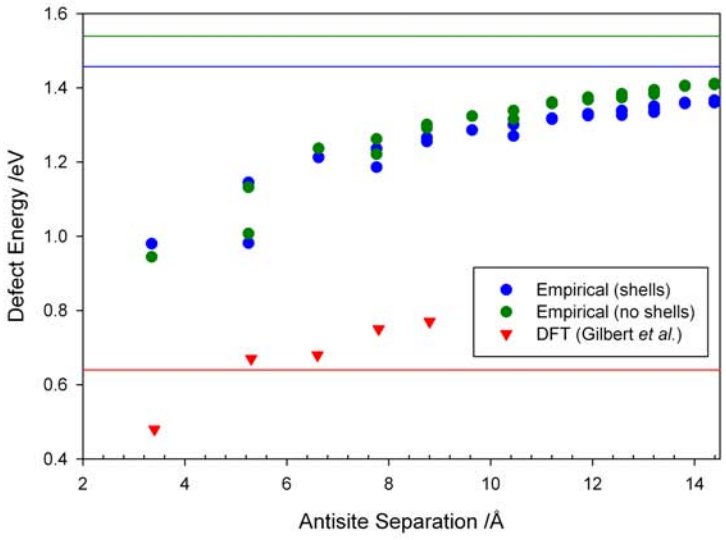

Figure 4.3: Plot showing the variation in the binding energy of a $\{Al^{\bullet}_{Mg}{:}Mg_{Al}\}$ defect cluster as a function of the separation between the two defects as predicted by the empirical model and the DFT work of Gilbert *et al.* [121]. The solid lines represent the energies of the defect pairs when infinitely separated.

ergy in each case is also very similar, therefore this difference in energy must be a strain issue. Diagram 4.4 shows the arrangement of these two different clusters. Whilst it may be difficult to discern in figure 4.3, the empirical model both with and without shells predicts that the nearest neighbour configuration is the lowest in energy, however, the similar energy obtained for one of the clusters at 5.3 Å highlight the importance of considering the strain on the lattice.

The defect volume for the nearest neighbour $\{Al^{\bullet}_{Mg}{:}Mg_{Al}\}$ cluster is predicted to be -0.29 Å by a model with shells and -0.95 Å without. This data is inline with experimental observations which suggest that as the inversion is increased, the lattice parameter is decreased [43]. Conversely, by merely assuming that antisite defects are completely isolated then the lattice is predicted to expand by 0.58 Å in the model with shells compared to an increase of 0.05 Å in the model without shells. Consequently, this suggests that the antisite defects must be occurring in clusters in spinel in order to replicate the experimentally observed decrease in lattice parameter [43].

Table 4.6 shows the defect and binding energies for the vacancy and interstitial intrinsic defects clustered to antisite defects. Again, a comparison with the DFT results of Gilbert *et al.* [121] is

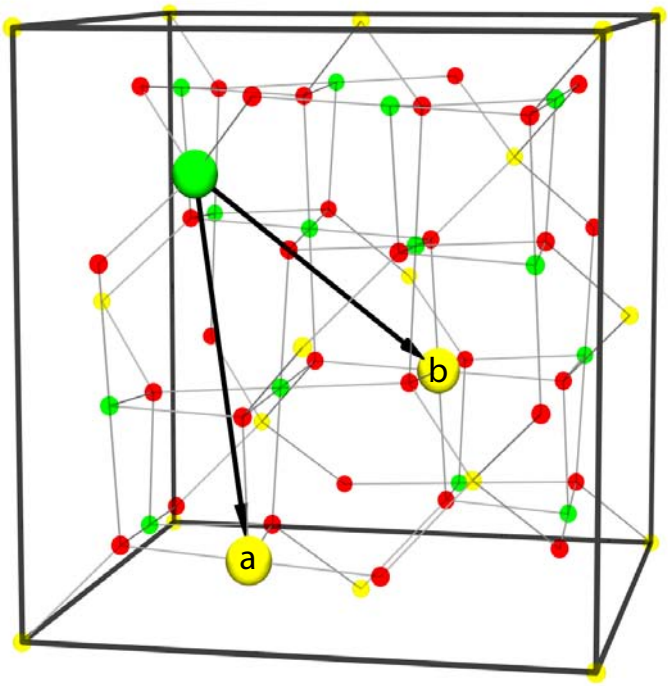

Figure 4.4: Diagram showing a $Al^{\bullet}_{Mg}$ defect (represented by the large green sphere) and two possible second nearest neighbour Mg_{Al} defects, represented by the large yellow spheres and marked with an a and b.

made. The defect cluster energies presented in table 4.6 are for the lowest energy configuration of the defects in the cluster. These were obtained by placing an intrinsic point defect in a unit cell and then sampling all arrangements of the antisite defects around it.

In general, the empirical and DFT techniques both predict that as the number of antisite defects in the clusters increases the magnitude of the binding energy is increased. A notable exception to this is for V_{Mg} binding energies determined by DFT. Gilbert *et al.* [121] again cite strain as the cause for this counterintuitive behaviour. The empirical potentials overestimate the binding energy compared with the DFT data, which is due to the full charge model overemphasizing the electrostatic interaction between oppositely charged defects.

Considering these defect clusters in table 4.6, it is possible to construct a series of equations analogous to the isolated Schottky and Frenkel processes; shown in equations 4.6-4.9 for dimer clusters, equations 4.10-4.13 for trimer clusters and equation 4.14 for quatramer clusters.

$$Mg_{Al} + Al^{\bullet}_{Mg} + Mg_{Mg} \rightleftharpoons \{Mg_i^{\bullet\bullet} : Mg_{Al}\}^{\bullet} + \{V_{Mg} : Al^{\bullet}_{Mg}\} \tag{4.6}$$

$$Mg_{Al} + Al^{\bullet}_{Mg} + Al_{Al} \rightleftharpoons \{Al_i^{\bullet\bullet\bullet} : Mg_{Al}\}^{\bullet\bullet} + \{V_{Al} : Al^{\bullet}_{Mg}\} \tag{4.7}$$

$$Mg_{Al} + Al^{\bullet}_{Mg} + O_O \rightleftharpoons \{O_i : Al^{\bullet}_{Mg}\} + \{V_O^{\bullet\bullet} : Mg_{Al}\}^{\bullet} \tag{4.8}$$

$$4Mg_{Al} + 3Al^{\bullet}_{Mg} + Mg_{Mg} + 2Al_{Al} + 4O_O \rightleftharpoons \{V_{Mg} : Al^{\bullet}_{Mg}\} + 2\{V_{Al} : Al^{\bullet}_{Mg}\} + 4\{V_O^{\bullet\bullet} : Mg_{Al}\}^{\bullet} + MgAl_2O_4 \tag{4.9}$$

$$2Mg_{Al} + 2Al^{\bullet}_{Mg} + Mg_{Mg} \rightleftharpoons \{Mg_i^{\bullet\bullet} : 2Mg_{Al}\} + \{V_{Mg} : 2Al^{\bullet}_{Mg}\} \tag{4.10}$$

$$2Mg_{Al} + 2Al^{\bullet}_{Mg} + Al_{Al} \rightleftharpoons \{Al_i^{\bullet\bullet\bullet} : 2Mg_{Al}\}^{\bullet} + \{V_{Al} : 2Al^{\bullet}_{Mg}\} \tag{4.11}$$

Table 4.6: Defect and binding energies for intrinsic point defects clustered with antisite defects, calculated using empirical potentials with and without shells. The binding energies are compared to similar values determined using DFT by Gilbert *et al.* [121]. Reaction energies are normalised per defect.

Defect Cluster	Defect Energy (Shells) /eV	Binding Energy (Shells) /eV	Defect Energy (no Shells) /eV	Binding Energy (no Shells) /eV	Binding Energy (DFT) /eV
O_i	-14.01	0.0	-13.00	0.0	0.0
$\{O_i : Al_{Mg}^{\bullet}\}$	-44.27	-1.80	-43.76	-2.36	-0.83
$\{O_i : 2Al_{Mg}^{\bullet}\}$	-73.76	-2.82	-73.59	-3.80	-1.32
V_{Mg}	26.70	0.0	28.09	0.0	0.0
$\{V_{Mg} : Al_{Mg}^{\bullet}\}$	-2.57	-0.81	-1.22	-0.91	-0.1
$\{V_{Mg} : 2Al_{Mg}^{\bullet}\}$	-31.61	-1.39	-30.26	-1.54	-0.0025
V_{Al}	56.48	0.0	57.00	0.0	0.0
$\{V_{Al} : Al_{Mg}^{\bullet}\}$	26.57	-1.45	26.87	-1.72	-0.36
$\{V_{Al} : 2Al_{Mg}^{\bullet}\}$	-3.05	-2.61	-2.44	-2.64	-0.89
$\{V_{Al} : 3Al_{Mg}^{\bullet}\}$	-32.38	-3.48	-32.36	-4.15	-
$V_O^{\bullet\bullet}$	25.00	0.0	25.48	0.0	0.0
$\{V_O^{\bullet\bullet} : Mg_{Al}\}^{\bullet}$	53.42	-1.55	53.57	-1.85	-0.57
$\{V_O^{\bullet\bullet} : 2Mg_{Al}\}$	82.48	-2.49	82.34	-3.02	-0.89
$Mg_i^{\bullet\bullet}$	-15.87	0.0	-15.71	0.0	0.0
$\{Mg_i^{\bullet\bullet} : Mg_{Al}\}^{\bullet}$	13.07	-1.04	12.98	-1.24	-0.36
$\{Mg_i^{\bullet\bullet} : 2Mg_{Al}\}$	42.37	-1.73	42.09	-2.08	-0.67
$Al_i^{\bullet\bullet\bullet}$	-42.75	0.0	-41.90	0.0	0.0
$\{Al_i^{\bullet\bullet\bullet} : Mg_{Al}\}^{\bullet\bullet}$	-14.28	-1.51	-13.78	-1.83	-0.44
$\{Al_i^{\bullet\bullet\bullet} : 2Mg_{Al}\}^{\bullet}$	14.63	-2.59	14.88	-3.11	-0.83
$\{Al_i^{\bullet\bullet\bullet} : 3Mg_{Al}\}$	43.84	-3.36	43.89	-4.04	-

$$2Mg_{Al}+2Al^{\bullet}_{Mg}+O_O \rightleftharpoons \{O_i : 2Al^{\bullet}_{Mg}\} + \{V^{\bullet\bullet}_O : 2Mg_{Al}\} \quad (4.12)$$

$$8Mg_{Al}+6Al^{\bullet}_{Mg}+Mg_{Mg}+2Al_{Al}+4O_O \rightleftharpoons \{V_{Mg} : 2Al^{\bullet}_{Mg}\} + 2\{V_{Al} : 2Al^{\bullet}_{Mg}\} + 4\{V^{\bullet\bullet}_O : Mg_{Al}\}^{\bullet} + MgAl_2O_4 \quad (4.13)$$

$$3Mg_{Al}+3Al^{\bullet}_{Mg}+Al_{Al} \rightleftharpoons \{Al^{\bullet\bullet\bullet}_i : 3Mg_{Al}\} + \{V_{Al} : 3Al^{\bullet}_{Mg}\} \quad (4.14)$$

Using the cluster energies shown in table 4.6 it is possible to determine the reaction energies for the processes highlighted in equations 4.6-4.14; these are shown in table 4.7.

Table 4.7: Process energies for intrinsic defect processes involving defect clusters predicted using empirical pair potentials with and without shells. Also included is comparable data obtained using DFT by Gilbert *et al.* [121].

Process	Cluster	Reaction Energy (Shells) /eV	Reaction Energy (no Shells) /eV	Reaction Energy (DFT) /eV
Mg Frenkel	Isolated	5.41	6.19	3.34
	Dimer	4.49	5.11	3.10
	Trimer	3.85	4.38	3.09
Al Frenkel	Isolated	6.86	7.55	4.39
	Dimer	5.38	5.78	3.98
	Trimer	4.27	4.68	3.52
	Quatramer	3.44	3.46	-
O Frenkel	Isolated	5.49	6.25	4.43
	Dimer	3.82	4.14	3.73
	Trimer	2.84	2.84	3.33
Schottky	Isolated	5.32	5.99	3.53
	Dimer	3.90	4.31	3.08
	Trimer	2.95	3.29	2.77

Table 4.7 shows that as the size of defect clusters are increased the reaction energies for the defect processes are decreased. As antisite defect clustering lowers the energies for the intrinsic

defect reaction processes, clustering will elevate the concentration and indeed the ordering of concentrations will be modified. In the isolated case the empirical method predicted that the Schottky process has the lowest energy, however, when including the effects of antisite defect clustering, the oxygen Frenkel process becomes the most favourable. Conversely the DFT simulations predict that the magnesium Frenkel would dominate, however, assuming antisite clustering the Schottky process is dominant.

There are a number of other dimer clusters between the intrinsic point defects that one would expect to be bound, these are shown in table 4.8.

4.3.4 Defect clusters observed in damage simulations

The MD simulations of Smith *et al.* [73] also highlighted the presence of a variety of high energy, kinetically stabilised defect structures following the dissipation of a thermal energy spike. One of the more prevalent defect clusters observed in these simulations is the, so called, thermal crowdion. The thermal crowdion can be considered as an extended split cation interstitial. In the split interstitial structure there are two cations occupying two of the 8*b* sites surrounding a vacant tetrahedral, 8*a*, site, however, in a thermal crowdion there are two adjacent vacant 8*a* sites and a cation occupying the 8*b* interstice located between the two vacancies. Additionally there is a cation occupying one of the three remaining 8*b* sites surrounding each vacant 8*a* site. Whilst the structure is observed on the tetrahedral sublattice, this defect structure is not merely limited to Mg^{2+} interstitial ions, an example of a mixed cation crowdion would be $Al_i^{\bullet\bullet\bullet}$-$V_{Mg}$-$Mg_i^{\bullet\bullet}$-$V_{Mg}$-$Mg_i^{\bullet\bullet}$ shown in figure 4.5.

Figure 4.5 shows that crowdion formation is, in effect, a local translation to a rocksalt structure, a phenomenon which has been observed on a macroscopic scale [69]. Tables 4.9 and 4.10 compare the defect energies of the crowdion defect clusters and their equivalent split interstitial defect cluster with and without shells. The MD simulations of both Smith *et al.* [73] and Bacorisen *et al.* [74] did not include a shell model and therefore many of the crowdions in table 4.10 were not observed. Of the crowdion defects which were predicted to be thermally stable, all were found to be higher in energy than the equivalent interstitial cluster, except when there are three $Al_i^{\bullet\bullet\bullet}$ defects sharing the two vacant tetrahedral sites, this is probably due to the large electrostatic interaction between an $Al_{Mg}^{\bullet}$ defect and the highly positive $Al_i^{\bullet\bullet\bullet}$-$V_{Mg}$-$Al_i^{\bullet\bullet\bullet}$defect.

Table 4.8: Defect and binding energies for intrinsic point defects clusters calculated using empirical potentials with and without shells. The binding energies are compared to similar values determined using DFT by Gilbert *et al.* [121].

Defect Cluster	Defect Energy (Shells) /eV	Binding Energy (Shells) /eV	Defect Energy (no Shells) /eV	Binding Energy (no Shells) /eV	Binding Energy (DFT) /eV
$\{V_O^{\bullet\bullet} : V_{Mg}\}$	47.64	-4.06	49.00	-4.57	-2.04
$\{V_O^{\bullet\bullet} : V_{Al}\}$	76.82	-4.67	77.13	-2.01	-5.35
$\{O_i : Mg_i^{\bullet\bullet}\}$	-31.66	-1.91	-31.43	-2.17	-0.32
$\{O_i : Al_i^{\bullet\bullet\bullet}\}^{\bullet}$	-60.87	-3.53	-56.78	-5.44	-1.28

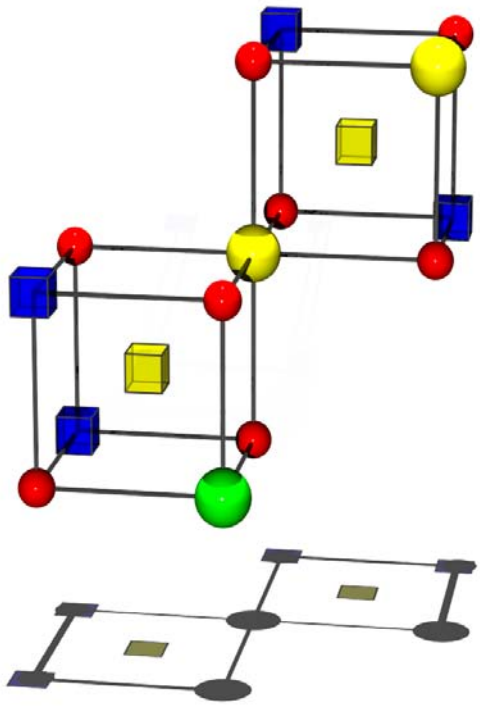

Figure 4.5: Idealised illustration of a $Al_i^{\bullet\bullet\bullet}$-$V_{Mg}$-$Mg_i^{\bullet\bullet}$-$V_{Mg}$-$Mg_i^{\bullet\bullet}$ crowdion defect cluster. The transparent yellow cubes represent the two adjacent vacant tetrahedral lattice sites, the larger yellow and green spheres represent the Mg^{2+} and Al^{3+} cations respectively and the transparent blue cubes are the unoccupied 8*b* sites.

Also, the $Mg_i^{\bullet\bullet}$-V_{Mg}-$Mg_i^{\bullet\bullet}$-V_{Mg}-$Mg_i^{\bullet\bullet}$ crowdion defect was not locally stable and decayed to form a split $Mg_i^{\bullet\bullet}$-V_{Mg}-$Mg_i^{\bullet\bullet}$ defect. In the remaining cases the differences in energy between the split interstitials and the crowdions are very similar (ie. < 0.51 eV).

Table 4.9: Energies of formation of crowdion defect clusters and their equivalent split interstitials, the differences in these two energies represents the relative stability of the crowdion.

Crowdion Cluster	Defect Energy /eV	Equivalent Interstitial Species	Defect Energy /eV
$Mg_i^{\bullet\bullet}$-V_{Mg}-$Mg_i^{\bullet\bullet}$-V_{Mg}-$Mg_i^{\bullet\bullet}$	Unstable	$Mg_i^{\bullet\bullet}$-V_{Mg}-$Mg_i^{\bullet\bullet}$	-15.87
$Mg_i^{\bullet\bullet}$-V_{Mg}-$Al_i^{\bullet\bullet\bullet}$-$V_{Mg}$-$Mg_i^{\bullet\bullet}$	-42.60	$Al_i^{\bullet\bullet\bullet}$-$V_{Mg}$-$Mg_i^{\bullet\bullet}$	-42.64
$Al_i^{\bullet\bullet\bullet}$-$V_{Mg}$-$Mg_i^{\bullet\bullet}$-$V_{Mg}$-$Mg_i^{\bullet\bullet}$	-42.63	$Al_i^{\bullet\bullet\bullet}$-$V_{Mg}$-$Mg_i^{\bullet\bullet}$	-42.64
		$\{Al_{Mg}^{\bullet}$:$Mg_i^{\bullet\bullet}\}$	-43.18
$Al_i^{\bullet\bullet\bullet}$-$V_{Mg}$-$Mg_i^{\bullet\bullet}$-$V_{Mg}$-$Al_i^{\bullet\bullet\bullet}$	-69.17	$\{Al_{Mg}^{\bullet}$:$Mg_i^{\bullet\bullet}$-V_{Mg}-$Al_i^{\bullet\bullet\bullet}\}$	-69.68
$Al_i^{\bullet\bullet\bullet}$-$V_{Mg}$-$Al_i^{\bullet\bullet\bullet}$-$V_{Mg}$-$Mg_i^{\bullet\bullet}$	-69.50	$Al_i^{\bullet\bullet\bullet}$-$V_{Mg}$-$Al_i^{\bullet\bullet\bullet}$	-69.59
		$\{Al_{Mg}^{\bullet}$:$Al_i^{\bullet\bullet\bullet}$-$V_{Mg}$-$Mg_i^{\bullet\bullet}\}$	-69.58
$Al_i^{\bullet\bullet\bullet}$-$V_{Mg}$-$Al_i^{\bullet\bullet\bullet}$-$V_{Mg}$-$Al_i^{\bullet\bullet\bullet}$	-96.15	$\{Al_{Mg}^{\bullet}$:$Al_i^{\bullet\bullet\bullet}$-$V_{Mg}$-$Al_i^{\bullet\bullet\bullet}\}$	-96.00

There was also another very interesting extended defect present after the collisional phase of Smith *et al.*'s [73] cascade simulations, which is the highly symmetrical $Al_i^{\bullet\bullet\bullet}$ ring. In this defect cluster three neighbouring Al^{3+} cations are moved from their octahedral lattice site and onto the neighbouring tetrahedral interstice, as shown in figure 4.6. Should this defect occur in a region which is partially inverse then it is possible for one, or more, of the Al^{3+} cations to be replaced by Mg^{2+} cations. Table 4.11 contains the formation energies of the various ring defects. In each case the energies are large and positive indicating that they are not thermodynamically favourable and that they are observed as a result of large kinetic barriers to their removal. Formation of these ring defects may prove highly beneficial in terms of spinel's radiation tolerance as it allows the lattice to 'suck' energy out of the cascade to form these defects, which will then readily reform the perfect lattice. Gilbert *et al.* [121] present a formation energy for a pure aluminium interstitial ring of 7.34 eV, although as this is a large defect it is likely that the defect energy has not converged with the size of the cell.

Table 4.10: Energies of formation of crowdion defect clusters and their equivalent split interstitials, the differences in these two energies represents the relative stability of the crowdion.

Crowdion Cluster	Defect Energy /eV	Equivalent Interstitial Species	Defect Energy /eV
$Mg_i^{\bullet\bullet}$-V_{Mg}-$Mg_i^{\bullet\bullet}$-V_{Mg}-$Mg_i^{\bullet\bullet}$	Unstable	$Mg_i^{\bullet\bullet}$-V_{Mg}-$Mg_i^{\bullet\bullet}$	-15.72
$Mg_i^{\bullet\bullet}$-V_{Mg}-$Al_i^{\bullet\bullet\bullet}$-$V_{Mg}$-$Mg_i^{\bullet\bullet}$	-41.62	$Al_i^{\bullet\bullet\bullet}$-$V_{Mg}$-$Mg_i^{\bullet\bullet}$	-41.94
$Al_i^{\bullet\bullet\bullet}$-$V_{Mg}$-$Mg_i^{\bullet\bullet}$-$V_{Mg}$-$Mg_i^{\bullet\bullet}$	Unstable	$Al_i^{\bullet\bullet\bullet}$-$V_{Mg}$-$Mg_i^{\bullet\bullet}$	-41.91
		$\{Al_{Mg}^{\bullet}$:$Mg_i^{\bullet\bullet}\}$	-42.56
$Al_i^{\bullet\bullet\bullet}$-$V_{Mg}$-$Mg_i^{\bullet\bullet}$-$V_{Mg}$-$Al_i^{\bullet\bullet\bullet}$	-67.52	$\{Al_{Mg}^{\bullet}$:$Mg_i^{\bullet\bullet}$-V_{Mg}-$Al_i^{\bullet\bullet\bullet}\}$	68.24
$Al_i^{\bullet\bullet\bullet}$-$V_{Mg}$-$Al_i^{\bullet\bullet\bullet}$-$V_{Mg}$-$Mg_i^{\bullet\bullet}$	Unstable	$Al_i^{\bullet\bullet\bullet}$-$V_{Mg}$-$Al_i^{\bullet\bullet\bullet}$	-67.88
		$\{Al_{Mg}^{\bullet}$:$Al_i^{\bullet\bullet\bullet}$-$V_{Mg}$-$Mg_i^{\bullet\bullet}\}$	-68.03
$Al_i^{\bullet\bullet\bullet}$-$V_{Mg}$-$Al_i^{\bullet\bullet\bullet}$-$V_{Mg}$-$Al_i^{\bullet\bullet\bullet}$	Unstable	$\{Al_{Mg}^{\bullet}$:$Al_i^{\bullet\bullet\bullet}$-$V_{Mg}$-$Al_i^{\bullet\bullet\bullet}\}$	-93.50

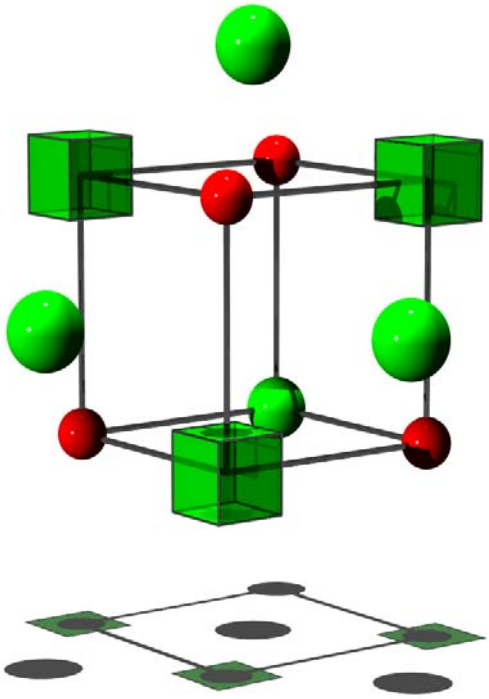

Figure 4.6: The aluminium interstitial ring defect cluster. The transparent green cubes represent unoccupied octahedral lattice sites whilst green spheres represent the $Al_i^{\bullet\bullet\bullet}$ defects.

Table 4.11: Formation energies for the ring cluster defects. For the magnesium containing clusters it is assumed that the Mg^{2+} cations are already present on the aluminium sublattice. Thus, the energy to form the relevant number of Mg_{Al} defects is subtracted from the ring formation energy.

Ring Cluster	Formation Energy (Shells) /eV	Formation Energy (no Shells) /eV
-$Al_i^{\bullet\bullet\bullet}$-$V_{Al}$-$Al_i^{\bullet\bullet\bullet}$-$V_{Al}$-$Al_i^{\bullet\bullet\bullet}$-$V_{Al}$-	9.07	9.18
-$Al_i^{\bullet\bullet\bullet}$-$V_{Al}$-$Mg_i^{\bullet\bullet}$-$V_{Al}$-$Al_i^{\bullet\bullet\bullet}$-$V_{Al}$-	8.28	8.11
-$Al_i^{\bullet\bullet\bullet}$-$V_{Al}$-$Mg_i^{\bullet\bullet}$-$V_{Al}$-$Mg_i^{\bullet\bullet}$-$V_{Al}$-	8.10	7.78
-$Mg_i^{\bullet\bullet}$-V_{Al}-$Mg_i^{\bullet\bullet}$-V_{Al}-$Mg_i^{\bullet\bullet}$-V_{Al}-	8.63	8.25

4.4 Summary

The first conclusion that can be drawn from the results presented in this chapter is that the empirical pair potential model is capable of accurately replicating the structure and elastic properties of spinel. Once the accuracy of the model had been firmly established it was possible to draw the following conclusions concerning the nature of defect properties in spinel:

- Interstitial species in spinel are predicted to exhibit complex split interstitial structures rather than existing as simple interstitial ions located at unoccupied 8*b* Wyckoff sites. Both cation species form split interstitials where a Mg^{2+} cation is displaced from its 8*a* site and two interstitial ions lie on the surrounding 8*b* Wyckoff sites. The interstitial is thus aligned along a $\langle 110 \rangle$ direction (see diagram 4.1(c)). Similarly, the oxygen interstitial also forms a split interstitial aligned along the $\langle 110 \rangle$ direction. This conclusion is supported by the parallel DFT simulations of Gilbert *et al.* [121].

- The reaction energy for the antisite process, reaction 4.1, is an order of magnitude lower than for the Schottky and Frenkel processes, therefore the defect chemistry of spinel is dominated by the presence of antisite defects. This is evident from the reordering of the thermodynamics of the Frenkel and Schottky processes when considering vacancy & interstitial/antisite clusters. Assuming defects are at the dilute limit then the Schottky process is lower in energy than the Frenkel processes, however, when clustering is introduced the oxygen Frenkel process is lower in energy than the Schottky and remaining Frenkel processes.

- As the level of defect clustering is increased then the energy for the Schottky and Frenkel processes is decreased, thus there will be an increase in their concentrations, relative to in the dilute limit.

- The extended defect clusters observed in the MD simulations of Smith *et al.* [73] were shown to be metastable, but are of high energy and as such are unlikely to occur as a result of thermal processes. Formation of these extended clusters may be an important issue with respect to spinel's radiation tolerance, however, it is currently very difficult to examine this dependence explicitly. The crowdion defects resemble a localised tranformation of the spinel matrix to a disordered rock salt structure, a phenomenon that has been observed both experimentally [71] and by simulation [72].

5

Cation diffusion in spinel

This work has been published in Solid State Ionics [124].

5.1 Introduction

The concentration of point defects (such as antisite defects) in a real material is related not only to the thermodynamics of the equilibrium concentrations but also to the rate at which matter can be transported (ie. the extent to which a state of equilibrium is reached). Consequently, if we are to understand how defects are distributed in a spinel lattice it is essential to gain a thorough understanding of the migration pathways that are responsible for the diffusion of the defects. Furthermore, understanding the time dependent evolution of point defects after radiation damage is of fundamental importance in understanding the processes responsible for the excellent irradiation tolerance demonstrated by spinel. This chapter deals with the mechanisms underpinning transport of cations via the intrinsic point defects discussed in chapter 4, by determining the migration energies and the prefactor for diffusion, D_0.

Whilst there is substantial work in the literature concerning cation diffusion in ceramic oxide materials, such as MgO [125, 126] and Al_2O_3 [127, 128], there is comparatively little similar quantitative data available for $MgAl_2O_4$. Nevertheless Martinelli *et al.* [129] concluded from their conductivity experiments on spinel that, at 1000 ^{o}C magnesium is the more mobile cation. Liermann and Ganguly [130] obtained an activation energy of 202 kJ mol^{-1} (2.09 eV) for Mg^{2+} self diffusion whilst Grimes [131] predicted a value of 3.74 eV; unfortunately, there is

no equivalent data for Al^{3+} cation self diffusion. A $Mg^{2+} \rightleftharpoons Al^{3+}$ 'interdiffusion' activation energy of 234 kJ mol^{-1} (2.42 eV) was determined by Watson and Price [132]. Assuming that migration of the aluminium cation is the rate limiting step in this process, as suggested by Martinelli *et al.* [129], then this may be the activation energy for Al^{3+} self diffusion.

The work presented here focuses on the processes by which point defects can facilitate mass transport of cations through the spinel lattice. Previously, Yasuda *et al.* [133] investigated the activation energies for diffusion of vacancy point defects by following the shrinkage process of interstitial type dislocation loops generated by irradiation. Their work estimated the migration energy of the rate limiting vacancy defect (ie. the slowest moving) to be 2.0 eV, but were unable to determine which type of vacancy this was. Uberuaga *et al.* [116] used a long time scale dynamical technique TAD [22] to investigate the mobility of many of the intrinsic defects found in $MgAl_2O_4$ and concluded that V_{Al} migration had the highest migration energy, with a value of 2.00 eV. This value agrees with the value that was obtained by Yasuda [133].

5.2 Methodology

Migration pathways were determined by defining a line between the initial and final positions of the point defect or defects that mediate the migration process (ie. the interstitial ion if it is an interstitial mechanism or the lattice vacancy if it is a lattice ion that is transported). A grid of points was generated perpendicular to the direction of migration and then incremented along the line joining the defect's start and end locations (see figure 5.1). At each point in every grid a defect calculation was conducted within the Mott-Littleton [89] framework whereby the location of the migrating ion was fixed at that point but the surrounding ions are fully relaxed using energy minimization. This allows the minimum energy pathway between the end points to be unambiguously identified. The change in the system energy, ΔE_{sys}, is then defined as the difference between the energy of the migrating species and when fully relaxed. Whilst this technique may appear to be computationally intensive, it allows the determination of non-linear migration pathways and to accurately locate saddle points. This approach has previously been successfully employed to study anisotropic oxygen diffusion in La_2NiO_4 [134]. In cases where similar mechanisms were analysed, these results are comparable with similar energies calculated using the nudged elastic band method [116].

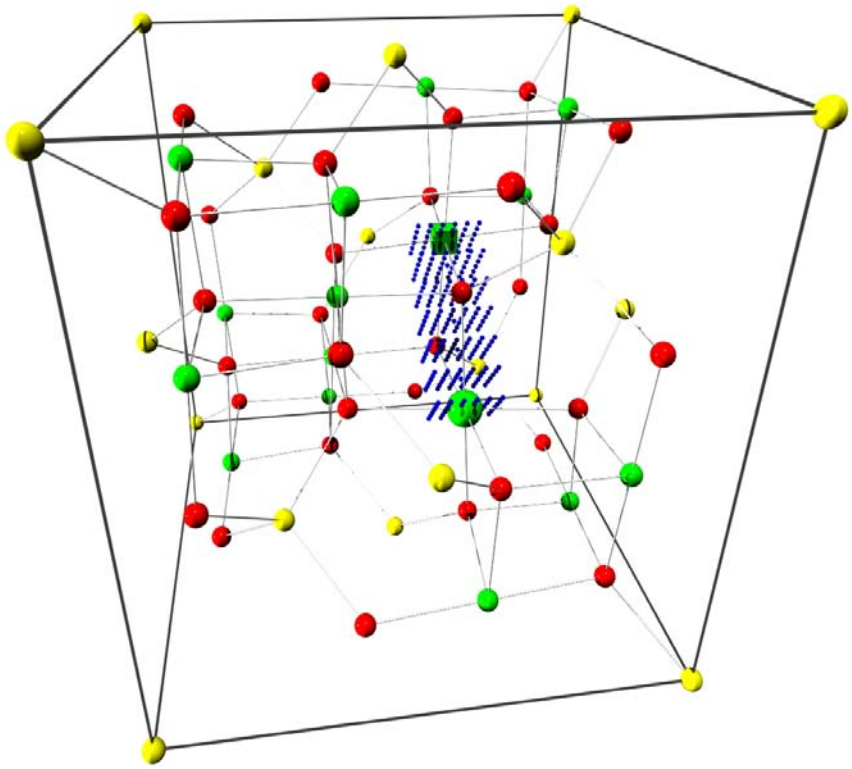

Figure 5.1: The grid methodology used to calculate the migration energies. In this example it is the migration of an Al^{3+} ion into a vacant aluminium site. A defect energy calculation using the Mott-Littleton [89] methodology is conducted with the migrating ion fixed at the points shown by the blue points.

Cation migration through spinel can occur via a number of different mechanisms. Recall, there are two different cation sublattices and these are capable of supporting vacancy mediated migration mechanisms. In addition, there is the possibility of migration between the two cation sublattices via vacancies; these latter processes are described by equations 5.1 and 5.2.

$$Al_{Al} + V_{Mg} \rightleftharpoons Al^{\bullet}_{Mg} + V_{Al} \tag{5.1}$$

$$Mg_{Mg} + V_{Al} \rightleftharpoons Mg_{Al} + V_{Mg} \tag{5.2}$$

In competition with vacancy mediated diffusion mechanisms cations can also migrate via interstitial mechanisms. Chapter 4 predicted that in spinel both cation interstitial species form complex split interstitial structures ($Al_i^{\bullet\bullet\bullet}$-$V_{Mg}$-$Mg_i^{\bullet\bullet}$ and $Mg_i^{\bullet\bullet}$-V_{Mg}-$Mg_i^{\bullet\bullet}$) around the tetrahedral sites, which are by far the lowest energy interstitial cation species. As a consequence interstitial migration will be effectively restricted to the magnesium sublattice.

5.3 Results and discussion

5.3.1 Migration energies

Vacancy migration

First we consider migration of Mg^{2+} cations via vacancy mechanisms on the magnesium and the aluminium sublattices. In the case of Mg^{2+} migrating on the aluminium sublattice we are considering Mg_{Al} cation antisite migration. Figure 5.2 is a contour plot showing the total change in the system energy, ΔE_{sys}, as the migrating Mg^{2+} ion explores the $(1\bar{1}\bar{2})$ plane in the region between two vacant magnesium lattice sites. Figure 5.3 is then a plot of ΔE_{sys} as a function of the reaction co-ordinate (reaction co-ordinate is defined as the distance along the vector between the initial and final locations of the defect and is a simple parameter that facilitates comparison of different migration processes independent of how convoluted the actual pathway might be) for this process of Mg^{2+} diffusing via a vacancy mechanism on the magnesium sublattice. As shown in figure 5.2, the Mg^{2+} cation migrates along the [111] direction,

with no deviation in the [$\bar{1}$10] direction (ie. the reaction co-ordinate and the pathway happen to be the same in this case). Also evident in both figures 5.2 and 5.3, is the presence of a stable V_{Mg}-$Mg_i^{\bullet\bullet}$-V_{Mg} situated halfway along the reaction co-ordinate (which gives rise to two equal saddle points). The migration energy for this process (ie. the saddle point) is predicted to be 0.54 eV, which compares favourably with the value of 0.56 eV obtained by Uberuaga *et al.* [116] using an NEB technique on a model without shell polarisability.

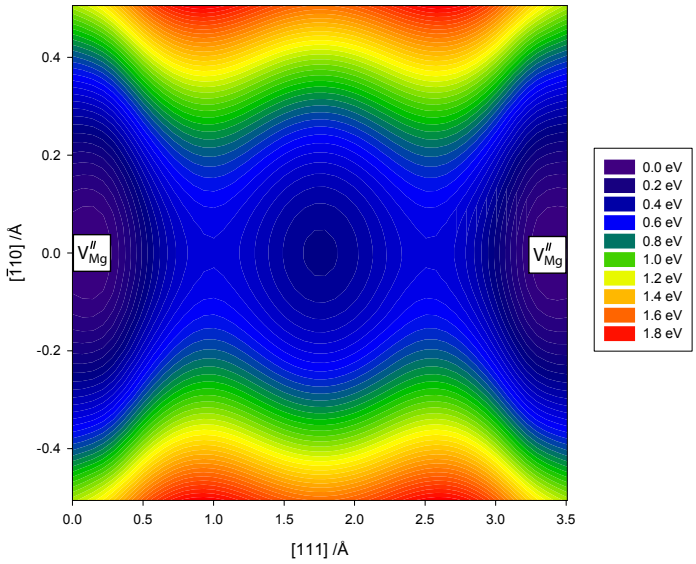

Figure 5.2: Contour plot showing the change in system energy as a Mg^{2+} cation migrates between two vacant magnesium lattice sites in the (1$\bar{1}\bar{2}$) plane.

A contour plot showing the change in system energy as a Mg_{Al} defect explores the (1$\bar{1}$0) plane is shown in figure 5.4. It is evident from figure 5.4 that the migrating Mg^{2+} cation is forced to deviate roughly 0.5 Å in the [001] migration owning to the local environment. Consequently, the reaction co-ordinate and the distance along the path are now no longer identical. The change in the energy of the system, ΔE_{sys}, as a function of the reaction co-ordinate is shown in figure 5.5 and the migration energy for this process is predicted to be 1.03 eV (as will be described later other steps are required for net migration but nevertheless this step is still necessary). A comparison of these two processes reveals that migration of Mg^{2+} via a vacancy mechanism will occur preferentially on the magnesium sublattice, all else (in particular concentrations) being equal.

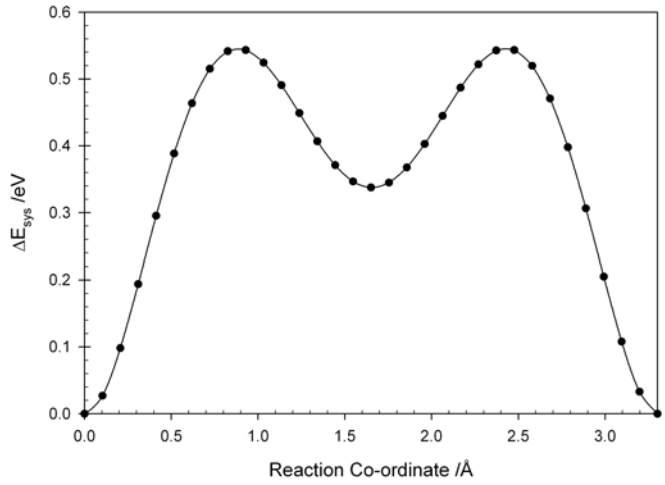

Figure 5.3: Plot of the change in the energy of the system, ΔE_{sys}, as a function of the reaction co-ordinate for a Mg_{Mg} cation migrating via a vacancy process on the magnesium sublattice showing two equal saddle points and a central metastable intermediate corresponding to a V_{Mg}-$Mg_i^{\bullet\bullet}$-V_{Mg} defect configuration.

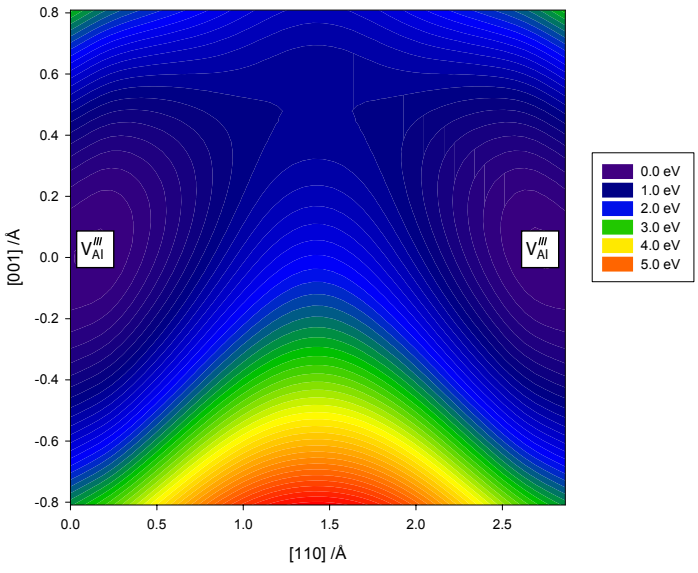

Figure 5.4: Contour plot showing the change in system energy as a Mg^{2+} cation migrates between two vacant aluminium lattice sites in the $(1\bar{1}0)$ plane.

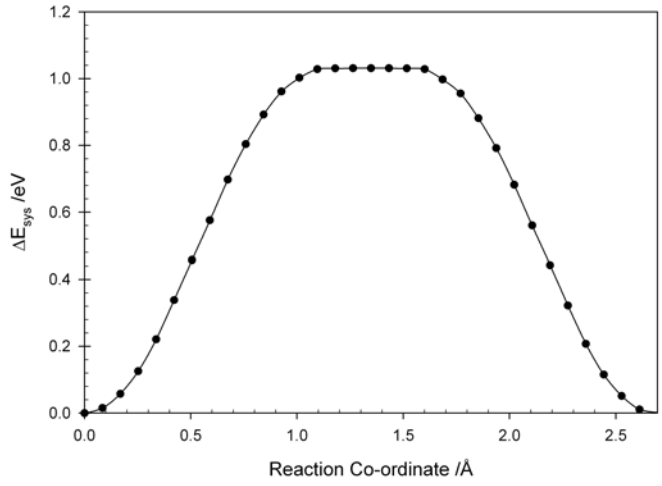

Figure 5.5: Plot of the change in the energy of the system, ΔE_{sys}, as a function of the reaction co-ordinate for a Mg_{Al} defect migrating via a vacancy process on the aluminium sublattice.

A similar analysis was adopted to investigate Al^{3+} cation migration via vacancy mechanisms. Figure 5.6 shows a predicted deviation of 0.6 Å in the [001] direction; this is greater than that predicted for Mg_{Al} migration via the same process, however, unlike in the Mg_{Al} case, there is evidence of a very small metastable intermediary. The presence of this V_{Al}-$Al_i^{\bullet\bullet\bullet}$-$V_{Al}$ intermediary is more evident in figure 5.7, which shows the change in the energy of the system, ΔE_{sys}, as a function of the reaction co-ordinate. Overall the migration energy for this process is predicted to be 1.83 eV (a value of 2.00 eV was obtained by Uberuaga *et al.* [116]).

Migration of an $Al_{Mg}^{\bullet}$ defect from one vacant magnesium site to the other is very similar to the equivalent Mg^{2+} process, in that there is no deviation from the reaction co-ordinate, as shown in figure 5.8. Furthermore, there is also a stable intermediary, however, this time it is a V_{Mg}-$Al_i^{\bullet\bullet\bullet}$-$V_{Mg}$ defect cluster. The change in the energy of the system as a function of the reaction co-ordinate is plotted in figure 5.9 and the migration energy for this isolated process is 0.88 eV.

The analysis above reveals an interesting possibility, that is, Al^{3+} will preferentially migrate on the magnesium sublattice rather than its own sublattice. There are, however, a series of other steps, in addition to the step reported in figure 5.9, in order for net Al^{3+} ion transport across the magnesium sublattice to be achieved. In particular, once the Al^{3+} ion has moved from one magnesium site to another, the transport-mediating V_{Mg} defect must migrate around in such a

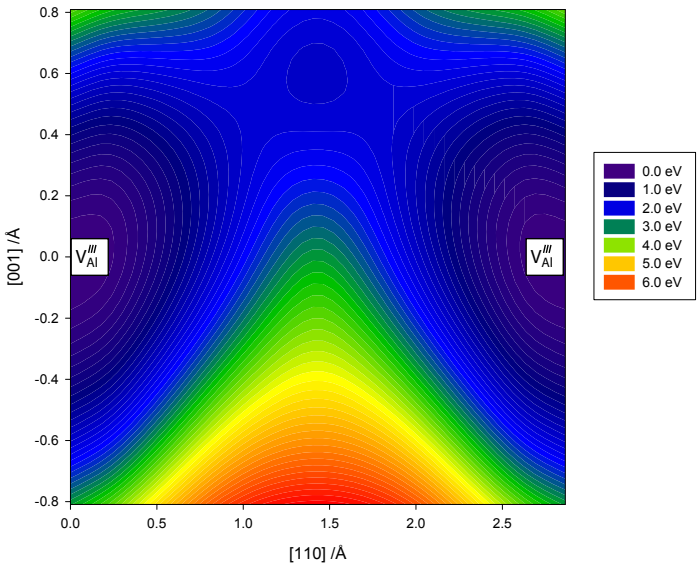

Figure 5.6: Contour plot showing the change in the system energy as a Mg^{2+} cation migrates between two vacant aluminium lattice sites in the $(1\bar{1}0)$ plane.

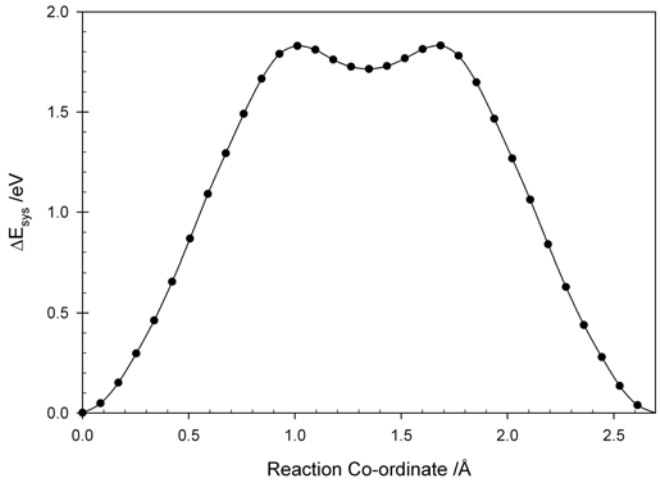

Figure 5.7: Plot of the change in the energy of the system, ΔE_{sys}, as a function of the reaction co-ordinate for a Mg_{Al} migrating via a vacancy process on the aluminium sublattice showing two equal saddle points and a central metastable intermediate corresponding to a V_{Al}-$Al_i^{\bullet\bullet\bullet}$-$V_{Al}$ defect configuration.

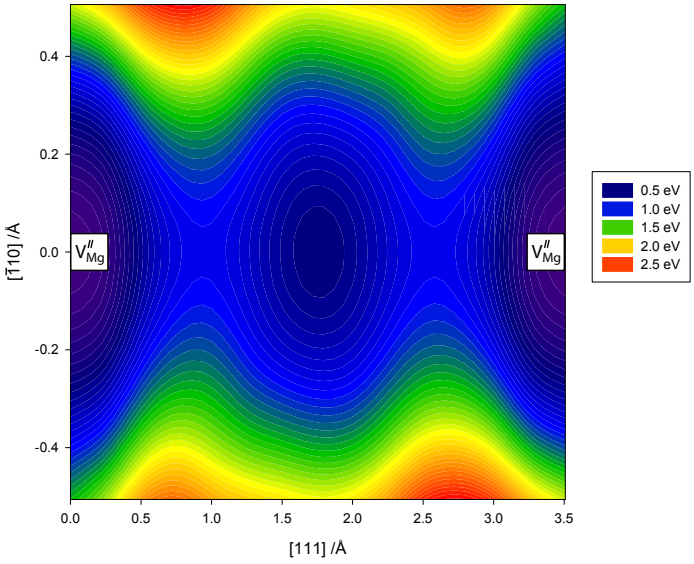

Figure 5.8: Contour plot showing the change in the system energy as a $Al^{\bullet}_{Mg}$ migrates between two vacant magnesium lattice sites in the $(1\bar{1}\bar{2})$ plane.

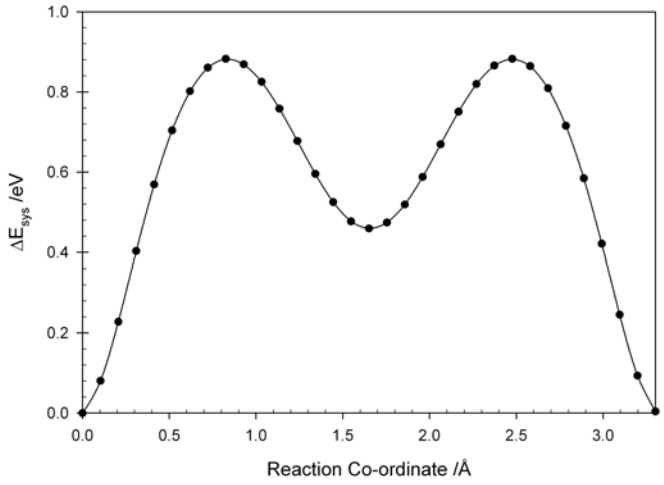

Figure 5.9: Plot of the change in the energy of the system, ΔE_{sys}, as a function of the reaction co-ordinate for $Al^{\bullet}_{Mg}$ migration via a vacancy process on the magnesium sublattice showing two equal saddle points and a central metastable intermediate corresponding to a V_{Mg}-$Al^{\bullet\bullet\bullet}_{i}$-$V_{Mg}$ defect configuration.

way that it facilitates the continued migration of the aluminium ion; this process is illustrated in figure 5.10 (this process is analogous to impurity diffusion in Si [135]). The energy landscape for Al^{3+} transport is then shown in figure 5.11, from which it is clear that the rate determining step is indeed the motion of the Al^{3+} ion itself, confirming that the overall migration energy for aluminium transport on the magnesium sublattice via a V_{Mg} mechanism is 0.88 eV.

As discussed in chapter 4, magnesium aluminate has an antisite formation energy that is low compared to other defect formation processes [75,136]. In order to facilitate changes in antisite defect concentrations, cations must be transported between the two sublattices. This can be achieved if a vacancy is transferred from one cation sublattice to the other, as described in equations 5.1 and 5.2. These processes create and in reverse destroy antisite defects. It is worth mentioning that antisite defects can also be formed via interstitial processes (as will be shown later, these processes form an essential step in the diffusion of an aluminium interstitial).

Equation 5.1 shows that migration of an Al^{3+} cation into a neighbouring vacant magnesium site results in formation of an $Al^{\bullet}_{Mg}$ antisite defect and a V_{Al} defect. A contour plot showing the change in the energy of the system as an Al^{3+} cation moves in the $(1\bar{1}0)$ plane is given in figure 5.12 and a plot of ΔE_{sys} as a function of reaction co-ordinate is given in figure 5.13. These defects are oppositely charged and form a partially charge compensating defect cluster which is 0.13 eV lower in energy than the starting V_{Mg} defect, so that, as shown in figure 5.13 the initial and final energies are not equal. The migration energy to form an $Al^{\bullet}_{Mg}$ antisite defect in this manner is 2.74 eV and for the reverse process, annihilation of the antisite defect, is 2.88 eV. Associated with these large energies is a substantial deviation from the vector between the initial and final positions of the Al^{3+} ion (as shown in figure 5.13), as the direct path would bring the Al^{3+} cation very close to an oxygen lattice site.

In the case of an Mg^{2+} ion migrating onto a vacant aluminium site (equation 5.2), a Mg_{Al} antisite defect and a V_{Mg} defect are created. Figures 5.14 and 5.15 show the contour plot of the change in system energy in the $(1\bar{1}0)$ plane and as a function of the reaction co-ordinate respectively. Both of these defects are negatively charged and will repel each other resulting in a relatively high formation energy for the product defect cluster (1.11 eV greater than the initial V_{Al} defect). Figure 5.15 shows that the migration energy for these processes are 2.44 eV for the forward process and 1.33 eV for the reverse process. As the resulting defects are oppositely charged, the defects will experience a force acting to move them further apart.

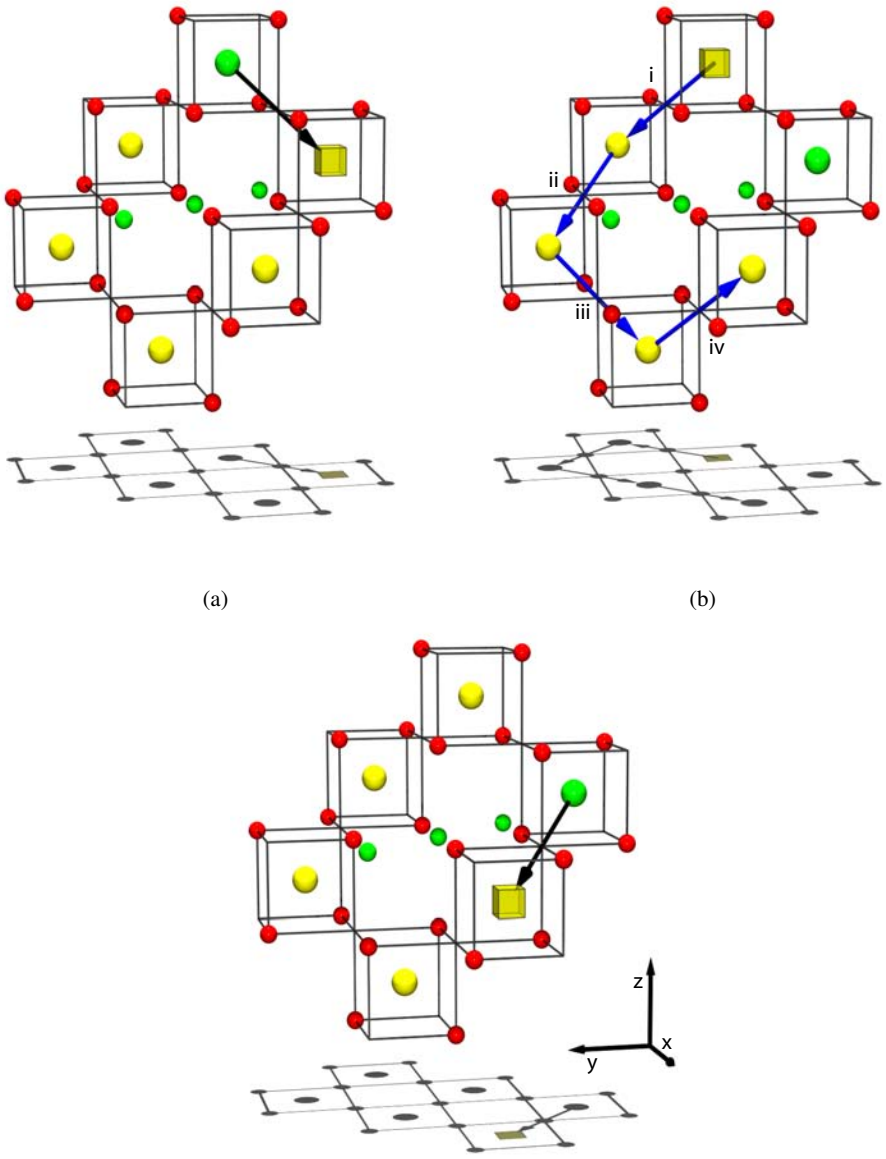

(a) (b)

(c)

Figure 5.10: Illustration of Al^{3+} transport via a vacancy mechanism on the magnesium sublattice: (a) The initial swap of the Al^{3+} cation ($Al^{\bullet}_{Mg}$) with a magnesium vacancy, (b) migration of the V_{Mg} (via the four step process, labeled i - iv) to a position which allows, (c) the $Al^{\bullet}_{Mg}$ to continue its migration. The final step shown in (c) is equivalent to the first step (a). Black arrows represent motion of the Al^{3+} cation whilst the blue arrows represent the movement of the V_{Mg} defect.

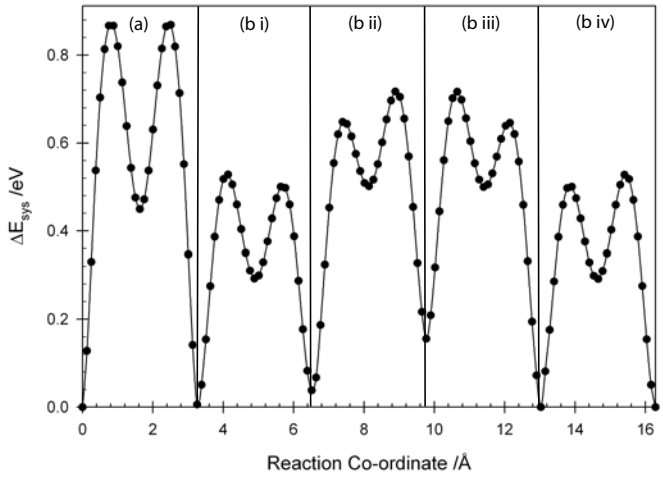

Figure 5.11: Plot showing the change in the energy of system, ΔE_{sys}, as a function of the reaction co-ordinate for an Al^{3+} cation migrating via a vacancy mechanism on the magnesium sublattice. The labels correspond to the steps shown in figure 5.10 In step (a) the $Al^{\bullet}_{Mg}$ is followed; in (b i - b iv) the movement of the V_{Mg} is followed.

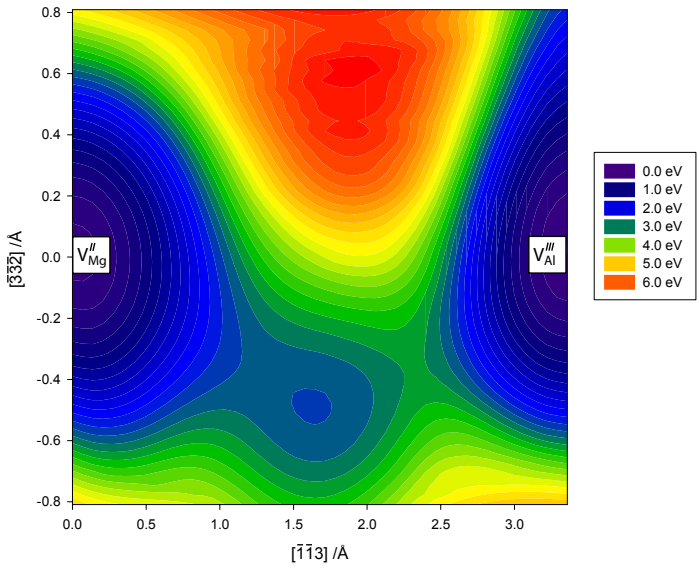

Figure 5.12: Contour plot showing the change in the system energy as an Al^{3+} cation migrates off of its lattice site and onto a neighbouring vacant aluminium lattice site, thus creating an $Al^{\bullet}_{Mg}$ defect, in the (110) plane.

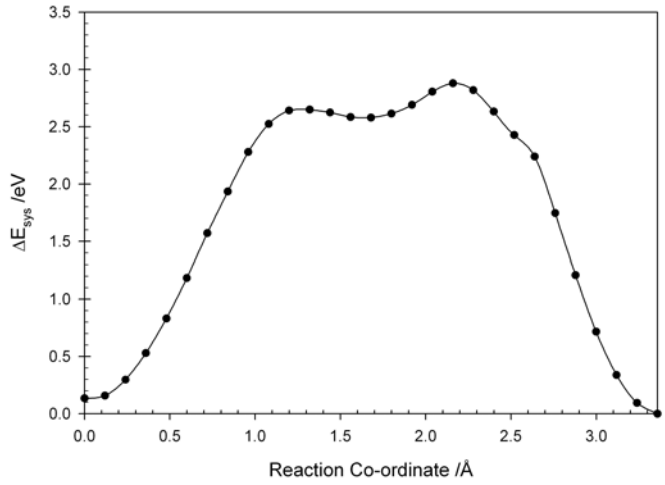

Figure 5.13: Plot showing the generation and annihilation of an $Al^{\bullet}_{Mg}$ antisite defect. The forward process starts with a Al_{Al}+V_{Mg}defect cluster; the Al^{3+} then hops onto the vacant magnesium site forming the partially charge compensating V_{Al}-$Al^{\bullet}_{Mg}$ defect cluster.

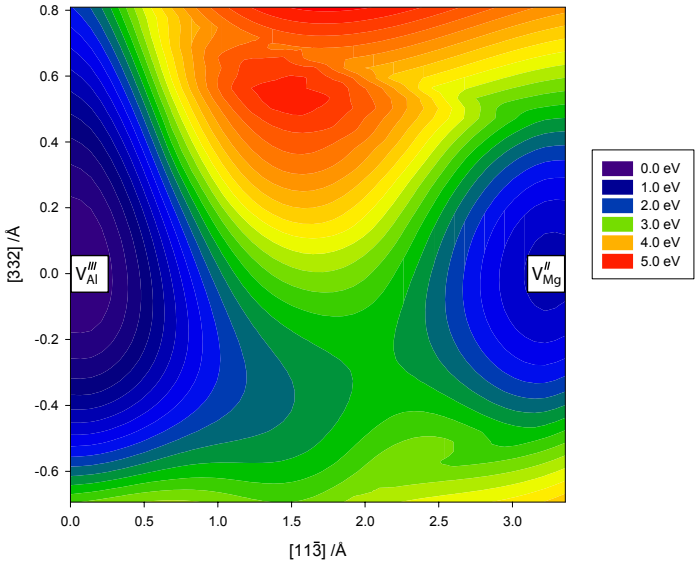

Figure 5.14: Contour plot showing the change in the system energy as an Mg^{2+} cation migrates off of its lattice site and onto a neighbouring vacant aluminium lattice site, thus creating an Mg_{Al} defect, in the (110) plane.

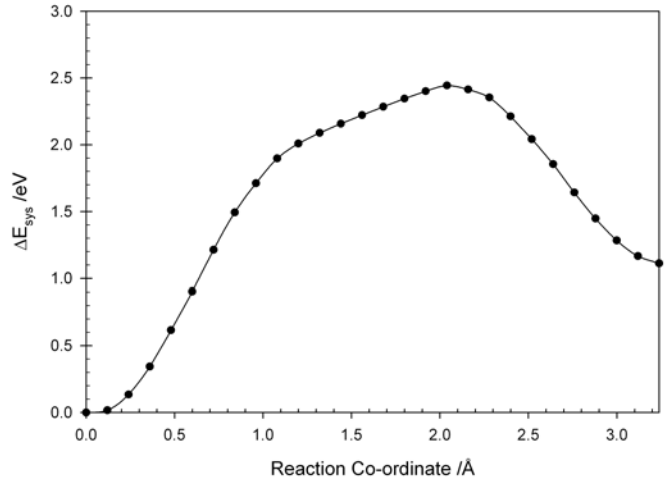

Figure 5.15: Plot showing the generation and annihilation of an Mg_{Al} antisite defect. The forward process starts with a Mg_{Mg}+V_{Al} defect cluster; the Mg^{2+} then hops onto the vacant magnesium site forming the like charged V_{Mg} and Mg_{Al} defects.

The activation energies for creation and annihilation of antisite defects via a vacancy mechanism (figures 5.13 & 5.15) are thus demonstrated to be high. Consequently, under equilibrium conditions the change in concentrations of these defects is very slow, particularly compared to processes occurring on the magnesium sublattice. This may explain why the antisite defect concentrations in synthetic spinels are, in general, so much larger than those in natural samples, that have been allowed to equilibrate over geological timescales [37, 38].

Interstitial migration

Interstitial migration in spinel is a little harder to visualise than vacancy migration, as a consequence of the complex split structure that interstitial species are predicted to exhibit [73, 75, 116]. The starting point for magnesium interstitial migration is therefore the $Mg_i^{\bullet\bullet}$-V_{Mg}-$Mg_i^{\bullet\bullet}$ split interstitial structure that is aligned along $\langle 110 \rangle$. From this starting point there are three distinct activated processes, two of which are capable of facilitating mass transport (as previously stated in [116]). All three are illustrated in figure 5.16.

The first process involves the reorientation of the split interstitial defect around a vacant tetra-

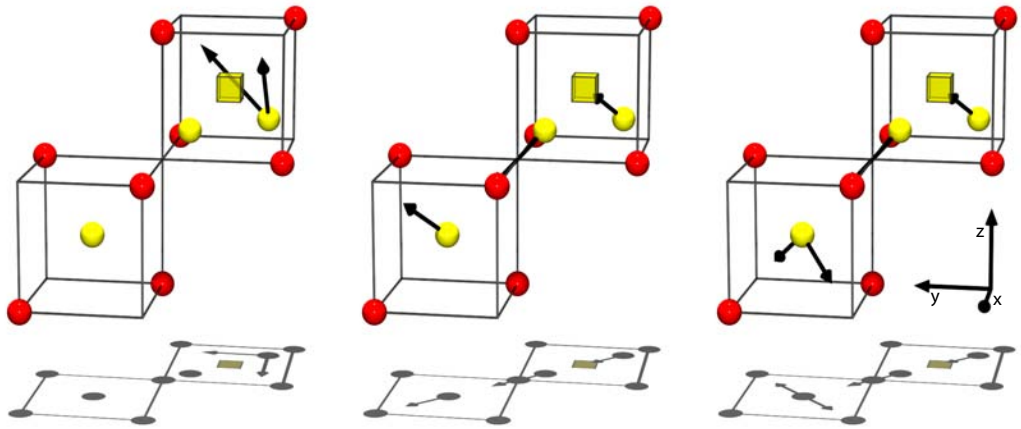

(a) (b) (c)

Figure 5.16: Magnesium interstitial migration. There are three ways in which a magnesium cation can migrate. (a) shows how the split magnesium interstitial can reorient itself, however,this pathway does not facilitate transport by itself. The pathways shown in (b) and (c) do allow overall matter transport. In mechanism (b) the initial and final split interstitial defects are aligned along the same plane, however, in (c) the orientation of the final split interstitial has a different orientation than the initial split interstitial defect.

hedral site. This occurs when one of the Mg^{2+} interstitial ions moves from its initial interstitial site to one of the remaining unoccupied interstitial sites surrounding the same vacant tetrahedral magnesium site (illustrated in 5.16(a)). The second interstitial ion remains unaltered. In total there are four octahedral interstitial sites surrounding a tetrahedral magnesium site; as two of these are occupied by the interstitial ions of the initial split interstitial, there are two remaining interstitial sites into which the interstitial Mg^{2+} ions can move, hence there are four symmetrically identical possible pathways (consequently the geometric term, $z = 4$). As the interstitial defect is still centered about the same vacant magnesium site matter transport cannot be facilitated by this process.

Both of the magnesium interstitial mechanisms by which matter transport is achieved involve the concerted motion of a split interstitial defect from one tetrahedral site to one of its nearest neighbours (shown in 5.16(b) & 5.16(c)). The difference between the two mechanisms is in the orientation of the final split interstitial with respect to the initial structure. For the process shown in 5.16(b), the initial and final split interstitial defects are aligned in the same plane, consequently this process can be considered as one dimensional. Conversely, with the

process highlighted in 5.16(c) the final split interstitial has become rotated out of the initial plane. Furthermore, there are two orientations in which the final interstitials can reside. For both mechanisms subsequent equivalent steps will facilitate transport through the lattice. From figure 5.16(b) it appears that there is only one possible pathway and thus one would expect the geometric term to be unity; however, the process can proceed either forward or backward along the plane of the initial split interstitial and therefore $z = 2$. Similarly the process illustrated in 5.16(c) can occur forward or backwards with respect to the plane of the initial split interstitial making the geometric term, $z = 4$.

The change in the energy of the system as a function of the reaction co-ordinates for each of these processes is given in figures 5.17, 5.18 and 5.19 for the rearrangement (5.16(a)), inplane (5.16(b)) and migrate and twist (5.16(b)) $Mg_i^{\bullet\bullet}$ interstitial migration processes respectively. Contour plots have not been given in these cases as the migration processes are no longer restricted to a single plane, therefore, these plots would be misleading. In these figures it is the progress of the central Mg^{2+} ion, along the reaction co-ordinate (as this ion is part of both the initial and final split interstitials), which is followed on the x-axis.

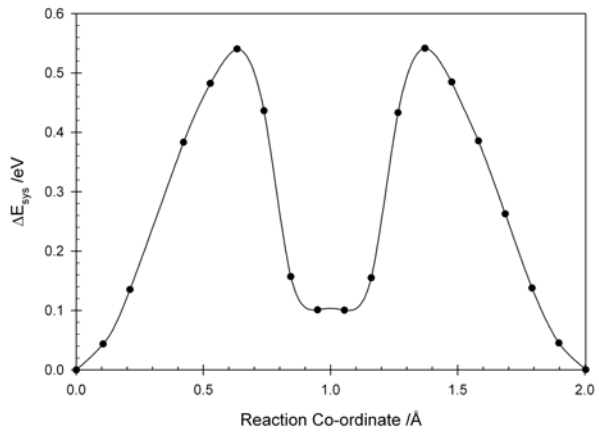

Figure 5.17: Plot showing the change in the energy of system, ΔE_{sys}, as a function of the reaction co-ordinate for the $Mg_i^{\bullet\bullet}$ rearrangement process, illustrated in figure 5.16(a).

In each case a metastable intermediary defect structure is predicted, where there is an $Mg_i^{\bullet\bullet}$ defect located near the unoccupied octahedral interstice. The activation energy for a $Mg_i^{\bullet\bullet}$ cation to migrate while remaining in the same plane is 0.58 eV (see also [116]) whilst for the nonlinear, migrate and twist mechanism it is 0.46 eV (see also [116]). For the rearrangement

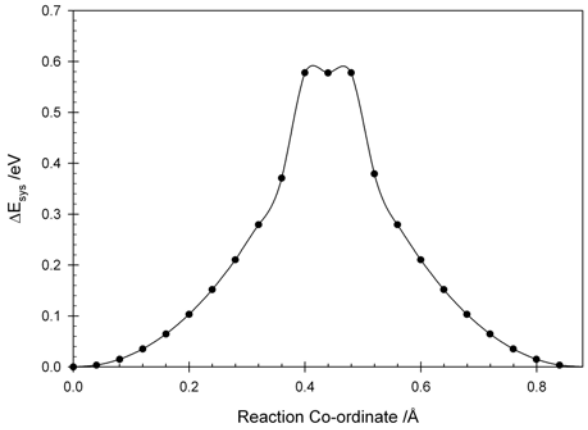

Figure 5.18: Plot showing the change in the energy of system, ΔE_{sys}, as a function of the reaction co-ordinate for the $Mg_i^{\bullet\bullet}$ inplane process, illustrated in figure 5.16(b).

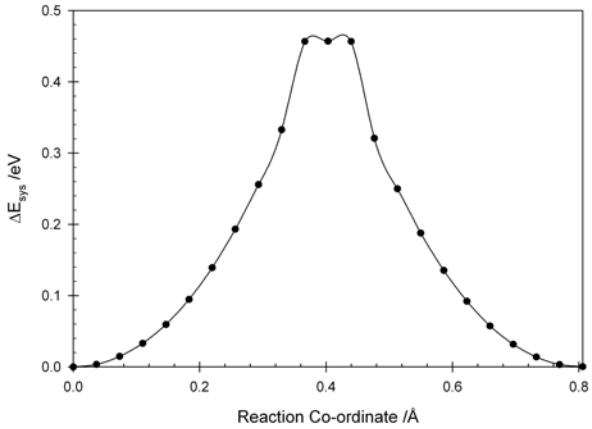

Figure 5.19: Plot showing the change in the energy of system, ΔE_{sys}, as a function of the reaction co-ordinate for the $Mg_i^{\bullet\bullet}$ migrate and twist process, illustrated in figure 5.16(c).

process, the migration energy was 0.54 eV. Consequently the activation energy for Mg^{2+} matter transfer via an intersititial mechanism is 0.46 eV. Although this is slightly lower in energy than the vacancy mediated process (0.54 eV) the energies are sufficiently close that other factors (eg. Vineyard and geometric terms) could dictate which will be the dominant process in facilitating Mg^{2+} transport.

Aluminium interstitial migration is significantly more complex than its magnesium equivalent. The chosen starting point for Al^{3+} transport via an interstitial mechanism will be the $Al_i^{\bullet\bullet\bullet}$-$V_{Mg}$-$Mg_i^{\bullet\bullet}$ interstitial defect as shown in figure 5.20. It is, however, important to recognise that this configuration is not the lowest energy point along the transport cycle that results in the overall transport of Al^{3+} ions via an interstitial process. This is because the $Al_i^{\bullet\bullet\bullet}$-$V_{Mg}$-$Mg_i^{\bullet\bullet}$ defect is of higher energy than an $Al_{Mg}^{\bullet}$ antisite defect adjacent to a $Mg_i^{\bullet\bullet}$-V_{Mg}-$Mg_i^{\bullet\bullet}$ split magnesium interstitial (as observed in [116]). Consequently, although the $Al_i^{\bullet\bullet\bullet}$-$V_{Mg}$-$Mg_i^{\bullet\bullet}$ cluster may be 'locally' stable it is not at the zero energy in figure 5.20. Nevertheless, since the $Al_i^{\bullet\bullet\bullet}$-$V_{Mg}$-$Mg_i^{\bullet\bullet}$ defect cluster must be involved in the overall interstitial transport mechanism, by starting with the $Al_i^{\bullet\bullet\bullet}$-$V_{Mg}$-$Mg_i^{\bullet\bullet}$ split interstitial cluster and ending with an equivalent cluster, mass transport is facilitated. So, the first step involves movement of the $Al_i^{\bullet\bullet\bullet}$ from the $Al_i^{\bullet\bullet\bullet}$-$V_{Mg}$-$Mg_i^{\bullet\bullet}$ cluster towards the V_{Mg} site so that the $Mg_i^{\bullet\bullet}$ forces a neighbouring magnesium ion (Mg_{Mg}) off its lattice site thereby forming an $Al_{Mg}^{\bullet}$ antisite defect and an adjacent $Mg_i^{\bullet\bullet}$-V_{Mg}-$Mg_i^{\bullet\bullet}$ defect (see figures 5.20(a) & 5.20(b)); this process is highlighted in equation 5.3.

$$Al_i^{\bullet\bullet\bullet} - V_{Mg} - Mg_i^{\bullet\bullet} + Mg_{Mg} \quad Al_{Mg}^{\bullet} + Mg_i^{\bullet\bullet} - V_{Mg} - Mg_i^{\bullet\bullet} \tag{5.3}$$

The split magnesium interstitial defect, $Mg_i^{\bullet\bullet}$-V_{Mg}-$Mg_i^{\bullet\bullet}$, must then loop around (figures 5.20(c)-5.20(h)) so it can facilitate the formation of a new $Mg_i^{\bullet\bullet} - V_{Mg} - Al_i^{\bullet\bullet\bullet}$ cluster. This final part of the mechanism is achieved by, first, one of the appropriately orientated $Mg_i^{\bullet\bullet}$ ions from the $Mg_i^{\bullet\bullet}$-V_{Mg}-$Mg_i^{\bullet\bullet}$ cluster in figure 5.20(f), moving onto the unoccupied octahedral interstitial site neighbouring the $Al_{Mg}^{\bullet}$ antisite defect. This forces the Al^{3+} ion off the tetrahedral magnesium site onto one of the remaining unoccupied octahedral interstitial sites, thereby creating the new $Mg_i^{\bullet\bullet} - V_{Mg} - Al_i^{\bullet\bullet\bullet}$ cluster (figure 5.20(f)). Then finally the Al^{3+} ion, in figure 5.20(g), moves across to be associated with an adjacent octahedral site (figure 5.20(h)). By following all these steps the Al^{3+} ion has moved from being associated with a split interstitial across one

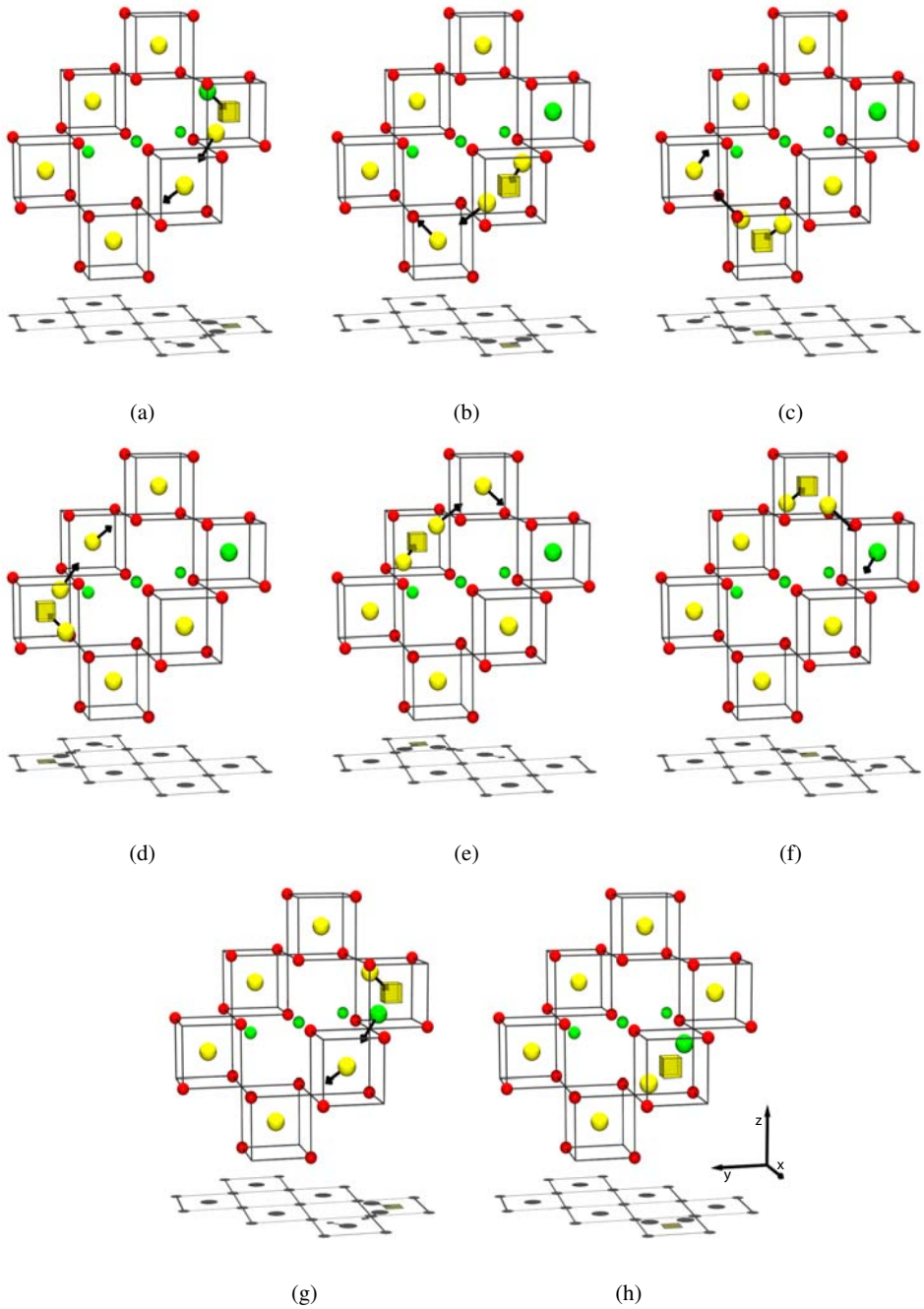

Figure 5.20: Illustration of Al^{3+} cation migration via an interstitial mechanism starting with the $Al_i^{\bullet\bullet\bullet}$-$V_{Mg}$-$Mg_i^{\bullet\bullet}$ defect cluster. The process begins in (a) with the $Al_i^{\bullet\bullet\bullet}$ moving onto the vacant magnesium (V_{Mg}) site thus generating an $Al_{Mg}^{\bullet}$ defect adjacent to a $Mg_i^{\bullet\bullet}$-V_{Mg}-$Mg_i^{\bullet\bullet}$ split interstitial defect. This $Mg_i^{\bullet\bullet}$-V_{Mg}-$Mg_i^{\bullet\bullet}$ defect then migrates around a loop as shown in steps (b) - (e) such that it can force the Al^{3+} ion off the magnesium site thereby generating the $Mg_i^{\bullet\bullet}$-V_{Mg}-$Al_i^{\bullet\bullet\bullet}$ defect cluster, shown in (f). To complete the process the Al^{3+} cation then moves from being associated with the initial tetrahedral site to an adjacent one as shown in (g) to reach the final state (h) which is equivalent to the starting position, (a).

tetrahedral site (figure 5.20(a)) to the next tetrahedral site (figure 5.20(h)) at which point the whole process can start again.

The change in system energy, ΔE_{sys}, for aluminium interstitial ion migration as a function of the reaction co-ordinate is shown in figure 5.21. The rate determining step for aluminium interstitial migration is 1.47 eV. This migration energy for aluminium interstitial migration is therefore much higher than that for the magnesium vacancy assisted mechanism and, as such, the lowest migration energy for aluminium transport in spinel remains via a vacancy mechanism, but on the magnesium sublattice.

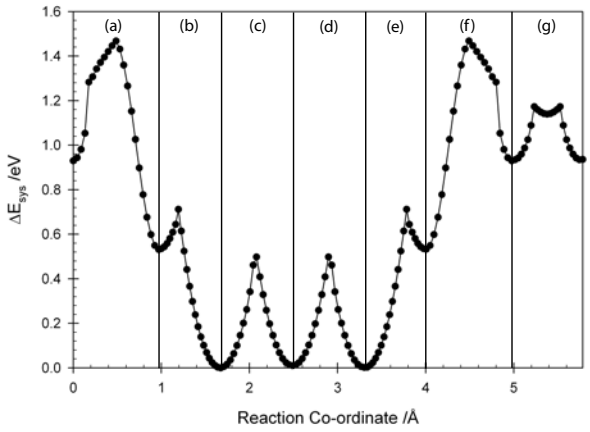

Figure 5.21: Plot of change in system energy against reaction co-ordinate for aluminium interstitial migration. The labels refer to the steps in figure 5.20. Steps (a), (f) and (g) involve the movement of the $Al_i^{\bullet\bullet\bullet}$ ion; in all the other steps, it is a Mg^{2+} cation moving.

5.3.2 Calculation of prefactors

Table 5.1 provides a summary of the migration energies and also the Vineyard terms, geometric factors, jump distances, correlation factors and their resultant product, D_0 (see equation 2.26). It also reports values for d_x via each mechanism at both 500 and 1500 K (this is the temperature range of interest). The Vineyard terms were calculated using the CLSMAN software package using a model without shells due to computational efficiency demands.

Jump distances

In table 5.1 the jump distances for the vacancy mediated processes are simply the distances between the appropriate lattice sites. For interstitial process these are the distance between the tetrahedral sites, about which the initial and final defects are located. As rearrangement processes (figure 5.16(a)) do not lead to net migration, the effective jump distance in these processes are zero and so do not contribute to diffusion. It may, however, be important for reorienting the interstitial in the lattice in some circumstances.

Despite the very different types of migration mechanisms considered here, the distances between the defect start and end point locations (ie. the jump distances) are all very similar. Therefore, this term, despite being squared in the expression for D_0 (equation 2.26), will not significantly differentiate between processes.

Vineyard terms

The Vineyard terms for the processes considered (shown in table 5.1) are all of similar order, with the exception of an Al^{3+} cation migrating via a vacancy mechanism on the aluminium sublattice. Larger Vineyard terms are expected for processes that have softer modes.

Geometric terms

There is some variation in the geometric terms determined in table 5.1. For example, processes that involve the migration of an antisite defect have a geometric term that is unity. This is simply a consequence of this antisite defect being the only ion capable of making this specific 'hop'. Conversely, the creation of an Mg_{Al} antisite defect via a vacancy transferring from the aluminium sublattice has a large geometric term because every tetrahedral magnesium site is surrounded by 12 nearest aluminium sites. The aluminium vacancy could then migrate into any of these equivalent sites, thus creating the Mg_{Al} defect.

Correlation factors

For simplicity, for all of the processes reported here, it has been assumed that the correlation factors are unity. Clearly there will be some correlation affects, however, as these values are all expected to fall in the region 0.4-1.0 [21] this will not lead to a re-ordering of the diffusion processes.

The values of the d_x terms for the various mechanisms at two temperatures are also shown in table 5.1. The temperatures chosen are 500 and 1500 K as these represent the upper and lower bounds of our region of interest. At low temperatures (ie. 500 K) the ordering of the d_x term is the same as the ordering of the activation energies, that is the process with the lowest activation energy has the highest d_x term. This is still the case for the optimum transport mechanisms for each cation at the higher temperature, that is, the migrate and twist (figure 5.16(c)) and the Al^{3+} via a V_{Mg} mechanisms are the dominant transport mechanisms across the whole temperature range. There is, however, a slight re-ordering in the preference of the remaining mechanisms by which Al^{3+} cations may be transported (albeit these mechanisms are far less important for Al^{3+} transport). As shown in table 5.1 the $Al_i^{\bullet\bullet\bullet}$ mechanism has a higher d_x (-21.83 10^{-8}m^2 s^{-1}) than the aluminium vacancy mechanism (-24.07 10^{-8} m^2 s^{-1}) at 500 K but at 1500 K the vacancy mechanism has the greater d_x term.

5.4 Summary

Table 5.1 provides a summary of the activation energies and prefactors for the major migration mechanisms involving the basic intrinsic cation defects. From the analysis of these results the following conclusions were reached:

- Mg^{2+} cations are considerably more mobile than Al^{3+} ions. Our data agrees with the observations made by Martinelli *et al.* [129] that Mg^{2+} is more mobile than Al^{3+} in $MgAl_2O_4$.
- The difference in the barrier for Mg^{2+} ion diffusion via vacancy and interstitial mechanisms is small. Furthermore, although there are differences in the geometric and Vineyard terms (see Table 5.1) these are not so great that a definitive conclusion can be drawn

regarding a preferred mechanism, vacancy or interstitial. Indeed, the dominant mechanism may well be determined by the availability of the appropriate mediating defect, that is, through defect concentrations [75]. This is in contrast to materials such as MgO, where all interstitial species are significantly more mobile than all vacancy species [137].

- The preferred mechanism for Al^{3+} ion migration is via a vacancy mechanism on the magnesium sublattice as opposed to a vacancy mechanism on its own sublattice or an interstitial mechanism. This result may very well have implications for a number of other materials in which high concentrations of antisite defects are present.

- Creation and annihilation of antisite defects via cation vacancy mechanisms will be particularly slow. This may explain the difference in the levels of cation inversion present in synthetic spinels and those which have annealed over geological timescales.

- Though important to determine, differences between the terms contributing to prefactors (ie. the Vineyard terms, geometric terms and jump distances) are not sufficient, in the case of $MgAl_2O_4$, to change the preferred mechanisms by which cation transport is facilitated over that dictated by the migration energies alone.

Table 5.1: Table showing the activation energies, attempt frequencies geometric terms, jump distances and overall prefactors for the intrinsic point defect migration properties considered in this study as well as the predicted d_x terms at 500 and 1500 K.

Migration Process	Activation Energy /eV	Vineyard Term / 10^{12} s^{-1}	Geometric Term	Jump Distance / 10^{-10} m	Prefactor / 10^{-8} m^2 s^{-1}	Log d_x @500 K / 10^{-8} s^{-1}	Log d_x @1500 K / 10^{-8} s^{-1}
Mg_{Mg}+V_{Mg} V_{Mg}+Mg_{Mg}	0.54	4.30	4	3.30	31.22	-11.95	-8.32
Mg_{Al}+V_{Al} V_{Al}+Mg_{Al}	1.03	13.87	1	2.70	16.85	-17.16	-10.23
$Mg_i^{\bullet\bullet}$ $Mg_i^{\bullet\bullet}$							
• rearrangement (5.16(a))	0.54	8.24	4	0.00	0.00	0.00	0.00
• inplane (5.16(b))	0.58	8.90	2	3.30	32.31	-12.34	-8.44
• migrate and twist (5.16(c))	0.46	7.34	4	3.30	53.29	-10.91	-7.82
Al_{Al}+V_{Al} V_{Al}+Al_{Al}	1.83	32.4	6	2.70	236.20	-24.07	-11.78
$Al_{Mg}^{\bullet}$+V_{Mg} V_{Mg}+$Al_{Mg}^{\bullet}$	0.88	4.60	1	3.30	8.35	-15.95	-10.03
$Al_i^{\bullet\bullet\bullet}$ $Al_i^{\bullet\bullet\bullet}$	1.47	5.34	1	3.30	9.69	-21.83	-11.95
Al_{Al}+V_{Mg} V_{Al}+$Al_{Mg}^{\bullet}$	2.74	1.83	12	3.36	41.32	-34.00	-15.59
V_{Al}+$Al_{Mg}^{\bullet}$ Al_{Al}+V_{Mg}	2.88	0.97	1	3.36	1.83	-36.77	-17.41
Mg_{Mg}+V_{Al} V_{Mg}+Mg_{Al}	2.44	1.44	6	3.24	15.12	-31.41	-15.02
V_{Mg}+Mg_{Al} Mg_{Mg}+V_{Al}	1.33	10.38	1	3.24	18.16	-20.15	-11.21

6

Oxygen self-diffusion in spinel

6.1 Introduction

In the previous chapter the diffusion processes responsible for cation transport were investigated, however, anion diffusion was neglected. This chapter aims to rectify this by examining the principle mechanisms responsible for oxygen diffusion by determining the migration energy and the other, temperature independent, terms in a similar fashion to the approach applied to cation diffusion. The methodology is identical to that employed in chapter 5.

The oxygen ions, in spinel, form a pseudo FCC lattice (an in depth description of the cation sublattices can be found in 2.3.2). However, the FCC approximation is a simplification, in that, the O^{2-} anions relax away from the idealised FCC sites, in the $\langle 111 \rangle$ direction, by an amount defined by the u parameter [33]. For a perfect FCC arrangment the u parameter is zero. In a 'normal' spinel O^{2-} anions relax away from the nominally divalently charged tetrahedral sites and are attracted towards the octahedral sites (and the u parameter is increased). Upon cation exchange the electrostatic repulsion between the Mg_{Al} and the surrounding O^{2-} ions forces the anions to shift back towards the ideal FCC sites. Conversely, the O^{2-} anions surrounding an $Al^{\bullet}_{Mg}$ defect are drawn closer to the tetrahedral site, again moving closer to the ideal FCC site. Clearly the level of inversion present in spinel will have significant impact on the overall structure of the oxygen sublattice and consequently its ability to facilitate oxygen self-diffusion. The results presented in this chapter ignore the impact of inversion on oxygen transport, although this is examined in more detail later.

Owing to the availability of a convenient radioactive tracer isotope of oxygen (^{18}O) there have been several experimental investigations into the self diffusion of oxygen in spinel. Ando and Oishi [138] conducted radioactive tracer experiments and determined an activation energy of 105 kcal mol^{-1} (4.55 eV) for oxygen self diffusion in single crystal spinel. Furthermore, they observed only a very slight increase in this activation energy, 106 kcal mol^{-1} (4.59 eV), for oxygen transport in a single crystal with Al_2O_3 excess, thus implying that the concentration of the mediating oxygen defects are unaffected by Al^{3+} incorporation. In a later study Oishi and Ando [139] performed a similar study, however, this time on a polycrystalline sample as opposed to a single crystal. This new study yielded an activation energy of 91.9 kcal mol^{-1} (3.99 eV), and demonstrated the importance of processes such as grain boundary diffusion when considering self diffusion in spinel. By conducting depth profiling experiments on a spinel single crystal, Reddy and Cooper [140] obtained a value of 415 kJ mol^{-1} (4.30 eV), whilst Ryerson and McKeegan [141] obtained a value of 404 kJ mol^{-1} (4.19 eV) using a gas-solid isotope exchange technique. In addition to the activation energy Ryerson and McKeegan [141] reported a value for the pre-exponential term, D_0, of 2.2 10^{-7} $m^2 s^{-1}$ (+8.7/-1.8 10^{-8} $m^2 s^{-1}$). Clearly there is good agreement between the experimental data, however, the degree of inversion present in the crystals used is not reported in any of these studies making a full comparison difficult. Furthermore, whilst these studies all agree on the activation energy there is little discussion of the mechanisms responsible for oxygen self diffusion.

Uberuaga *et al.* [116] used the atomistic simulation technique TAD [99] to determine the migration energies for the intrinsic defect processes capable of facilitating oxygen transport. Their work showed that, the migration energy for oxygen interstitial migration (0.29 eV) is lower than for vacancy mediated migration (1.67 eV). The *ab initio* simulations of Lodziana and Piechota [142] found a migration energy of 4.3 eV for migration of the charge neutral V_O defect. These values are not directly comparable with the experimental observations made above as this only represents the migration energy and does not include the energy to form the defect, however, they are useful in terms of predicting the mechanism responsible for oxygen self-diffusion in spinel.

6.2 Results and discussion

6.2.1 Vacancy migration

Each oxygen ($48f$) site in spinel is surrounded by 12 nearest neighbour oxygen sites, therefore, should an oxygen ion be removed to create an oxygen vacancy, $V_O^{\bullet\bullet}$, it is possible for any of these 12 O^{2-} anions to 'hop' onto the vacant site. As a result, however, of the displacement described by the u parameter these 12 anions do not all reside at equivalent distances from the now vacant site. The model predicted that six cations reside at a separation of 2.80 Å from the vacant site, a further three at a separation of 2.38 Å and the remainder at 3.12 Å. Figure 6.1 presents a cross section through a spinel unit cell in the (100) plane and shows an example of the three different vacancy mechanisms possible as a result of the oxygen positional parameter displacement. The change in the energy of the system, ΔE_{sys}, as a function of the reaction co-ordinate for the vacancy mechanisms are shown in figures 6.2-6.4 and the activation energies are presented in table 6.1.

Figure 6.2 shows the migration energy for an O^{2-} anion to 'hop' into the vacant site, following process (1) shown in figure 6.1. The activation energy for this process is predicted to be 1.40 eV, compared to a value of 1.67 eV determined by Uberuaga *et al.* [116] using a nudged elastic band (NEB) technique on a model that does not include the effects of polarisation. By making repeated identical jumps this mechanism is capable of facilitating oxygen transport throughout the lattice.

Neither of the processes (2) and (3) shown in figure 6.1 are capable of supporting overall transport of the oxygen on their own, however, transport is possible via a combination of the two. The migration energies as a function of the reaction coordinates for processes (2) and (3) are shown in figures 6.3 and 6.4 respectively. A migration energy of 1.55 eV (compared to 1.49 eV [116]) for process (2) and a migration energy of 3.27 eV (compared to 3.65 eV [116]) was obtained for process (3). Consequently the overall migration energy for an oxygen ion migrating via a vacancy mechanism is predicted to be 1.40 eV.

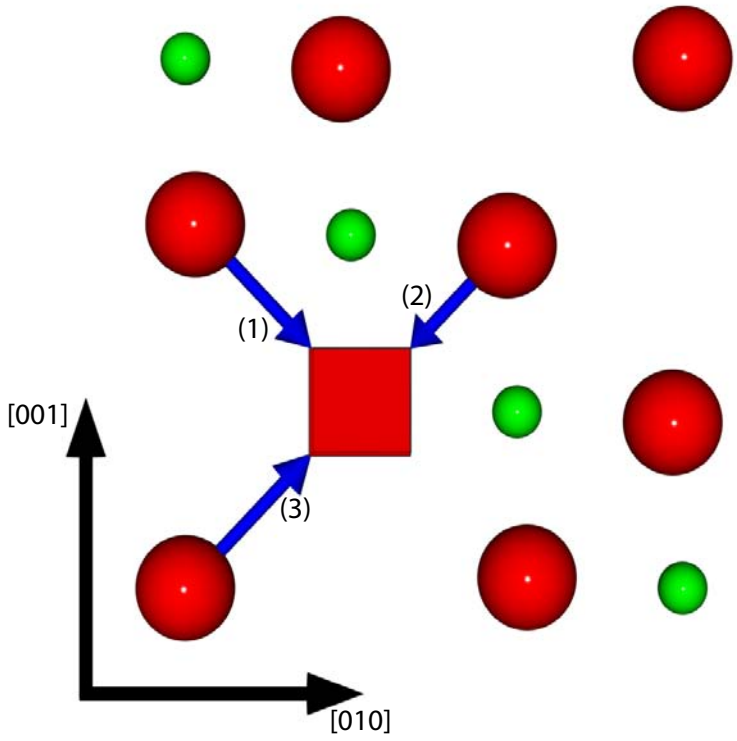

Figure 6.1: Cross-section through a single spinel unit cell in the [100] plane. Here the red spheres represent O^{2-} anions and the green spheres represent the Al^{3+} cations. Due to relaxation of the cations away from the tetrahedral sites and the contraction about the octahedral lattice sites the oxygen-oxygen ion separations are no longer equidistant. There are, in fact, three distinct groups of nearest neighbour oxygen sites to any given vacant oxygen site. The blue arrows therefore represent examples of each of three different V_O migration mechanisms possible in spinel, labeled (1),(2) and (3). The distance the oxygen anion has to cover are 2.8 Å, 2.38 Åand 3.12 Åfor processes (1), (2) and (3) respectively.

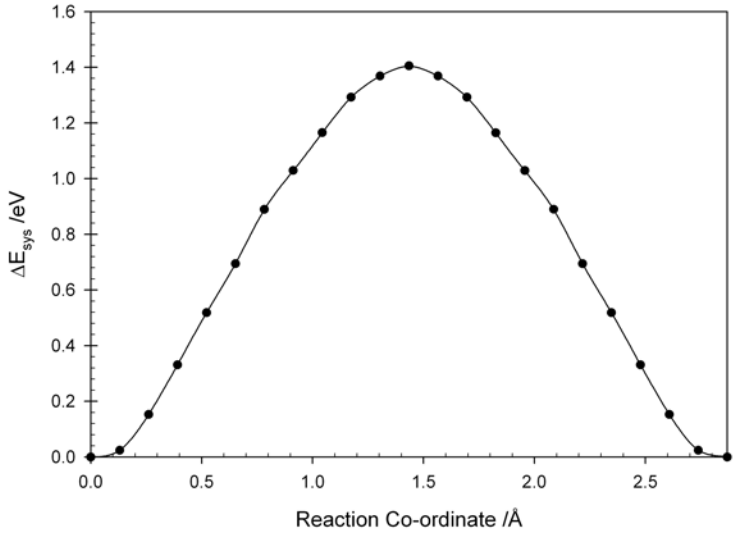

Figure 6.2: Change in the energy of the system, ΔE_{sys}, as a function of the reaction co-ordinate for the oxygen vacancy migration process (1) shown in figure 6.1.

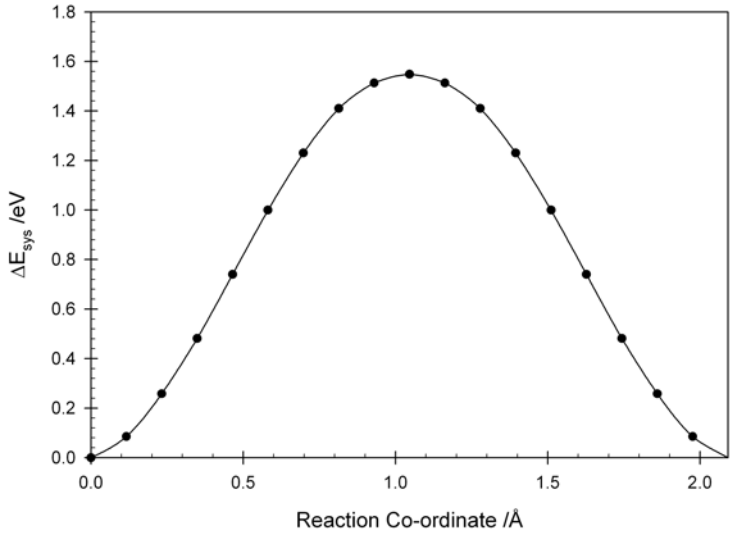

Figure 6.3: Change in the energy of the system, ΔE_{sys}, as a function of the reaction co-ordinate for the oxygen vacancy migration process (2) shown in figure 6.1.

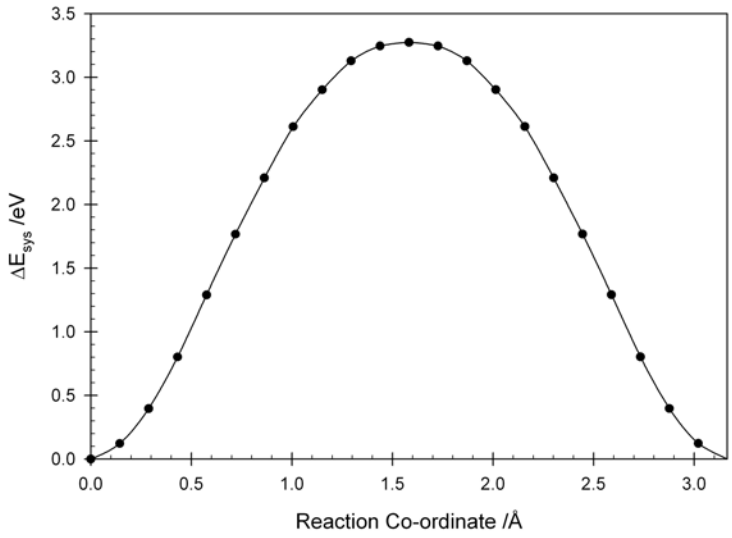

Figure 6.4: Change in the energy of the system, ΔE_{sys}, as a function of the reaction co-ordinate for the oxygen vacancy migration process (3) shown in figure 6.1.

6.2.2 Interstitial migration

Previous work [73, 75] has shown that the most energetically stable configuration for an O_i interstitial defect is to form a complex O_i -$V_0^{\bullet\bullet}$-O_i defect aligned along one of the $1\bar{1}0$ directions. For interstitial migration to occur, one of the oxygen interstitials from the O_i -$V_0^{\bullet\bullet}$-O_i defect must move onto the $V_O^{\bullet\bullet}$ site thereby forcing the other O_i defect to require a neighbouring O_O off its site creating another O_i -$V_0^{\bullet\bullet}$-O_i defect shifted along $1\bar{1}0$; this is shown in figure 6.5. By repeating the process this mechanism can facilitate O^{2-} transport, however, the mechanism is only one dimensional (1D). The migration energy as a function of the reaction co-ordinate (the reaction co-ordinate here represents the motion of the central O_i interstitial as this is present in both the initial and the final O_i -$V_0^{\bullet\bullet}$-O_i defects) is shown in the plot given in figure 6.6. A migration energy of 0.16 eV (0.29 eV was predicted by Uberuaga *et al.* [116]) was predicted using this simulation technique. The jump distance given in table 6.1 is the distance between the sites about which the initial and final O_i -$V_0^{\bullet\bullet}$-O_i defects are centred.

Uberuaga *et al.* [116] also highlight two separate oxygen interstitial rotation processes which allow the O_i -$V_0^{\bullet\bullet}$-O_i defects to access the other $1\bar{1}0$ directions in order to facilitate 3D transport. The migration energies for these were predicted to be 0.64 and 0.67 eV. Unfortunately, it

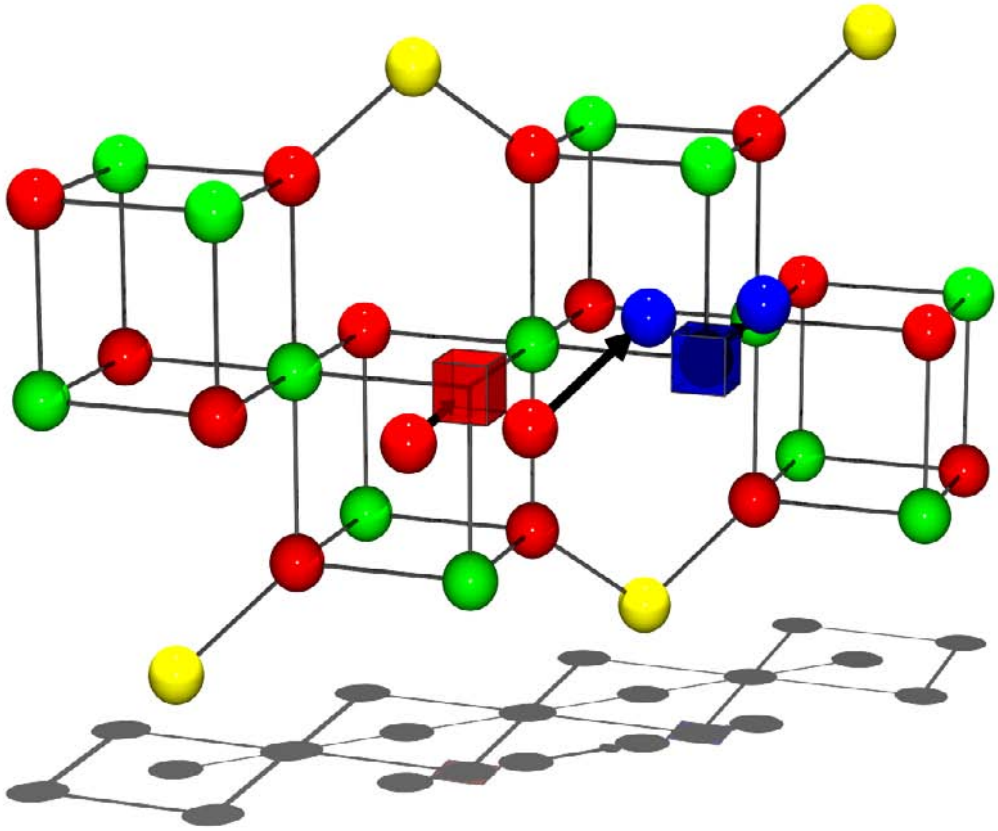

Figure 6.5: Oxygen interstitial migration. The red spheres represent oxygen ions, green ions represent aluminiuim ions, the magnesium ions are represented by the yellow spheres and the red cube represents the initial site, about which, the interstitial is split. For migration to occur the left interstitial ion must collapse onto the vacant site, thereby forcing the other interstitial ion to become associated with the neighbouring oxygen site and forcing the lattice ion from it's site creating the blue coloured split interstitial.

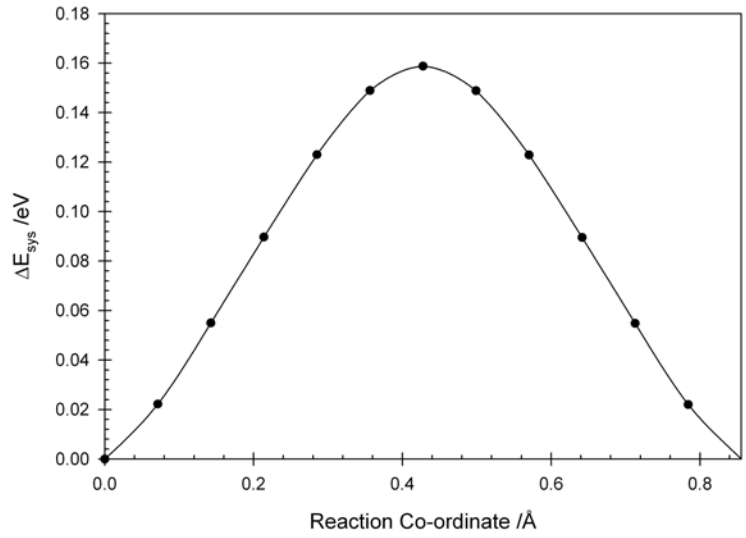

Figure 6.6: Migration energy as a function of the reaction co-ordinate for oxygen interstitial migration. It is the motion of the central interstitial ion which is followed on the x-axis, as it is part of both the initial and final O_i -$V_0^{\bullet\bullet}$-O_i defects.

was not possible to determine equivalent values using the static based technique applied in this chapter. The reason for this is that in region of the saddle point the force on the oxygen anions cause the core and the shell to decouple. It may be possible to modify the spring constant or add a further term to the harmonic coupling between the core and the shell, however, this involves modifying the forces between ions and would be inconsistent with the other energies calculated here. Uberuaga *et al.* [116] predicted the migration energies for these processes to be roughly 0.35 eV greater in energy than the 1D diffusion process, therefore it is expected that these rotation mechanisms will not represent the principle mechanisms for oxygen interstitial diffusion in spinel.

Also included in table 6.1 are the temperature independent terms, ie. the geometric term, jump distance and the Vineyard term. Using these values the prefactor, D_0^x, for each process was determined and also included in table 6.1. In order to allow a full comparison of the diffusion mechanisms suggested here the diffusivities (excluding the concentration term) at 500 K and 1500 K (these temperatures were chosen as they represent the upper and lower bounds of the region of interest) are reported in table 6.1.

Table 6.1 shows that the attempt frequencies for each of the processes is within an order of magnitude, with vacancy mechanism (3) having the softest modes and consequently the largest Vineyard term. The jump distances, all fall within 2.38 - 3.12 Å and therefore despite being squared in D_0 do not differentiate between the processes. Consequently, there is less than an order of magnitude difference in the overall diffusion prefactors. For the most favourable vacancy mechanism (mechanism 6.1(1)) the pre-exponential factor, D_0, is 85.85 10^{-8} s^{-1} m^2 and for the interstitial mechanism D_0 was found to be 22.40 10^{-8} m^2 s^{-1} . The D_0 value predicted for the interstitial mechanism agrees exceptionally well with the experimental value of 2.2 10^{-7} $m^2 s^{-1}$ (+8.7/-1.8 10^{-7} $m^2 s^{-1}$) obtained by Ryerson and McKeegan [141] which suggests that the interstitial mechanism is responsible for the diffusion they observed (although correlation has not been included it is expected to be close to unity).

At both 500 and 1500 K the ordering of the diffusion processes is dictated by the migration energies for each process. Across the entire temperature range of interest it is the oxygen interstitial diffusion mechanism that has the largest value of d_x, therefore the most favourable mechanism for oxygen self diffusion is via O_i defects (presuming the concentrations of O_i and $V_O^{\bullet\bullet}$ defects are the same).

6.3 Summary

The results obtained in this chapter lead to the following conclusions:

- A comparison of the d_x values at both 500 and 1500 K (ie. across the entire temperature range of interest) for all of the point defects in spinel predicts that the O_i defect is the most mobile point defect in spinel.
- As was the case for cation diffusion the calculation of the diffusion prefactors is important, however, it is not sufficient to cause a reordering of the interstitial and vacancy mediated oxygen self diffusion mechanisms examined here.

Table 6.1: Activation energies, attempt frequencies geometric terms, jump distances and overall prefactors for the O^{2-} migration processes considered, as well as the predicted d_x terms at 500 and 1500 K.

Migration Process	Activation Energy /eV	Vineyard Term / 10^{12} s^{-1}	Geometric Term	Jump Distance / 10^{-10} m	Prefactor / 10^{-8} m^2 s^{-1}	Log d_x @500 K / 10^{-8} s^{-1}	Log d_x @1500 K / 10^{-8} s^{-1}
$V_O^{\bullet\bullet}$							
Mechanism 1	1.40	10.95	6	2.80	85.85	-12.18	-2.77
Mechanism 2	1.55	7.57	3	2.38	21.44	-14.29	-3.88
Mechanism 3	3.27	32.20	3	3.12	156.72	-30.77	-8.79
O_i	0.16	8.57	2	2.87	22.40	-0.26	0.81

7
Defect clustering and diffusion in spinel

7.1 Introduction

The preceding chapters, (5 and 6) examined the role of point defects in facilitating the transport of both cations and oxygen ions in spinel. The simple mechanisms proposed for cation (chapter 5) and oxygen transport (chapter 6) are predominantly facilitated by isolated point defects, with some mechanisms, most noticeably Al^{3+} migrating via a vacancy mechanism on the magnesium sublattice, requiring the presence of more than one defect. However, in many ceramic materials, it is unlikely that defects will find themselves completely isolated, therefore, the processes discussed previously will be perturbed by the presence of other defect species.

In much the same way as oppositely charged molecules are attracted to each other, point defects with opposite charges will be attracted to each other. There is, therefore, a driving force (ie. minimising the Coulombic interaction) for these defects to form clusters by minimising the separation between them. In order for these clustered point defects to move apart, and break the cluster, they need to overcome the binding energy that holds them together. As the point defects that facilitate diffusion in spinel are all charged these defects will become bound to each other, which in turn, may affect their ability to promote mass transport.

A further, more subtle, way in which the presence of a point defect, unrelated to the isolated diffusion process, can affect the migration mechanisms discussed in chapters 5 and 6 is related to a defect's effect on the local environment. When a defect is introduced into a crystal, the lattice relaxes to accommodate it. Consequently, the region immediately surrounding a point

defect has been modified, to some extent, from the the perfect lattice; this perturbed region is known as a defect's strain field. Clearly, any point defect migrating through the strain field of another point defect will encounter an environment that is subtly different from the perfect lattice. Since the region the defect is migrating through is altered, the energies of the processes facilitating transport are also modified.

In this chapter the accelerated dynamics technique, TAD [99], is used to investigate how point defect mediated cation and oxygen transport in spinel is affected by defect-defect interactions. TAD has been used previously to examine the behaviour of isolated defects in spinel [116] and more complex cluster diffusion processes in MgO [137]. Uberuaga *et al.* [143] showed, using TAD, that in MgO vacancies are immobile but interstitial clusters, containing $3O_i$ and $3Mg_i^{\bullet\bullet}$ defects, diffuse on the nanosecond timescale. The complex pathway by which this defect cluster can diffuse would have been practically impossible to predict from observations of the crystal structure, thus demonstrating the power of a technique that requires no *a priori* knowledge of the diffusion processes.

7.2 Methodology

An overview of the TAD simulation technique can be found in section 3.7. The simulations conducted here employ a 2x2x2 supercell, containing 448 ions, which is tessellated infinitely through space to represent the spinel lattice. Again the potential parameters of Smith *et al.* [73] were used, however, in order to ensure that the model was computationally tractable, a shell model was not employed. T_{high} and T_{low} were selected to ensure that the processes observed were relevant whilst achieving a reasonable boost factor when compared to ordinary MD. The defect starting locations within the cell were selected at random.

7.3 Results and discussion

7.3.1 Isolated defects

In order to allow a direct comparison of the point defect migration process in the isolated and clustered cases, TAD simulations were first conducted on the isolated point defects. For these simulations, T_{high} was set to 3000 K and T_{low} was set at 1500 K. The results of the TAD simulations of spinel supercells containing the intrinsic point defects are presented in trace form in figure 7.1 (a trace is a superposition of the defect's locations after every TAD transition) and the overall migration energies for mass transport facilitated by each isolated point defect is presented in table 7.1.

Figure 7.1(a) shows that during the course of the simulation the V_{Mg} defect diffuses in 3D and as such is able to explore the entire supercell. It migrates via a metastable V_{Mg}-$Mg_i^{\bullet\bullet}$-V_{Mg} defect cluster (as predicted in chapter 5), hence interstitial ions are indicated in 7.1(a). The migration energy for the V_{Mg} defect to enter the metastable, V_{Mg}-$Mg_i^{\bullet\bullet}$-V_{Mg}, state was predicted to be 0.68 eV and the barrier for it to leave the metastable state was 0.09 eV. Chapter 5 predicted migration energies of 0.56 eV and 0.21 eV for the two equivalent process. The origin of this discrepancy is likely the inclusion of a shell model in the static calculations presented in chapter 5.

Magnesium interstitial diffusion (figure 7.1(b)) is a combination of the mechanisms highlighted in figure 5.16, with migration energies of 0.56 eV, 0.74 eV and 0.52 eV for processes 5.16(c), 5.16(b) and 5.16(a) respectively. Using the static method applied in chapter 5 the migrate and twist $Mg_i^{\bullet\bullet}$ diffusion mechanism (figure 5.16(c)) was also predicted to have the lowest migration energy with a value of 0.46 eV and the inplane mechanism (figure 5.16(b)) the highest migration energy of 0.58 eV. Chapter 5 predicted a migration energy of 0.54 eV for the rearrangement process. Furthermore, the model that includes the polarisability of the oxygen ions (applied in chapter 5) suggests that all of the $Mg_i^{\bullet\bullet}$ migration processes will migrate via a metastable intermediary. The migration energies to escape from the metastable intermediate states are negligible for the migrate and twist (figure 5.16(c)) and inplane (figure 5.16(b)) mechanisms but more significant (0.44 eV) for the $Mg_i^{\bullet\bullet}$ rearrangement process (figure 5.16(a)). In contrast, the TAD simulations predict that $Mg_i^{\bullet\bullet}$ migration via the migrate and twist mechanism

is the only processes to enter an intermediate state and the migration barrier for escape is 0.07 eV.

Aluminium diffusion via a vacancy mechanism on its native sublattice is shown in figure 7.1(c). As in the V_{Mg} case the process has an metastable intermediary, V_{Al}-$Al_i^{\bullet\bullet\bullet}$-$V_{Al}$ state. The activation energies to enter and then leave the intermediate state are 1.98 eV and 0.32 eV respectively. By comparison the model applied in chapter 5 predicted values of 1.83 eV and 0.12 eV for the same processes.

For interstitial diffusion it was predicted in chapter 5 that the $Al_i^{\bullet\bullet\bullet}$-$V_{Mg}$-$Mg_i^{\bullet\bullet}$ interstitial defect was unstable and would decay to the $[Al_{Mg}^{\bullet}$:$Mg_i^{\bullet\bullet}$-V_{Mg}-$Mg_i^{\bullet\bullet}]^{\bullet\bullet\bullet}$ defect cluster. Both the $Al_{Mg}^{\bullet}$ and $Mg_i^{\bullet\bullet}$-V_{Mg}-$Mg_i^{\bullet\bullet}$ defects are positively charged therefore they will repel each other and because it is the more mobile defect, the $Mg_i^{\bullet\bullet}$ interstitial diffuses away, as shown in figure 7.1(d). The activation energy for the decay process is 0.85 eV compared with 0.54 eV predicted in chapter 5.

Oxygen vacancy and interstitial migration during the simulations are shown in figures 7.1(e) and 7.1(f) respectively. During the $V_O^{\bullet\bullet}$ simulation only two of the three processes described in figure 6.1 were observed and the activation energies for processes 6.1(a) and 6.1(b) are 1.53 eV and 1.68 eV (values of 1.40 eV and 1.55 eV were predicted in chapter 6). The final oxygen vacancy migration process discussed in chapter 6 was not observed in the TAD simulations, this is due to the significantly higher energy barrier for this transition (a value of 3.27 eV was predicted in chapter 6).

The simulation showing O_i diffusion (figure 7.1(f)) predicts that oxygen interstitial diffusion will occur in one dimension; with a migration energy of 0.30 eV. For the equivalent process a value of 0.16 eV was predicted using a static based technique in chapter 6. In order for the mechanism to become 3D the O_i defect must undergo a rotation process that will allow it to access other 110 directions. Two rotation mechanisms were suggested by Uberuaga *et al.* [116] both of which were detected during the TAD simulation presented in figure 7.1(f) and migration energies of 0.68 eV and 0.69 eV were determined, however, neither of these processes were accepted in the simulation.

Table 7.1 gives the simulation times for each of the simulations presented in figure 7.1. The longest simulated time was for the supercell containing a V_{Al} defect (0.60 10^3 ns) and the

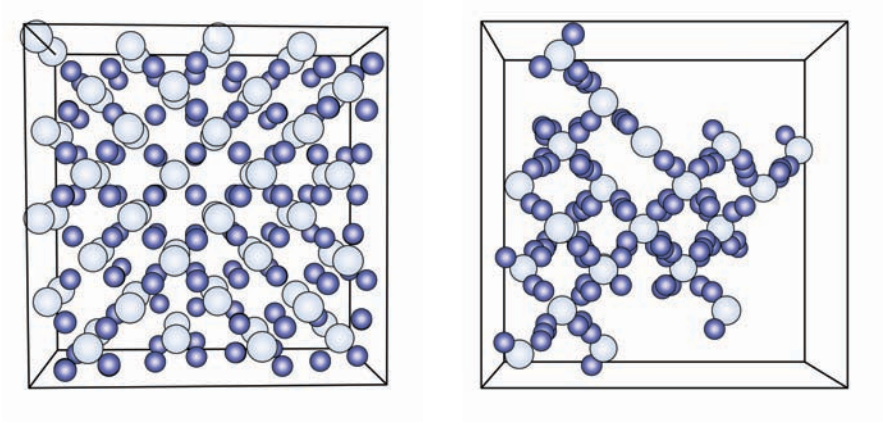

(a) Magnesium Vacancy

(b) Magnesium interstitial

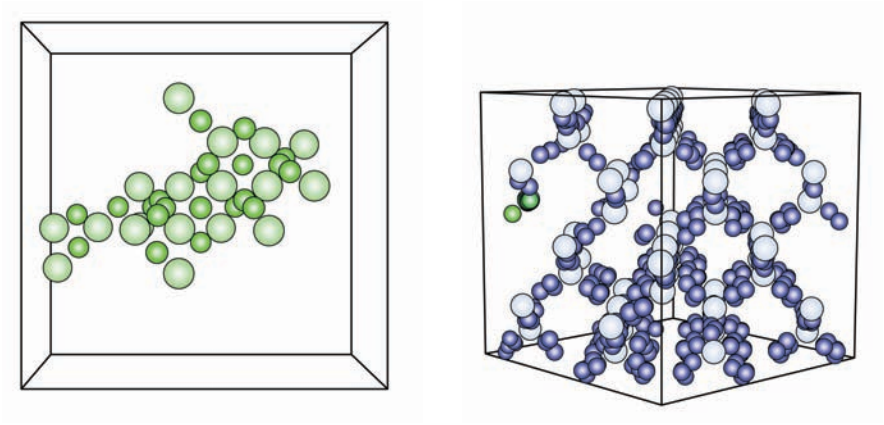

(c) Aluminium Vacancy

(d) Aluminium Interstitial

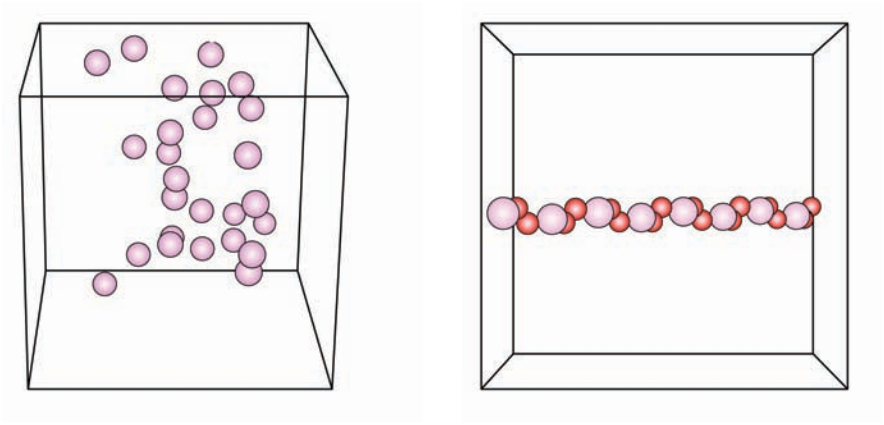

(e) Oxygen Vacancy

(f) Oxygen Interstitial

Figure 7.1: Traces of the time dependant evolution of the isolated point defects, at 1500 K. The pale blue spheres represent V_{Mg}, blue spheres represent $Mg_i^{\bullet\bullet}$, pale green spheres represent V_{Al}, green spheres represent $Al_i^{\bullet\bullet\bullet}$, pale pink spheres represent $V_O^{\bullet\bullet}$, pink spheres represent O_i and a dark green sphere represent $Al_{Mg}^{\bullet}$ defects. The colours denoting each defect species in this figure are used in all traces presented in this chapter.

Table 7.1: Table containing a summary of the simulation times (ie. the duration of the simulated period) at 1500 K and the migration energies of the isolated intrinsic defects predicted using TAD. The $Al_i^{\bullet\bullet\bullet}$ defect collapses to form $Al_{Mg}^{\bullet}$ and $Mg_i^{\bullet\bullet}$ defects, after which, there is no further migration of the Al^{3+} cation.

Defect	Simulation Time /ns	Migration Energy /eV
V_{Mg}	9.50	0.68
$Mg_i^{\bullet\bullet}$	0.37	0.53
V_{Al}	0.60 10^3	1.98
$Al_i^{\bullet\bullet\bullet}$	3.52	*unstable*
$V_O^{\bullet\bullet}$	6.56	1.53
O_i	0.88 10^{-3}	0.30

shortest was for the supercell containing an O_i defect (0.88 10^{-3} ns). However, these two simulations were run for significantly different periods of time so it is useful to consider the simulation time per hour CPU time. For the V_{Al} simulation a simulation rate of 3.2 ns per hour CPU time compared with 17.6 fs per hour CPU time for the O_i simulation. The reason for the difference in the simulation rates is related to the migration energies for the processes occurring within the supercell. For a system with a low migration energy (as is the case in the O_i simulation) it is more probable, than for a system with predominantly high migration energies (eg. V_{Al}), that the system will have undergone a transition to a new state each time the basin-constrained MD is paused. Should a transition have occurred since the last time the basin-constrained MD simulation was paused then an NEB calculation must be performed to determine the activation energy for the transition. Consequently, in a system with lower migration barriers, more transitions will occur, requiring the simulation to spend more time performing NEB simulations as opposed to continuing the high temperature MD simulation.

7.3.2 Defect clustering

As the concentration of cation antisite defects are predicted to be orders of magnitude greater than the other point defects [75] it is probable that a vacancy or interstitial defect migrating through the lattice will become bound to an oppositely charged antisite defect. The simulations

in chapter 5 predicted that antisite defects will diffuse more slowly than interstitial and vacancy defects, therefore, it is instructive to consider how the presence of an antisite defect will affect diffusion of the other intrinsic point defects.

Influence of an $Al_{Mg}^{\bullet}$ defect on migration of a V_{Mg} defect

Figure 7.2 shows the evolution of a spinel supercell containing an $Al_{Mg}^{\bullet}$ defect and a V_{Mg} defect. This figure shows that the $Al_{Mg}^{\bullet}$ defect is not observed to diffuse on the time scale of the simulation (17.50 ns). The results in chapter 5 predicted that the preferred mechanism for Al^{3+} cation diffusion is via a vacancy mechanism on the magnesium sublattice. However, the TAD simulation failed to predict a single migration of a magnesium vacancy to an $Al_{Mg}^{\bullet}$ defect, an essential part of the process proposed in chapter 5; although the transition was detected during the course of the simulation (a migration energy of 1.18 eV was predicted here compared with 0.88 eV predicted in chapter 5). For the $Al_{Mg}^{\bullet}$ defect to migrate onto a neighbouring magnesium site the V_{Mg} defect must be located on one of the four nearest neighbour sites. Figure 7.3 shows how the spacial separation between the V_{Mg} defect and the $Al_{Mg}^{\bullet}$ evolves during the course of the simulation. Initially the V_{Mg} defect is located on a nearest neighbour site to the $Al_{Mg}^{\bullet}$ defect (the defects are separated by 3.51 Å). The V_{Mg} defect migrates via an intermediary V_{Mg}-$Mg_i^{\bullet\bullet}$-V_{Mg} (as discussed in chapter 5 and in section 7.3.1), therefore, as these processes occur, the separation between the $Al_{Mg}^{\bullet}$ defect and this metastable intermediate is computed from the central $Mg_i^{\bullet\bullet}$ defect. During the simulation the largest separation observed between the defects was 14.06 Å. This separation is sufficient for the V_{Mg} defect to interact significantly with the $Al_{Mg}^{\bullet}$ defect image in a neighbouring supercell. Therefore, given a high enough concentration of $Al_{Mg}^{\bullet}$ defects (in the simulation shown in figure 7.2, 1.5 % of the Mg_{Mg} lattice ions were replaced with $Al_{Mg}^{\bullet}$ defects), the V_{Mg} defect can move from antisite to antisite and so may diffuse without ever becoming completely dissociated from the $Al_{Mg}^{\bullet}$ defects (subject to the distribution of $Al_{Mg}^{\bullet}$ defects).

Figure 7.3 indicates a significant fluctuation in the separation between the two defects during the simulation, despite them being bound together. In a traditional MD simulation a plot of the separation between two defects in a crystal would be a smooth continuous function, however, the plot shown in 7.3 is not a continuous smooth curve because the defect positions are only reported once a transition has occurred. Therefore, in figure 7.3 the defects appear to jump

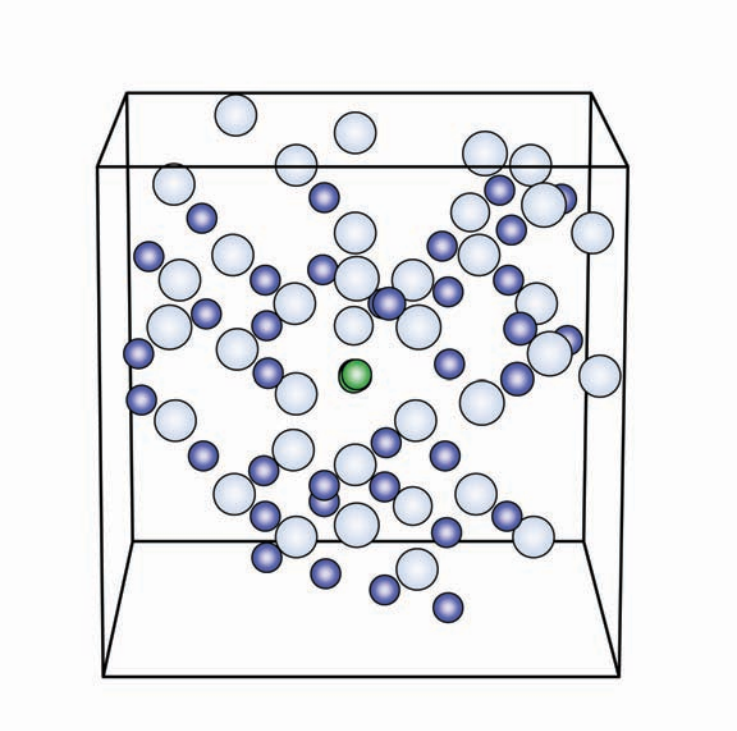

Figure 7.2: Trace of the long timescale evolution of a spinel supercell containing an $Al^{\bullet}_{Mg}$ and a V_{Mg} defect.

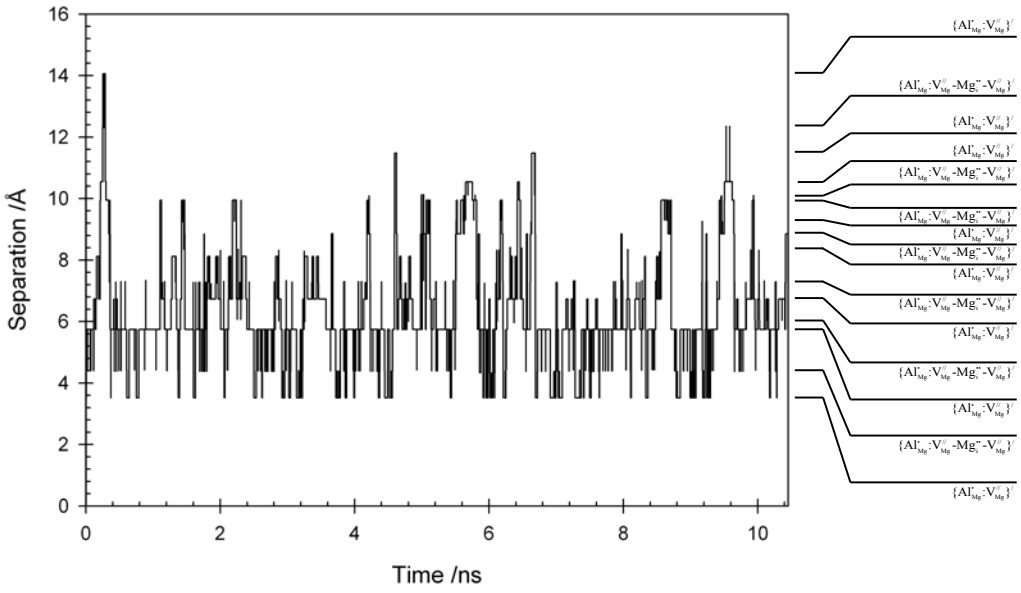

Figure 7.3: Plot of the defect separation as a function of the simulation time for a spinel supercell containing an $Al^{\bullet}_{Mg}$ and a V_{Mg} defect.

from one relaxed state to the next relaxed state. As the separation between defects are only reported once a transition has occurred; the residency time, at a given defect separation, is the time between transitions (represented by horizontal sections of the plot shown in figure 7.3).

The probability, G(r), of the $Al^{\bullet}_{Mg}$ and V_{Mg} defects residing at one of the set of separations, r, is calculated as the total simulation time spent at r as a fraction of the total simulation time. G(r) is then plotted as a function of the separation between the defects in figure 7.4. Figure 7.4 predicts that residence at the second nearest neighbour configuration is roughly five times more probable than the nearest neighbour configuration. Furthermore, within this cell (ie. at this concentration and subject to these geometric constraints) the $Al^{\bullet}_{Mg}$ defect can only migrate during the 10% of the time, during which the defects are in a nearest neighbour configuration. The second nearest neighbour configuration is 0.005 eV higher in energy than the nearest neighbour configuration, however, there are 12 second nearest neighbour sites and four adjacent sites. So by examining the thermodynamics of the system, it would be expected that the ratio between the probabilities, G(r), of the first and second nearest neighbour configurations would be close to 1:3 at low temperatures. During the simulation the defects sample a nearest neighbour configuration 68 times compared with the 231 times for the second nearest neigh-

bour configuration. This represents a ratio of roughly 1:3.4, therefore, the average time spent at a second nearest neighbour configuration must be greater than the average residency time for a first nearest neighbour configuration (the simulations predicts 23.2 and 12.5 ps respectively). The lifetime of each state is related to the migration energies for migration out of that state (ie. a state that corresponds to a shallow minimum on the potential energy surface will have a shorter lifetime than a state corresponding to a deep well). Figure 7.5 shows the potential energy surface in the region immediately surrounding the $Al^{\bullet}_{Mg}$ defect.

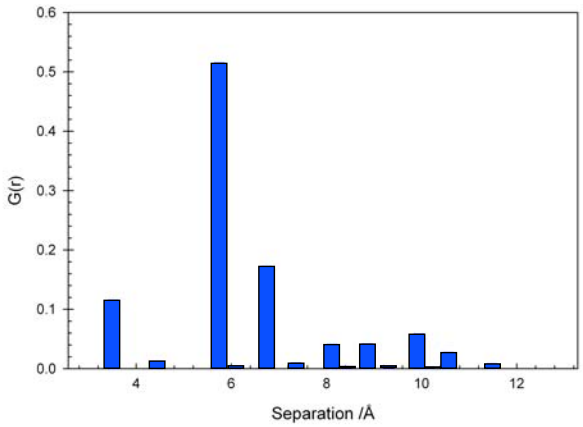

Figure 7.4: Plot of the probability distribution, G(r), as a function of the separation between an $Al^{\bullet}_{Mg}$ and a V_{Mg} defect.

From figure 7.5 it is possible to see that the migration energies for the escape from the two nearest neighbour sites. When the defects are in a nearest neighbour configuration the barrier for the $Al^{\bullet}_{Mg}$ defect to migrate is 1.18 eV and to move to one of the of the three second nearest neighbour sites is 0.66 eV. The migration energies to escape from the second nearest neighbour configuration are 0.60 eV to migrate to the intermediate state linking the first and second nearest neighbours, 0.87 eV to migrate to a neighbouring third nearest neighbour site and 0.72 eV to migrate to one of the two available fourth nearest neighbour sites. By determining the jump distances and attempt frequencies for each of the processes described above it is possible to determine (using equation 2.28) the overall rate of escape, d_x, from the first and second nearest neighbour configurations. The Log of the d_x values, at 1500 K, for escape from the first nearest neighbour configuration is -12.97 compared to a value -12.55 for escape from the second nearest neighbour sites, this implies that the nearest neighbour site would have a greater residency time. This is contrary to the lifetimes observed in the simulation, therefore,

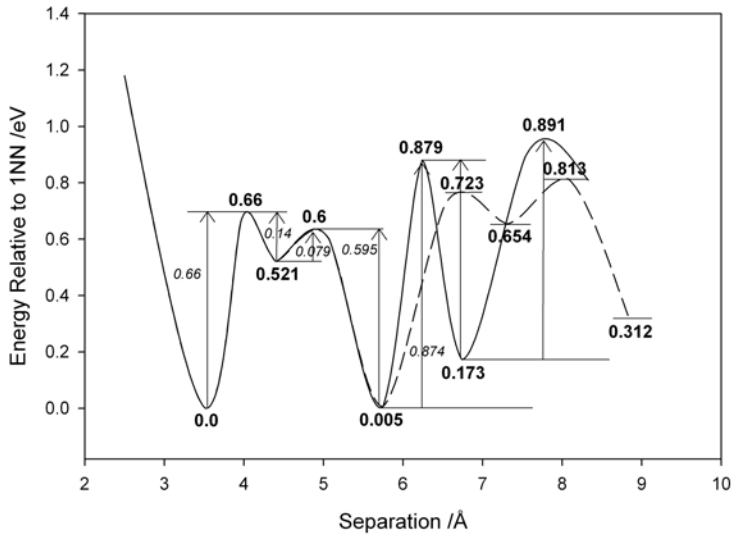

Figure 7.5: The potential energy surface near to the $Al^{\bullet}_{Mg}$ defect. All energies are presented relative to the energy of the nearest neighbour configuration.

there must be another factor influencing the lifetime of the first and second nearest neighbour configurations.

The final factor which has not been discussed so far in this section, but is included in a TAD simulation, is entropy. Migrational entropy is included in the determination of the rate constants to escape from the two configurations above via the Vineyard equation (equation 2.22), however, configurational entropy was not considered. Determining the configurational entropy is not trivial, however, to give an indication as to whether entropy is likely to be a major factor an identical TAD simulation was conducted at 500 K (as $G = H - TS$, reducing the temperature should reduce any entropic effects thereby bringing the ratio of probabilities for the nearest and second nearest neighbours closer to the 1:3 ratio predicted by the enthalpies alone). During this simulation the ratio of probabilities for the nearest and second nearest neighbour sites is reduced to 1:3.20 and the average lifetime of the second nearest neighbour configuration is also reduced to less than that of the nearest neighbour configuration (0.30 and 0.42 ms respectively). Therefore, in future work it is important to consider the relative free energy of the states rather than simply comparing the relative enthalpies if detailed differences are to be discussed.

Figure 7.6 shows the migration energy of a V_{Mg} defect plotted as a function of the separation

from an $Al^{\bullet}_{Mg}$ defect. Included in 7.6 are the migration energies for the isolated V_{Mg} defect. A comparison of the migration energy of the isolated V_{Mg} defect with the various migration energies for the V_{Mg} defect migrating within the strain field of the $Al^{\bullet}_{Mg}$ defect, shows that there is a distribution of energies as opposed to the single values of the isolated case.

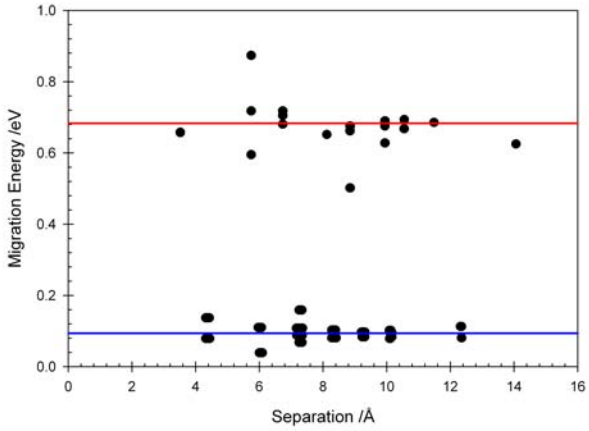

Figure 7.6: Plot of the migration energies as a function of the separation between a V_{Mg} defect and an $Al^{\bullet}_{Mg}$ defect. The horizontal lines represent the activation energies for the isolated V_{Mg} diffusion processes, the red line represents the migration energy to reach the intermediate state and the blue line is the migration energy to escape from the intermediate state.

Influence of an $Al^{\bullet}_{Mg}$ defect on migration of a V_{Al} defect

Figure 7.7 shows the long timescale evolution of a spinel supercell containing a V_{Al} defect and an $Al^{\bullet}_{Mg}$ defect during a simulation lasting 1.23 ms. The separation between the $Al^{\bullet}_{Mg}$ defect and the V_{Al} defect is then plotted as a function of the simulation time in figure 7.8 and a probability distribution, G(r), of the defect separations is given in figure 7.9. Figure 7.7 shows that during the course of the simulation the V_{Al} defect is able to migrate only as far as a second nearest neighbour site (5.27 Å) from the $Al^{\bullet}_{Mg}$ defect.

The two peaks in figure 7.9 correspond to the nearest and second nearest neighbour $\{Al^{\bullet}_{Mg}{:}V_{Al}\}$ cluster configurations. Whilst there are three different V_{Al}-$Al^{\bullet\bullet\bullet}_{i}$-$V_{Al}$ intermediates observed during the simulation they have a very short lifetime and so are not visible in figure 7.9. Figure 7.9 shows that the V_{Al} defect spends most of its time (93%) on an adjacent site to the $Al^{\bullet}_{Mg}$ defect. The nearest neighbour configuration is 0.29 eV lower in energy than the second nearest

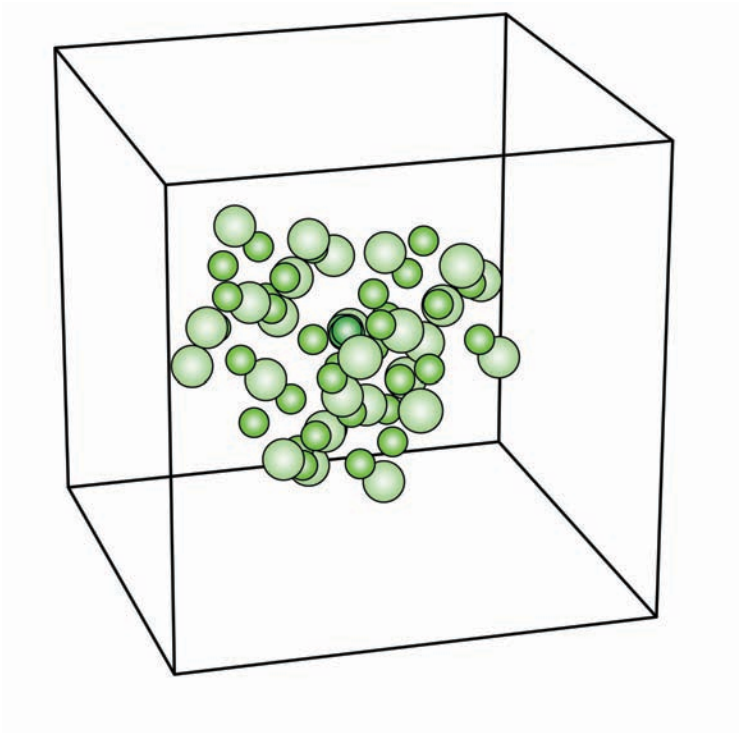

Figure 7.7: Trace of the long timescale evolution of a spinel supercell containing an $Al^{\bullet}_{Mg}$ and a V_{Al} defect.

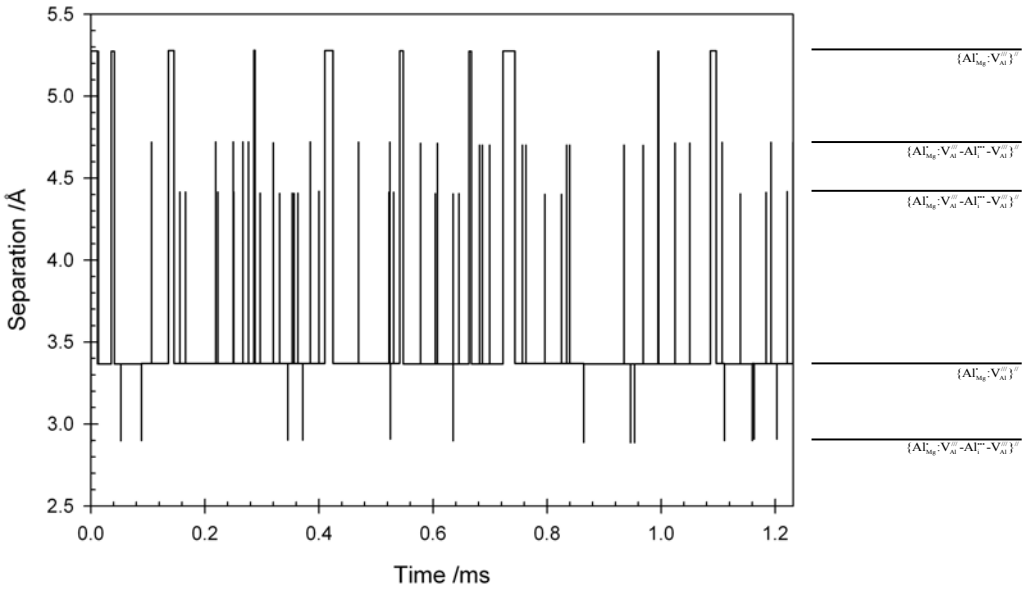

Figure 7.8: Plot of the defect separation as a function of the time for a spinel supercell containing an $Al^{\bullet}_{Mg}$ and a V_{Al} defect.

neighbour site, therefore, despite the larger number of second nearest neighbour sites the first nearest neighbour configuration is dominant.

Figure 7.10 shows how the migration energies are modified as the separation between the $Al^{\bullet}_{Mg}$ and V_{Al} defects is increased. Again this indicates that the small changes in the local environment resulting from the presence of an antisite defect can affect the migration energies of the more mobile vacancy and interstitial defects. In the most extreme case observed in this simulation the migration energy to escape from the metastable intermediate state is increased from 0.32 eV up to 0.55 eV. This may have a dramatic impact on the overall diffusion processes given competing processes with similar migration energies. This would undoubtedly be a fruitful area for further work.

Influence of an $Al^{\bullet}_{Mg}$ defect on migration of an O_i defect

The interaction between an $Al^{\bullet}_{Mg}$ defect and an O_i defect over a period of 0.43 ns is shown in figure 7.11. Initially the O_i defect is 6.08 Å from the $Al^{\bullet}_{Mg}$ defect, however, the O_i defect

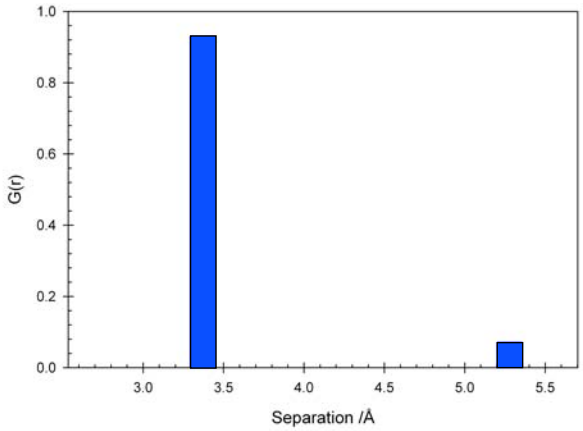

Figure 7.9: Plot of the probability distribution, G(r), as a function of the separation between the $Al^{\bullet}_{Mg}$ and a V_{Al} defect.

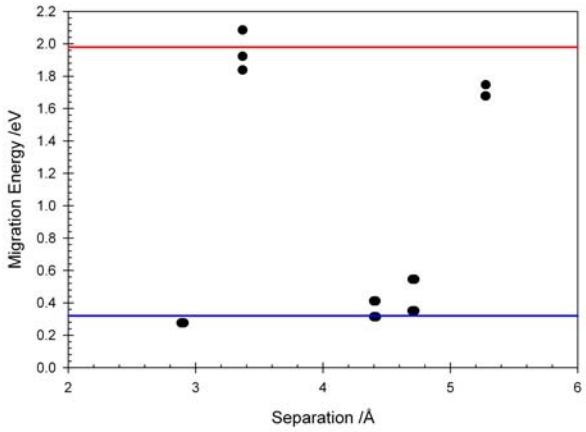

Figure 7.10: Plot of the migration energies as a function of the separation between the V_{Al} defect and the $Al^{\bullet}_{Mg}$ defect. The horizontal lines represent the activation energies for the isolated V_{Al} diffusion processes, the red line represents the migration energy to reach the intermediate state and the blue line is the migration energy to escape from the intermediate state.

quickly migrates towards the antisite defect until it occupies a nearest neighbour configuration (where the separation is 1.78 Å). Once this nearest neighbour configuration is established the interstitial defect undergoes a rotation mechanism to enter the lowest energy configuration. The migration energy to perform the rotation process was 0.73 eV, however, the energy gained due to the rotation is 1.38 eV. Due to the high migration energies for escape from this lowest energy configuration (1.5 eV) to a second nearest neighbour configuration and the very small migration energy to move between equivalent nearest neighbour sites (0.12 eV) the separation between the defects is unchanged throughout the remainder of the simulation, as shown in figure 7.12.

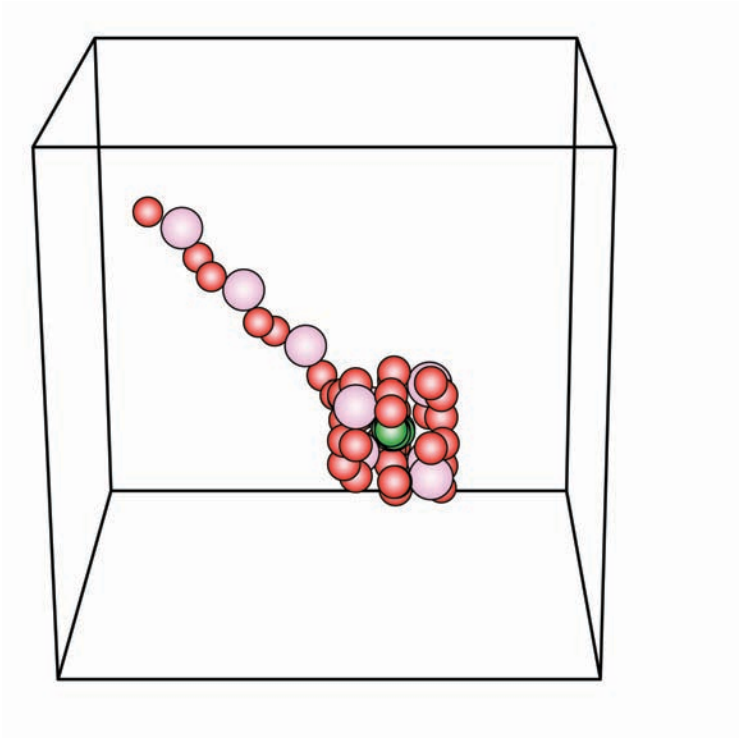

Figure 7.11: Trace of the long timescale evolution of a spinel supercell containing an $Al^{\bullet}_{Mg}$ and an O_i defect.

A plot of the migration energies for O_i defect diffusion as a function of its separation from the $Al^{\bullet}_{Mg}$ defect is given in figure 7.13. The migration barrier to move between nearest neighbour sites is significantly lower than the isolated O_i migration energies. This significant change in the migration energy arises due to the distortion in the oxygen sublattice in the region immediately surrounding the antisite defect.

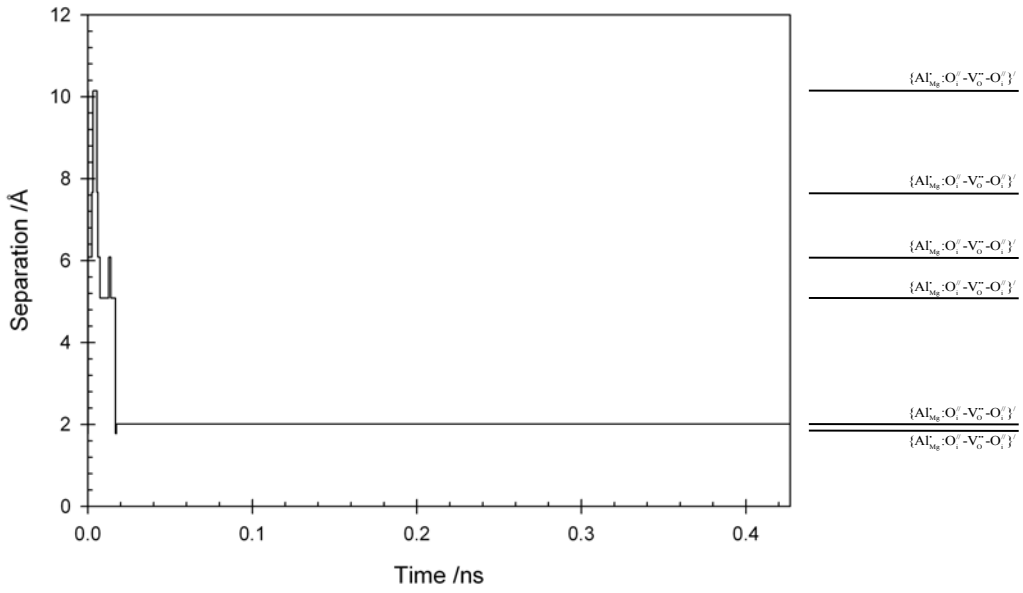

Figure 7.12: Plot of the defect separation as a function of the simulation time for a spinel supercell containing an $Al^{\bullet}_{Mg}$ and a V_{Al} defect.

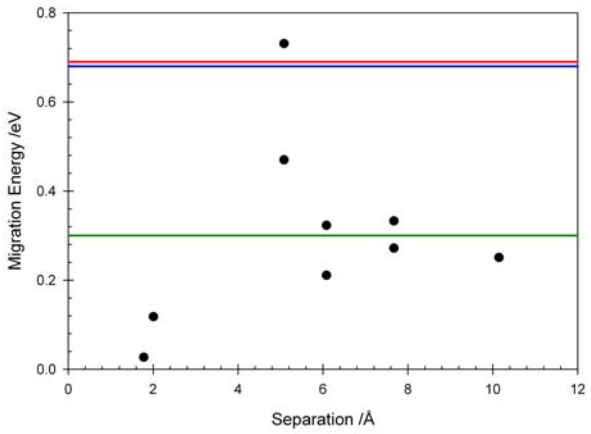

Figure 7.13: Plot of the migration energies as a function of the separation between an O_i defect and an $Al^{\bullet}_{Mg}$ defect. The horizontal lines represent the migration energies for the isolated O_i diffusion processes, the green line represents the 1D diffusion process and the blue and red lines represent the migration energies for the rotation processes.

Influence of an Mg_{Al} defect on migration of an $Mg_i^{\bullet\bullet}$ defect

A trace of a spinel supercell containing an Mg_{Al} defect and a $Mg_i^{\bullet\bullet}$ defect evolving for a period of 1.63 ns is shown in figure 7.14. Figure 7.15 shows how the separation between the two defects changes as a function of time during the simulation. From figure 7.15 it is possible to see that the $Mg_i^{\bullet\bullet}$ defect can migrate to a separation from the Mg_{Al} defect in excess of 9.0 Å; this separation is sufficient to enable the $Mg_i^{\bullet\bullet}$ defect to become associated with an Mg_{Al} defect image in a neighbouring cell.

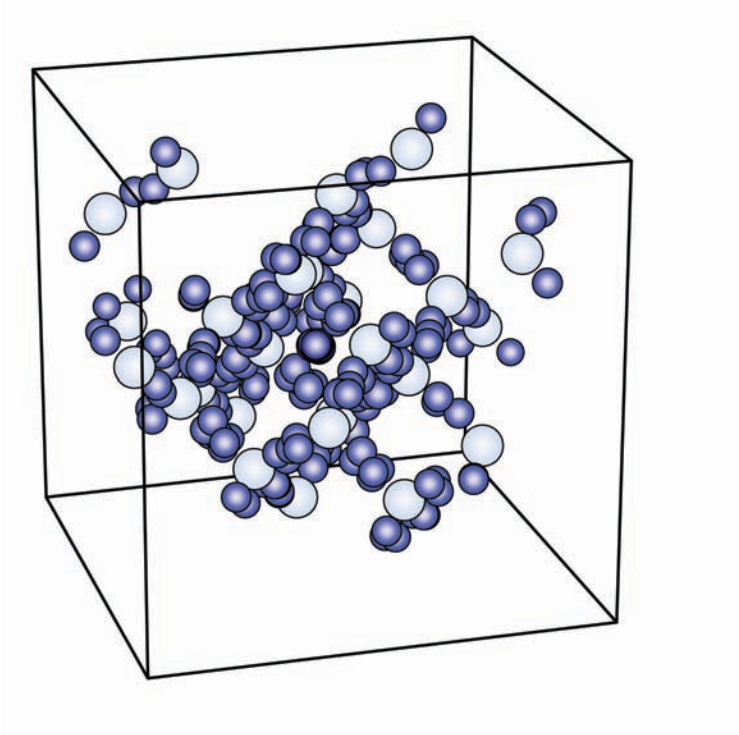

Figure 7.14: Long timescale evolution of a spinel supercell containing a Mg_{Al} and $Mg_i^{\bullet\bullet}$ defect. The darker blue sphere at the centre of the supercell represents a Mg_{Al} defect.

The lowest energy configuration for the $\{Mg_{Al}{:}Mg_i^{\bullet\bullet}\}^{\bullet}$ cluster is for the $Mg_i^{\bullet\bullet}$-V_{Mg}-$Mg_i^{\bullet\bullet}$ defect to be located on one of the six nearest neighbour magnesium lattice sites relative to the Mg_{Al} defect and the second lowest energy configuration sees the $Mg_i^{\bullet\bullet}$-V_{Mg}-$Mg_i^{\bullet\bullet}$ cluster centred on one of the 12 second nearest neighbour sites. The intermediate states represent isolated $Mg_i^{\bullet\bullet}$ defects. During the simulation the nearest neighbour site is visited on more occasions than the second nearest neighbour configuration, however, the average lifetime of the second nearest neighbour configuration is longer, resulting in the plot shown in figure 7.16.

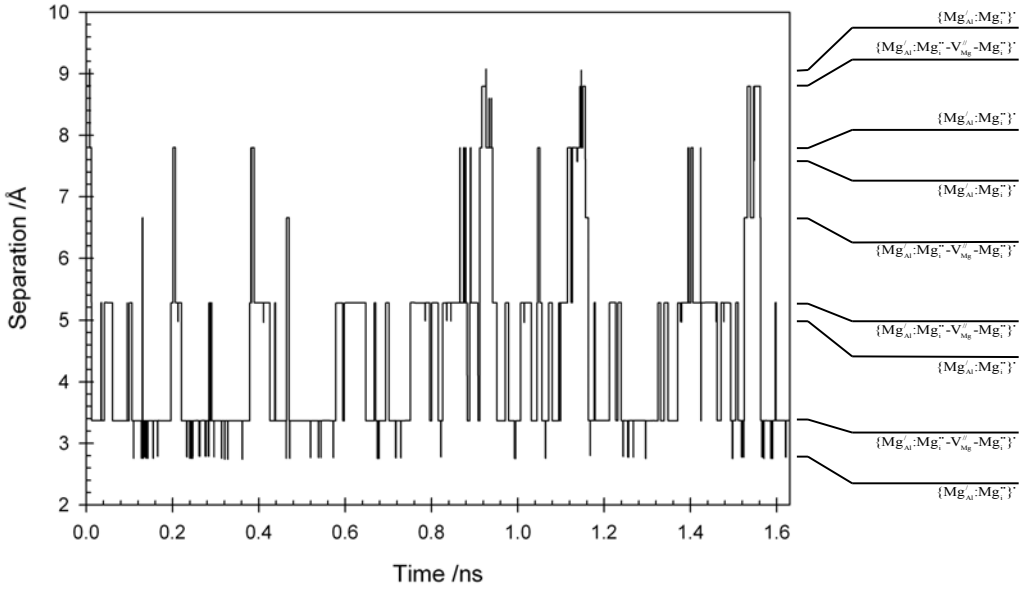

Figure 7.15: Plot showing the defect separation as a function of the simulation time for a spinel supercell containing an Mg_{Al} and a $Mg_i^{\bullet\bullet}$ defect.

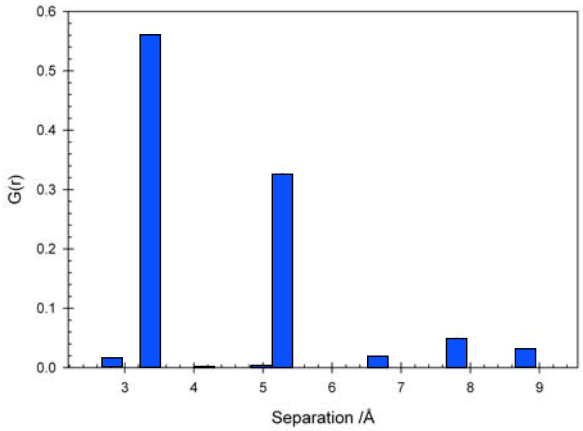

Figure 7.16: Plot of the probability distribution, G(r), as a function of the separation between an Mg_{Al} and a $Mg_i^{\bullet\bullet}$ defect.

A plot showing the migration energies observed during the simulation as a function of the separation between the defects prior to the relevant transition is given in figure 7.17. The presence of the Mg_{Al} defect causes distortion in the environment immediately surrounding the antisite defect, therefore, there is a distribution in the migration energies compared with the isolated $Mg_i^{\bullet\bullet}$ defect.

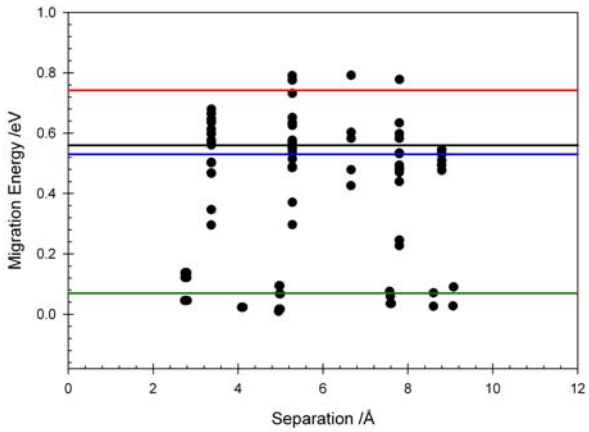

Figure 7.17: Plot showing the migration energy as a function of the separation between a $Mg_i^{\bullet\bullet}$ defect and a Mg_{Al} defect. The horizontal lines represent the migration energies for the isolated $Mg_i^{\bullet\bullet}$ diffusion processes, the red line represents the inplane (figure 5.16(b)), the black line is the migrate and twist mechanism (figure 5.16(c)), the blue line represents the rearrangement process (figure 5.16(a)) and the green line represents the activation energy to escape from the intermediate stage entered during the migrate and twist mechanism.

Influence of an Mg_{Al} defect on migration of an $Al_i^{\bullet\bullet\bullet}$ defect

The presence of an Mg_{Al} defect does not act to stabilise the $Al_i^{\bullet\bullet\bullet}$-$V_{Mg}$-$Mg_i^{\bullet\bullet}$ defect. That is, the cluster is predicted to decay within 22.76 ps to form an $Al_{Mg}^{\bullet}$ defect and an $Mg_i^{\bullet\bullet}$-V_{Mg}-$Mg_i^{\bullet\bullet}$ defect. Once the $Al_i^{\bullet\bullet\bullet}$ defect has decayed, the $Mg_i^{\bullet\bullet}$-V_{Mg}-$Mg_i^{\bullet\bullet}$ diffuses away from the $Al_{Mg}^{\bullet}$ defect, however, it is then attracted to the Mg_{Al} defect. Figure 7.18 shows a trace of the evolution of a spinel supercell containing an $Al_i^{\bullet\bullet\bullet}$ defect and an Mg_{Al} defect for 0.35 ns.

The variation in the separation between the Mg_{Al} defect and $Mg_i^{\bullet\bullet}$ defect, resulting from the collapse of the $Al_i^{\bullet\bullet\bullet}$ defect, is plotted as a function of simulation time in figure 7.19. Once the $Al_i^{\bullet\bullet\bullet}$ defect has decayed the cell contains the stationary (at least on the timescale of this

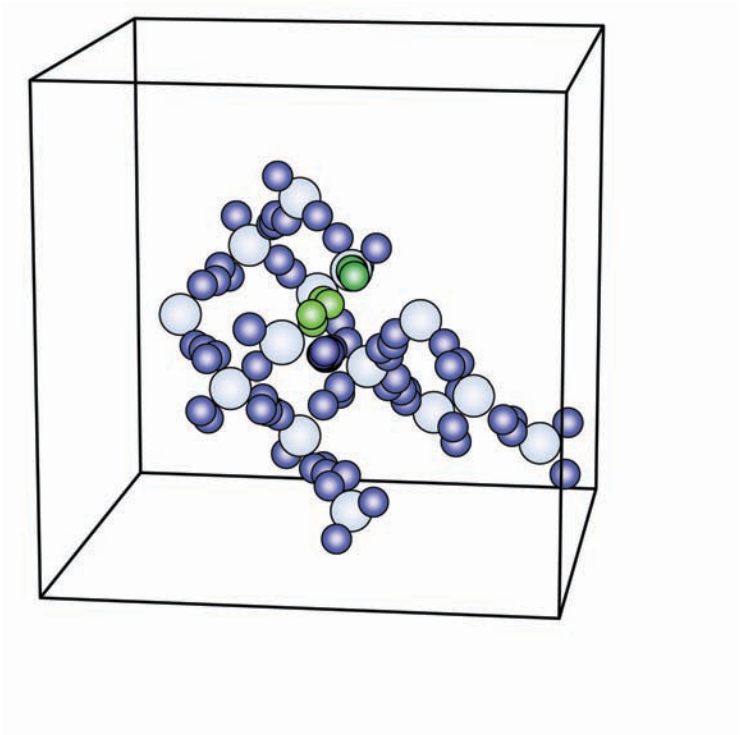

Figure 7.18: Trace of a long timescale evolution of a spinel supercell containing a Mg_{Al} and an $Al_i^{\bullet\bullet\bullet}$ defect.

simulation) Mg_{Al} and $Al_{Mg}^{\bullet}$ defects in a nearest neighbour configuration and a $Mg_i^{\bullet\bullet}$ defect. Initially, the $Mg_i^{\bullet\bullet}$ defect is repelled by the $Al_{Mg}^{\bullet}$ defect and so moves around to become bound with the Mg_{Al}. The interaction between the $Mg_i^{\bullet\bullet}$ and Mg_{Al} defects is very similar to that observed in the $\{Mg_{Al}{:}Mg_i^{\bullet\bullet}\}^{\bullet}$ example shown in figure 7.14. Consequently, figure 7.19 is similar to that obtained for a supercell containing an Mg_{Al} defect and an $Mg_i^{\bullet\bullet}$ defect (figure 7.15). A plot of the probability distribution of the defects separation during the simulation is given in 7.20, and this is again very similar to the $\{Mg_{Al}{:}Mg_i^{\bullet\bullet}\}^{\bullet}$ case (figure 7.16).

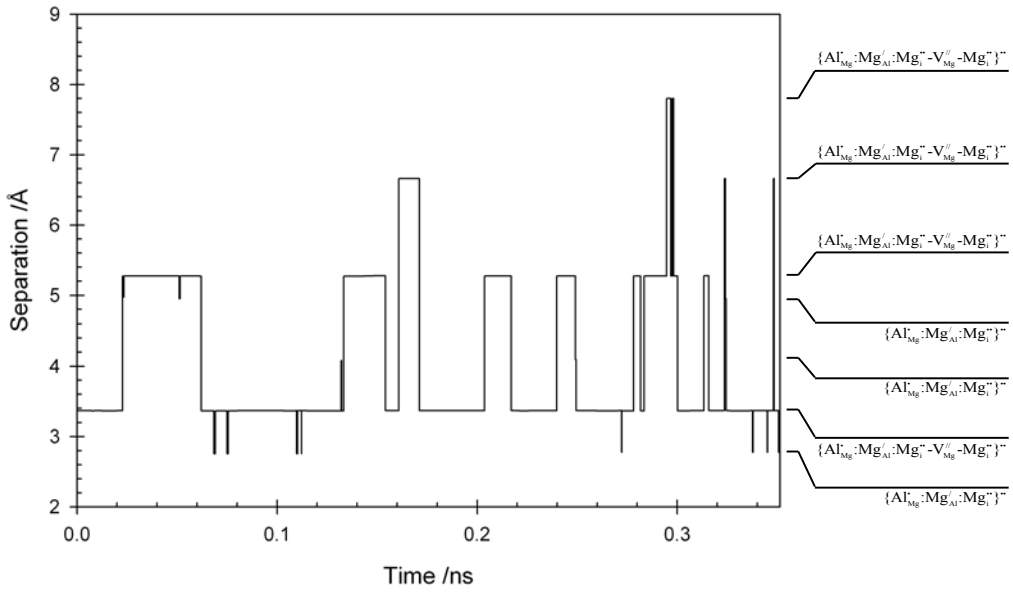

Figure 7.19: Plot of the defect separation as a function of the simulation time for a spinel supercell containing a Mg_{Al} and an $Al_i^{\bullet\bullet\bullet}$ defects.

An activation energy of 0.49 eV was obtained for the initial decay of the $Al_i^{\bullet\bullet\bullet}$-$V_{Mg}$-$Mg_i^{\bullet\bullet}$ split interstitial to form the $Al_{Mg}^{\bullet}$ and $Mg_i^{\bullet\bullet}$-V_{Mg}-$Mg_i^{\bullet\bullet}$ defects. After the $Al_i^{\bullet\bullet\bullet}$-$V_{Mg}$-$Mg_i^{\bullet\bullet}$ defect has decayed the simulation continues to follow the migration of an $Mg_i^{\bullet\bullet}$ defect within the strain field of an antisite pair. The presence of the $Al_{Mg}^{\bullet}$ defect increases the variation in the migration energies for the $Mg_i^{\bullet\bullet}$ defect (figure 7.17) compared to an $Mg_i^{\bullet\bullet}$ defect migrating within the strain field of an Mg_{Al} (figure 7.21), particularly at smaller separations.

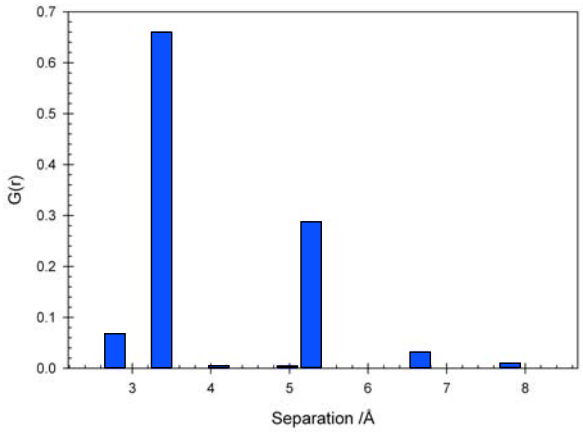

Figure 7.20: Plot of the probability distribution, G(r), as a function of the separation between a Mg_{Al} and an $Mg_i^{\bullet\bullet}$ defect.

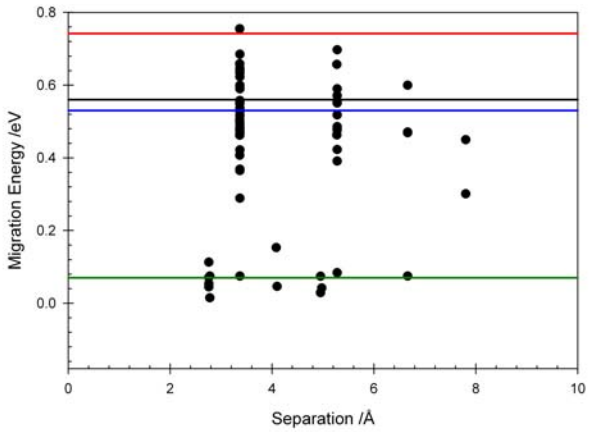

Figure 7.21: Plot of the migration energies as a function of the separation between the Mg_{Al} defect and the $Mg_i^{\bullet\bullet}$ interstitial formed as a result of the $Al_i^{\bullet\bullet\bullet}$ defect decaying. The horizontal lines represent the migration energies for the isolated $Mg_i^{\bullet\bullet}$ diffusion processes, the red line represents the the inplane (figure 5.16(b)), the black line is the migrate and twist mechanism (figure 5.16(c)), the blue line represents the rearrangement process (figure 5.16(a)) and the green line represents the activation energy to escape from the intermediate stage entered during the migrate and twist mechanism.

Influence of an Mg_{Al} defect on migration of a $V_O^{\bullet\bullet}$ defect

The final intrinsic defect/antisite pair to be investigated is that of $V_O^{\bullet\bullet}$ diffusion in a supercell also containing an Mg_{Al} defect. Figure 7.22 shows how this supercell evolves during the 0.28 ms simulation. As was the case in each of the previous cluster simulations the antisite defect is not observed to diffuse over the timescale of the simulation and the $V_O^{\bullet\bullet}$ defect migrates around it. From figure 7.22 it appears that the $V_O^{\bullet\bullet}$ defect is only very weakly bound to the Mg_{Al} defect as it visits several lattice sites in the second and third nearest neighbour configurations, however, the duration of time spent in these configurations is actually very small, as shown in figures 7.23 and 7.24. The nearest neighbour configuration, in which the Mg_{Al} defects and $V_O^{\bullet\bullet}$ are separated by 1.90 Å, is the lowest energy configuration observed in the simulations. Then the second nearest neighbour configuration is 0.24 eV higher in energy and the third and fourth nearest neighbours are 0.91 and 0.78 eV higher in energy. Since the migration energies to 'hop' from the first nearest neighbour to either second, third and forth nearest neighbours are high (1.38, 1.90 and 1.82 eV respectively), the average lifetime of the nearest neighbour configuration is large, 4.98 ns.

Figure 7.25 is a comparison of the migration energies for $V_O^{\bullet\bullet}$ migration when isolated and in the presence of an Mg_{Al} defect. The migration energies observed in the simulation containing the Mg_{Al} defect show significant deviation from the migration energies obtained for the isolated $V_O^{\bullet\bullet}$ defect. In the vacancy or interstitial defect/antisite clusters discussed previously, the presence of the antisite defect creates a distribution in the migration energies centred about the migration energy for the defect in isolation, however, for oxygen defects the antisite defect modifies the $V_O^{\bullet\bullet}$ migration energies such that they cannot be easily assigned to a similar processes observed for the isolated oxygen defect. This is probably due to the significant distortion of the oxygen sublattice resulting from the introduction of the antisite defect. Combined with the high binding energies predicted between oxygen defects and the oppositely charged antisite defect (chapter 4) this suggests that oxygen diffusion may be particularly sensitive to the level of inversion present in a spinel material.

All of the previous cluster simulations have examined the interaction between an antisite defect and vacancy or interstitial defects. In general, these simulations have all demonstrated very similar behaviour, ie. the antisite defect is immobile and the vacancy or interstitial defect migrates around it to varying degrees, dependent on the specific defects involved. This suggests

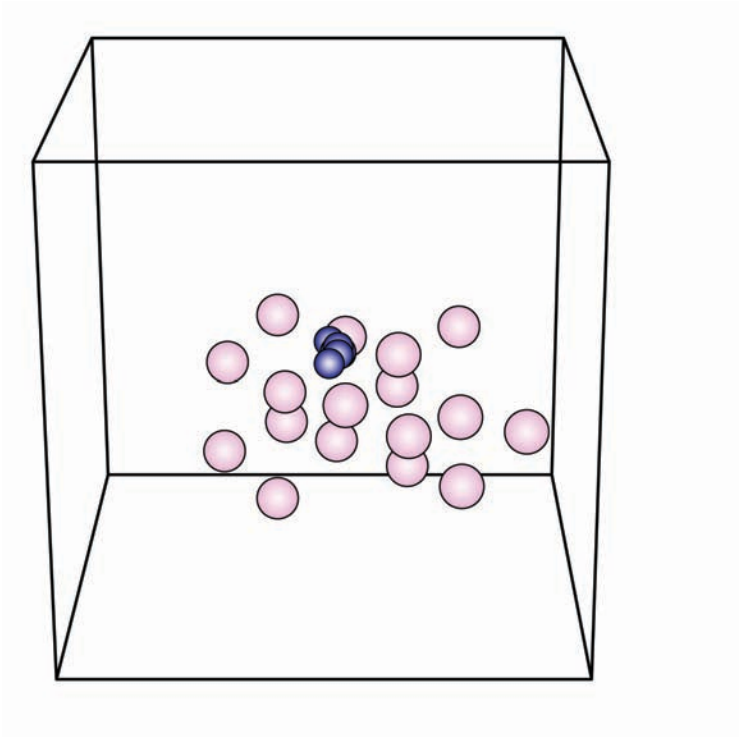

Figure 7.22: Trace of a long timescale evolution of a spinel supercell containing a Mg_{Al} and an $V_O^{\bullet\bullet}$ defect.

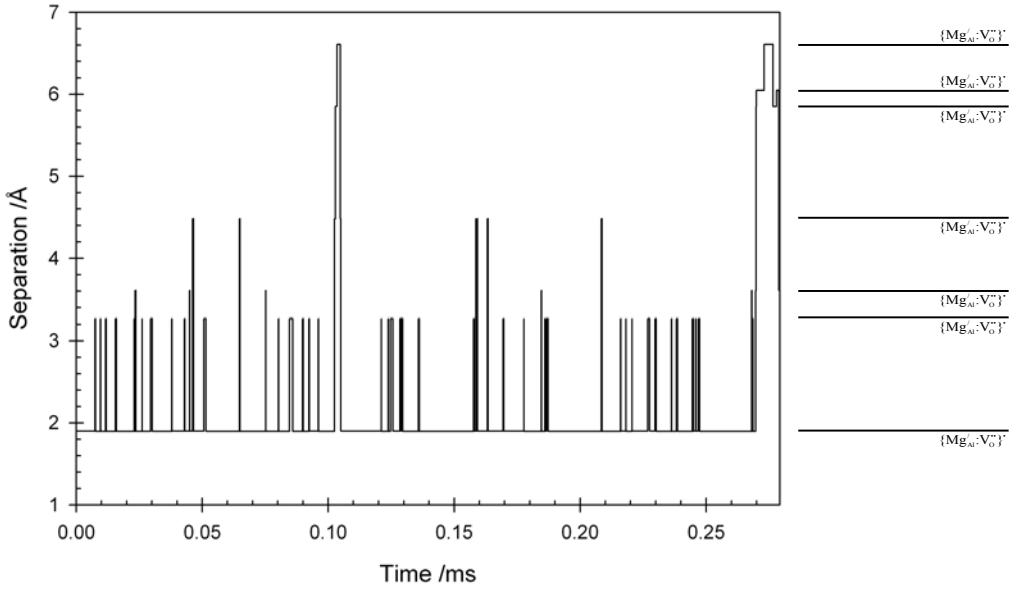

Figure 7.23: Plot of the defect separation as a function of the simulation time for a spinel supercell containing an Mg_{Al} and a $V_O^{\bullet\bullet}$ defect.

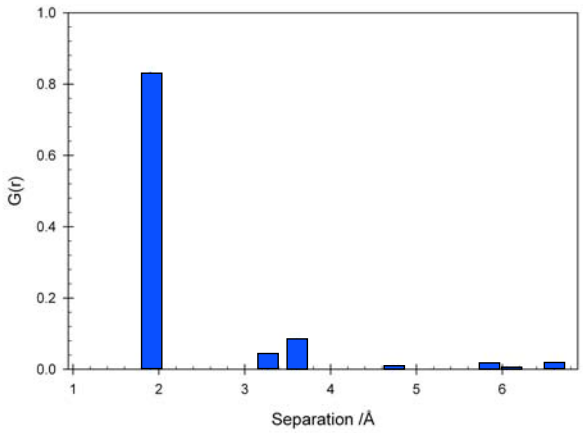

Figure 7.24: Plot of the probability distribution, G(r), as a function of the separation between a Mg_{Al} and an $V_O^{\bullet\bullet}$ defect.

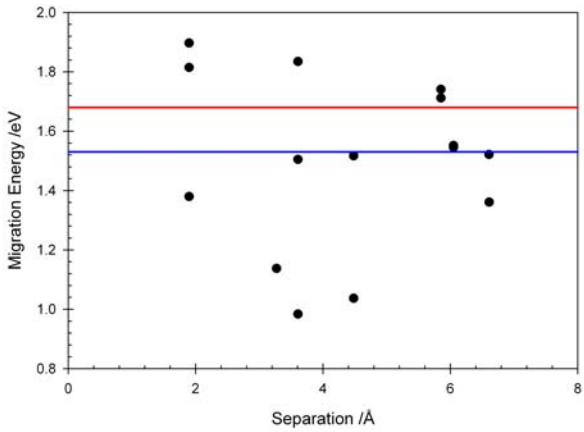

Figure 7.25: Plot of the migration energies as a function of the separation between an $V_O^{\bullet\bullet}$ defect and a Mg_{Al} defect. The horizontal lines represent the migration energies for the isolated $V_O^{\bullet\bullet}$ diffusion processes.

that mass transport will decrease as the level of inversion present in a crystal increases, due to the antisite defects acting to trap the other defects that facilitate diffusion. Furthermore, this has implications from a radiation damage perspective, because diffusion of defects is an essential aspect of interstitial-vacancy point defect recombination. If vacancy and interstitial defects are unable to diffuse through the lattice, because they have become trapped by an antisite defect, they will be unable to recombine with each other and so the number of defects retained will be higher. When Bacorisen *et al.* [74] performed MD cascade simulations in $MgAl_2O_4$, $MgGa_2O_4$ and $MgIn_2O_4$, they found that more damage was retained in the more inverted $MgGa_2O_4$ and $MgIn_2O_4$ than in the perfect, $MgAl_2O_4$ spinel. Of course in the simulations of Bacorisen *et al.* [74] they also changed the chemistry of the spinel material as well as the level of inversion so it difficult to be definitive. Clearly, it would be desirable to repeat these simulations on $MgAl_2O_4$ with levels of inversion relevant to real spinel crystals.

Whilst it is expected that clusters formed from antisite defects and interstitial/vacancy defects will dominate, there are a number of other clusters which can form from combinations of the interstitial and vacancy defects. These have also been investigated using TAD.

Mutual interactions between diffusing $V_O^{\bullet\bullet}$ and V_{Mg} defects

In the simulation shown in figure 7.26 the V_{Mg} and $V_O^{\bullet\bullet}$ defects were placed 10.15 Å apart in the spinel supercell. Initially, the V_{Mg} defect migrates towards the $V_O^{\bullet\bullet}$ defect, which is effectively stationary during the 0.59 ps taken for the magnesium vacancy to enter a second nearest neighbour configuration. The total duration of the simulation shown in figure 7.26 is 8.35 ms. A plot of the separation between the two vacancies as a function of the simulation time is given in figure 7.27 and it shows that the separation decreases very rapidly at the start of the simulation until the defects are adjacent to each other. This nearest neighbour arrangement of the $\{V_O^{\bullet\bullet}{:}V_{Mg}\}$ cluster represents the lowest energy configuration and the second nearest neighbour configuration is 1.93 eV higher in energy. It is because of this large difference in the energies of the first and second nearest neighbour states coupled with the large migration energy to leave the nearest neighbour configuration (2.04 eV) and the very small migration energy to move from the second nearest neighbour configuration to a nearest neighbour configuration that gives rise to the probability distribution shown in figure 7.28.

At roughly 3.6 ms an Al^{3+} cation moves off of it site and forms a V_{Al}-$Al_i^{\bullet\bullet\bullet}$-$V_{Mg}$ defect cluster then the $Al_i^{\bullet\bullet\bullet}$ defect then falls back onto the vacant aluminium site. The migration energy for the Al^{3+} cation to migrate from its lattice site is 2.97 eV. Overall, however, the cluster does not undergo net transport.

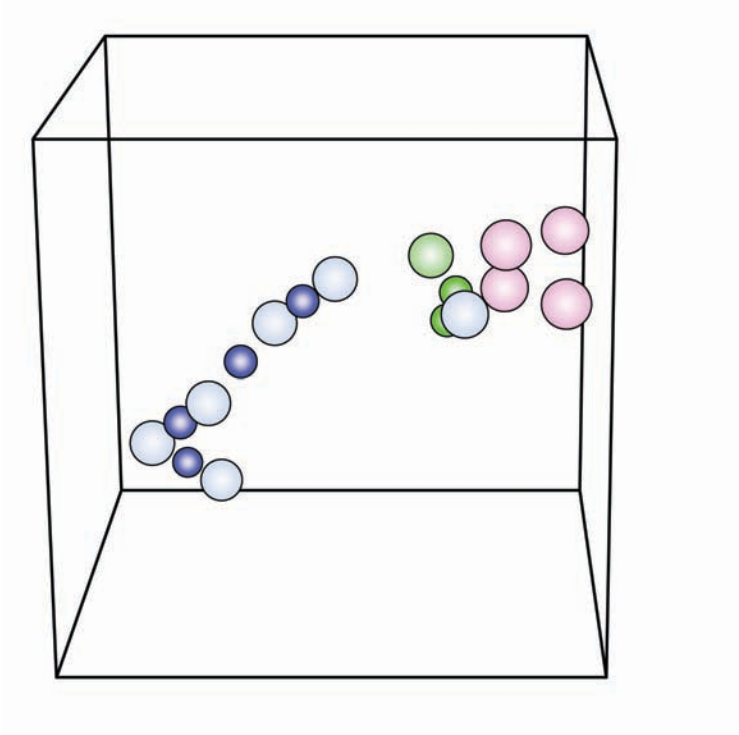

Figure 7.26: Trace of the long timescale evolution of a spinel supercell containing a V_{Mg} and an $V_O^{\bullet\bullet}$ defect.

The migration energy as a function of the separation between the defects is presented in figure 7.29. Clearly as the only defect to perform any 'hops' at larger separations is the V_{Mg} defect the migration energies are similar to the migration energies for an isolated V_{Mg} defect. At smaller separations the $V_O^{\bullet\bullet}$ defect is also observed to migrate with an migration energy of 2.04 eV and a neighbouring aluminium cation is observed to move off its lattice site with a barrier of 2.97 eV.

Mutual interactions between diffusing $V_O^{\bullet\bullet}$ and V_{Al} defects

Figure 7.30 shows the evolution of a spinel supercell containing V_{Al} and $V_O^{\bullet\bullet}$ defects for a duration of 63 ns. The V_{Al} and $V_O^{\bullet\bullet}$ defects are initially separated by 9.28 Å. During the

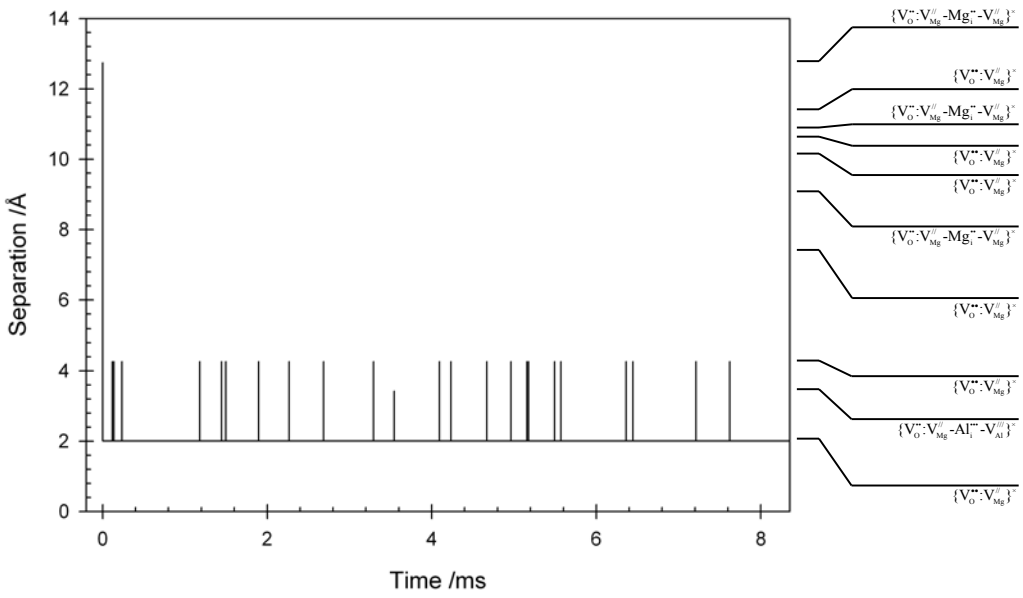

Figure 7.27: Plot of the defect separation as a function of the simulation time for a spinel supercell containing a V_{Mg} and an $V_O^{\bullet\bullet}$ defect.

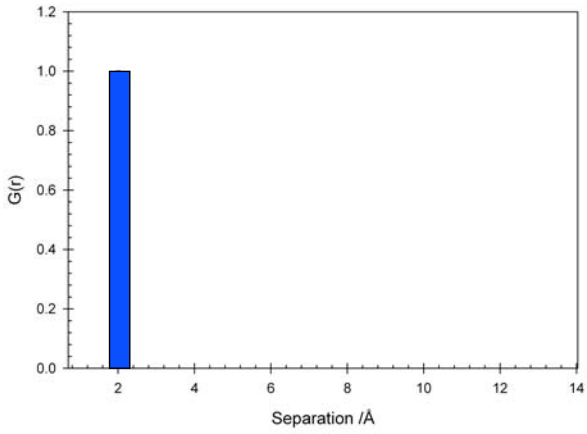

Figure 7.28: Plot of the probability distribution, G(r), as a function of the separation between the defects in a supercell containing a V_{Mg} and an $V_O^{\bullet\bullet}$ defect.

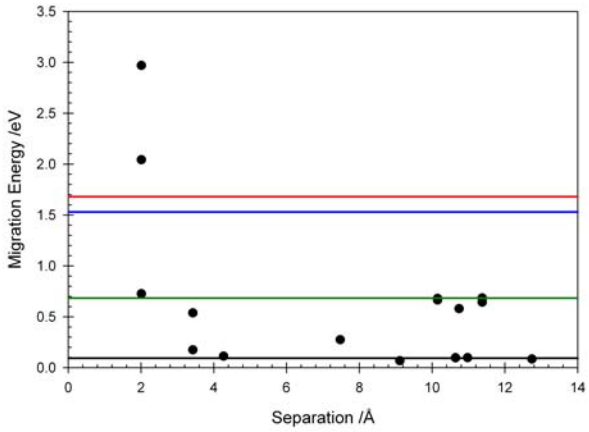

Figure 7.29: Plot of the migration energy as a function of the separation between an $V_O^{\bullet\bullet}$ defect and a Mg_{Al} defect. The horizontal lines represent the migration energies for the isolated $V_O^{\bullet\bullet}$ and V_{Mg} diffusion processes. The red and blue lines represent the migration energies for the $V_O^{\bullet\bullet}$ diffusion process and the green line represent the migration energy to reach the intermediate V_{Mg}-$Mg_i^{\bullet\bullet}$-V_{Mg} state and the black line is the migration energy to leave the intermediate state.

simulation the $V_O^{\bullet\bullet}$ defect migrates towards the effectively stationary V_{Al} defect until they enter a nearest neighbour configuration. There is a very significant Coulombic driving force for this process as the aluminium vacancy has a charge of -3 and the oxygen vacancy has a charge of +2. An indication of the very strong Coulombic interaction is demonstrated by the difference in energy of the nearest and and fourth nearest neighbour defect configurations of -3.30 eV. Once the defects are in a nearest neighbour configuration there were two migration processes detected. The first of these is for the Al^{3+} cation to migrate towards a second nearest neighbour configuration via an $Al_i^{\bullet\bullet\bullet}$-$V_{Mg}$-$Mg_i^{\bullet\bullet}$ intermediary with a migration energy of 1.23 eV and the second is for the oxygen vacancy to migrate to occupy a second nearest neighbour site with respect to the V_{Al} defect with a migration energy of 1.29 eV. Both of these configurations are short lived, therefore the nearest neighbour configuration is clearly the dominant configuration for the $\{V_O^{\bullet\bullet}{:}V_{Al}\}$ cluster (figure 7.32).

Figure 7.33 shows how the migration energy varies as a function of the separation between the defects. At larger separations the $V_O^{\bullet\bullet}$ defect migrates towards the V_{Al} defect with a migration energy between the two migration energies predicted for the isolated $V_O^{\bullet\bullet}$ defect. The red horizontal line plotted in figure 7.33 indicates the migration energy required for a V_{Al} defect form a V_{Al}-$Al_i^{\bullet\bullet\bullet}$-$V_{Al}$ intermediate state. Despite this transition being observed in the simula-

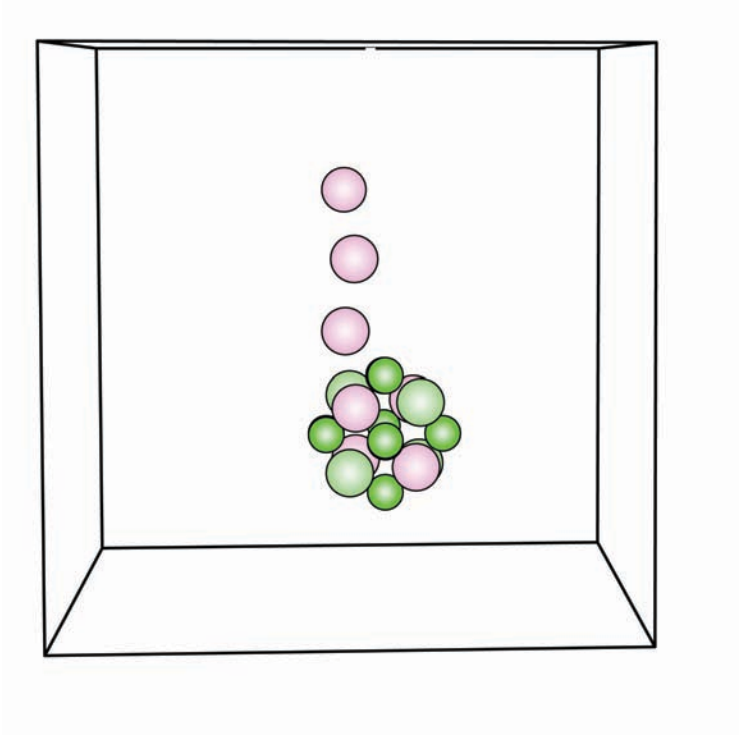

Figure 7.30: Trace of the long timescale evolution of a spinel supercell containing V_{Al} and $V_O^{\bullet\bullet}$ defects.

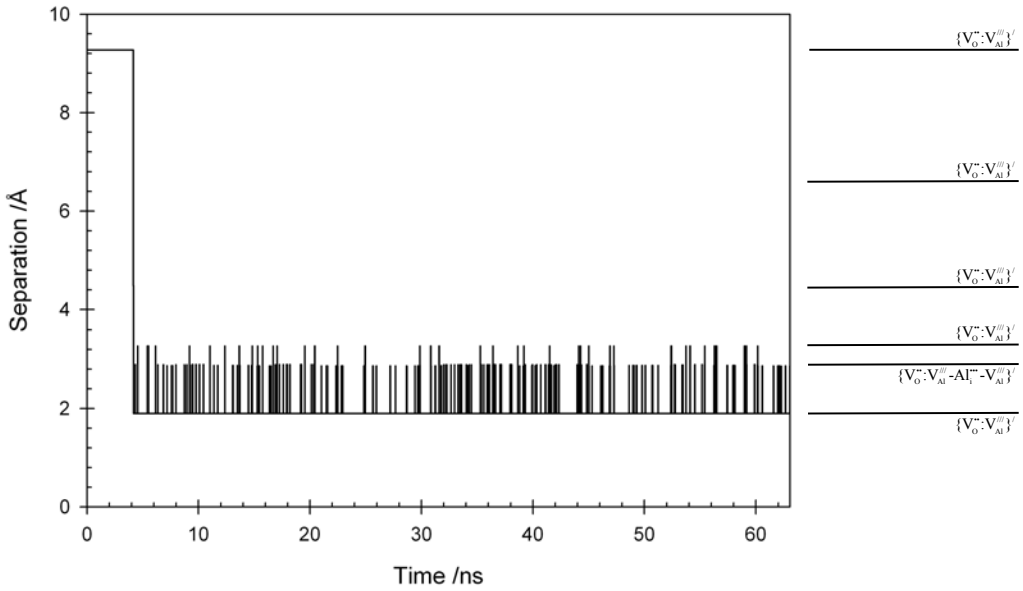

Figure 7.31: Plot of the defect separation as a function of the simulation time for a spinel supercell containing a V_{Al} and an $V_O^{\bullet\bullet}$ defects.

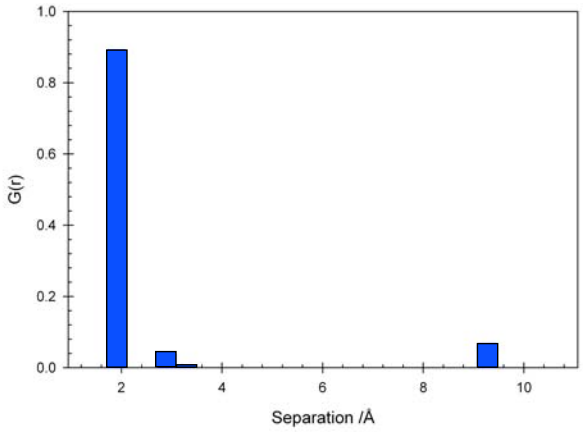

Figure 7.32: Plot of the probability distribution, G(r), as a function of the separation between the defects in a supercell containing V_{Al} and $V_O^{\bullet\bullet}$ defects.

tion shown in figure 7.33 there were no transitions observed in the simulation with migration energies close to this value. In fact the presence of the $V_O^{\bullet\bullet}$ defect reduces the migration energy to enter the intermediate state to 1.23 eV. This is further evidence of the significant effect that changes in the local environment can have on the migration energies for defect diffusion.

Mutual interactions between diffusing $Mg_i^{\bullet\bullet}$ and O_i defects

The evolution of a spinel supercell containing a $Mg_i^{\bullet\bullet}$ and an O_i defect, for a simulation time of 9.66 ns, is shown in figure 7.34: unlike any of the other clusters discussed, the cluster itself is mobile and able to move throughout the supercell. The exact mechanism for this process is complex but should be pictured as a 'tethered' hoping process whereby the more mobile O_i defect migrates around the $Mg_i^{\bullet\bullet}$ defect and then eventually the $Mg_i^{\bullet\bullet}$ defect hops and the O_i is dragged along. A brief summary showing six consecutive timesteps in the simulation is given in figure 7.35. In figure 7.35 the $Mg_i^{\bullet\bullet}$-V_{Mg}-$Mg_i^{\bullet\bullet}$ defect moves upwards across the cell as the O_i defect migrates around it. The migration energy for the $Mg_i^{\bullet\bullet}$ defect as predicted, in section 7.3.1, was 0.53 eV, however, the presence of the O_i defect leads to a small decrease in the migration energy to 0.49 eV.

The dominant configuration of the defects as they migrate through the lattice is a split $Mg_i^{\bullet\bullet}$-V_{Mg}-$Mg_i^{\bullet\bullet}$ with an octahedral O_i defect located 4.32 Å from the vacant magnesium site.

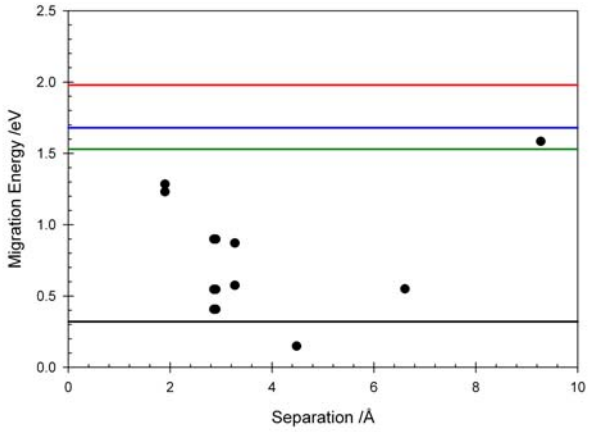

Figure 7.33: Plot of the migration energy as a function of the separation between an $V_O^{\bullet\bullet}$ defect and a V_{Al} defect. The horizontal lines represent the migration energies for the isolated $V_O^{\bullet\bullet}$ and V_{Al} diffusion processes, the red line is the migration energy to enter the intermediate, V_{Mg}-$Al_i^{\bullet\bullet\bullet}$-$V_{Mg}$, state and the blue and green lines are the $V_O^{\bullet\bullet}$ diffusion migration energies.

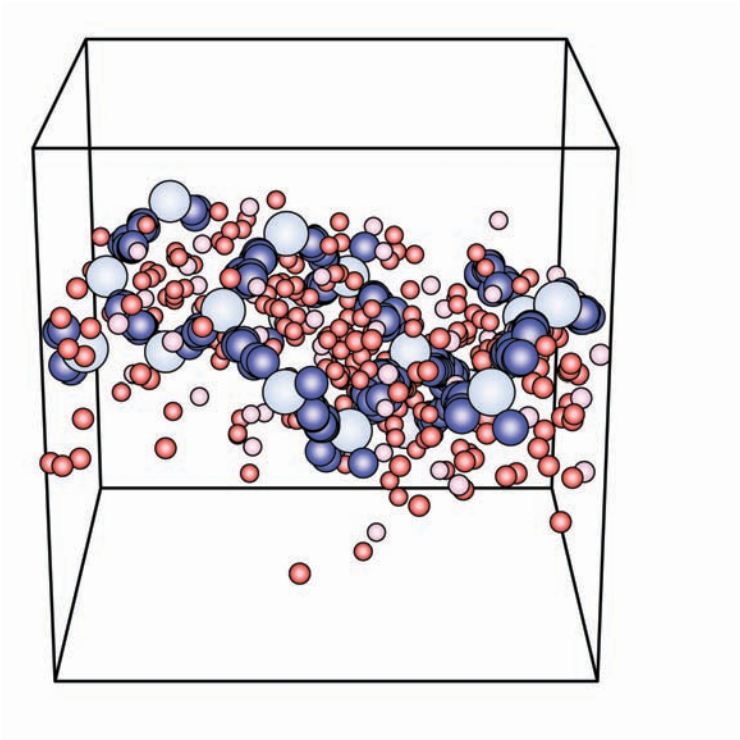

Figure 7.34: Trace of the long timescale evolution of a spinel supercell containing a $Mg_i^{\bullet\bullet}$ and an O_i defect.

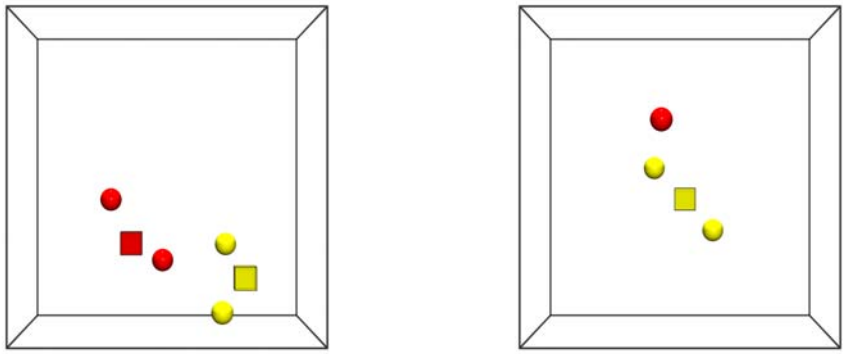

(a) Step 1

(b) Step 2

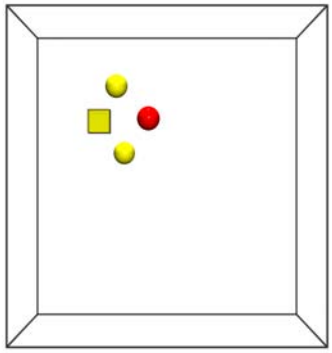

(c) Step 3

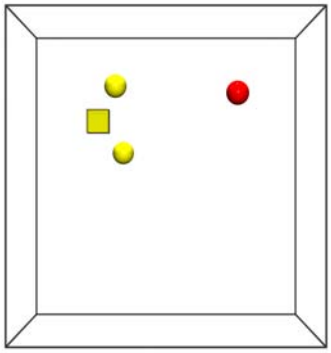

(d) Step 4

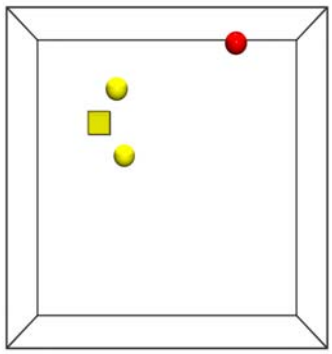

(e) Step 5

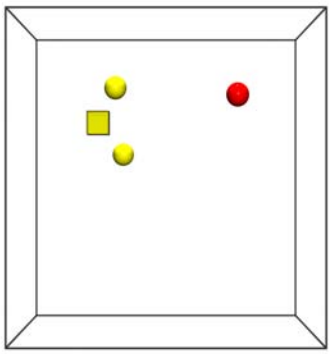

(f) Step 6

Figure 7.35: Six consecutive steps in the simulation of a spinel simulation containing an O_i and a $Mg_i^{\bullet\bullet}$ defect. Figures (a)-(f) show the interplay between the O_i and $Mg_i^{\bullet\bullet}$ defects as they migrate in a cooperative, 'tethered' mechanism. The red spheres represent oxygen interstitial ions, the red cube represents an oxygen vacancy, the yellow spheres represent magnesium interstitial ions and the transparent yellow cube represents a magnesium vacancy.

Both the O_i and $Mg_i^{\bullet\bullet}$ defects form complex split interstitial structures aligned along the 110 directions, therefore, their interaction energy is not merely dependant on the separation between them but also their relative orientations. A plot showing how the separation between the defects changes as a function of simulation time is given in figure 7.36. Initially the defects are situated 4.51 Å apart in an $\{O_i : Mg_i^{\bullet\bullet}\text{-}V_{Mg}\text{-}Mg_i^{\bullet\bullet}\}$ configuration. For the first 85 ps the separation between the defects alternate between this initial defect configuration and an $\{O_i\text{-}V_0^{\bullet\bullet}\text{-}O_i : Mg_i^{\bullet\bullet}\text{-}V_{Mg}\text{-}Mg_i^{\bullet\bullet}\}$ configuration where the vacancy defects are separated by 6.09 Å. After 85 ps the cluster enters a $\{O_i : Mg_i^{\bullet\bullet}\text{-}V_{Mg}\text{-}Mg_i^{\bullet\bullet}\}$ configuration where the defects are separated by 4.32 Å. The presence of two very similar defect clusters with only a slight difference in the separation between them arises as a result of the slight distortion in oxygen sublattice associated with the oxygen *u* parameter. The dominant configuration of the defects as they migrate through the lattice is a split $Mg_i^{\bullet\bullet}\text{-}V_{Mg}\text{-}Mg_i^{\bullet\bullet}$ with an octahedral O_i defect located 4.32 Å from the vacant magnesium site (figure 7.37).

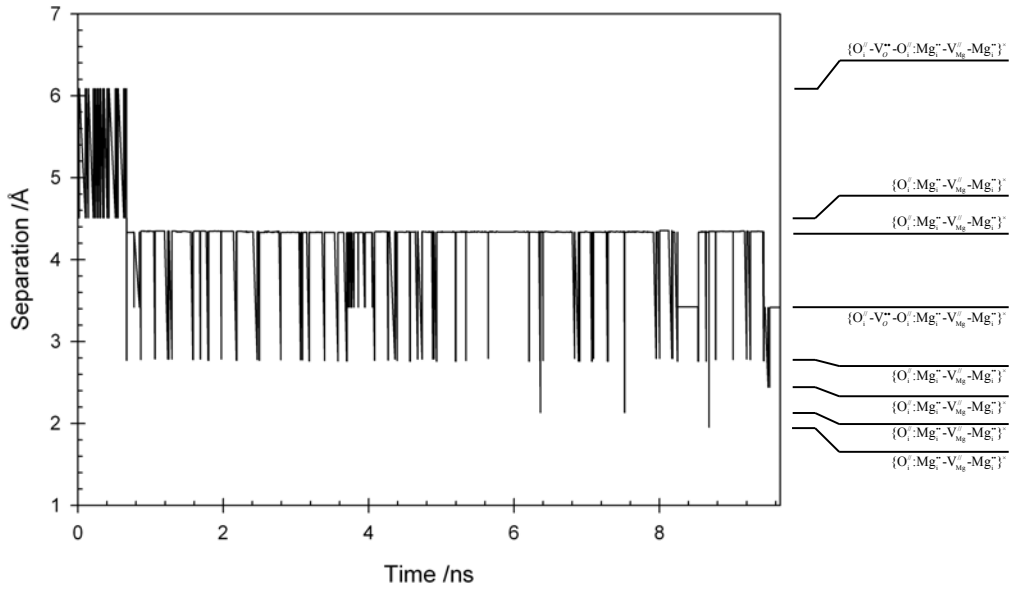

Figure 7.36: Plot of the defect separation as a function of the simulation time for a spinel supercell containing a $Mg_i^{\bullet\bullet}$ and an O_i defect.

A comparison between the migration energies of the isolated O_i and $Mg_i^{\bullet\bullet}$ defects and the defects in the supercell shown in figure 7.34 is given in figure 7.38. As the majority of the migration processes that occur during the simulation involve the O_i defect the migration energies

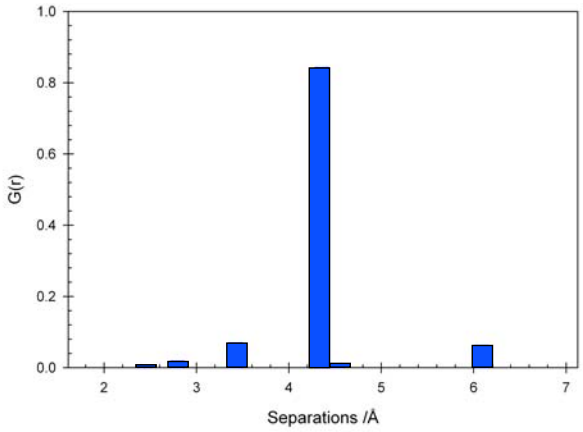

Figure 7.37: Plot of the probability distribution, G(r), as a function of the separation between the defects in a supercell containing a $Mg_i^{\bullet\bullet}$ and an O_i defect.

are predominantly distributed around the green line representing the isolated O_i defect migration. There are a number of processes with higher energy barriers, corresponding to either the $Mg_i^{\bullet\bullet}$ inplane process (figure 5.16(b)) or the O_i rearrangement processes, however, in general it suggests that the presence of the O_i defect acts to reduce the migration energy for $Mg_i^{\bullet\bullet}$ diffusion in spinel. This cooperative diffusion process is similar to that observed by Uberuaga *et al.* [137, 143] for interstitial clusters in MgO.

Mutual interactions between diffusing $Al_i^{\bullet\bullet\bullet}$ and O_i defects

The final defect cluster to be examined is the $\{Al_i^{\bullet\bullet\bullet}{:}O_i\}^{\bullet}$ cluster. In previous examples the $Al_i^{\bullet\bullet\bullet}$-$V_{Mg}$-$Mg_i^{\bullet\bullet}$ interstitial defect has proven to be unstable and decay to form an $Al_{Mg}^{\bullet}$ defect and an $Mg_i^{\bullet\bullet}$-V_{Mg}-$Mg_i^{\bullet\bullet}$ defect. As shown in figure 7.39 the presence of the O_i defect is not sufficient to stabilise the $Al_i^{\bullet\bullet\bullet}$-$V_{Mg}$-$Mg_i^{\bullet\bullet}$ defect and so it decays within the first 0.19 ns of the 1.5 ns simulation. After the $Al_i^{\bullet\bullet\bullet}$ defect has collapsed, the cell contains an $Al_{Mg}^{\bullet}$, an O_i and an $Mg_i^{\bullet\bullet}$ defect. Once it has formed, the $Al_{Mg}^{\bullet}$ defect is not seen to move throughout the remainder of the simulation, however, it does serve to 'anchor' the O_i interstitial defect thereby inhibiting the cooperative $\{O_i{:}Mg_i^{\bullet\bullet}\}$ cluster diffusion mechanism described above. The separation between the O_i defect and the $Mg_i^{\bullet\bullet}$ defect as a function of the simulation time is shown in figure 7.40 and is very similar the pattern obtained for the $\{O_i{:}Mg_i^{\bullet\bullet}\}$ cluster without the

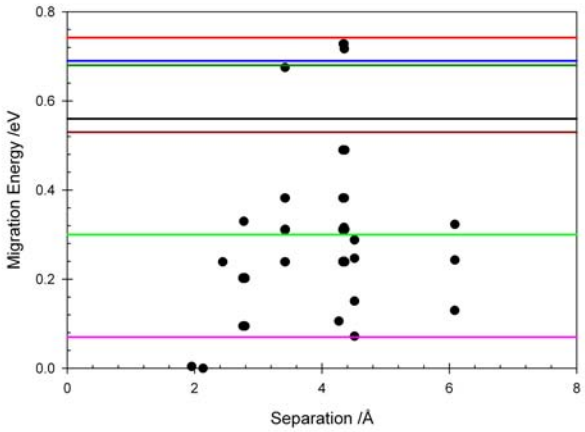

Figure 7.38: Plot of the migration energies as a function of the separation between an O_i defect and a $Mg_i^{\bullet\bullet}$ defect. The horizontal lines represent the migration energies for the isolated O_i and $Mg_i^{\bullet\bullet}$ diffusion processes: the red line is the migration energy for the migrate in plane, $Mg_i^{\bullet\bullet}$ mechanism (figure 5.16(b)), the blue and green lines are the O_i rotation mechanisms, the black and brown lines represent the migrate and twist mechanism (figure 5.16(c)) and the rearrangement process (figure 5.16(a)) and the light green line is the linear O_i migration energy and finally the pink line is the migration energy to escape from the intermediate state which is part of the $Mg_i^{\bullet\bullet}$ migrate and twist process.

antisite defect nearby, shown in figure 7.36. The dominant configuration for the O_i and $Mg_i^{\bullet\bullet}$ defects is for them to be in a second nearest neighbour (figure 7.41) configuration, similar to the $\{O_i : Mg_i^{\bullet\bullet}\}$ cluster.

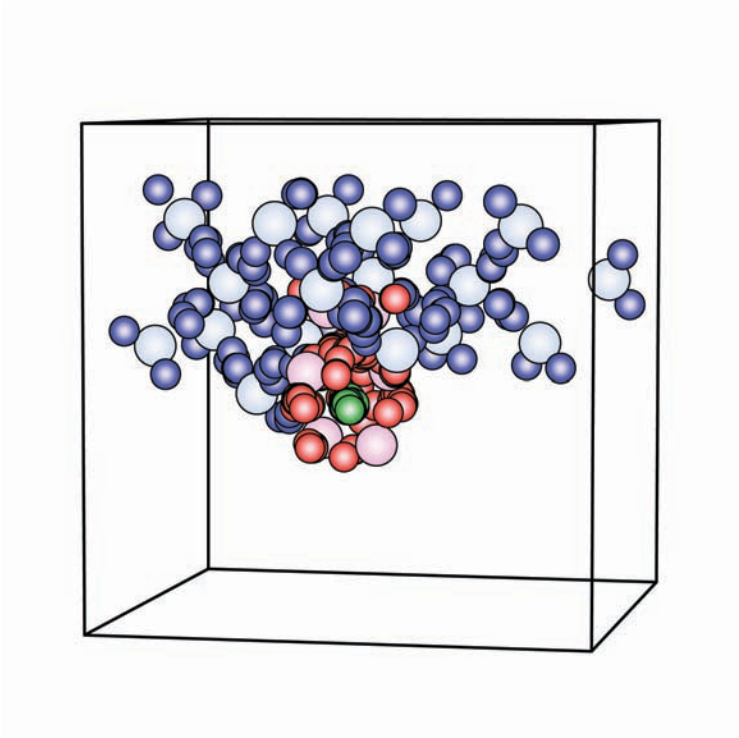

Figure 7.39: Trace of the long timescale evolution of a spinel supercell containing an $Al_i^{\bullet\bullet\bullet}$ and an O_i defect.

Figure 7.42 shows how the separation between the O_i and the $Mg_i^{\bullet\bullet}$ defect affects their migration energy. The distribution of the migration energies is increased compared to an isolated $\{O_i : Mg_i^{\bullet\bullet}\}$ cluster due to the presence of the $Al_{Mg}^{\bullet}$ defect. More interesting is the appearance of several higher energy migration processes that appear unrelated to the isolated diffusion process of the O_i and $Mg_i^{\bullet\bullet}$ defects. The highest energy migration process (1.27 eV) found in the simulation shown in figure 7.39 represents a realignment of the $Mg_i^{\bullet\bullet}$-V_{Mg}-$Mg_i^{\bullet\bullet}$ defect, very similar to isolated $Mg_i^{\bullet\bullet}$ rearrangement process (0.72 eV). This clearly demonstrates the affect that the presence of other point defects can have on the diffusion processes responsible for mass transport in a complex oxide material, such as spinel.

The migration energies, E_m, quoted in table 7.1 represent the energies required for the migration of the intrinsic point defects in an otherwise perfect spinel crystal, however, in a real

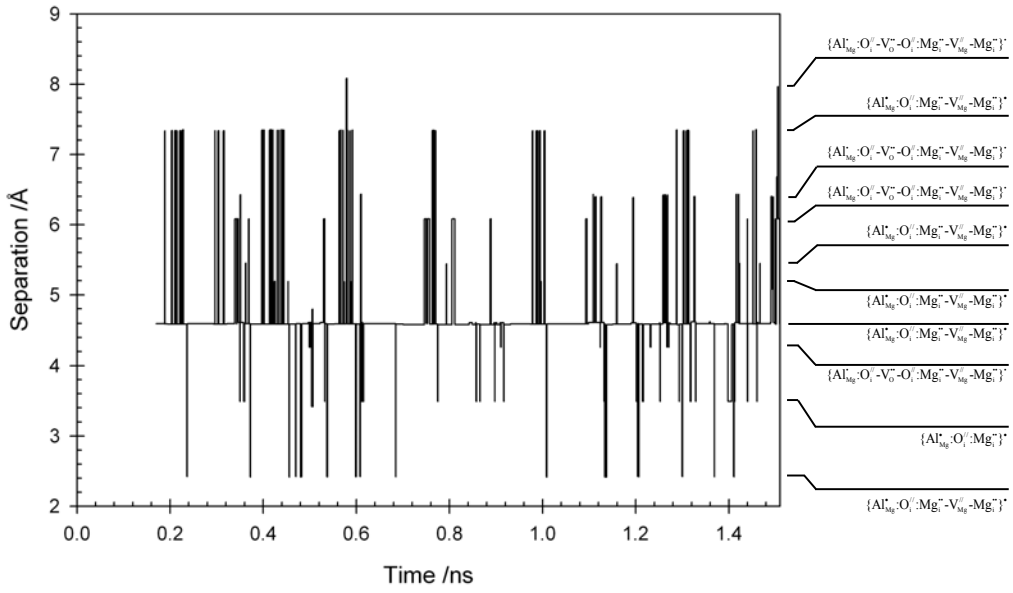

Figure 7.40: Plot of the defect separation as a function of the simulation time for a spinel supercell containing an $Al_i^{\bullet\bullet\bullet}$ and an O_i defect.

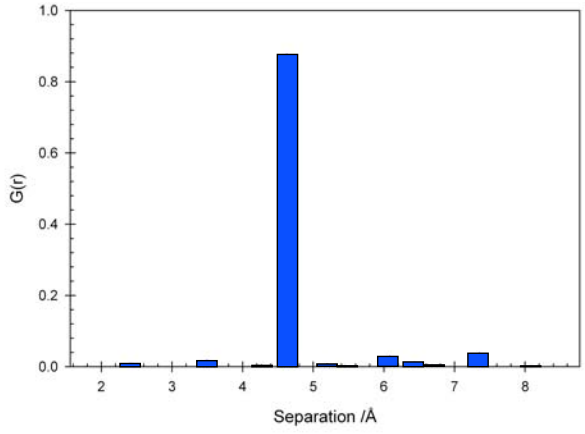

Figure 7.41: Plot of the probability distribution, G(r), as a function of the separation between the defects in a supercell containing an $Al_i^{\bullet\bullet\bullet}$ and an O_i defects. After the $Al_i^{\bullet\bullet\bullet}$-$V_{Mg}$-$Mg_i^{\bullet\bullet}$ defect has collapsed the separation is measured between the Mg_{Al} and the resultant $Mg_i^{\bullet\bullet}$ defect.

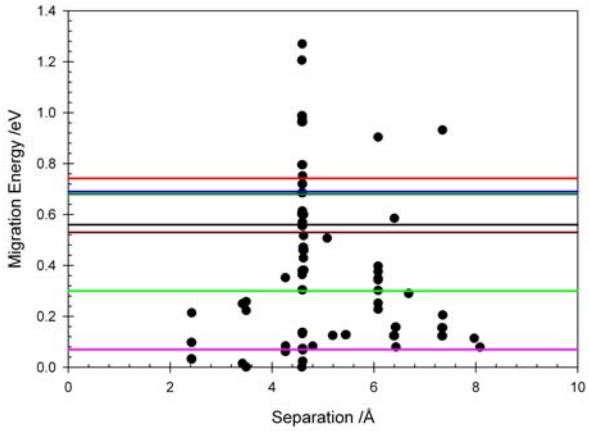

Figure 7.42: Plot of the migration energy as a function of the separation for an O_i defect and an $Mg_i^{\bullet\bullet}$ defect (the $Mg_i^{\bullet\bullet}$ defect is the result of the decay of the $Al_i^{\bullet\bullet\bullet}$-$V_{Mg}$-$Mg_i^{\bullet\bullet}$ defect). The horizontal lines represent the migration energies for the isolated O_i and $Mg_i^{\bullet\bullet}$ diffusion processes: the red line is the migration energy for the migrate inplane, $Mg_i^{\bullet\bullet}$ mechanism (figure 5.16(b)), the blue and green lines are the O_i rotation mechanisms, the black and brown lines represent the migrate and twist mechanism (figure 5.16(c)) and the rearrangement process (figure 5.16(a)) respectively, and the light green line is the linear O_i migration energy and finally the pink line is the migration energy to escape from the intermediate state, which is part of the $Mg_i^{\bullet\bullet}$ migrate and twist process.

material there will be a degree of cation inversion that can, as suggested above, have a significant impact on defect diffusion. Should a point defect become trapped by a highly immobile antisite defect then it will no longer be able to continue to facilitate mass transport until it has become dissociated from the antisite and is free to move. In order to become dissociated from the antisite defect, sufficient energy is required to overcome the energy that binds them together. Therefore, an approximation to the migration energy in a real material can be given by summing the isolated migration energy and the binding energy. These clustered E_m values are given in table 7.2.

In the isolated case the O_i defect was was the most mobile, however, due to the large binding energy present between it and the $Al^{\bullet}_{Mg}$ defect this model predicts in a real material containing a significant concentration of antisite defects the V_{Mg} defect will be most mobile. Effectively, at negligible levels of inversion (and assuming the concentration of the V_{Mg} and O_i defects was the same) oxygen is predicted to be the most mobile ion in spinel. At higher levels of inversion, however, the magnesium cation is predicted to be more mobile. Independent of the level of inversion present in the crystal the aluminium cation is predicted to be the least mobile.

Table 7.2: Comparison of isolated and clustered migration energies for defect migration in spinel. The clustered migration energies are the sum of the isolated migration energies and the binding energies determined without a shell model in chapter 4.

Defects	Antisite Defect	Binding Energy /eV	Isolated E_m /eV	Clustered E_m /eV
V_{Mg}	$Al^{\bullet}_{Mg}$	-0.91	0.68	1.59
$Mg_i^{\bullet\bullet}$	Mg_{Al}	-1.24	0.53	1.77
V_{Al}	$Al^{\bullet}_{Mg}$	-1.72	1.98	3.7
$Al_i^{\bullet\bullet\bullet}$	Mg_{Al}	-1.82	*unstable*	*unstable*
$V_O^{\bullet\bullet}$	Mg_{Al}	-1.85	2.47	4.32
O_i	$Al^{\bullet}_{Mg}$	-2.36	0.30	2.66

7.4 Summary

The simulations presented in this chapter have highlighted the complexity introduced by considering the diffusion of clusters of point defects as opposed to isolated defects. Although it was only possible to investigate some very simple dimer defect clusters it is possible to offer

the following general predictions concerning the nature of defect cluster diffusion:

- The TAD simulations suggest that the Mg_{Al} and $Al^{\bullet}_{Mg}$ defects are extremely immobile, in fact, at no point in the simulations presented in this chapter were antisite defects shown to migrate from the sites on which they were placed at the start of the simulation. Also evident from the simulations is the attraction between the stationary antisite defects and the more mobile vacancy and interstitial defects responsible for mass transport in spinel. If the vacancy and interstitial defects become bound to the immobile antisite defects then they are clearly unable to facilitate diffusion. Therefore, at the concentrations described here, the simulations predict that the introduction of antisite disorder will retard mass transport. This observation is important with regards to spinel's radiation tolerance as it suggests that in a spinel with a high degree of inversion the defects created during a thermal energy spike are unable to migrate through the lattice and recombine, therefore, a higher level of damage will remain after irradiation. The efficiency of point defect recombination is central to spinel's radiation tolerance and therefore by introducing antisite defects and restarding the process spinel's tolerance to irradiation will be reduced.

- The above point appears to contradict the prediction in chapter 5, that the most favourable mechanism for Al^{3+} transport is via a vacancy mechanism on the magnesium sublattice (ie. the $Al^{\bullet}_{Mg}$ was not observed to migrate during the simulation). In both the model where polarisability was included (chapter 5) and the TAD simulations presented in this chapter it was predicted that the lowest migration energy for Al^{3+} diffusion is via a vacancy mechanism on the magnesium sublattice. For comparison, chapter 5 predicted a migration energy of 0.88 eV for the $Al^{\bullet}_{Mg}$ + V_{Mg} process and 1.83 eV for the V_{Al} process, the equivalent values obtained using the model that does not include polarisation are 1.18 eV and 1.72 eV. Clearly, therefore, it would be expected that the $Al^{\bullet}_{Mg}$ defect would 'hop' onto a neighbouring vacant magnesium site more regularly than a V_{Al} defect 'hops' onto a neighbouring aluminium site. During the simulation of a spinel supercell containing a V_{Al} defect, the average time for each V_{Al} hop is 15 ns, however, the $Al^{\bullet}_{Mg}$ defect was not observed to migrate during a simulation of duration 17.5 ns. One reason why the $Al^{\bullet}_{Mg}$ migration is retarded is due to the presence of other processes competing with the $Al^{\bullet}_{Mg} + V_{Mg}$ $V_{Mg} + Al^{\bullet}_{Mg}$ process. These competing processes see the V_{Mg} defect exchanging with neighbouring Mg_{Mg} ions and moving the V_{Mg} defect away from the $Al^{\bullet}_{Mg}$ defect. As the $Al^{\bullet}_{Mg}$ defect can only migrate when the V_{Mg} is on an adjacent magnesium site

this will impede Al^{3+} diffusion. The TAD simulation (shown in figure 7.2) predicts that, at 1500 K, the V_{Mg} defect spends only 11% of the simulation on a site adjacent to the $Al_{Mg}^{\bullet}$(figure 7.4), therefore the Al^{3+} can only attempt a 'hop' for 11% of the time. The factors responsible for the fraction of time spent in the nearest neighbour configuration include the relative energies of the different configurations and the relative migration energies to move between them. In chapter 5 the migration energy for the V_{Mg} defect to migrate to a second nearest neighbour site from the $Al_{Mg}^{\bullet}$ defect was predicted to be 0.53 eV (compared with 0.88 eV for the $Al_{Mg}^{\bullet}$ 'hop'). Excluding the effects of polarisation, however, the migration energy for the V_{Mg} migration to a second nearest neighbour site was 0.66 eV (compared with 1.18 eV for the $Al_{Mg}^{\bullet}$ 'hop'). As the processes are competing this suggests that the $Al_{Mg}^{\bullet}$ migration process is considerably less probable when the shell model is not employed, as is the case in the TAD simulations. One possible solution to this apparent contradiction would be to implement the shell model in the TAD code and then repeating the simulation of a spinel supercell containing an $Al_{Mg}^{\bullet}$ and V_{Mg} defect.

- As a result of the high binding energy between the O_i defect and the $Al_{Mg}^{\bullet}$ defect the O_i defect is no longer predicted to be the most mobile defect when considering migration in a sample containing some degree of cation inversion. In a sample with a significant degree of cation inversion this model predicts that the V_{Mg} defect will be the most mobile.

- The local distortion in the lattice resulting from a point defect's strain field can lead to significant spread in the energies of defect migration processes. In particular, the introduction of antisite defects can cause significant perturbation of the oxygen sublattice; coupled to the high binding energies between oxygen and antisite defects this suggests that oxygen diffusion is strongly dependant on the level of inversion present in the sample. Thus, when considering experimental measurements of the activation energy for diffusion it would be important to know the level of inversion, although the experimental values for oxygen diffusion [139–141] are all in very reasonable agreement with each other (the levels of inversion present in the experimental spinel crystals were not reported).

- In general defect clustering is predicted to act in a manner that is detrimental to mass transport, however, one notable exception was highlighted. The $\{O_i : Mg_i^{\bullet\bullet}\}$ defect cluster has a lower migration energy than an isolated $Mg_i^{\bullet\bullet}$ defect, that is, the presence

of the O_i defect acts to promote Mg^{2+} transport in spinel. This process is similar to the $\{O_i : Mg_i^{\bullet\bullet}\}$ interstitial cluster diffusion process observed by Uberuaga *et al.* [137, 143] in MgO. These complex migration processes would be very difficult to predict from the crystal structure and therefore it demonstrates the power of accelerated dynamical techniques, such as TAD, to predict complex diffusion mechanisms.

8

Nonstoichiometry in spinel

This work has been accepted for publication in Philosophical Magazine [144].

8.1 Introduction

The MgO-Al_2O_3 'pseudo binary' phase diagram [25] (shown in figure 2.9) exhibits only one intermediate phase, magnesium aluminate spinel, $MgAl_2O_4$. At temperatures below 1300 K, spinel is shown as a line compound, occurring at an exactly equimolar fraction of MgO and Al_2O_3 whilst above this temperature the spinel phase can exhibit considerable nonstoichiometry. Interestingly, the high temperature spinel phase field is not symmetric about the stoichiometric ratio, but accommodates a greater degree of Al_2O_3 than MgO excess. Such is the degree to which the spinel phase can accommodate excess alumina, that at 2200 K the spinel phase is still evident in the phase diagram at an mole fraction of 0.9 Al_2O_3 [25]. Furthermore, cubic γ-alumina has been shown to closely resemble a defect spinel spinel material [145].

Given the predominance of the antisite defect process, cation antisite defects play a central role in the accommodation of nonstoichiometry. These charged defects are compensated for by other, oppositely charged, point defects (but not their opposite cation antisite species, as that would not lead to a change in stoichiometry). In particular, spinel crystals with an Al_2O_3 excess are characterised by $Al_{Mg}^{\bullet}$ defects [146, 147], which can be charge compensated by either O_i , V_{Mg} or V_{Al} defects (see equations 8.1-8.3). MgO rich spinel crystals incorporate Mg_{Al} defects [148], charge compensated for by either $V_O^{\bullet\bullet}$, $Mg_i^{\bullet\bullet}$or $Al_i^{\bullet\bullet\bullet}$ (see equations 8.4-

8.6).

$$
\begin{aligned}
3Al_2O_3 + 2Mg_{Mg} \qquad & 2Al^{\bullet}_{Mg} + O_i + 2MgAl_2O_4 \\
& Al^{\bullet}_{Mg} + \{O_i : Al^{\bullet}_{Mg}\} + 2MgAl_2O_4 \\
& \{O_i : 2Al^{\bullet}_{Mg}\} + 2MgAl_2O_4
\end{aligned} \tag{8.1}
$$

$$
\begin{aligned}
4Al_2O_3 + 3Mg_{Mg} \qquad & 2Al^{\bullet}_{Mg} + V_{Mg} + 3MgAl_2O_4 \\
& Al^{\bullet}_{Mg} + \{V_{Mg} : Al^{\bullet}_{Mg}\} + 3MgAl_2O_4 \\
& \{V_{Mg} : 2Al^{\bullet}_{Mg}\} + 3MgAl_2O_4
\end{aligned} \tag{8.2}
$$

$$
\begin{aligned}
4Al_2O_3 + 3Mg_{Mg} + Al_{Al} \qquad & 3Al^{\bullet}_{Mg} + V_{Al} + 3MgAl_2O_4 \\
& 2Al^{\bullet}_{Mg} + \{V_{Al} : Al^{\bullet}_{Mg}\} + 3MgAl_2O_4 \\
& Al^{\bullet}_{Mg} + \{V_{Al} : 2Al^{\bullet}_{Mg}\} + 3MgAl_2O_4 \\
& \{V_{Al} : 3Al^{\bullet}_{Mg}\} + 3MgAl_2O_4
\end{aligned} \tag{8.3}
$$

$$
\begin{aligned}
3MgO + 2Al_{Al} + O_O \qquad & 2Mg_{Al} + V^{\bullet\bullet}_{O} + MgAl_2O_4 \\
& Mg_{Al} + \{V^{\bullet\bullet}_{O} : Mg_{Al}\}^{\bullet} + MgAl_2O_4 \\
& \{V^{\bullet\bullet}_{O} : 2Mg_{Al}\} + MgAl_2O_4
\end{aligned} \tag{8.4}
$$

$$
\begin{aligned}
4MgO + 2Mg_{Mg} \qquad & 2Mg_{Al} + Mg^{\bullet\bullet}_{i} + MgAl_2O_4 \\
& Mg_{Al} + \{Mg^{\bullet\bullet}_{i} : Mg_{Al}\}^{\bullet} + MgAl_2O_4 \\
& \{Mg^{\bullet\bullet}_{i} : 2Mg_{Al}\} + MgAl_2O_4
\end{aligned} \tag{8.5}
$$

$$
\begin{aligned}
4MgO + 3Al_{Al} \qquad & 3Mg_{Al} + Al_i^{\bullet\bullet\bullet} + MgAl_2O_4 \\
& 2Mg_{Al} + \{Al_i^{\bullet\bullet\bullet} : Mg_{Al}\}^{\bullet\bullet} + MgAl_2O_4 \\
& Mg_{Al} + \{Al_i^{\bullet\bullet\bullet} : 2Mg_{Al}\}^{\bullet} + MgAl_2O_4 \\
& \{Al_i^{\bullet\bullet\bullet} : 3Mg_{Al}\} + MgAl_2O_4 \qquad (8.6)
\end{aligned}
$$

Equations 8.1-8.6 also describe how it is possible for the antisite defects accommodating MgO or Al_2O_3 excess and their charge compensating point defects to form clusters. Defect clustering was shown to reduce the reaction energy for the Frenkel and Schottky processes in section 4.3.3 and [75, 121] and may play a significant role in the incorporation of nonstoichiometry.

There have been several studies of the mechanisms by which excess MgO and Al_2O_3 are incorporated into spinel. Unfortunately, in the case of Al_2O_3 excess, there is considerable disagreement concerning the type of defect that compensates for the $Al_{Mg}^{\bullet}$ antisite defects. The experimental work of Jagodzinski and Saalfeld [149] suggests that cation vacancies are the primary charge compensating defect in an Al_2O_3 rich material. Sheldon *et al.* [150] go further and suggest that the vast majority of these vacancy defects will be located on the octahedral sublattice, ie. V_{Al} defects. Conversely, the X-ray microanalysis of a single crystal, $(MgO)\cdot(Al_2O_3)_{2.4}$, by Soeda *et al.* [151] and Sawabe *et al.* [152] suggests that the concentration of vacancies on the tetrahedral sublattice is increased. Okuyama *et al.* [153] suggest, from their hydrogen solubility experiments, that as the degree of Al_2O_3 excess is increased the concentration of oxygen vacancy defects is increased. Clearly, as the $Al_{Mg}^{\bullet}$ defect and the $V_O^{\bullet\bullet}$ defect share the same charge, the excess Al_2O_3 must be accommodated in another way; they suggest magnesium vacancies. Conversely, radioactive tracer diffusion experiments by Ando *et al.* appeared to show very little change in oxygen ion diffusion when moving away from a stoichiometric spinel sample to an Al_2O_3 rich material [138], which suggests the concentration of oxygen carriers in spinel is unchanged. Oxygen vacancy defects are, however, proposed as the principle means of charge compensation in an MgO rich material [148].

Spinel's impressive tolerance to radiation induced damage is normally attributed to three important factors: i). the rate of interstitial-vacancy recombination is very quick, ii). its ability to accommodate a significant degree of disorder on its cation sublattices and iii). complex chemistry ensures that the critical size of a dislocation loop is unusually large [61]. The search

for materials which improve upon spinels, already impressive resistance to neutron irradiation induced amorphisation led Sickafus *et al.* [146] and Soedi *et al.* [151] to hypothesize that as the concentration of cation vacancies increases in an Al_2O_3 rich spinel, the rate of interstitial vacancy recombination will be enhanced, thus leading to improved irradiation tolerance. Contrary to this expectation, Sickafus *et al.* [146] discovered that Al_2O_3 excess spinel actually undergoes a transformation to a metastable crystalline state at a lower dose rate than the stoichiometric spinel (1-2 dpa for the Al_2O_3 rich sample versus 10 dpa for the stoichiometric sample) when irradiated by Xe^{2+} ions under cryogenic conditions. However, Ne^{+} irradiation studies of Soeda *et al.* [151], at 873 K, suggest that the structural vacancies present in the Al_2O_3 rich spinel do in fact increase the effectiveness of interstitial-vacancy recombination. This discrepancy between the results of Sickafus *et al.* [146] and Soeda *et al.* [151] may be due to the cryogenic temperatures employed by Sickafus, effectively retarding interstitial vacancy recombination, regardless of the relative concentrations of the vacancy defects.

The aim of this chapter is to use atomistic simulation techniques to predict energies, for the processes described by equations 8.1-8.6 and draw conclusions concerning the most likely method of charge compensation in both MgO and Al_2O_3 excess spinel.

8.2 Results and discussion

The binding energy for the defect species, described in equations 8.1-8.6, determined using the empirical pair potential model, are reported in the first column of numbers in table 8.1. This table predicts that all the defect clusters, described in equations 8.1-8.6, are stable compared to their constituent defects. Furthermore as each series of defect cluster incorporate more species (eg. $\{V_{Al}{:}Al^{\bullet}_{Mg}\}$ $\{V_{Al}{:}2Al^{\bullet}_{Mg}\}$ $\{V_{Al}{:}3Al^{\bullet}_{Mg}\}$), the total binding energy increases - larger clusters are more stable.

Therefore, for each incorporation process (ie. 8.1-8.6) the reaction energy to dissolve one formula unit of Al_2O_3 or MgO (shown in table 8.1) decreases as the defects form larger clusters. However, the degree to which clusters are formed will depend on several factors, specifically: the degree of nonstoichiometry (greater nonstoichiometry leads to more clustering), the temperature (higher temperatures promote the dissolution of defect clusters) and the level of inversion present in the lattice (itself a function of the temperature [43]). Clearly the degree of

cluster formation is a complex issue. Nevertheless, we can consider two limiting situations. The first assumes that deviations from stoichiometry are small enough that the antisite defects concentrations are still dominated by the antisite reaction (ie. $[Al^{\bullet}_{Mg}] \quad [Mg_{Al}]$) but other defect concentrations are controlled by the nonstoichiometry rather than by Schottky or Frenkel equilibria. The second, is focused on larger deviations from stoichiometry, where all point defect concentrations (including the antisite defects) are dominated by the nonstoichiometry.

8.2.1 Small deviations from stoichiometry

At the small deviations limit, take as an example excess Al_2O_3, accommodated by $Al^{\bullet}_{Mg}$ defects, charged compensated for by O_i defects (ie. equation 8.1). It is possible to determine the relative concentrations of the clustered (ie. $\{O_i : 2Al^{\bullet}_{Mg}\}$) and isolated (ie. O_i), charge compensating, defects using mass action analysis and the binding energies obtained using the empirical model. We start from equation 8.7, which describes the process whereby two $Al^{\bullet}_{Mg}$ defects form a cluster with a charge compensating O_i defect.

$$O_i + 2Al^{\bullet}_{Mg} \qquad \{O_i : 2Al^{\bullet}_{Mg}\} \tag{8.7}$$

The reaction energy for this process is the binding energy for the $\{O_i : 2Al^{\bullet}_{Mg}\}$ cluster (ie. -2.82 eV from table 8.1). In order to compare the relative populations of the isolated and cluster defects it is necessary to consider the mass action equation 8.8, which is derived from equation 8.7;

$$\frac{\left[\{O_i : 2Al^{\bullet}_{Mg}\}\right]}{\left[O_i\right]\left[Al^{\bullet}_{Mg}\right]^2} = \exp\left(\frac{2.82}{k_B T}\right) \tag{8.8}$$

where, k_B is Boltzmann's constant and T is the temperature. By assuming that the antisite concentrations are dominated by the intrinsic antisite process (equation 4.1), for which the energy is 1.46 eV, it is possible to obtain the following relation [75].

$$\left[Al^{\bullet}_{Mg}\right] = \left[Mg_{Al}\right] = \exp\left(\frac{-0.73}{k_B T}\right) \tag{8.9}$$

Substituting equation 8.9 into 8.8 and rearranging gives,

$$\left[\{\mathrm{O_i} : 2\mathrm{Al}^{\bullet}_{\mathrm{Mg}}\}\right] = \left[\mathrm{O_i}\right] \exp\left(\frac{1.36}{k_B T}\right) \tag{8.10}$$

Clearly, even at this low nonstoichiometry limit, the concentration of $\mathrm{O_i}$ defects bound in neutral trimer clusters will dwarf the concentration of those found in isolation (eg. by a factor of 10^6 at 1000 K). Extending this to the other process for incorporation of nonstoichiomety in spinel (ie. equations 8.2-8.6), it is possible to show that defect clusters will be stable over isolated defects (both charged or neutral clusters) if $BE_x + 0.73n \quad 0$, where BE_x is the binding energy of the defect cluster and n is the number of antisite defects in the defect cluster. Using the values reported in table 8.1 it is clear that for reactions 8.1, 8.3, 8.4, and 8.6 clusters are stable up to the charge neutral clusters. For reaction 8.2, however, clusters in this very low temperature regime will only dominate up to the pair $\{\mathrm{V_{Mg}}{:}\mathrm{Al}^{\bullet}_{\mathrm{Mg}}\}$. Similarly for reaction 8.5, the dimer $\{\mathrm{Mg}^{\bullet\bullet}_{\mathrm{i}}{:}\mathrm{Mg_{Al}}\}$ cluster will dominate rather than the $\{\mathrm{V_{Mg}}{:}2\mathrm{Mg_{Al}}\}$ cluster. Irrespective, we conclude that clusters will dominate despite the very low level of nonstoichiometry.

8.2.2 High nonstoichiometry regime

At greater deviations from stoichiometry, and again taking solution of Al_2O_3 as the example, the concentration of $\mathrm{Al}^{\bullet}_{\mathrm{Mg}}$ defects is no longer controlled by equation 2.29 and we need to explicitly choose a concentration for $\mathrm{Al}^{\bullet}_{\mathrm{Mg}}$ defects. Thus, by substituting, for example, a modest value eg. $\left[\mathrm{Al}^{\bullet}_{\mathrm{Mg}}\right] = 0.1$, into equation 8.8 yields,

$$\left[\{\mathrm{O_i} : 2\mathrm{Al}^{\bullet}_{\mathrm{Mg}}\}\right] = \left[\mathrm{O_i}\right] \cdot 0.1^2 \cdot \exp\left(\frac{2.82}{k_B T}\right) \tag{8.11}$$

Equation 8.11 predicts that in this greater nonstoichiometric regime, defect clusters are again dominant (eg. by a factor of 10^{12} at 1000 K). Equivalent relationships to equation 8.11, that describe to the relative concentration of $\{\mathrm{V_{Mg}}{:}2\mathrm{Al}^{\bullet}_{\mathrm{Mg}}\}$ to the $\mathrm{V_{Mg}}$ defect etc. show that these neutral clusters are entirely dominant at a nonstoichiometry of 0.1 or greater, below 1000 K. Consequently, when comparing the reaction energies for the processes shown in equations 8.1-8.6, only the reactions involving the largest (ie. most bound) clusters need to be considered.

Consequently, only the incorporation energies per formula unit of Al_2O_3 and MgO involving the largest defect clusters are compared with the DFT simulations of Gilbert *et al.* [121]. These values are included in the last column in table 8.1.

The empirical model data in table 8.1 shows that the most thermodynamically favourable method for accommodating Al_2O_3 excess is via three $Al_{Mg}^{\bullet}$ defects clustered with the charge compensating V_{Al} defect to form the neutral $\{V_{Al} : 3Al_{Mg}^{\bullet}\}$ cluster, as described by equation 8.3. For the same reaction the DFT simulations predicted an incorporation energy per formula unit of 0.46 eV but importantly this was not predicted to be the lowest energy process. DFT simulations suggest that charge compensation of the excess $Al_{Mg}^{\bullet}$ concentration is via $\{V_{Mg}:2Al_{Mg}^{\bullet}\}$ clusters (ie. reaction 8.2), with an incorporation energy of 0.40 eV. Clearly, the difference in energies, predicted by the DFT simulations, is very small (0.06 eV), that is, the simulations do not predict a strong difference in the energies associated with the two processes.

The difference in the absolute energies obtained using the empirical model and DFT arises as a result of employing full charges in the pair potential, overestimating the Coulombic interaction between the defects. Nevertheless, both models agree that the least favourable method for Al_2O_3 excess incorporation is via $\{O_i :2Al_{Mg}^{\bullet}\}$ clusters (ie. reaction 8.1). Overall, therefore, the simulations predict that as the extent of Al_2O_3 excess is increased, there may be a concomitant rise in the concentration of both cation vacancy species. It is, however, not possible to predict, from these results, which will dominate. This would require many calculations to be carried out with explicit high defect concentrations and even then we may well find both cation vacancies are involved.

Both empirical and DFT simulations predict that lowest energy process for excess MgO incorporation is via $\{Mg_i^{\bullet\bullet}:2Mg_{Al}\}$ clusters (equation 8.5). Additionally, both methods predict that the incorporation energy of MgO per formula unit by $\{V_O^{\bullet\bullet}:2Mg_{Al}\}$ clusters is only marginally larger (0.03 and 0.09 eV for the empirical and DFT simulations respectively). Consequently, the models predict that a MgO rich material will incorporate both $Mg_i^{\bullet\bullet}$ and $V_O^{\bullet\bullet}$ defects. Conversely, the energy for MgO excess incorporation by $\{Al_i : 3Mg_{Al}\}$ clusters was predicted to be a high energy process. This is likely related to the observation that the $Al_i^{\bullet\bullet\bullet}$-$V_{Mg}$-$Mg_i^{\bullet\bullet}$ defect is only metastable and decays to form the $\{Al_{Mg}^{\bullet}:Mg_i^{\bullet\bullet}\}^{\bullet\bullet\bullet}$ defect cluster [75, 116].

Significantly, the incorporation energy, per formula unit, for Al_2O_3 excess is lower than for

MgO. This offers one explanation for the asymmetry observed in the phase diagram [25].

8.3 Summary

The results presented here allow us to draw the following conclusions:

- In nonstoichiometric spinel the defect chemistry will be dominated by clusters formed from antisite defects, which accommodate the nonstoichiometry, and other point defects present in the lattice that preserve overall charge neutrality.
- Al_2O_3 excess nonstoichiometry will be characterised by an increased concentration of cation vacancy defects, as predicted by Jagodzinski and Saalfield [149], although given the small energy difference between the V_{Mg} charge compensation process (equation 8.2) and the V_{Al} charge compensation process (equation 8.3) there is no clear preference for one over the other. It may well be that both are involved even at significant nonstoichiometry.
- MgO excess nonstoichiometry will be characterised by an increased concentration of defect clusters involving either $Mg_i^{\bullet\bullet}$ and $V_O^{\bullet\bullet}$ defects and at higher deviations from stoichiometry these are the charge neutral $\{Mg_i^{\bullet\bullet} : 2Mg_{Al}\}$ and $\{V_O^{\bullet\bullet} : 2Mg_{Al}\}$ defect clusters.
- The incorporation energy, per formula unit, for Al_2O_3 is lower than for MgO, which may explain why the spinel lattice accommodates a greater degree of Al_2O_3 excess than MgO excess, as observed in the phase diagram [25].

Table 8.1: Defect formation energies for the species considered in equations 8.1-8.6, the cluster binding energies and finally the energy for incorporation, per formula unit, of Al_2O_3 and MgO via reactions 8.1-8.6 determined from the empirical pair potential method and DFT [121].

Excess	Reaction	Defect Cluster	Cluster Binding Energy /eV	Energy per Formula Unit Incorporated /eV	Energy per Formula Unit Incorporated (DFT)/eV
Al_2O_3	8.1	O_i	0.0	2.08	
		$\{O_i : Al_{Mg}^{\bullet}\}$	-1.80	1.48	
		$\{O_i : 2Al_{Mg}^{\bullet}\}$	-2.82	1.14	0.89
	8.2	V_{Mg}	0.0	1.30	
		$\{V_{Mg} : Al_{Mg}^{\bullet}\}$	-0.81	1.10	
		$\{V_{Mg} : 2Al_{Mg}^{\bullet}\}$	-1.39	0.95	0.40
	8.3	V_{Al}	0.0	1.63	
		$\{V_{Al} : Al_{Mg}^{\bullet}\}$	-1.45	1.27	
		$\{V_{Al} : 2Al_{Mg}^{\bullet}\}$	-2.61	0.98	
		$\{V_{Al} : 3Al_{Mg}^{\bullet}\}$	-3.48	0.76	0.46
MgO	8.4	$V_O^{\bullet\bullet}$	0.0	2.03	
		$\{V_O^{\bullet\bullet} : Mg_{Al}\}^{\bullet}$	-1.55	1.51	
		$\{V_O^{\bullet\bullet} : 2Mg_{Al}\}$	-2.49	1.20	0.81
	8.5	$Mg_i^{\bullet\bullet}$	0.0	1.60	
		$\{Mg_i^{\bullet\bullet} : Mg_{Al}\}^{\bullet}$	-1.04	1.34	
		$\{Mg_i^{\bullet\bullet} : 2Mg_{Al}\}$	-1.73	1.17	0.72
	8.6	$Al_i^{\bullet\bullet\bullet}$	0.0	2.37	
		$\{Al_i^{\bullet\bullet\bullet} : Mg_{Al}\}^{\bullet\bullet}$	-1.51	2.00	
		$\{Al_i^{\bullet\bullet\bullet} : 2Mg_{Al}\}^{\bullet}$	-2.59	1.73	
		$\{Al_i^{\bullet\bullet\bullet} : 3Mg_{Al}\}$	-3.36	1.53	1.06

9

General relationships for cation substitution in oxides

This work has been submitted to Journal of Physics and Chemistry of Solids [154].

9.1 Introduction

In a perfect crystal, each ion occupies a defined symmetry site within a unit cell. Substitutional disorder occurs when a lattice ion is replaced by an ion of a different type [10]. An impurity ion can occupy lattice sites with little disturbance to the overall crystal if the substitutional ion is of similar size and the same charge as the ion it replaces. Differences in size between the host ion and the substitutional ion will induce stress in the lattice; in response the ions of the crystal adjust their positions until each ion experiences zero (time averaged) force.

One measure of the relative size of the host and substitutional ion, ε, is described by equation 9.1,

$$\varepsilon = \frac{a_{sub} - a_{host}}{a_{host}} \tag{9.1}$$

where, a_{host} and a_{sub} are lattice parameters of the host and substituent oxide lattices so that ε might be described as a lattice "strain" term. The reason for using lattice parameters and their differences as a guide to cation size changes is that it avoids problems associated with defining an artificial measure such as cation radius [155, 156]. Consequently, here, when we discuss

cation size difference, it implicitly refers to differences in lattice parameter of the rocksalt structures to which the different cations give rise.

We use atomistic simulation, both a parameterised empirical model and a density functional theory (DFT) quantum mechanical approach, to establish relationships between: i) ε and the internal energy of solution and ii) ε and the volume change resulting from the substitution of cations into simple binary, MO, metal oxides. A particular aim is to determine if such relationships can be identified that are independent of the host oxide.

The cations selected for this study are; Ba^{2+}, Ca^{2+}, Cd^{2+}, Co^{2+}, Mg^{2+}, Mn^{2+} and Sr^{2+}, the oxides of which all exhibit the rocksalt structure. A rocksalt unit cell is assigned the $Fm\bar{3}m$ space group where the cation and oxygen sublattices form interpenetrating face centred cubic arrays, such that the cations and anions are octahedrally coordinated. The cations are assigned to the 4*a* Wyckoff sites and the oxygen anions are assigned to the 4*b* sites [157].

Substitution of a divalent cation, S, into a rocksalt oxide, MO, is an isovalent process (ie. the charge of the substitutional cation and the host cation it replaces are identical) and is illustrated (in Kröger-Vink notation [15]) by equation 9.2,

$$SO + M_M \qquad S_M + MO \tag{9.2}$$

where, M_M represents an M^{2+} cation on its host lattice site, SO contains the substitutional cation in an oxide and S_M shows the substitutional cation, now residing on a host cation lattice site. As this is an isovalent process, there are no charge compensating defects to consider.

9.2 Methodologies

9.2.1 Empirical pair potentials

The pair potential parameters used here are taken from [158] except for the Mn^{2+}-O^{2-} potential, which was derived specifically for this work, giving A_{ij}=697.84 eV, ρ_{ij}=0.3252 Å and C_{ij}=0.0 eV Å^6. This Mn^{2+}-O^{2-} potential replicates the MnO lattice parameter to within 0.4%.

Due to the relatively high polarisability of O^{2-}, the shell model of Dick and Overhauser [85] was applied to describe this polarisability. In this model the core was assigned a charge of 0.04 |e| and the shell -2.04 |e| thereby ensuring the overall charge on the ion was equal to the full valence charge. The core and shell interact through a harmonic force constant of k = 6.3 eV $Å^{-2}$.

Defect volumes were calculated within the Mott-Littleton methodology [94]. In order to compare the relative magnitude of defect volumes between host lattices, each defect volume is divided by the volume of the host primitive unit cell, V_{pMO} (ie. we introduce a normalisation factor).

To allow direct comparison with the DFT simulations described below (where there is currently no equivalent to the Mott-Littleton methodolgy), empirical potential based defect energies were also determined using a supercell method. In this approach, the lattice energy of a perfect host supercell that contains xMO formula units, $E_{M_xO_x}$, a cell in which one of the cations has been substituted for an extrinsic ion, $E_{\mathrm{M}_{x-1}\mathrm{SO}_x}$, and the primitive cell of the substituted ion oxide E_{SO} are all calculated. The defect energy, E_{sol}, is then the difference between the lattice energies (after they have been fully relaxed subject to energy minimisation), as shown in equation 9.3.

$$E_{sol} = \frac{(x-1)}{x} E_{\mathrm{M}_x\mathrm{O}_x} + E_{\mathrm{SO}} - E_{\mathrm{M}_{x-1}\mathrm{SO}_x} \tag{9.3}$$

In the supercell approach the cell containing the substitutional defect is tesselated through space, therefore, there is the possibility that if the supercell is not sufficiently large, the strain fields of the defects will overlap significantly. Such defect-defect interactions will not occur for defects in the dilute limit (as determined using the Mott-Littleton methodology [89]). This problem can be assessed by selecting a range of supercells to establish whether the interactions between defect images are of significance. Here two different supercells were adopted, one constructed of 2 2 2 full unit cells (ie. x=32) and a 3 3 3 supercell (ie. x=108).

In the supercell approach the defect volume is calculated by determining the volume of a perfect unit cell, V_{MO}, and subtracting this from the volume of a cell containing a substitutional defect, $V_{\mathrm{M}_{1-x}\mathrm{S}_x\mathrm{O}}$. This volume is again divided by the volume of the relaxed, perfect primitive unit cell of the host lattice, ie. $\left(V_{\mathrm{MO}} - V_{\mathrm{M}_{1-x}\mathrm{S}_x\mathrm{O}}\right)/V_{\mathrm{pMO}}$.

All empirical simulations were conducted using the CASCADE simulation package [119].

9.2.2 Density Functional Theory

One limitation of first principles simulation are the high demands they place on the computational resources, therefore, their application is usually limited to smaller systems than empirical potential based simulations. The DFT simulations of isovalent substitution reported here employed a 2 2 2 cubic supercell.

In the simulations the exchange correlation energy was modelled using the Local Density Approximation (LDA) and a *k*-point grid with separations of 0.05 $Å^{-1}$. Ultrasoft pseudopotentials were used and the planewave cutoff energy was converged at a value of 420 eV. The DFT simulations were conducted using the CASTEP [108] software package.

9.3 Results and discussion

9.3.1 Solution energy as a function of ε

Figure 9.1, shows the internal energy of solutions for divalent cations (ie. Mg^{2+}, Ca^{2+}, Cd^{2+}, Co^{2+}, Mn^{2+}, Sr^{2+} and Ba^{2+}) substituted into a series of rocksalt materials (ie. MgO, CaO, CdO, CoO, MnO, SrO and BaO), as a function of ε. The enthalpies of solution were determined using all three approaches described previously.

In the case of Mott-Littleton calculations, the enthalpy of solution is a balance between the difference in the lattice energies of the host and substituted cation oxides and the defect energy of the substituted ion. Substitution of larger cations results in positive defect energies but the lattice energy differences are negative (ie. host lattice energy is more negative than that of the substituted cation oxide). Small substitutional cations have negative defect energies but the balance in lattice energies is positive. Figure 9.1 shows that the solution enthalpy in both these circumstances, is always positive (ie. the total process is endothermic). Furthermore, as the magnitude of ε increases (ie. the difference between the host and substitutional lattice parameters increases), the enthalpy of solution increases. Effectively, when a larger

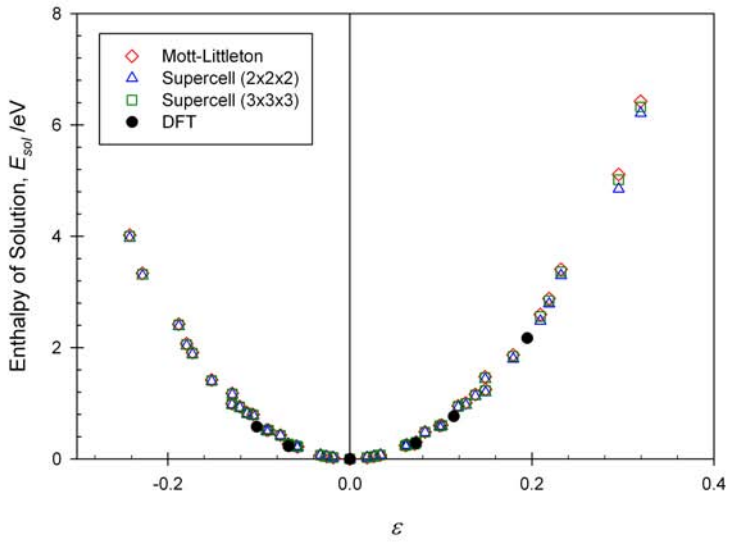

Figure 9.1: Plot showing how the enthalpy of solution, E_{sol}, for isovalent cation substitution into rocksalt MO oxides, changes as a function of ε (equation 9.1). The hollow points in the plot represent those determined using an empirical technique, whilst the solid points were determined using DFT.

cation is substituted onto a host lattice site, the surrounding ions are forced to move away to accommodate the defect. Conversely, when a smaller cation is substituted onto a lattice site the surrounding ions contract around the defect (these processes are illustrated in figure 9.2). The greater the degree of relaxation the lattice must undergo to accommodate the substitutional defect, the greater the enthalpy of solution. As the charge on the host and substitutional cation are identical, when ε = 0, the enthalpy of solution is, of course, zero.

By fitting a quadratic function (of the form, $E = m\varepsilon^2 + n\varepsilon + o$) to each of the data sets (Mott-Littleton, Supercell 2 2 2 and 3 3 3 and DFT) it is possible to: i) assess to what extent the different approaches are predicting similar results and ii) allow predictions of the enthalpy of solution for divalent cation substitution into rocksalt oxides for other combinations of host and substitute cations, as long as the lattice parameter of the host lattice and the substitutional rocksalt oxide are known.

The quadratic function parameters, reported in table 9.1, show that there is excellent agreement between the empirical pair potential data and that obtained using DFT, particularly in the region immediately surrounding the origin. As the difference in the size of the host and substitutional cation increases, the strain field due to the resulting defects increases, therefore the extent to

which the strain fields of the defect images, in neighbouring supercells, will overlap. This is particularly evident for larger separations between the hollow points circled in figure 9.1. The enthalpy of solution, E_{sol}, predicted by the Mott-Littleton methodology, represents a defect that is truly at the dilute limit, so it is unsurprising to see that, as the size of the supercell increases (from 2 2 2 to 3 3 3), and consequently the separation between defect images increases, the predicted enthalpies of solution obtained from the supercell technique converge towards the Mott-Littleton value (similar conclusions have been drawn by Jackson *et al.* [159]). Nevertheless, the difference is relatively small and thus the 2 2 2 supercell, used in the DFT simulations, is an adequate approximation to the dilute limit.

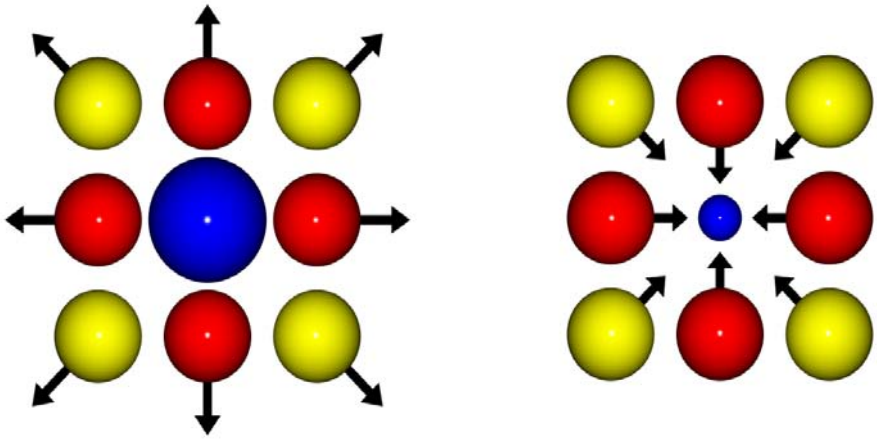

(a) (b)

Figure 9.2: Diagrams showing the effects of a substitutional cation (blue) with a larger ionic radius (a) and one with a smaller ionic radius (b) on a host binary oxide (red spheres represent oxygen and the yellow spheres represent the host cation).

Table 9.1: Coefficients; m and n for quadratic functions fitted to the equation $E = m\varepsilon^2 + n\varepsilon + o$ relating strain, ε, and the internal energy of solution, E_{sol}.

Model	m	n	R^2
Mott-Littleton	62.830	-0.489	0.996
Supercell (2 2 2)	61.240	-0.556	0.996
Supercell (3 3 3)	62.310	-0.496	0.996
DFT	54.847	0.624	0.794

The m parameters, reported in table 9.1, are all in the range 54-63 which reflects the good agreement between the different techniques as shown in figure 9.1. Furthermore, the n parameters

are all much smaller then the m parameters. It also follows that the energy curves are highly symmetric about the y-axis (ie. $E_{sol}(\varepsilon) \quad E_{sol}(-\varepsilon)$). We next consider the extent to which the defect volumes are also a symmetric function of ε.

9.3.2 Defect volume as a function of ε

As mentioned above, the larger the mismatch between the size of the host and substituent cations, the greater the relaxation the lattice undergoes to accommodate substitutional disorder. This relationship is highlighted in figure 9.3, where the normalised defect volume is plotted against ε. This shows that when an ion is replaced by a like charged cation with a smaller ionic radius, the lattice contracts around it, that is, the normalised defect volume is negative. Conversely, when the substituent cation is larger, the normalised defect volume is positive and so the crystal expands. Of course, the plot passes through the origin because, in the absence of strain or electronic effects, there is no relaxation required when a cation is substituted by an ion with the same charge and radius.

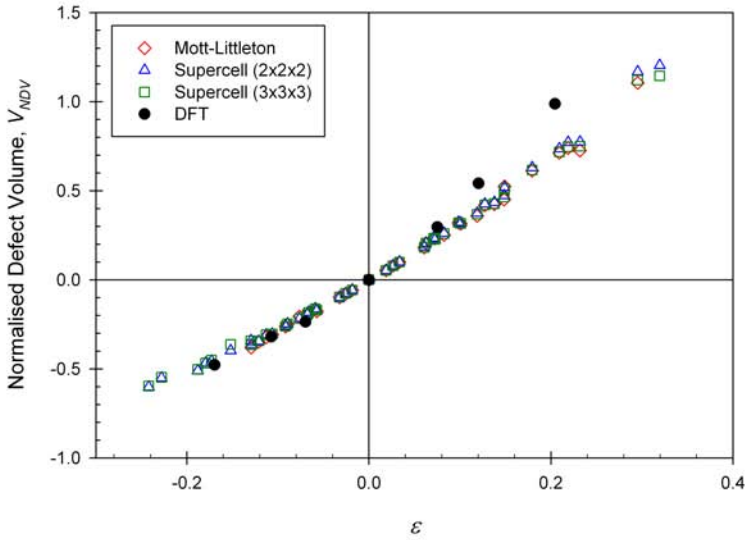

Figure 9.3: Plot showing how the normalised defect volume, V_{NDV}, varies as a function of ε. The hollow points in the plot represent those determined using an empirical technique, whilst the solid points were determined using DFT.

The data presented in figure 9.3 predicts that the correlation between ε and the normalised defect volume is somewhat non-linear: that is, the substitution of smaller cations leads to a

smaller change in the volume of a crystal, for the same change in the magnitude of ε, than substitution of a larger cation (or $V_{NDV}(\varepsilon) < V_{NDV}(-\varepsilon)$). This observation is distinct from the conclusion drawn from figure 9.1, that the change in solution energy is symmetric (ie. either a positive or negative change in ε, of equal magnitude, will require the same energy). To investigate the symmetry issue further, the relationship between solution energy and defect volume is illustrated in figure 9.4. This suggests that the energy penalty associated with a reduction in the lattice volume, due to the substitution of a small cation onto a site previously occupied by a large cation, is greater than for an expansion of the lattice of equal magnitude, due to substitution of a larger cation on a smaller lattice site. This should be expected, due in particular, to the increasing repulsion between the surrounding oxygen anions as they move closer together, when contracting around the smaller substitutional cation.

Figure 9.3 shows that there is some divergence between the defect volumes determined using the empirical and DFT simulations, particularly as the strain on the lattice increased. This is due to the limitations of the more simple classical potential based technique, which overestimates elastic constants and as such the simulated lattice is not representatively compliant.

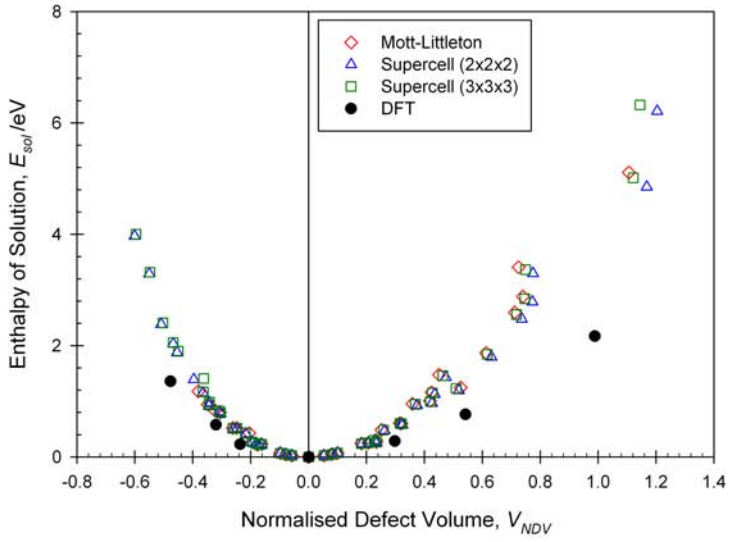

Figure 9.4: Plot showing how the enthalpy of solution, E_{sol}, varies as a function of the normalised defect volume, V_{NDV}. The hollow points in the plot represent those determined using an empirical technique, whist the solid points were determined using DFT.

9.4 Concluding comments

Using both empirical and quantum mechanical approaches we have examined changes in both enthalpy of solution and the lattice volume arising from isovalent cation substitution into a range of host materials that exhibit the rocksalt structure. Throughout, we analyse energy and volume changes in terms of a lattice 'strain' related term, ε, that is defined as the difference in the lattice parameter of the host and substitutional cation oxides divided by the host lattice parameter (see equation 9.1). The following conclusions can be drawn:

- To a good approximation the enthalpy of solution increases proportionally to the square of the strain term. As such, the solution enthalpy is symmetric about ε=0 (see figure 9.1).
- The volume change (defect volume) is less symmetric about ε=0 (see figure 9.3). That is, smaller substitute cations give rise to proportionally smaller lattice contractions than larger substitute cations give rise to lattice expansion. Figure 9.4 describes this in terms of the energy penalty, where an incremental defect volume expansion is less energetically costly than the same defect contraction.

Within this group of materials, that assume the rocksalt structure, these relationships are 'general' and as such can be used to predict solution enthalpies and volume changes for other combinations of host and substitute cations not simulated here. Equivalent relationships may exist for aliovalent cation substitutions and for other host lattice crystal structures, although these relationships would likely be different from those reported here.

10

Conclusions and further work

10.1 Spinel

This thesis presents results of investigations into the types, concentrations and configurations of the intrinsic point defects found in spinel and their role in processes such as mass transport and the accommodation of nonstocihiometry. A number of simulation techniques have been applied in order to gain an insight into the behaviour of the point defects in isolation and examining the interactions between them.

Chapter 4 considered the structure and relative concentrations of the isolated point defects and the effects of defect clustering. The lowest energy configuration for the interstitial defects in spinel were predicted to be a complex split interstitial structure, as shown in figures 4.1 and 4.2, rather than an interstitial ion located on an 8*b* Wyckoff site. A similar investigation by Gilbert *et al.* [121], conducted using DFT, also concluded that split interstitial defects were lower in energy than their isolated equivalent. There was further agreement between the simulations conducted in this thesis and the parallel study by Gilbert *et al.* [121] as to which is the lowest energy defect process in spinel. Both predicted that the reaction energy for the antisite process (reaction 4.1) is an order of magnitude lower than the Frenkel and Schottky processes (reactions 4.2 - 4.5). Consequently, the defect chemistry of spinel is dominated by the presence of antisite defects. Clustering between the antisite defects present in the lattice and the interstitial and vacancy defects leads to a decrease in the reaction energies of the Frenkel and Schottky processes. Effectively, the presence of the antisite defects promotes an increase in the concentrations of interstitial and vacancy defects. A measure of the dominance of defects clustered

with antisite defects compared to those found in isolation can be found in chapter 8. The approach adopted in chapter 8 assumes that the dominance of defect clustering can be attributed to the binding energy between the antisite defect and the vacancy/interstitial defect. A more rigorous approach would be to solve, simultaneously, all of the isolated and clustered Frenkel and Schottky mass action equations (including a further equation to maintain overall charge neutrality). This would show the absolute concentrations predicted by the model as a function of temperature as well as allowing the calculation of the formation energy, E_f, for each of the intrinsic point defects in spinel. This mass action analysis should also be applied using the reaction energies predicted using DFT, as it is expected that the use of a full charge model will lead to an overestimation of the defect concentrations, particulary when oppositely charged defects are clustered together. Once the formation energies for the intrinsic point defects are known then they can be added to the migration energies, E_m, obtained in chapters 5 and 6 to obtain the overall activation energies, E_a, for magneisum, aluminium and oxygen transport.

The defect volume calculations shown in chapter 4 predict a positive defect volume (ie. the crystal will expand) for the introduction of both isolated Mg_{Al} and $Al^{\bullet}_{Mg}$ defects, however, the simulations also predict that the defect volume is negative for the introduction of a $\{Mg_{Al}{:}Al^{\bullet}_{Mg}\}$ cluster in the nearest neighbour configuration. Andreozzi *et al.* [43] predict that as the level of inversion in spinel increases there is a slight decrease in the defect volume. This, therefore, implies that there is at least some level of clustering between the antisite defects in spinel. This assertion of clustered regions of antisite disorder in spinel is further supported by two sets of simulations of Ball *et al.* [50]. In the first, that employed a mean field approach overestimated the rate of change in the lattice parameter as a function of the level of inversion as this approach assumes that all arrangements of antisite defect within a given cell are equally probable. Conversely, when they used an approach that allowed near neighbour clusters to evolve, the variation in the lattice parameter was correctly predicted. Although, the most energetically favourable configuration for an antisite pair is to form a nearest neighbour configuration, however, it would be interesting to examine whether it continues to be favourable to build more extended regions of antisite disorder. This can be achieved by determining the lowest energy configuration for antisite clusters containing increasing numbers of antisite defects, and then calculating the binding energy per antisite defect. A minimum (ie. most negative value) in the binding energy per antisite defect will highlight the optimum size of a disordered region in spinel (although this neglects the effects of entropy). It would also be appropriate to calculate

the defect volume for the lowest energy antisite cluster configurations to allow comparison with the experimental values.

In chapters 5, 6 and 7 the mechanisms of point defect mediated mass transport are discussed in detail. Initially a static method was adopted to examine the diffusivity (ie. the ease with which a defect can migrate) of the isolated defects by determining the migration energies, E_m, and the diffusion prefactor, D_0. The O_i interstitial defect was found to be the most mobile defect in spinel with a migration energy of 0.16 eV. Therefore, assuming that the concentrations of the point defects are all equivalent, oxygen will be the most mobile ion in spinel. Of the cations, Mg^{2+} was found to be more mobile than Al^{3+}. Interestingly, the migration energy for Al^{3+} diffusion was predicted to be lowest via an $Al^{\bullet}_{Mg}$ defect migrating via a V_{Mg} defect on the magnesium sublattice. Whilst the diffusion prefactors for each process were calculated they did not lead to a significant reordering of the defect mobility. There was, however, one significant assumption applied when determining the diffusion prefactors, which was that the correlation factor for all processes will be unity. While it is expected that the values for all processes will be in the region 0.4 - 1.0 [21], it would clearly be desirable to determine these terms explicitly, particularly for $Al^{\bullet}_{Mg}$ migration via a vacancy mechanism on the magnesium sublattice.

Oxygen interstitial migration was discussed in detail in chapter 6 and a migration energy for O_i transport was determined to be 0.16 eV. In order for the O_i interstitial defect to migrate in 3D the split O_i-$V_0^{\bullet\bullet}$-O_i defect must rotate to access other $1\bar{1}0$ directions. Uberuaga *et al.* [116] predicted two rotation mechanisms with migration energies of 0.64 eV and 0.67 eV. Unfortunately, due to the strong forces acting on the oxygen ion in the region of the saddle point the core and shell in the simulations decoupled and it was not possible to determine equivalent migration energies using a model that included the effects of polarisation. It is possible to strengthen the interaction between the oxygen core and shell by means of a k_4 term added to the spring constant (equation 3.11). Unfortunately, this additional stiffening of the force constant acting between the oxygen core and shell will have a minor affect on the defect and lattice energies. The oxygen interstitial rotation barriers should be calculated by adding this additional parameter, however, similar simulations should also then be conducted on the other diffusion processes so the impact on other migration energies can be predicted consistently.

The empirical pair potential based approach, employed in the static lattice simulations dis-

cussed in chapters 5 and 6 and the TAD simulations presented in chapter 7, assume that a full charge model is appropriate for examining the migration processes of point defects in spinel. DFT simulations of the charge density of spinel have suggested that the charges in spinel are in fact closer to 1.78 $|e|$, 2.56 $|e|$ and -1.73 $|e|$ for magnesium, aluminium and oxygen ions respectively, therefore, the full charge model adopted here will overestimate the Coulombic interaction between the defects and the surrounding perfect lattice, which in turn, will affect the migration energies. This problem could be overcome by developing a partial charge model, however, there is still a level of complexity which cannot be modeled using an empirical based method. The empirical potential approach used here assumes fixed charges and so will not account for any changes in the charge states of the migrating ion and the immediate surroundings. In order to account for any charge transfer processes as well as any other electronic effects which occur when ions migrate, DFT nudged elastic band simulations should be performed.

Clustering of point defects was shown to have a significant impact on the thermodynamics of the intrinsic defect concentrations. Chapter 7, investigated how defect clustering can also influence defect diffusion. In general, clustering of defects was predicted to impede diffusion, particularly when vacancy and interstitial defects become clustered to the highly immobile antisite defects. There was, however, one notable exception; the migration energy for $Mg_i^{\bullet\bullet}$ diffusion was reduced by the presence of an O_i defect. This type of cooperative diffusion mechanism has also been observed using TAD in MgO [137, 143]. Unfortunately, there appears to be some disagreement between the TAD simulation of a spinel supercell containing an $Al_{Mg}^{\bullet}$ defect an a V_{Mg} defect with the assertion in chapter 5 which predicts that Al^{3+} will preferentially migrate via a vacancy mechanism on the magnesium sublattice. In the TAD simulation the $Al_{Mg}^{\bullet}$ defect is not predicted to migrate during the 17.5 ns simulation but the V_{Al} defect is predicted to migrate after 15 ns (both simulations employed the same T_{high} and T_{low}). It is not immediately obvious whether this discrepancy is a result of the inclusion of the shell model in chapter 5 but not in the TAD simulations. Currently the TAD code is not able to incorporate a shell model, however, this modification should be made. Once this has been carried out the cluster simulations presented in chapter 7 should be repeated.

Chapter 7 examined very simple dimer clusters, however, it has already been shown that the point defects in spinel can, and in fact are likely to, form clusters that are larger than those examined. In its current form, the TAD code can only be applied to relatively small systems as it is not currently configured to run in parallel. Therefore, when modeling larger systems, which

involve not only defect-defect interactions but cluster-cluster interactions, a different simulation technique may be more appropriate. Kinetic Monte Carlo (KMC) [101] is a simulation technique that can be applied to follow the evolution of large systems to comparatively very long times scales. One of the drawbacks to KMC is that it is unable to evolve a system without some prior knowledge of the migration energies of the defects/clusters. This information can be obtained by performing a basin constrained MD simulation [99] (similar to that performed in the TAD simulations in chapter 7) and creating a library of possible transitions. Clearly, given the significant increase in the number of migration barriers obtain from dimer clusters in chapter 7, this is likely to require the formation of a very significant library of migration energies. Ideally, it would be useful if the KMC code could generate migration energies on the fly, possibly by creating a small basin constrained MD simulation, should it encounter an arrangement of defects it does not already have in its library. Once the library has been made, a large KMC simulation, containing a number of defects representative of the relative concentrations determined from the mass action analysis discussed above, should be run.

The results presented in chapter 8 suggest that the most favourable mechanism for accommodation of excess Al_2O_3 is via $Al_{Mg}^{\bullet}$ defects clustered to charge compensating V_{Al} defects. Accommodation of excess MgO is expected to be achieved by incorporation of Mg_{Al} defects in clusters charge compensated by both $V_O^{\bullet\bullet}$ and V_{Mg} defects. At low levels of Al_2O_3 or MgO excess the clustering between defects would be expected to be lower than at higher concentrations, simply because there are fewer defects in the crystal to cluster together, however, as deviation from a stoichiometric ratio increases the level of clustering would also be expected to increase. This can be examined in more detail by performing a mass action analysis of the defects associated with Al_2O_3 and MgO excess, across a wide temperature range, assuming that the concentration of antisite defects is controlled by the degree of nonstoichiometry.

The damage cascade simulations of Bacorisen *et al.* [74] compared the evolution of radiation induced defects in $MgAl_2O_4$, $MgIn_2O_4$ and $MgGa_2O_4$. They concluded that more of the radiation induced damage is retained the higher the degree of inversion present in the initial spinel lattice. However, in addition to changing the level of inversion they also changed the chemistry of the lattice by changing the trivalent cation specie. Therefore, it would be interesting to investigate the level of retained damage after a thermal spike as a function of cation version in $MgAl_2O_4$ alone.

10.2 Cation substitution

In chapter 9, iso cation substitution into rocksalt metal oxide materials was studied. For isovalent cation substitution of divalent cations into rocksalt metal oxides it was shown that as the magnitude of the size difference between the substitute and host cations increases the internal energy of solution for the substitution process increases. The simulations also predict that substitution of a host cation with an alternative cation of smaller ionic radius, results in a smaller change in the volume of the crystal compared to substitution of a cation that is an equal magnitude larger. Therefore, the energy change resulting from the contraction about the substitutional defect is greater than for the equivalent expansion, due to anharmonic variation of the ion-ion interaction energies. The generality of the trends observed here could be investigated by substituting a number of other divalent cations in the rocksalt oxides considered above or by examining isovalent cation substitution into another MO crystal structure, such as the wurtzite structure (eg. ZnO).

Aliovalent cation substitution occurs when there is a charge difference between the substitutional defect and the host cation it replaces. In order to maintain overall charge neutrality of the crystal, the substitutional defect must also be accompanied by other oppositely charged intrinsic defects. An investigation, similar to the one carried ont in chapter 9, but this time focused on aliovalent cation substitution into the rocksalt oxides, would illustrate the combined effects of charge and size mismatches for cation substitution.

Bibliography

[1] M. Barber, *Bronze and the Bronze Age*. The History Press LTD, 2002.

[2] J. W. Gibbs, *Statistical Mechanics; Thermodynamics*. New York: C. Scribner, 1902.

[3] J. Fourier *Ann. Chim. Phys.*, vol. 27, p. 136, 1824.

[4] *Kyoto Protocol to the United Nations Framework Convention on Climate Change*. United Nations, 1998.

[5] T. Watanabe, S. B. Sinnott, J. S. Tulenko, R. W. Grimes, P. K. Schelling, and S. R. Phillpot *J. Nucl. Mater.*, vol. 375, p. 388, 2008.

[6] E. M. Michie, R. W. Grimes, S. K. Fong, and B. L. Metcalfe *J. Solid State Chem.*, vol. 181, p. 3287, 2008.

[7] S. Malang, A. R. Raffray, A. Sagara, and A. Ying *J. Phys. C: Solid State Phys.*, vol. 14, p. L121, 1981.

[8] F. W. Clinard, G. F. Hurley, and R. W. Klaffky *Res. Mech.*, vol. 8, p. 207, 1983.

[9] M. Haüy, *Essai D'une theorie sur la structure des crystaux, appliquee a plusieurs genres de substances crystallisees*. Chez Gogue & Nee de la Rochelle Librares, 1784.

[10] N. N. Greenwood, *Ionic Crystals, Lattice Defects and Nonstoicheometry*, vol. 1. Butterworths, 1968.

[11] T. Hahn, *International Tables for Crystallography*, vol. A: Space Group Symmetry. Kluwer Academic Publishers, 1992.

[12] U. Shmueli, *International Tables for Crystallography*, vol. B: Reciprocal Space. Kluwer Academic Publishers, 1993.

[13] A. J. C. Wilson, *International Tables for Crystallography*, vol. C: Mathematical, Physical and Chemical Tables. Kluwer Academic Publishers, 1992.

[14] F. Agullo-Lopez, C. R. A. Catlow, and P. D. Townsend, *Point Defects in Materials*. Academic Press, 1988.

[15] F. Kröger, *The chemistry of imperfect crystals*, vol. 2. North-Holland Publishing Company, Ltd., 2nd ed., 1974.

[16] P. Atkins, *Physical Chemistry*. W. H. Freeman & Company, 5th ed., 1994.

[17] E. Steiner, *The Chemistry Maths Book*. Oxford University Press, 1996.

[18] A. Fick *Phil. Mag. and Jour. Sci.*, vol. 10, p. 31, 1855.

[19] R. Brown *Phil. Mag.*, vol. 4, p. 161, 1828.

[20] A. Einstein *Ann. Phys.*, vol. 17, p. 549, 1905.

[21] H. Mehrer, *Diffusion in Solids*, vol. 155. Springer, 2007.

[22] A. F. Voter, F. Montalenti, and T. C. Germann *Ann. Rev. Mater. Res.*, vol. 32, p. 321, 2002.

[23] G. H. Vineyard *J. Phys. Chem. Solids*, vol. 3, p. 121, 1957.

[24] F. Jensen, *Introduction to Computational Chemistry*. John Wiley & Sons, 2001.

[25] H. Hallstedt *J. Am. Ceram. Soc.*, vol. 75, p. 1497, 1992.

[26] E. Soignard, M. Somayazulu, H. K. Mao, J. J. Dong, O. F. Sankey, and P. F. McMillan *Solid State Commun.*, vol. 120, p. 237, 2001.

[27] E. Soignard, D. Machon, P. F. McMillan, J. Dong, B. Xu, and K. Leinenweber *Chem. Mater.*, vol. 17, p. 5465, 2005.

[28] S. Sun and H. Zeng *J. Am. Chem. Soc.*, vol. 124, p. 8204, 2002.

[29] W. H. Bragg *Phil. Mag.*, vol. 30, p. 305, 1915.

[30] S. Nishikawa *Proc. Math. Phys. Soc.*, vol. 8, p. 199, 1915.

[31] T. F. W. Barth and E. Posnjak *J. Wash. Acad. Sci.*, vol. 21, p. 255, 1931.

[32] Y. Chiang, D. Birnie, and W. D. Kingery, *Physical Ceramics*. Wiley, 1997.

[33] N. W. Grimes, P. Thompson, and H. F. Kay *P. Roy. Soc. A*, vol. A386, p. 333, 1983.

[34] K. E. Sickafus, J. M. Willis, and N. W. Grimes *J. Am. Ceram. Soc.*, vol. 82, p. 3279, 1999.

[35] S. Hafner and F. Laves *Z. Kristallogr.*, vol. 115, p. 331, 1961.

[36] G. C. Gobbie, R. Christoffereson, M. T. Otten, B. Miner, P. R. Buseck, G. J. Kennedy, and C. A. Fyfe *Chem. Lett.*, vol. 6, p. 771, 1985.

[37] U. Schmocker, H. R. Boesch, and F. Waldner *Phys. Lett.*, vol. 40A, p. 237, 1972.

[38] U. Schmocker and F. Waldner *J. Phys. C: Solid State Phys.*, vol. 9, p. L235, 1976.

[39] F. T. Docherty, A. J. Craven, D. W. McComb, and J. Shakle *Ultramicroscopy*, vol. 86, p. 273, 2001.

[40] R. O. Sack *Cont. Miner. Petro.*, vol. 79, p. 169, 1982.

[41] F. Princivalle, A. Della Giusta, A. De Min, and E. M. Piccirillo *Miner. Mag.*, vol. 63(2), p. 257, 1999.

[42] T. Yamanka and Y. Takeuchi *Z. Kristallogr.*, vol. 165, p. 65, 1983.

[43] G. B. Andreozzi, F. Princivalle, H. Skogby, and A. D. Giusta *Am. Mineral.*, vol. 85, p. 1164, 2000.

[44] B. J. Wood, R. J. Kirkpatrick, and B. Montez *Am. Mineral.*, vol. 71, p. 999, 1986.

[45] H. Maekawa, S. Kato, K. Kawamura, and T. Yokokawa *Am. Mineral.*, vol. 82, p. 1125, 1997.

[46] R. C. Paterson, C. A. Lager, and R. L. Hitterman *Am. Mineral.*, vol. 76, p. 1455, 1991.

[47] S. A. T. Redfern, R. J. Harrison, H. S. C. O'Neil, and D. R. R. Wood *Am. Mineral.*, vol. 84, p. 299, 1999.

[48] S. P. Slotznick and S. Shim *Am. Mineral.*, vol. 93, p. 470, 2008.

[49] A. Seko, K. Yuge, F. Oba, A. Kuwabara, I. Tanaka, and T. Yamamoto *Phys. Rev. B*, vol. 73, p. 094116, 2006.

[50] J. A. Ball, M. Pirzada, R. W. Grimes, M. O. Zacate, D. W. Price, and B. P. Uberuaga *J. Phys.: Condens. Matter*, vol. 17, p. 7621, 2005.

[51] H. S. C. O'Neill and A. Navrotsky *Amer. Miner.*, vol. 68, p. 181, 1983.

[52] E. J. Palin and R. J. Harrison *Am. Mineral.*, vol. 92, p. 1334, 2007.

[53] H. S. C. O'Neill and A. Navrotsky *Amer. Miner.*, vol. 69, p. 733, 1984.

[54] R. L. Millard, R. C. Paterson, and B. K. Hunter *Am. Mineral.*, vol. 77, p. 44, 1992.

[55] M. Y. Lavrentiev, J. A. Purton, and N. L. Allan *Am. Mineral.*, vol. 88, p. 1522, 2003.

[56] E. J. Palin and R. J. Harrison *Mineral. Mag.*, vol. 71(6), p. 611, 2007.

[57] F. Nestola, T. Boffa Ballaran, T. Balic-Zunic, F. Princivalle, L. Secco, and A. Dal Negro *Am. Mineral.*, vol. 92, p. 1838, 2007.

[58] F. W. Clinard, G. F. Hurley, and L. W. Hobbs *J. Nucl. Mater.*, vol. 108/109, p. 655, 1982.

[59] G. R. Hopkins and R. J. Price *Nucl. Eng. Des. Fusion*, vol. 2, p. 111, 1984.

[60] K. E. Sickafus, L. Minervini, R. W. Grimes, J. A. Valdez, M. Ishimaru, F. Li, K. J. McClellan, and T. Hartmann *Science*, vol. 289, p. 748, 2000.

[61] L. W. Hobbs and F. W. Clinard *J. Phys. (Paris)*, vol. C6, p. 232, 1980.

[62] K. E. Sickafus, A. C. Larson, N. Yu, M. Nastasi, G. W. Hollenberg, F. A. Garner, and R. C. Bradt *J. Nucl. Mater.*, vol. 219, p. 128, 1995.

[63] Z. Li, C. K. Chan, F. A. Garner, and R. C. Bradt *J. Nucl. Mater.*, vol. 219, p. 139, 1995.

[64] T. Yano *J. Am. Ceram. Soc.*, vol. 82[12], p. 3355, 1999.

[65] P. M. G. Damen, A. Van Veen, H. Matzke, H. Schut, J. A. Valsez, C. J. Wetteland, and K. E. Sickafus *J. Nucl. Mater.*, vol. 306, p. 180, 2002.

[66] S. J. Zinkle *J. Nucl. Mater.*, vol. 219, p. 113, 1995.

[67] S. J. Zinkle *J. Am. Ceram. Soc.*, vol. 72, p. 1343, 2005.

[68] M. Shimada, S. Matsumura, K. Yasuda, C. Kinoshita, Y. Chimi, N. Ishikawa, and A. Iwase *J. Nucl. Mater*, vol. 329-333, p. 1446, 2004.

[69] N. Yu, K. E. Sickafus, and M. Nastasi *Phil. Mag. Lett.*, vol. 70, p. 235, 1994.

[70] R. Devanathan, N. Yu, K. E. Sickafus, and M. Nastasi *J. Nucl. Mater.*, vol. 232, p. 59, 1996.

[71] M. Ishimaru, Y. Hirotsu, I. V. Afanasyev-Charkin, and K. E. Sickafus *J. Phys.: Condens. Mater.*, vol. 14, p. 1237, 2002.

[72] T. Yamamoto, A. Chartier, K. Yasuda, C. Meis, K. Shiiyama, and S. Matsumura *Nucl. Instr. Methods. B*, vol. 266, p. 2711, 2008.

[73] R. Smith, D. Bacorisen, B. P. Uberuaga, K. E. Sickafus, J. A. Ball, and R. W. Grimes *J. Phys.: Condens. Mater.*, vol. 17, p. 875, 2005.

[74] D. Bacorisen, R. Smith, B. P. Uberuaga, K. E. Sickafus, J. A. Ball, and R. W. Grimes *Phys. Rev. B*, vol. 74, p. 214105, 2006.

[75] J. A. Ball, S. T. Murphy, R. W. Grimes, D. Bacorisen, R. Smith, B. P. Uberuaga, and K. E. Sickafus *Solid State Sci.*, vol. 10, p. 717, 2008.

[76] G. E. Moore *Electronics*, vol. 38, p. 8, 1965.

[77] E. Schrodinger *Phys. Rev.*, vol. 28, p. 1049, 1926.

[78] M. Born and J. Mayer *Z. Phys.*, vol. 75, p. 1, 1932.

[79] M. Born and J. Mayer *J. Chem. Phys.*, vol. 1, p. 270, 1933.

[80] C. Kittel, *Introduction to Solid State Physics*. John Wiley & Sons, Inc., 1st ed., 1954.

[81] M. Born, *Atomic Physics*. Blackie & Son, Ltd., 6th ed., 1956.

[82] M. Born and Landé *Verhandlungen der Deustschen Physik Gesellschaft*, vol. 21/24, p. 210, 1918.

[83] J. E. Lennard-Jones *P. Roy. Soc. A-Math. Phy.*, p. 463, 1924.

[84] R. A. Buckingham *P. Roy. Soc. A-Math. Phy.*, vol. 168, p. 264, 1936.

[85] B. G. Dick and A. W. Overhauser *Phys. Rev.*, vol. 112, p. 90, 1958.

[86] A. R. Cleave, *Atomic Scale Simulations for Waste Form Applications*. PhD Thesis, Imperial College London, 2005.

[87] D. F. Shanno *Math. Comput.*, vol. 24, p. 647, 1970.

[88] W. Jost *J. Chem. Phys.*, vol. 1, p. 466, 1933.

[89] N. F. Mott and M. J. Littleton *Trans. Faraday Soc.*, vol. 34, p. 485, 1938.

[90] C. R. A. Catlow and W. C. Mackrodt, *Lecture Notes in Physics: Computer Simulation in Solids*, vol. 166. Springer, 1982.

[91] C. R. A. Catlow *Annu. Rev. Mater. Sci.*, vol. 16, p. 517, 1986.

[92] M. J. Rushton, *Simulations of Glass and Ceramic Systems for Nuclear Waste Applications*. PhD Thesis, Imperial College London, 2006.

[93] R. W. Grimes, C. R. A. Catlow, and A. M. Stoneham *J. Phys.:Condens. Matter*, vol. 1, p. 7367, 1989.

[94] C. R. A. Catlow, J. Corish, P. W. M. Jacobs, and A. B. Lidiard *J. Phys. C: Solid State Phys.*, vol. 14, p. L121, 1981.

[95] L. Verlet *Phys. Rev.*, vol. 159, p. 98, 1967.

[96] C. R. A. Catlow, *Computer modeling in Inorganic Crystallography*, vol. 1. Academic Press, 1996.

[97] A. F. Voter *J. Chem. Phys.*, vol. 106, p. 4665, 1997.

[98] A. F. Voter *Phys. Rev. B*, vol. 57, p. 13985, 1998.

[99] M. R. Sorensen and A. F. Voter *J. Chem. Phys.*, vol. 112, p. 9599, 2000.

[100] G. Henhelman and H. Jonsson *J. Chem. Phys.*, vol. 115, p. 9657, 2001.

[101] A. F. Voter, *Radiation effects in solids*, vol. 235. Springer Netherlands, 2007.

[102] R. Elber and K. Karplus *Chem. Phys. Lett.*, vol. 139, p. 375, 1987.

[103] M. Born and R. Oppenheimer *Ann. Physik*, vol. 84, p. 457, 1927.

[104] P. A. M. Dirac *Proc. Camb. Phil. Soc.*, vol. 35, p. 416, 1939.

[105] P. W. Atkins and R. S. Friedman, *Molecular Quantum Mechanics*. Oxford University Press, 1997.

[106] E. Kaxiras, *Atomic and Electronic Structure of Solids*. Cambridge University Press, 2003.

[107] J. C. Slater *Phys. Rev.*, vol. 34, p. 1293, 1929.

[108] M. D. Segall, P. J. D. Lindan, M. J. Probert, C. J. Pickard, P. J. Hasnip, S. J. Clark, and M. C. Payne *J. Phys.: Condens. Matter*, vol. 14, p. 2717, 2002.

[109] P. Hohenberg and W. Kohn *Phys. Rev.*, vol. 136, p. B864, 1964.

[110] W. Kohn and L. J. Sham *Phys. Rev.*, vol. 140, p. A1133, 1965.

[111] J. P. Perdew, K. Burke, and M. Ernzer *Phys. Rev. Lett.*, vol. 77(18), p. 3868, 1996.

[112] J. C. Phillips and L. Kleinman *Phys. Rev.*, vol. 116, p. 287, 1959.

[113] R. Carr and M. Parrinello *Phys. Rev. Lett.*, vol. 55, p. 22, 1985.

[114] M. C. Payne, M. P. Teter, D. C. Allan, T. A. Arias, and J. D. Joannopoulos *Rev. Mod. Phys.*, vol. 64(4), p. 1045, 1992.

[115] J. H. J. Crawford and L. M. Slifkin, *Point Defects in Solids*, vol. 1. New York and London: Plenum, 1972.

[116] B. P. Uberuaga, D. Bacorisen, R. Smith, J. A. Ball, R. W. Grimes, A. F. Voter, and K. E. Sickafus *Phys. Rev. B*, vol. 75, p. 104116, 2007.

[117] H. Yao, O. Lizhi, and W.-Y. Ching *J. Am. Ceram. Soc.*, vol. 90[10], p. 3194, 2007.

[118] A. Yoneda *J. Phys. Earth*, vol. 38, p. 19, 1990.

[119] M. Leslie, "Technical report," *Uk Science and Engineering Research Council - Daresbury Laboratory, Warrington (UK)*, 1982.

[120] S. S. De Souza and A. R. Blak *Rad. Eff. Def. Solids*, vol. 146, p. 123, 1998.

[121] C. A. Gilbert, R. Smith, S. D. Kenny, S. T. Murphy, R. W. Grimes, and J. A. Ball *in preparation*, vol. -, pp. –, -.

[122] S. D. Kenny, A. P. Horsfield, and H. Fujitani *Phys. Rev. B*, vol. 76, p. 184103, 2007.

[123] Y. M. Chiang and W. D. Kingery *J. Am. Ceram. Soc.*, vol. 73, p. 841, 1990.

[124] S. T. Murphy, B. P. Uberuaga, J. A. Ball, A. R. Cleave, K. E. Sickafus, R. Smith, and R. W. Grimes *Solids State Ionics*, vol. 180, p. 1, 2008.

[125] D. Henderson, D. H. Bowen, A. Briggs, and R. D. King *J. Phys. Paris*, vol. C4, p. 1496, 1971.

[126] M. J. L. Sangster and D. K. Rowell *Phil. Mag.*, vol. A44, p. 613, 1981.

[127] W. D. Kingery *J. Nucl. Mater.*, vol. 24, p. 21, 1967.

[128] P. W. M. Jacobs and E. A. Kotomin *Phil. Mag.*, vol. A68, p. 695, 1993.

[129] J. R. Martinelli, E. Sonder, R. A. Weeks, and R. A. Zuhr *Phys. Rev. B*, vol. 33, p. 5698, 1986.

[130] H. P. Liermann and J. Ganguly, "Diffusion kinetics of fe2+ and mg in aluminous spinel: Experimental determination and applications," *Geochim. Cosmochichim. Acta*, vol. 66, no. 16, pp. 2903–2913, 2002.

[131] N. Grimes *Phil. Mag.*, vol. 25, p. 67, 1972.

[132] E. B. Watson and J. D. Price *Geochim. Cosmochichim. Acta*, vol. 66, no. 12, pp. 2123–2138, 2002.

[133] K. Yasuda, C. Kinoshita, K. Fukuda, and F. Garner *J. Nucl. Mater.*, vol. 283-287, p. 937, 2000.

[134] A. R. Cleave, J. A. Kilner, S. J. Skinner, S. T. Murphy, and R. W. Grimes *Solid State Ionics*, vol. 179, p. 823, 2008.

[135] H. Bracht and A. Chroneos *J. Appl. Phys.*, vol. 104, p. 076108, 2008.

[136] S. P. Chen, M. Yan, J. D. Gale, R. W. Grimes, R. Devanathan, K. E. Sickafus, and M. Nastasi *Phil. Mag. Lett.*, vol. 73(2), p. 51, 1996.

[137] B. P. Uberuaga, A. F. Voter, K. E. Sickafus, A. Cleave, R. W. Grimes, and R. Smith *J. Comput-Aided Mater. Design*, vol. 14, p. 183, 2007.

[138] K. Ando and Y. Oishi *J. Chem. Phys.*, vol. 61, p. 625, 1974.

[139] Y. Oishi and K. Ando *J. Chem. Phys.*, vol. 63, p. 376, 1975.

[140] K. P. R. Reddy and A. R. Cooper *J. Am. Ceram. Soc.*, vol. 64, p. 368, 1981.

[141] F. J. Ryerson and K. D. McKeegan *Geochim. Cosmochichim. Acta*, vol. 58, p. 3713, 1994.

[142] Z. Lodziana and J. Piechota *Phys. Rev. B*, vol. 74, p. 184117, 2006.

[143] B. P. Uberuaga, R. Smith, A. R. Cleave, F. Montalenti, G. Henkelman, R. W. Grimes, A. F. Voter, and K. E. Sickafus *Phys. Rev. Lett.*, vol. 92, p. 115505, 2004.

[144] S. T. Murphy, C. A. Gilbert, R. Smith, T. E. Mitchell, and R. W. Grimes *Philos. Mag.*, p. In press, 2009.

[145] G. W. Watson and D. J. Millock *Chem. Commun.*, p. 1076, 2001.

[146] K. E. Sickafus, N. Yu, and M. Nastasi *Nucl. Instr. Methods. B*, vol. 116, p. 85, 1996.

[147] T. R. Hinklin and R. M. Laine *Chem. Mater.*, vol. 20, p. 553, 2008.

[148] C.-T. Ting and H.-Y. Lu *J. Am. Ceram. Soc.*, vol. 82, p. 841, 1999.

[149] H. Jagodzinski and H. Saalfeld *Z. Kristallogr.*, vol. 110, p. 197, 1958.

[150] R. I. Sheldon, T. Hartmann, K. E. Sickafus, A. Ibarra, B. L. Scott, D. N. Argyriou, A. L. Larson, and R. B. Von Dreele *J. Am. Ceram. Soc.*, vol. 82, p. 3293, 1999.

[151] T. Soeda, S. Matsumura, C. Kinoshita, and N. J. Zaluzec *J. Nucl. Mater.*, vol. 283-287, p. 952, 2000.

[152] T. Sawabe and T. Yano *J. Nucl. Mater.*, vol. 373, p. 328, 2008.

[153] Y. Okuyama, N. Kurita, and N. Fukatsu *Solids State Ionics*, vol. 177, p. 59, 2006.

[154] S. T. Murphy, H. Lu, and R. W. Grimes *J. Phys. Chem. Solids*, p. Submitted, 2009.

[155] N. W. Grimes and R. W. Grimes *J. Phys.: Condens. Matter*, vol. 10, p. 3029, 1998.

[156] N. W. Grimes and R. W. Grimes *J. Phys.: Condens. Matter*, vol. 9, p. 6737, 1997.

[157] J.-Z. Zhao, L.-Y. Lu, X.-R. Chen, and Y.-L. Bai *Physica B.*, vol. 387, p. 245, 2007.

[158] K. J. W. Atkinson, R. W. Grimes, M. R. Levy, Z. L. Coull, and T. English *J. Eur. Ceram. Soc.*, vol. 23, p. 3059, 2003.

[159] R. A. Jackson, J. E. Huntingdon, and G. J. Ball *J. Mater. Chem.*, vol. 1, p. 1079, 1991.

Appendices

A

Kröger-Vink Notation

Kröger-Vink notation is a set of conventions used to describe electrical charge and lattice for point defect species in crystals [15]. There are three main parts to the notation; the main body, the subscript and the superscript. The body represents the chemistry of the defect and can by the chemical symbol for an ion (eg. Mg for a magnesium ion) or a V for a vacant lattice site. The subscript represents the location of the defect. Should the defect be located on a lattice site then its location is denoted by the symbol for the atom it has replaced, however, if the defect is positioned on an interstitial site it is denoted with a ($_i$). Finally the superscript represents the charge on the defect; a positive charge is denoted using a ($^\bullet$), a negative charge is denoted by a ( ) and a neutral defect is assigned a ( ). Some examples of Kröger-Vink notation for point defects in a metal oxide, MO, are given in the table below:

Table A.1: Examples of Kröger-Vink notation

Defect	Kröger-Vink notation
Cation Vacancy	V_M
Oxygen Vacancy	$V_O^{\bullet\bullet}$
Cation Interstitial	M_i
Oxygen Interstitial	$O_i^{\bullet\bullet}$
Cation on an oxygen site	$M_O^{\bullet\bullet\bullet\bullet}$

B

Spinel Lattice Sites

Table B.1 is a list of the fractional coordinates of the atoms in a spinel unit cell based on the *Fd3m* space group centred on $\bar{4}3m$.

Table B.1: Fractional coordinates of lattices sites in the cubic unit cell of spinel.

Lattice site	Equipoint	Point symmetry	Fractional coordinates of lattice sites
A-site cation (Mg^{2+})	8a	$\bar{4}3m$	0,0,0; 1/4,1/4,1/4
B-site cation (Al^{3+})	16d	$\bar{3}m$	5/8,5/8,5/8; 5/8,7/8,7/8; 7/8,5/8,7/8; 7/8,7/8,5/8
Anion (O^{2-})	32e	*3m*	*u,u,u; u,ū,ū; ū,u,ū; ū,ū,u;* (1/4-*u*),(1/4-*u*),(1/4-*u*)); (1/4+*u*),(1/4+*u*),(1/4-*u*)); (1/4+*u*),(1/4-*u*),(1/4+*u*)); (1/4-*u*),(1/4+*u*),(1/4+*u*));